Physical analysis of electroactive morphing concepts for the aerodynamic performance increase of future wing design through high-fidelity numerical simulation and turbulence modelling in high Reynols number

Abderahmane Marouf

To cite this version:

Abderahmane Marouf. Physical analysis of electroactive morphing concepts for the aerodynamic performance increase of future wing design through high-fidelity numerical simulation and turbulence modelling in high Reynols number. Fluids mechanics [physics.class-ph]. Université de Strasbourg, 2020. English. NNT : 2020STRAD025 . tel-03855969

HAL Id: tel-03855969

https://theses.hal.science/tel-03855969v1

Submitted on 16 Nov 2022

UNIVERSITÉ DE STRASBOURG

ÉCOLE DOCTORALE Mathématiques, Sciences de
l'Information et de l'Ingénieur (MSII)

Laboratoire ICUBE (UMR7357)

THÈSE présentée par :

Abderahmane MAROUF

soutenue le : 15 octobre 2020

Pour obtenir le grade de

Docteur de l'université de Strasbourg

Discipline/Spécialité : **Mécanique des fluides**

Physical analysis of electroactive morphing concepts for the aerodynamic performance increase of future wing design through High-Fidelity numerical simulation and turbulence modelling in high Reynolds number

---

DIRECTEURS DE THESE

Prof. Yannick HOARAU	**Université de Strasbourg, France**
Dr. Marianna BRAZA	**Directrice de recherche CNRS, IMFT Toulouse, France**

RAPPORTEURS

Prof. Frank THIELE	**Technische Universität Berlin, Germany**
Prof. Yiannis VENTIKOS	**Director of the Mechanical Engineering Dept, University College London, England**

EXAMINATEURS

Prof. Henda DJERIDI	**INP de Grenoble, France**
Dr. Denis DARRACQ	**AIRBUS Toulouse, France**
Dr. Flavien BILLARD	**DASSAULT Aviation, France**

Analyse physique de concepts du morphing électroactif pour accroître les performances aérodynamiques des ailes du futur par simulation numérique de Haute Fidélité et modélisation de la Turbulence à nombre de Reynolds élevé

Acknowledgements

This work has been conducted in a collaboration between the research group MécaFlu of the ICUBE Laboratory in Strasbourg and ASI (EMT2) team of the Institut de Mécanique des Fluides de Toulouse (IMFT).

First of all I would like to particularly thank the members of the jury for their devoted time and advices.

I would like to express my gratitude to thank to my supervisors, the head of the Mechanical department of ICUBE Prof. Yannick Hoarau and Dr. Marianna Braza from the IMFT for guiding, encouraging, supporting and trusting me during this project.

Warm thanks to my colleagues from Strasbourg and Toulouse and all the interns that were kindly exploited.

Most important I would like to thank all my family and all those who believed in me and helped me during all these years. A special thanks to my dear parents, Ante Jamaa, sisters and brothers. To my wife *Dounia* and my daughter *Eline*, thank you both for being my joy and for your support during all these years.

Preface

The present document examines the physical analysis electroactive morphing of future wing designs by means of high-fidelity numerical simulations and adapted turbulence modelling in high Reynolds numbers. This thesis constitutes a dissertation for obtaining the Doctorat de l'Université de Strasbourg degree in Fluid Dynamics, awarded by the Doctoral School MSII (Mathématique Sciences de l'Information et de l'ingénierie) with the collaboration of ICUBE-Strasbourg and Institut de Mécanique des Fluides de Toulouse (IMFT) laboratories.
This thesis was carried out under the supervision of Prof. Yannick HOARAU in the Mechanical department (MécaFlu team) at ICUBE and Dr. Marianna Braza in Aérodynamique Sillage et Interaction (ASI) group at IMFT from October 2017 to October 2020. It was supported by the university of Strasbourg.
All the simulations were performed with resources allocated by the French national computing centers as : HPC-Strasbourg, CINES (Centre Informatique National de l'Enseignement Supérieur), CALMIP (Calcul en Midi-Pyrénées), IDRIS (Institut du développement et des ressources en informatique scientifique) and CEA TGCC (Tres Grand Centre de calcul du CEA). Thanks to the PRACE (PaRtnership for Advanced Computing in Europe) allocation of 15 million CPU hours (project Number 2017174208) which was contributed to the SMS project.

ABSTRACT

This thesis aims at investigating efficient concepts for morphing wings design in different scales (reduced and near scale one), in the subsonic regime and at different stages of the flight. The study has been carried out by High-Fidelity numerical simulations using adapted turbulence modelling closures able to sensitise the coherent structures development. A special attention is paid to the fundamental mechanisms and physical understanding of the flow around the wing and their modification when the morphing is activated. Electroactive morphing concepts are implemented in the Navier Stokes MultiBlock (NSMB) solver and a large parametric study concerning the actuation frequencies and amplitudes has been accomplished in a similar way in synergy with the experimental studies in the H2020 European research project SMS, "Smart Morphing and Sensing for aeronautical configurations". The morphing concepts investigated in this thesis concern the effects of near trailing edge actuation and low deformation in the frequency range of (30 - 400) Hz by means of piezoactuators, as well as by high deformation cambering (as in experiments through Electromechanical or Shape Memory Alloys actuations), in low frequency (order of 1Hz) and finally, by associating both, in the context of hybrid electroactive morphing. The considered prototypes have been those of the SMS project, the Reduced scale (RS) and the Large Scale (LS) two element wing-flap high lift prototype of an A320 wing. Two- and three-dimensional simulations were carried out using adopted turbulence modelling approaches as the Organised Eddy Simulation OES model and Hybrid methods as the Detached Eddy Simulation, to reveal the surrounding turbulence and the wake's coherent structures as the Kelvin Helmholtz and von Kármán vortices leading to the alternating vortices in the wake using spectral analysis. These models have been able to capture the morphing effects through the actuations and to provide the aerodynamic performance increase. It has been shown that optimal trailing edge vibrations are able to suppress the three-dimensional motion in the wake and to lead to a lift increase of +4.28 % and lift-to-drag of +1.61 % on the RS prototype. An optimal vibration has been studied in case of the LS high lift prototype and provided a lift increase of +0.55 % together with noise sources reduction past the trailing edge of -15 to -20 dB. An optimal cambering system has been derived and studied for the LS prototype, being near full scale and leading to a lift-to-drag performance of +3.26 %. These benefits have been studied in the case of a full A320 aircraft and provided a +2.24 % lift-to-drag increase. Finally the simultaneous and bio-inspired association of the cambering and the trailing edge vibrations in the hybrid electroactive morphing context, revealed a -0.71 % of drag decrease, leading to a considerable augmentation of lift-to-drag ratio of +0.50 % compared to only cambering. These investigations have been carried out in the H2020 N° 723402 European Research programme SMS project.

Résumé

Cette thèse vise à étudier des concepts pour le design des ailes en morphing à différentes échelles (échelle réduite et proche à l'échelle réelle), en régime subsonique en différentes phases de vol. L'étude a été réalisée à l'aide des simulations numériques haute-fidélité utilisant des modèles de turbulence adaptés capables de capturer le développement des structures cohérentes. Une attention particulière est portée aux mécanismes fondamentaux et à la compréhension physique de l'écoulement autour de l'aile et à leur modification lorsque le morphing est activé. Les concepts de morphing électroactifs sont implémentés dans le solveur Navier Stokes MultiBlock (NSMB) et une étude paramétrique a été réalisée en synergie avec les études expérimentales du projet Smart Morphing and Sensing (SMS). Les concepts de morphing étudiés dans cette thèse concernent les effets de l'actionnement proche du bord de fuite à faible déformations dans une plage de fréquences de (30-400) Hz avec les actionneurs piézoélectriques, ainsi que par une cambrure à grande déformation (similaires aux expériences assurées par les actionneurs Electromécaniques et les Alliages à Mémoire de Forme) et faibles fréquences (de l'ordre 1 Hz) et enfin, en associant les deux, dans le cadre du morphing électroactif hybride. Les prototypes considérés ont été ceux du projet SMS, l'aile à échelle réduite (RS) et le système hypersustentateur à deux éléments à grande échelle (LS) d'une aile A320. Des simulations 2D et 3D ont été réalisées en utilisant l'approche de modélisation de la turbulence "Organised Eddy Simulation" OES et des méthodes hybrides comme la "Detached Eddy Simulation" DES, afin de révéler les structures turbulentes et cohérentes du sillage comme les instabilités de Kelvin Helmholtz et von Kármán conduisant à la création des tourbillons alternés en se basant sur l'analyse spectrale. Ces modèles ont été en mesure de capturer les effets de morphing grâce aux actionnements et de fournir une augmentation des performances aérodynamiques. Il a été démontré que les vibrations optimales du bord de fuite sont capables de supprimer le caractère tridimensionnel du sillage et de conduire à une augmentation de la portance avec +4.28 % et la finesse aérodynamique de +1.61 % sur le prototype RS. Une vibration optimale a été étudiée dans le cas du prototype LS qui a fourni une augmentation de la portance de +0.55 %, ainsi qu'une réduction des sources de bruit proche du bord de fuite de -15 à -20 dB. Le système de cambrure optimale a été étudié pour le prototype LS étant proche de l'échelle réelle, il a conduit à une augmentation de la finesse de +3.26 %. Ces bénéfices ont été étudiés dans le cas d'un avion A320 complet et ont permis une augmentation de CL/CD de +2.24 %. Enfin, l'association simultanée et bio-inspirée de la cambrure et des vibrations du bord de fuite dans le contexte de morphing électroactif hybride, a révélé une diminution de la trainée de -0.71 % et une augmentation de la finesse de + 0.50 % comparé à la cambrure seule. Ces recherches ont été menées dans le programme Européen H2020 N° 723402 du projet SMS.

Contents

List of Figures

List of Tables

Nomenclature

ρ	density	kg/m^3
p	pressure	Pa
T	temperature	K
C	chord length	m
S	reference surface	m^2
ν	dynamic viscosity	Pa s
f_a	frequency of actuation	Hz
St	Strouhal number $St = \frac{f.c}{U_{inf}}$	non-dimensional
Re	Reynolds number $Re = \frac{\rho UC}{\nu}$	non-dimensional
u, v, w	velocity components following (x,y,z) directions	m s^{-1}
$\omega_x, \omega_y, \omega_z$	vorticity components in (x,y,z)	1/s
M	Mach number $M = U/a$ with a is sound velocity	non-dimensional
U_∞	free stream velocity	m s^{-1}
CD, D	drag coefficient and force $CD = \frac{D}{1/2\rho S U_\infty^2}$	non-dimensional
CL, L	lift coefficient and force $CL = \frac{L}{1/2\rho S U_\infty^2}$	non-dimensional

vK	von Kármán
KH	Kelvin-Helmholtz
SL	Shear Layer
RS and LS	Reduced Scale and Large Scale
MFC	piezoelectric Macro-Fiber Composite Patches
SMA	Shape Memory Alloy
EMA	Electro-Mechanical Actuators
POD	Proper Orthogonal Decomposition
ROM	Reduced Order Model
PSD	Power Spectral Density
TT	Turbulent Turbulent Interface
TNT	Turbulent Non Turbulent Interface

Chapter 1

Introduction

About 3 billion people, 39 % of the world population take a flight every year for different purposes as for instance business, tourist trips, and about 5 trillion Euros worth of goods are transported by airplane. The increase of passengers is expected to reach over 6 billion by 2030, according to the current statistics and projections.

Polluted atmosphere due to the exhaust gas produced by airplanes and generated noise during take-off and landing are simultaneously increasing. This has imposed significant challenges on the aeronautical industry. Aircraft manufacturers as for instance Airbus and researchers are constantly looking for new innovative solutions to make the airplanes lighter with optimized shape in order to increase aerodynamic performances, achieving at the same time greater fuel efficiency to reduce the environmental footprint of air transportation. Coordinated by the Institut National Polytechnique de Toulouse (INPT), the Smart Morphing and Sensing for aeronautical configurations (SMS) project (`http://smartwing.org/SMS/EU/`) brought together 10 European partners from 5 countries with a common goal : to construct different scale prototypes of morphing A320 wing in different flight phases with the objective of increasing the aerodynamic performance, decreasing the noise sources and reduce the energy consumption, fuel and pollution regarding Nox and CO2, as dictated by the European Commission ACARE (Advisory Council for Aviation Research and Innovation in Europe), in H2020 and in Horizon Europe. These innovations are obtained thanks to a new generation of electroactive materials able to optimize the wing's aerodynamic shape and vibrational behaviour during all flight stages : take-off, climbing, cruise, approach and landing. A target focus of this new design is to obtain a decrease by at least 1% of fuel consumption and 0.5% of CO2 emission.

The electroactive morphing technology can contribute to decrease the weight issue by replacing to the hydromechanical systems mounted in the wing in order to move out the flap and the slat in different flight stages. It was noted that if 1 % drag reduction could be obtained by means of morphing concept and design, 140 million dollars per year could be saved on fuel necessary to operate the US aircraft fleet.

Nowadays, a fast and continuous progress of super computing performances and numerical methods for solving physical models for flow simulations have motivated the aeronautics industry to rely on Computational Fluid Dynamics (CFD). Real viscous flows around high complex geometries as for instance a complete airplance, fighter jets or rockets are practicable. The CFD reduces considerably the number of wind tunnels tests in the design of new products, thus the cost can be considerably decreased. In aeronautics, CFD applications are not only restricted to aerodynamics. Moreover, flow simulations are also useful in aeroelasticity, aeroacoustics and more recently in morphing designs.

High-Fidelity numerical simulations are now more reliable with the fast development of supercomputers enabling flow simulation around wings using millions of cells through parallel computations. The current CFD approaches are able to predict most instantaneous and dangerous instabilities around the wings which occur during the flight and can cause an airplane crash, as the deep dynamic-stall phenomena induced by high angle of attack and a full detachment of the boundary layer which leads to considerable loss in aerodynamic efficiency.

Advanced turbulence modelling have been widely investigated in order to capture more efficient and reliable physics when the flow is complex as for instance compressible flows around wings at high Reynolds numbers during the cruise flight stage (transonic regime). The buffet phenomenon appearing for a specific range of Reynolds-Mach numbers can be predicted with sufficient accuracy and may lead to critical conditions as for instance the amplification of the dip-flutter instability. (see collected studies in : (Doerffer et al. (2020)) as well as (Grossi et al. (2014), Simiriotis (2020), Szubert (2015), Tô et al. (2019), among other.

High-Fidelity numerical models have been recently built and used to simulate the fluid-structure interaction of morphing wings, partly bio-inspired from the birds wings. They are able to predict the flow modification and the morphing effects around the wing due to the modification and vibrational behaviour of selected parts of the wing's surface. The amplification of instabilities in the flow are essential mechanisms to be manipulated by the morphing. These phenomena are in particular at the origin of the coherent structures which can be identified in turbulent flows in the low and high Reynolds number ranges. The study of the effects linked to the presence of organised

structures within turbulent flows and the methods how to capture them are important steps in development of an effective morphing wing design through turbulence control thanks to fundamental understanding of the governing mechanisms.
The main challenges are to find out through a thorough investigation how to manipulate the coherent vortex structures thanks to shape modification with suitable vibrations and slight deformations, in order to optimally modify the pressure distribution around the wing to obtain a simultaneously increase of lift, decrease of drag and reduction of the aerodynamic noise sources. It is worth noticing that the wings noise represents a considerable percentage of the total noise produced by an airplane.

1.1 Manuscript organisation

During this thesis, the development of relevant methods for morphing within the framework of an hierarchical approach of flow modelling has been carried out and reported in this manuscript, articulated as follow :
chapter 2 is devoted to bibliography of most relevant morphing methods aiming at producing efficient morphing wings.
In this context, related to the flow instabilities and coherent structures development, the bibliography includes main studies that had contributed to the birth of coherent structures as the Reynolds number increases in the transition of the dynamic system composed of a body and the surrounding flow in its transition to turbulence. In this context , the natural instabilities are investigated, the development of the coherent structures and the creation and explanation of Turbulent-Non-Turbulent interfaces. Relevant studies in the state of the art concerning electroactive morphing wings are presented and focus on the flow modification through the actuations is mentioned.
In chapter 3, the numerical methods and turbulence modelling used in the present thesis are presented. These methods aiming to shape deformation and grid re-meshing are also described. In chapter 4, morphing of trailing edge through high-frequency and low-amplitude of deformation is examined and applied for a Reduced-Scale Airbus wing prototype of the SMS project with a fixed span. The study focuses on the wake dynamics and their modifications under spectral analysis, the actuations and suppression of three-dimensional instabilities using the POD approach and reconstruction of the dynamic system by means of a reduced number of the most energetic modes. Time-averaged aerodynamic performances are also evaluated for the static

(no morphing) and morphing configurations. This is followed by chapter 5 where a parametric analysis of the Large-Scale high lift two-element prototype two-element wing-flap constructed (LS prototype of the SMS project), *near scale 1* is examined under the same kind of vibrations. The frequency and amplitude of the piezo-actuations of the flap's trailing edge are investigated in order to figure out optimal morphing parametric ranges. Afterwards, in chapter 6, a new design of a cambered flap for the LS prototype is proposed, that allows producing optimal cambering in quasi-static configuration as well as in dynamic cambering using high amplitude-low frequency deformations. The study focuses on the effects of the camber downwards direction in the take-off conditions aiming at improving the lift and lift-to-drag ratio. Upward cambering is also considered at higher angles of attack near the stall conditions and investigated its effects aiming at attenuation of stall in case of manoeuvrability. Finally, chapter 7 deals with an innovative electroactive *hybrid morphing* simultaneously associating high cambering deformation and higher frequency vibration in low deformations for a real scale Airbus A320 airplane at take-off conditions. Optimal conditions obtained in chapter 4, 5 and 6 in terms of frequency and amplitude of the deformations are taken into account and used in chapter 7 providing a final evaluation of the aerodynamic performances.

Chapter 2

State of the art

Contents

FIGURE 2.1: Bio-inspiration

2.1 Introduction

For a thousand of years, humans have been observing birds from the ground with wonder and jealousy. This curiosity to understand how birds are able to fly in the air has motivated humans' desire to fly. Earliest concepts attempted directly at flying by emulating birds. As Leonardo da Vinci said "*a bird is an instrument working according to a mathematical law. It lies within the power of man to make this instrument with all its motions.*" Since then birds are the source of inspiration for airplanes development in order to become more energetically efficient. However, today they look quite different from birds in many aspects.

Based on their observations of all kinds of birds, Clement Ader, Otto Lilienthal, Wright brothers tried perfectly to imitate the birds and learn how they fly. Figure 2.2 demonstrates the Avion III built by Clément Ader that was inspired from the batlike configuration. It was equipped with two engines driving two propellers that had a featherlike structure.

FIGURE 2.2: Avion III of Clément Ader in the Museum arts et métiers at Paris, France (`www.gouvernement.fr`)

In fact, through experiments and comparison, researchers have found that airplanes can achieve better efficiency if they can behave more like birds in flight, and morphing technology makes it possible. The following sections will introduce the concept of morphing and its biological inspiration, the history of wing morphing technology, its benefits to the real flight, different wing-morphing approaches, as well as some of the limitations.

The designed aircrafts of nowadays are equipped with high-lift systems able to modify their locations to improve lift-to-drag ratio of the airplane. Nevertheless, birds can do better with their large adaptability and flexibility in the deformation of their wings. They have high manoeuvrability capacities and flight adaptation, especially when they are faced to different external situations. They can easily change the direction, velocity and angles of attack and pitching as can be seen in figure 2.3.

A novel discipline known as morphing wings has attracted researchers around the world and is mostly used in aeronautics. The morphing consists of the modification of original structural shapes using fully integrated smart materials within an integration of active devices (actuators and sensor systems). These devices are integrated inside structural parts of the airplane.

FIGURE 2.3: Bird Flight (from the top left to the right): loitering, approach, diving, landing, approach, take-off (Concilio et al. (2018)).

2.2 Morphing for future airplanes

Morphing airplanes have attracted a great interest in the past few decades because of their capabilities to increase both aerodynamic and the structural performances by changing the slat, wing, flap and winglets shapes according to different flight conditions.

Bio-inspired concepts

One of Airbus goals is to make flying cleaner, greener and quieter than ever before. Back again to nature, Airbus revealed at the Royal International Air Tattoo air show in the United Kingdom a bird-like aircraft known as bird of prey (see figure. 2.4), a new conceptual airliner for regional transportation partly bio-inspired from efficient mechanics of eagles by applying technologies of hybrid-electric propulsion, active control systems and advanced composite structures. The wings (slats, wings, flaps and winglets) and the tail (elevator and horizontal stabilizer) mimic those of a bird of prey and feathers for an active flight control. A multiple winglets will reduce the wing tip vortices intensity by spreading and breaking them, these rolling vortices don't merge because they are circulating in the opposite directions and they dissipate slowly and linger in the atmosphere. They are associated with induced drag and generate three-dimensional lift which reduces the effective angle of attack of the air on the wing.

FIGURE 2.4: Future concept of Airbus 'Bird of prey' presented in Royal International Air Tattoo air show in the UK (`www.airbus.com`)

This remains only a proposed concept and a new design for new future transport airplanes aiming to motivate researchers and engineers to think more about friendly airplanes looking more similar to birds and produce less air pollution in the environment.

Variable Camber Continuous Trailing Edge Flap (ACTE)

Since 2012, NASA has been working with the US Air Force research laboratory and FlexSys on the ACTE project (Adaptive Compliant Trailing Edge) (see figure 2.5). In order to construct an advanced design of a flap able to make deflection in the downward and upward directions in order to increase aerodynamic efficiency and reduce noise in the airport during the landing and take-off phases. This experiment was conducted on a modified Gulfstream III (G-III) business jet that was changed into an aerodynamic research test bench at Armstrong Flight Research Center of NASA, Cruz and Miller (2016). Several real flight tests were conducted into the project ACTE and revealed 3 to 10 % of drag reduction using only 2 degrees of upwards deflection. A considerable reduction of the wing weight up to 20 % using this new system of flaps has been achieved which allows to have more efficiency with low fuel consumption. In addition, through acoustic measurement, it was noticed that 4-6 dB noise reduction during approach & landing and structural load alleviation.

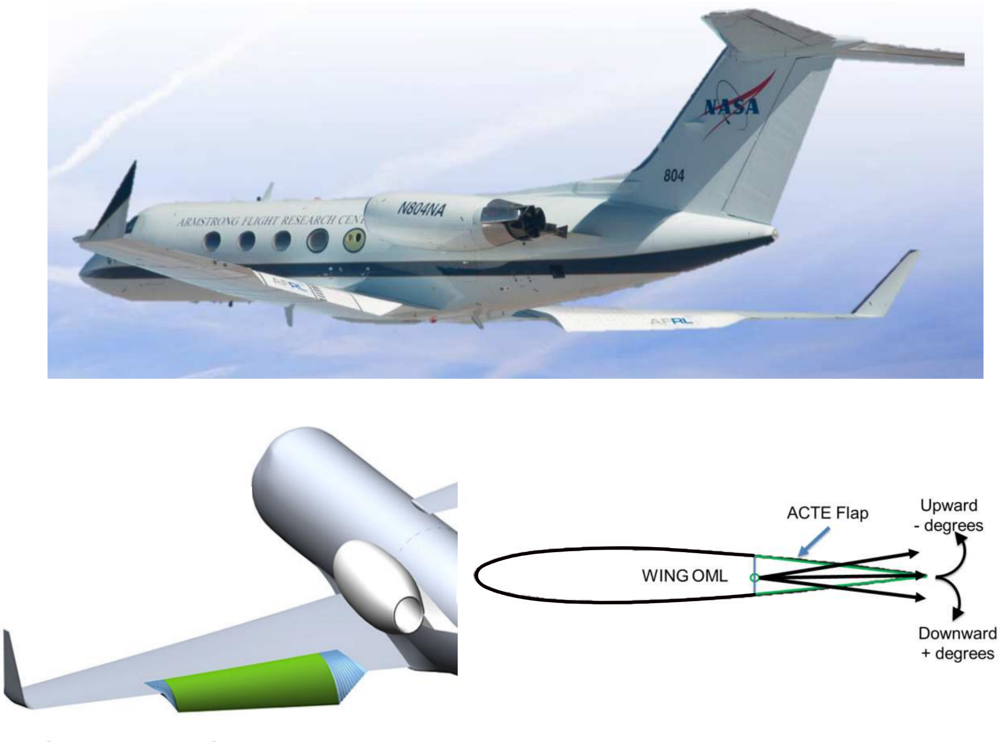

FIGURE 2.5: (Adaptative continuous flap deflection embedded on the Gulfstream III business (Cruz and Miller (2016))

Smart Intelligent Aircraft Structures (SARISTU) project

From September 2011 to August 2015, Airbus coordinated the Smart Intelligent Aircraft Structures (SARISTU) project, which brings together 64 partners from 16 countries and different sub-projects. Each of theses projects investigated a development of

a specific technology in order to be integrated into a full-scale wing test bench demonstrator. The projects exploited the adaptative leading-edge aimed to increase the aerodynamic performance during the take-off and landing phases and focused on providing new innovative winglet system with trailing edge adaptation. It aims to achieve a reduction in the weight of the aircraft and operating costs, as well as improving the specific aerodynamic performance of the flight profile. The project focuses on integration activities in three distinct technology areas: wing-compliant morphing, auto-sensing and multifunctional structures through the use of nano-reinforced resins.
The figure 2.6 shows what has been done in the activity on the conformal morphing of the wing:

- Design of a laminar wing by integrating suitable surface on the leading edge to reduce drag during all phases of flight as well as aerodynamic noise.
- Changing the aileron structure to reduce fuel consumption and to increase the lift-to-drag ratio.
- Optimization of trailing edge shape to reduce wing weight and performance gain.

However, Airbus announced that the SARISTU project exhibits no gain in aerodynamic performance in the global gain which was null through the added mass and systems concerning commercial factors.

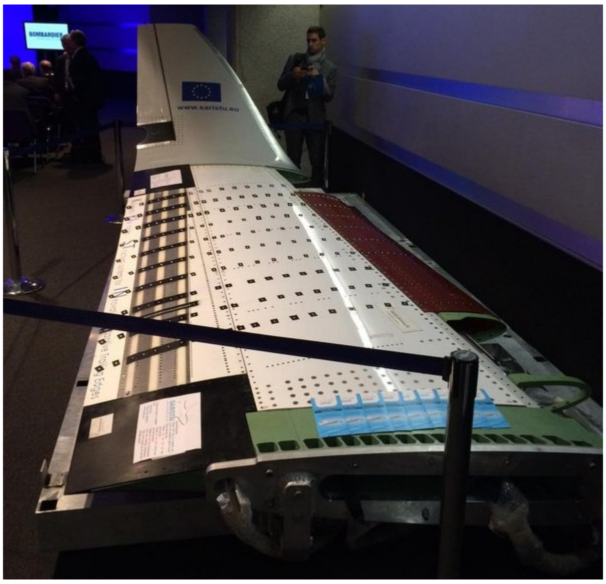

FIGURE 2.6: The wing from SARITSU project `www.SARITSU.eu`

Hybrid electroactive morphing at real scale, application to Airbus A320 wings

The multi-disciplinary team created by the IMFT (Institut de Mécanique des Fluides de Toulouse) and LAPLACE (Laboratoire Plasma et Conversion d'Energie), founded the Smart Morphing Centre in Toulouse `www.smartwing.org`, studying electroactive morphing concepts for future wing design in collaboration with AIRBUS ETCT "Emerging Technologies and Concepts Toulouse". In this context, thanks to the considerable support of the STAE Foundation "Sciences et Technologies pour l'Aéronautique et l'Espace", `http://www.fondation-stae.net/`, bio-inspired morphing concepts have been derived and thoroughly investigated (cf. the video devoted by the Journal of CNRS in these studies: `https://lejournal.cnrs.fr/videos/the-wings-of-the-future` in multiple time and length scales, as dictated by the turbulence structures surrounding the wing and developed in its wake. This multi-disciplinary team discovered and investigated the *hybrid morphing* concept wing (Scheller (2015)) by simultaneously actuating different classes of smart materials in low frequencies (order of 1 Hz) with high deformations (order of 15 % of the chord's length), and simultaneously create higher frequency vibrations (order of 500 Hz) with low deformations (order of 1 % of the chord's length), like the wings and feathers of the large span birds respectively.

This is one of the main original aspects of the H2020 N ° 723402 SMS European project that will be further investigated in the present PhD thesis. This project aims at improving the aerodynamic performances by increasing the lift, decreasing the drag and to attenuate the aerodynamic noise by means of novel electroactive morphing concepts (see figure 2.7). Instead of the classical high-lift system, a morphing flap is

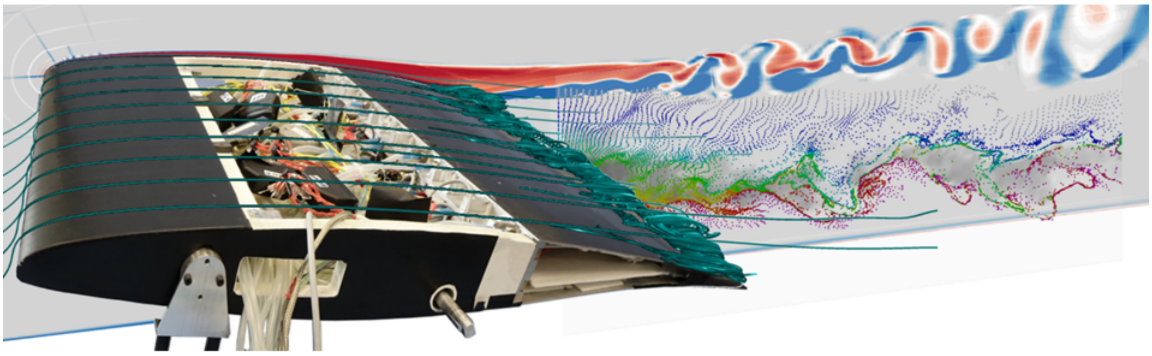

FIGURE 2.7: Reduced scale A320 morphing wing prototype of the SMS European project(IMFT-LAPLACE) : experimental (TRPIV) in S4 IMFT's subsonic wind tunnel and numerical (CFDSM) results

installed, able to change its shape dynamically to adapt it to different flight configurations as take-off, cruise and landing. The multidisciplinary team IMFT-LAPLACE created in 2010 the research platform (`http://smartwing.org`) including the participation of six French laboratories in the context of the national research projects EMMAV (Electroactive Morphing for Micro Air Vehicles), DYNAMORPH (Dynamic Regimes Electroactive Morphing) and SMARTWING followed by two research projects in collaboration with AIRBUS "Emerging Technologies and Concepts Toulouse" (ETCT). These activities were supported by the Foundation STAE (Sciences et Technologies de l'Aéronautique et Espace)[1] and preceded the European programme SMS, (2017-2020). This European project is unique thanks to its strong multidisciplinary character and degree of innovation. Figure 2.8 demonstrates different objectives that were set to investigate the aerodynamic performances increase through advanced Hi-Fi numerical simulations providing together with experimental measurements a large database for the morphing wing and the two-element wing-flap configuration at different scales and flow regimes.

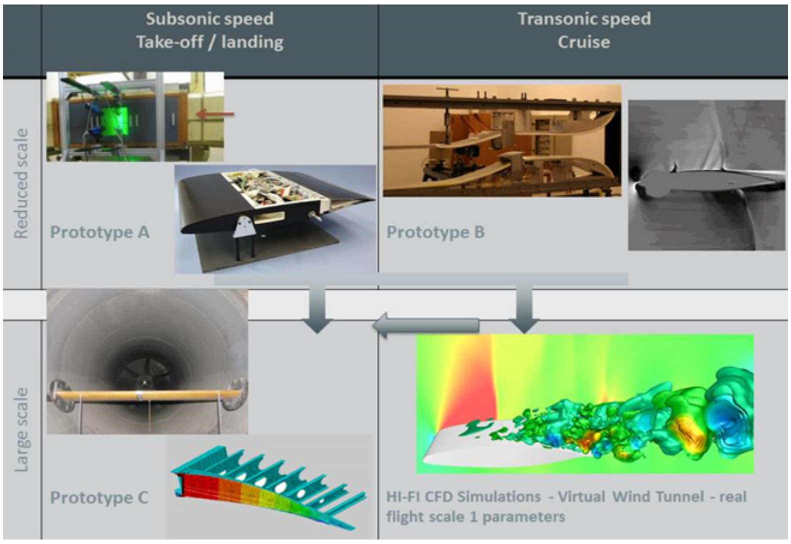

FIGURE 2.8: Schematic representation of the SMS prototypes and final target achievements

- The Reduced-Scale (RS) prototype with a chord of 70 cm at clean configuration was mounted in the IMFT S4 wind tunnel and tested in subsonic conditions. This model is able to camber at high deformation using low frequency control by means of SMA (Shape Memory Alloy). Furthermore, this mock-up

---

[1] http://fondation-stae.net

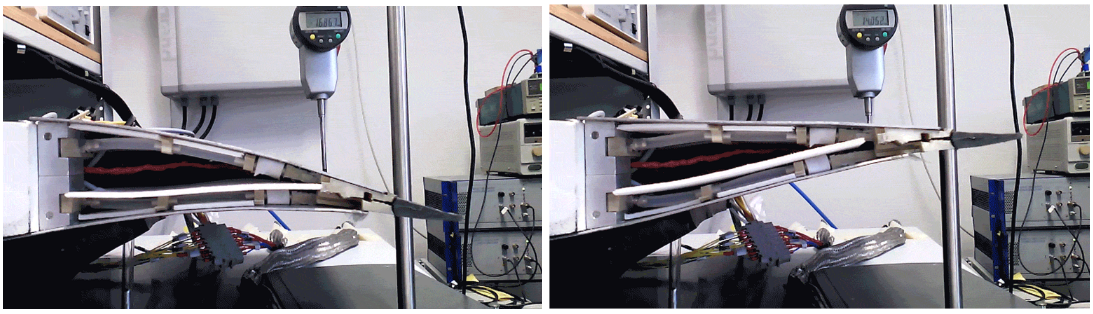

FIGURE 2.9: High-deformation low-amplitude morphing of the Reduced-Scale (RS) prototype of the SMS European project cambered by means of Shape (Jodin et al. (2017))

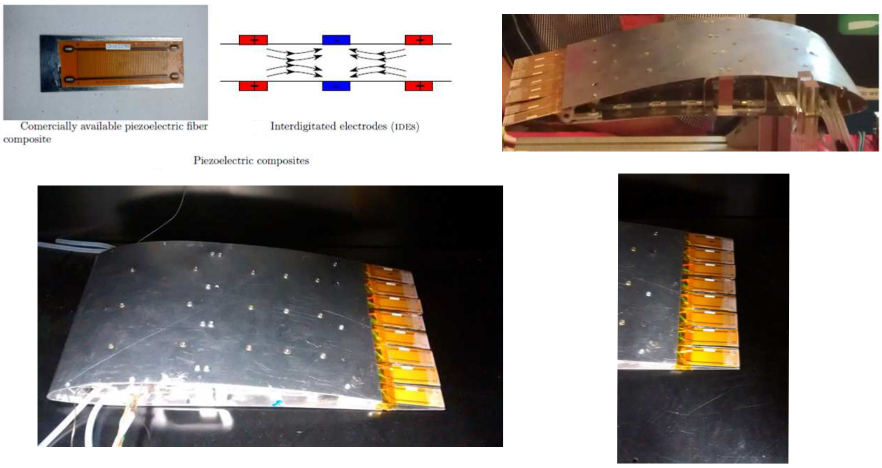

FIGURE 2.10: High-Frequency Low-Amplitude actuations of trailing edge (Scheller (2015))

is equipped by piezoelectric actuators near the trailing edge region along the span, allowing higher frequency vibrations at low amplitude deformation (see figures 2.9 and 2.10). In addition, numerical simulations were performed in the same context to produce a synergy with the experiments.

- The Large-Scale (LS) prototype with a chord of 2.40 m in clean configuration. This prototype is composed of a two-element wing-high lift flap system. The flap's chord is equal to 1 m. This dimension corresponds approximately to a mid-span dimension of the high lift flap of the A320 wing. Therefore, this configuration is near scale 1 and aims at demonstrating that the morphing concepts are applicable in real scale. The LS prototype can operate in take-off and landing positions up to a total chord of 2.72 m. The flap is able to come out of the fixed wing's part with the same geometrical law as in real flight. In addition, the high-lift flap is *deformable* in cambering. Experiments are conducted in the IMFT's large subsonic wind tunnel S1 for the take-off and clean configurations with a spanwise dimension of 2m. In these experiments, a novel system of multi-point sensing is tested for the first time in the state of the art, constructed by the SMS partner CEMENTYS Company. A main part of the experiments have been carried out in Polytechnic of Milano (POLIMI), SMS partner with the contribution of IMFT-LAPLACE, who provided the morphing flap having 2 m span and participated in its installation in the wind tunnel of POLIMI, where it was embedded in a 4 m span wing's configuration. In parallel numerical simulations were carried out for both configurations (IMFT and POLIMI) and for the take-off and landing by IMFT/ICUBE (present thesis) and CFS-Engineering - SMS partner.

FIGURE 2.11: The LS prototype in POLIMI's wind tunnel involving the high-lift morphing flap constructed in the IMFT's workshop thanks to the structural design by (Bmegaptche et al. (2019)), in collaboration with LAPLACE (D. Harribey - J.F. Rouchon). Photo in the POLIM wind tunner by courtesy of F. Auteri.

- The transonic Reduced-Scale (tRS) prototype of a 15 cm chord was designed and constructed by LAPLACE to be tested experimentally in the IMP-PAN transonic wind tunnel of 15 cm test section, as shown in figure. 2.12. This prototype is equipped by an appropriate piezo-actuator system applying vibrations in the range of 50 - 350 Hz) and slight deformation of the near trailing edge region (amplitude of order 1-5 mm). This prototype aims at investigating the aerodynamic performance increase, in particular the drag reduction, in cruise conditions.
- High-Fidelity numerical simulations in transonic conditions on the RS prototype as well as in full scale, investigating the morphing effects on the Shock Wave Boundary Layer (SWBL) interaction in the transonic regime corresponding to the cruise phase.

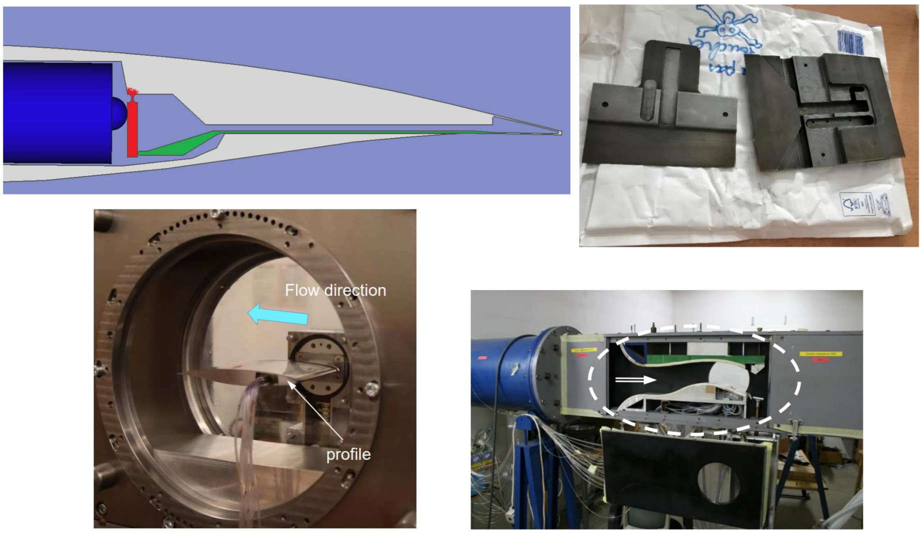

FIGURE 2.12: Transonic Reduced-Scale (TRS) design, prototype and wind tunnel transonic tests at IMP-PAN (`www.smartwing.org/SMS/EU`)

The SMS project covers all the flight stages using different scales prototypes and multidisciplinary teams around the Europe in order to achieve better aerodynamic performance as an increase of the lift, decrease of the drag and the aerodynamic noise by manipulating the surrounding turbulence, as dictated in prior studies of the research team IMFT-LAPLACE in the years 2010-2015 who made evidence of their research in Smart wing design through turbulence control: "Science imitating Nature". Thanks to this topic, they were honorifically invited by the Royal Society annual Exhibition in 2014 to animate the Morphing stand under the same title in collaboration with Imperial College London, `https://www.youtube.com/watch?v=AoAaCCvn38M/`.

There are several types of morphing structures used for different purposes but there is a lack of understanding the importance of the flow dynamics manipulation along the shear layers and downstream in the near wake, able to produce thanks to fluid-structure interaction highly beneficial feedback effects regarding the pressure and skin friction distributions all over the wing, thus providing considerable benefits in the forces and the noise reduction. These aspects will be investigated in detail in the present thesis. The morphing that concerns our study is more focused on the development of future innovative wings and more precisely the morphing of the hyper-lift flap of the wing of an Airbus A320. Compared to the previous projects, our study provides an original concept of partly bio-inspired morphing wings using electroactive materials. It combines numerical and experiments with a synergy to understand fundamental changes of the flow behaviour and its modification through the dynamic actuations. In addition, considerable efforts are focused on the understanding of the flow instabilities in the separated shear layers around the body and in the wake, as well as their modification through the vibrations and slight deformations operated by the actuation.

2.3 The transition to turbulence around bluff bodies as the Reynolds number increases

External aerodynamic flows are generally unsteady according to the Reynolds number, they can be laminar, transitional or fully turbulent. Thus, successive stages of the transition to three-dimensionality around a cylinder of an incompressible flow and a NACA0012 with a constant span will be described in this section. In addition, the wake modification of a cylinder at an imposed rotation at different speeds is examined in order to analyse the modification of the wake instabilities. Finally, turbulent wakes at high Reynolds is examined through its different Turbulent-Turbulent (TT) and Turbulent-Non-Turbulent (TNT) interfaces.

Successive stages of the transition to turbulence as Reynolds number increases: low Reynolds range

It is important to understand the mechanisms of the transition to turbulence for incompressible fluid flows at low and moderate Reynolds numbers to analyse the amplification of main instabilities and birth of coherent structures that *persist* in the high Reynolds number range in a fully turbulent flows are of the same kind as those born in the low Reynolds range. The flow around a body in high Reynolds number is not characterised by a chaotic turbulence only. This is the case at quite far distances, over hundreds of a characteristic length scale, e.g. the diameter of a cylinder of the chord of a wing. The turbulence in the near and intermediate region up to far distances is governed by a dual character, organised and chaotic. It contains well distinct coherent structures, formed after amplification of specific instabilities, interspersed and embedded by chaotic turbulence motion. In the following, the term "transition" corresponds to low Reynolds number successive stages of the flow and does not mean "high-Reynolds boundary layer transition".

The three-dimensional unsteady flow around a circular cylinder at a laminar regime

has been examined experimentally by (Williamson (1992)) among other quite numerous studies. DNS by Persillon and Braza (1998) found that the flow becomes three-dimensional in the range of $180 < Re < 300$. An undulation starts to appear in the turbulent structures associated to the von Kármán vortices in the transversal direction along the spanwise direction of the cylinder and some longitudinal vortices start to appear. This corresponds to the development of the secondary instability.
Two successive discontinuities were observed experimentally (Williamson (1992)) and numerically by DNS (Allain (1999), Persillon and Braza (1998)) in the evolution of the Strouhal number as a function of Reynolds number (see figure 2.13).
Theses discontinuities correspond to two different topologies present in the wake as illustrated in the figure 2.14:

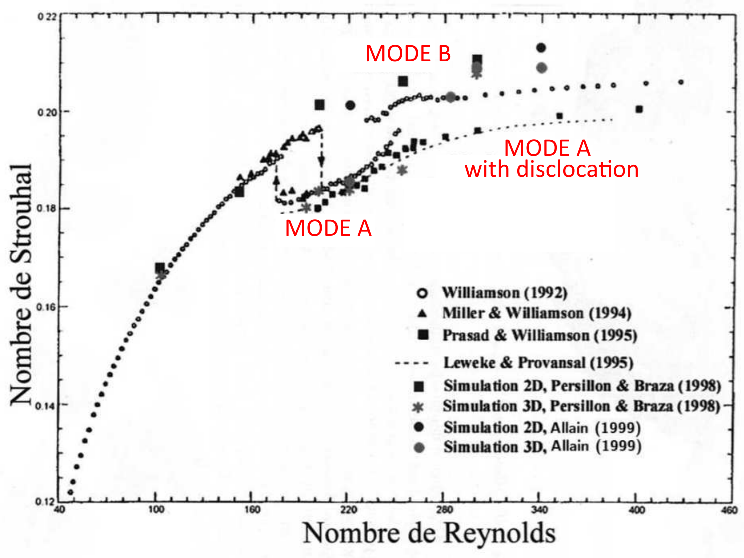

FIGURE 2.13: Evolution of Strouhal number versus Reynolds number in the wake region for a cylinder according to different authors

- Mode (A) (Williamson (1988)) occurs for a Reynolds 180 - 190 and 230 - 240. A discontinuous change happens located in the wake formation, when the primary wake vortices start to become unstable and generate large-vortex loops (see figure 2.14(a)) forming 'braid-like' structures, clearly obtained by DNS (Persillon and Braza (1998)).
- Mode (B) three-dimensional shedding transition occurs between Re = 230 and 260 which involves inception of finer-scale streamwise vortex structure with

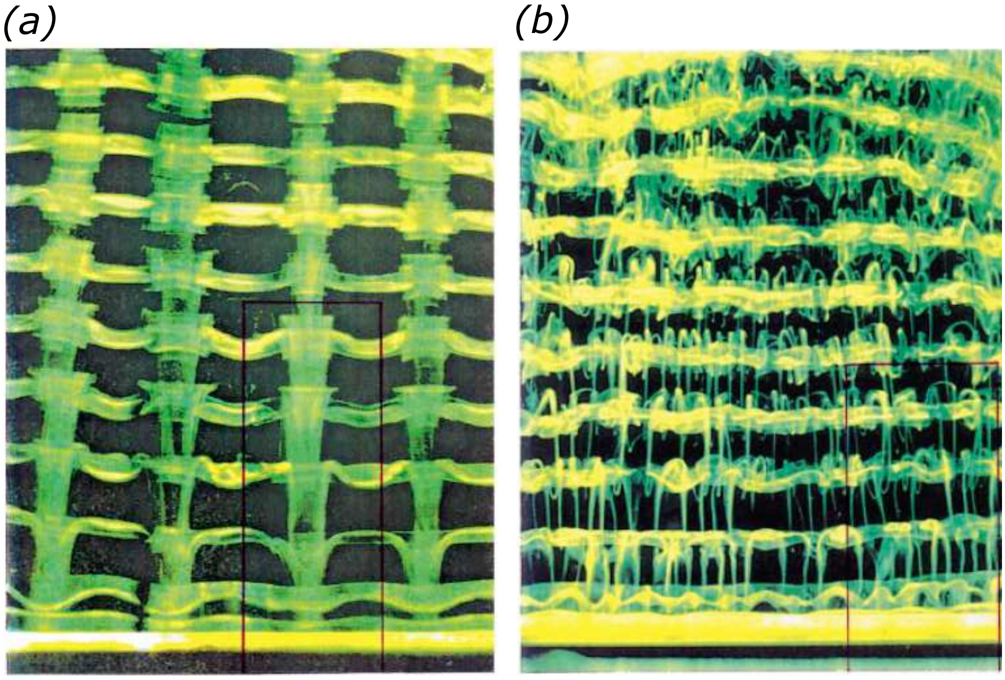

FIGURE 2.14: Wake mode (A) and (B) of three-dimensional vortex shedding. (a) mode (A) at Re = 180. (b) Mode B at Re = 230 and above (Williamson (1992))

higher frequencies seen in figure 2.13. This phenomenon was observed experimentally by (Williamson (1996)) highlighted in figure 2.14(b) and by means of numerical simulation (Persillon and Braza (1998))

Furthermore, natural vortex dislocation in the wake has been observed in (Braza et al. (2001)) by means of direct numerical simulation (see figure 2.15) for Reynolds number near to the appearance of the mode (A) and (B). The successive early stages of the transition to three-dimensionality can be summarised as follows according to the previous studies. Different early stages of it development as following:

- The amplitude of the w velocity component along the span is amplified with a linear form at the beginning before it displays a nonlinear evolution character with a saturation stage.
- This is followed by an appearance of the streamwise vorticity in the wake and along the spanwise direction presenting quasi-periodic counter-rotating vortices.
- Afterwards, a regular spanwise undulation appears "mode (A)", modifying the two-dimensional rows of vortices.

- Finally, a natural vortex dislocation develops by forming a break in the 'spinal column' of the von Kármán vortex row, creating a junction with the adjacent vortex row. This is due to phase irregularities in the frequency of the vortex shedding along the span.

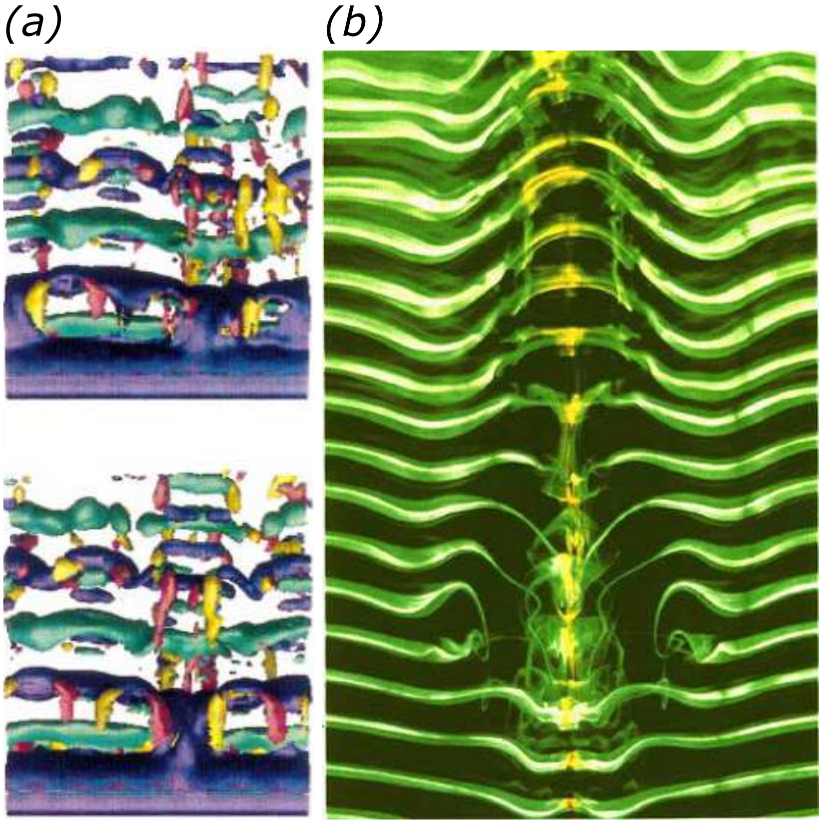

FIGURE 2.15: Natural vortex dislocation pattern: (a) results obtained direct numerical simulation (Braza 2001); (b) experimental visualizations, (Williamson (1992))

For Reynolds numbers of 300 to 10^{5-6}, the flow in the wake becomes turbulent but the boundary layer before the detachment point remains laminar. When Re = 1000, small vortices are developed in the shear-layer downstream the separation point, called "secondary vortices" (Braza et al. (1986)) that remain attached near the cylinder's wall. In higher Reynolds numbers, due to amplification of the shear layer instability in the separated shear layers, (Bloor (1964)), a series of Kelvin Helmholtz vortices appears in the shear layers for Reynolds numbers higher than 2600, whereas the shear layer instability undulation is detectable already beyond Reynolds number 2000. For higher Reynolds numbers, the Kelvin Helmholtz vortices cover a significant part of the separated shear layers together with the von Kármán vortices. (Braza et al. (1990)) confirmed by numerical simulation that the ratio of the shear layer frequency over the von Kármán frequency varies as $Re^{0.5}$ as was suggested by (Bloor (1964)). The two shear layers past the obstacle interact farther downstream and merge in the *alternating* vortex shedding produced by the von Kármán instability farther in the wake. This relation between the shear layer mode and the von Kármán mode will be widely used in the morphing concepts investigated in the present thesis.

Although the 3D motion becomes more important, all these vortex rows undergo a secondary instability yielding appearance of well distinct spanwise wavelengths. The larger is the vortex, the longer is the wavelength. The interaction of the frequencies associated to these two instabilities leads to the growth of the resulting alternating eddies and the filling of the energy spectrum in terms of frequencies. In the Reynolds number range between 5.10^4 o 10^5, the boundary layer is laminar up to the separation point, the flow undergoes the critical regime where the boundary layer upstream of the separation point becomes fully turbulent. The transition location (in the sense of boundary layer or shear layer transition) moves in the shear layers downstream the separation points, which in their turn move in more downstream positions. For higher Re the boundary layer is fully turbulent, this corresponds to the so-called *super-critical regime*. The critical regime is characterised by a drastic eduction of drag known as "drag crisis".

A quite detailed experimental study of the flow dynamics around a circular cylinder entering the critical regime (Reynolds numbers between 10^5 and 5.10^5 with emphasis n the Re = 140,000 is provided by TRPIV in two and three components in (Perrin (2005)), carried out in the S1 and S4 wind tunnels of IMFT. These measurements have been widely used in the European research projects FLOMANIA (flow Physics Modelling - an Integrated approach) and DESIDER, "Detached Eddy Simulation for industrial aerodynamics, known as the "IMFT's circular cylinder test case". This study has been of high importance for the validation of advanced turbulence modelling closures for highly detached flows with coherent structures, going from the URANS to the hybrid RANS-LES framework including the DES (Detached Eddy Simulation) and has two chapters devoted in the Book by (Haase et al. (2009)).

The low Reynolds number transition around wings at high incidence

Two-dimensional and three-dimensional transition have been studied by (Hoarau et al. (2003)) around an airfoil by DNS at high angles of attack 20° for Reynolds number up to 10 000. When Re = 5 the flow remains fully attached and steady. As the Re increases, a small attached vortex is formed in the near trailing edge region. The size of this vortex grows when Re increases. At Re = 70, the recirculation bubble reaches 40 % of the airfoil chord, unsteadiness starts to appear with a simultaneous regular vortex shedding motion. Finally when Re = 800, vortex shedding motion becomes very regular where the two- and three-dimensional transition mechanisms occur. New predominant frequencies appear, which are the fractions of the fundamental frequency in $800 \leq \text{Re} \leq 2000$. Beyond this region, the transition turns to a complex process due to the development of the shear-layer instability.

At higher Re, for two-dimensional transition period-doubling mechanism and the shear-layer instability mechanisms are identified. The first, conforms with the von Kármán instability evolution where subharmonic of the main vortex shedding frequency are captured. Beyond Re = 2000 shear-layer instability appears and give birth to an incommensurate frequency, due to the development of the Kelvin-Helmholtz instability in the separation region near the leading edge. Moreover, when Re increases a progressive undulation of the separated shear-layer transforms to a formed Kelvin-Helmholtz vortices. Theses vortices are shorter than the von Kármán ones and become smaller as the Re increases (see figure 2.16). This was demonstrated by (Hoarau et al. (2003)) who evaluated the shear-layer wavelength through a space-time tracking and found that it decreases according to the law $\lambda_{sl} \propto Re^{-0.44}$.

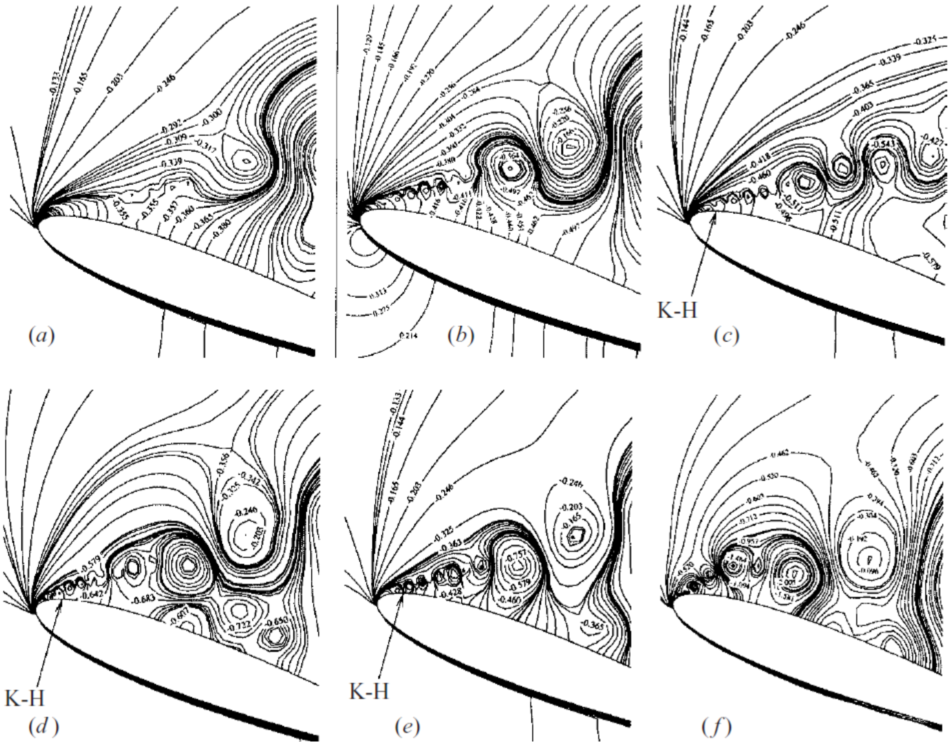

FIGURE 2.16: Iso-pressure contours illustrating the development of the shear-layer when Re increases. (a) : 2000, (b) 3000, (c) 4000, (d) 5000, (e) 7000, (f) 10000 (Hoarau et al. (2003))

In parallel of the two-dimensional instabilities illustrated previously, three-dimensional mechanism has been observed in the wake similar to one presented for the cylinder. At Re = 800 that was studied by (Hoarau et al. (2003)) the transition to three-dimensional turbulence mechanism starts with an undulation "secondary instability" of the von Kármán rows through an amplification of the W velocity component along the span (see figure 2.17). When the onset of the three-dimensional transition appears, counter-rotating cells are developed as an organised pattern of the W velocity. It is followed by an amplification of the iso-vorticity ω_x and ω_y in figure 2.18 known as spanwise-periodic fluctuation. The von Kármán rectilinear vortex rows are then pertubated due to these fluctuations and consequently modifies the iso-vorticity ω_z.

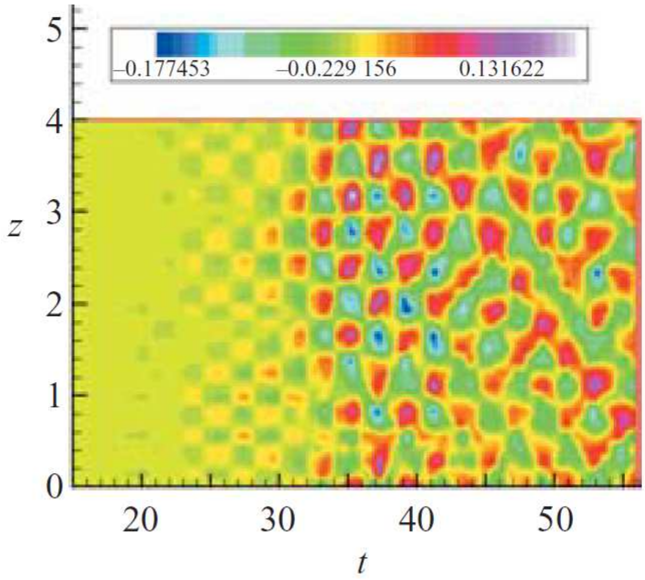

FIGURE 2.17: Spatial evolution of the longitudinal and vertical vorticity components, Re=800 (Hoarau et al. (2003))

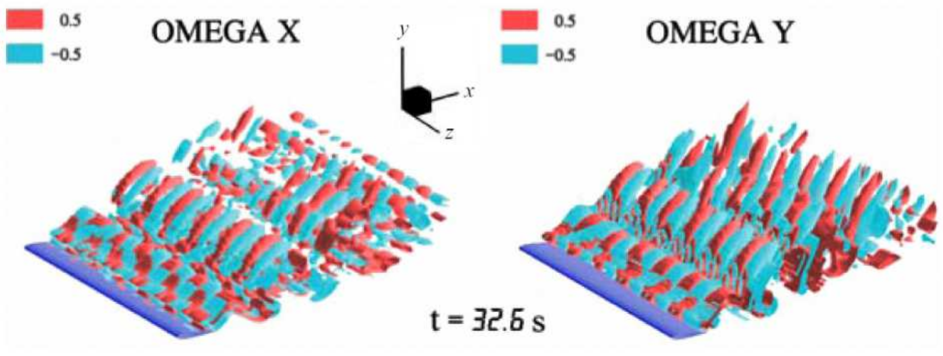

FIGURE 2.18: Spatial evolution of the longitudinal and vertical vorticity components, Re=800 (Hoarau et al. (2003))

The dynamics of this transition are more similar to the previous presented studies of bluff-body-wake including an asymmetric shearing mechanism.

Three-dimensional transition around a rotating cylinder

The flow around rotating cylinders has more representative similarities to the morphing wings through the trailing edge vibrations. (El-Akoury et al. (2008)) analysed numerically the flow near the threshold of the bifurcation to the secondary instability. Two parameters were considered Reynolds number and the rotation rate $\alpha = D\omega_0/(2U_{\text{inf}})$. Three-dimensional transition under the rotation effects with respect to the coherent structures located in the wake is highlighted and compared with no-rotation case in the figure 2.19. As reported previously the amplification of the w-velocity component (in the spanwise direction) in figure 2.19(a) (Re = 200, α=0) corresponds to the development of the secondary instability and leads to the three-dimensional modification of the von Kármán rows "mode (A)". When the rotation is applied at (Re=200, $\alpha = 1.5$) a drastic damping for the w-velocity occurs in time and followed by a complete disappear of the secondary instability. The rotation was found to increase the critical Reynolds number by means of the simpler oscillator model. At Reynolds number (Re = 300) and α= 0.5 (figure 2.19c) the rotations maintain the established mode (A) even at higher Reynolds and the amplification for the w-velocity has been established in this case.

Turbulent wake structure properties at high Reynolds numbers

Turbulent wake around wings at high Reynolds numbers and high angles of attack, have been the object of many studies. This region is considered as a source of large fluctuations contributing to significant pressure fluctuations that generate additional noise and increases the drag force. The turbulence wake is restrained in between two interfacial shear-layers as in the figure 2.20. Turbulent-Turbulent (TT) interface is the thin inner region that separates the lower-upper shear-layers and the counter-rotating von Kármán vortex shedding. This region is concentrated with chaotic small-scale vortices. The second interface is the Turbulent-Non-Turbulent interface (TNT). This region was firstly studied in (Corrsin and Kistler (1955)) and defined as a thin layer called laminar superlayer which matches irrotational region to a vortical flow. In addition, first Direct Numerical Simulation (DNS) of (Bisset et al. (2002)) distinguished

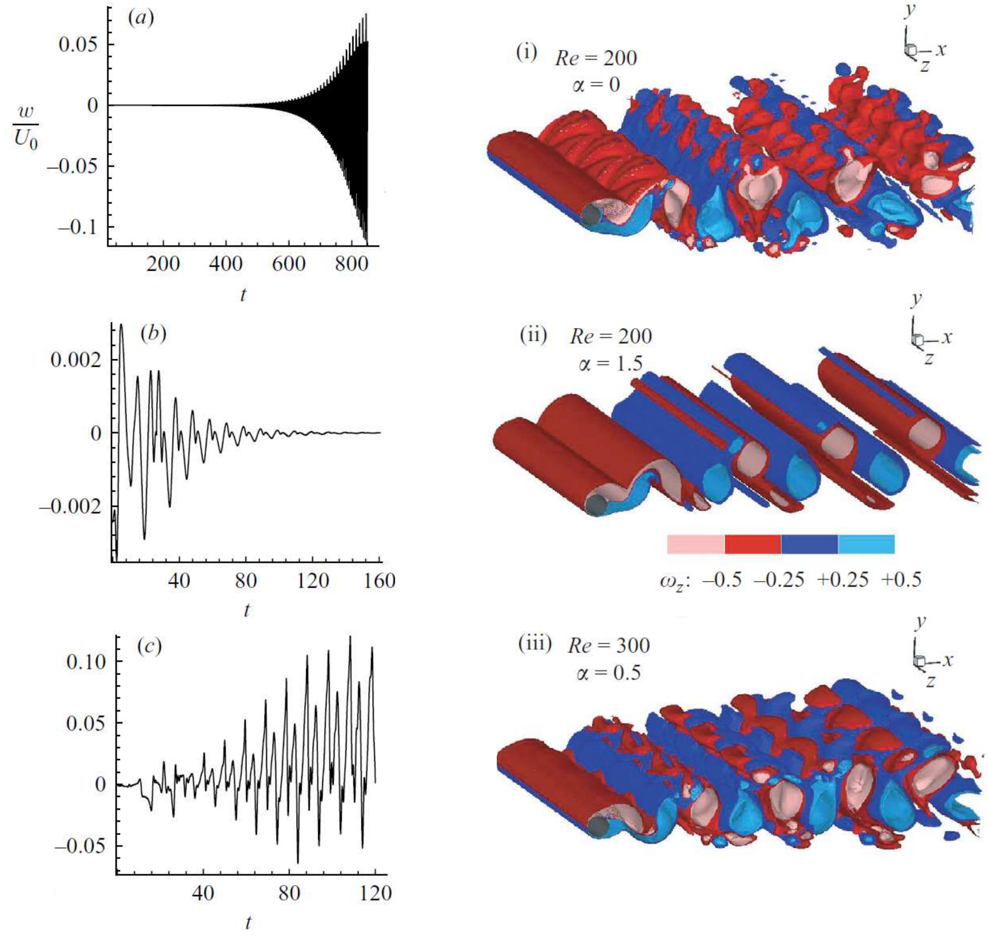

FIGURE 2.19: (left) : Temporal evolution of the w-velocity component. (Right) : Secondary instability and spanwise evolution of the coherent vortices (El-Akoury et al. (2008))

between a viscous (laminar) superlayer and TNT interface, they defined it as a layer of turbulent fluid. This last has a major role between the irrotational outer fluid and fully turbulent interior fluid. More recently, (Ishihara et al. (2015)) performed DNS of Turbulent Boundary Layer (TBL) and analysed the properties near the TNT interface by means of conditional statistics where small peaks in the spanwise vorticity are associated to small jump in the streamwise velocity (order of rms value of velocity fluctuations). It has been shown through conditional cross correlation near the TNT interface that the interface acts as a barrier to the irrotational fluctuations outside the TBL which is consistent with (Hunt and Durbin (1999)) who proposed the blocking mechanism.

Fundamental understanding of these mechanisms is needed to analyse trailing edge

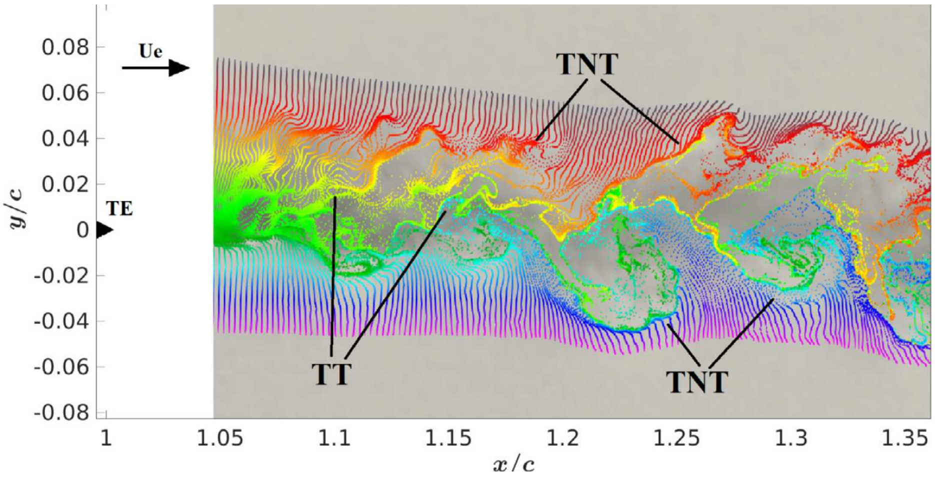

FIGURE 2.20: Instantaneous velocity field from experimental measurements, visualizations by means of streaklines for Re = 1 M, angle of attack $\alpha_0 = 10°$ (Simiriotis et al. (2019))

vibration through numerical simulations presented in the chapter 4 and 5. Uniform vibrations modify the original behaviour the turbulent wake structures through injection of small-scale vortices.

2.4 Morphing application at high Reynolds

This section will provide a literature review of recent morphing experimental and numerical studies that mainly investigated the wake structures modification and analysed the improvement of the aerodynamic forces.

Morphing of a flat plate by means of SMA

As part of the EMMAV (Electroactive Morphing for Micro Air Vehicles) research program (Chinaud et al. (2012)) investigated an actuator technology for the electroactive morphing using Shape Memory Alloys of a structure based on Titanium and Nickel. In this context LAPLACE laboratory developed a deformable plate which permits to analyse the fluid-structure coupling in the IMFT wind tunnel using innovative deforming technology. The deformations are expected to be in the range of centimetres coupled with high temporal dynamic range the order of 10 Hz. The deformation law of the SMA is defined by a thermo-mechanical that controls the displacement with minimizing the time necessary to change the plate position, presented in the figure 2.21. Experimental tests were performed by (Chinaud et al. (2014)) in the IMFT wind tunnel for a plate of a chord length 320 mm and a thickness of 15 mm along a span-wise length of 585 mm. The Reynold number is fixed at 200,000 and the plate is fixed at angle of -10° as illustrated in the figure 2.22. The measurements of the velocity field were performed at the standard conditions of 25° and P = 1 atm, by means of the Time Resolved Particle Image Velocimetry (TRPIV). Different positions of the cambered plate were selected and investigated in order to compare with the baseline static configuration. The study showed the ability of the SMA actuators to achieve bending of the trailing edge while supporting the loads applied by the fluid flow using time-averaged normalized velocity field measurement. The main flow dynamics revealed a shear-layer development past the trailing edge and the von Kármán vortices below it. Dynamic actuation and static deformation have been compared for different intermediate positions. A large recirculation area and a considerable increase of Reynolds stress gradients are produced by increasing the plate curvature. Moreover, the topology of the shear layer changes and an increase of shear in the mixing-layer

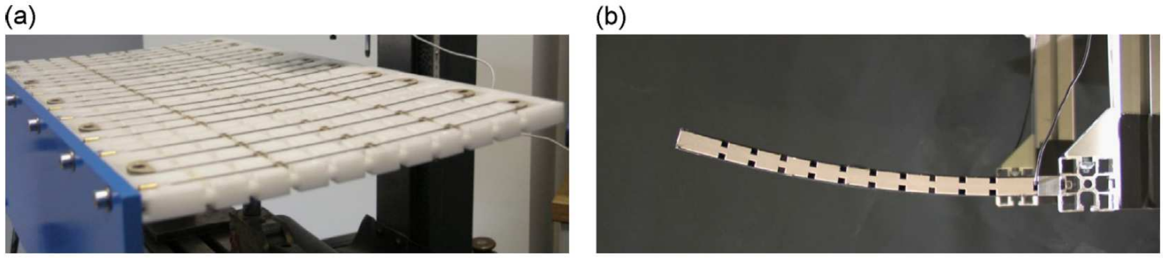

FIGURE 2.21: (a) SMS wires installed on the plate. (b) Deformation of the plate (Chinaud et al. (2014))

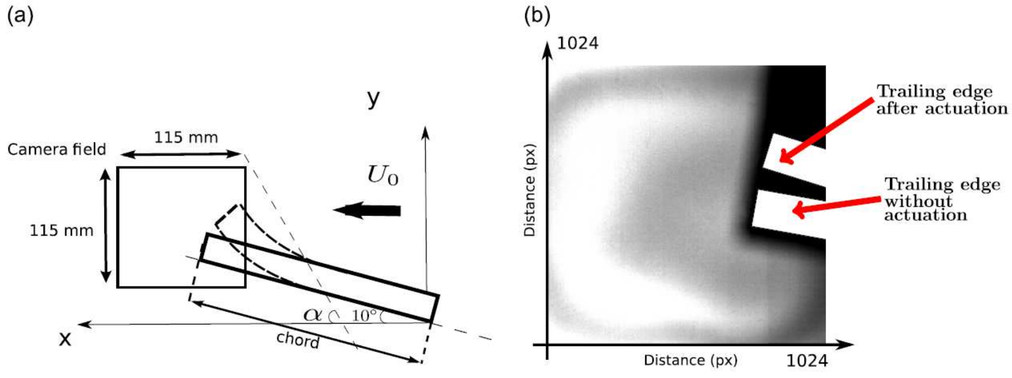

FIGURE 2.22: Descriptive sketches of trailing edge structure with and without deformation (Chinaud et al. (2014))

area past the trailing edge have been noticed in the dynamic case. In addition, different actuation positions produce a stronger interaction of the von Kármán within the shear-layer frequency of the Kelvin-Helmholtz vortices. This leads to a reduction of the frequency peaks (spectral energy) governing the mixing layer, which will induce a significant reduction of the trailing edge aerodynamic noise.

Morphing of a NACA0012 by means of piezoelectric actuation

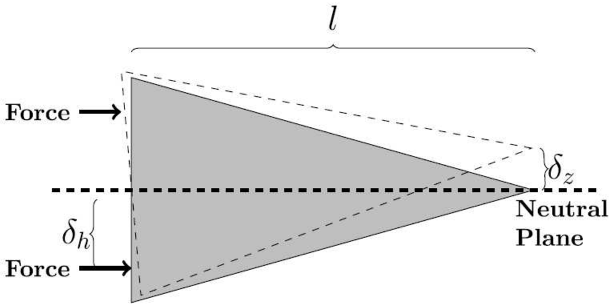

FIGURE 2.23: *Push − push* actuation control mechanism (Scheller (2015))

The study of (Chinaud et al. (2014)) focused on the effects of high-amplitude coupled with low-frequency actuations and quasi-static hypothesis. In the context of the research project DYNAMORPH, the previous study was continued by providing another type of morphing based on high-frequency [60 Hz - 90 Hz] and low-amplitude of deformation by means of piezoelectric actuation. (Scheller et al. (2015)) used a piezoelectric stack actuators as demonstrated in figure 2.23. Theses devices are embedded at the trailing edge of the NACA0012 aileron allowing trailing edge modification by ±1.5° as in figure 2.24. This prototype of 38.9 cm chord length has been mounted in the subsonic IMFT wind tunnel and tested at Re = 200, 000 with an angle of attack 10° using Particle Image Velocimetry (PIV) measurements. Reynolds stress fields as the longitudinal $\bar{u^2}$ and transversal $\bar{v^2}$ components located in shear layer near the trailing edge region of the actuated configurations in figure 2.25 are modified. When the actuation frequency increases, it induces a considerable impact on the wake vortex structures. The shear layer size is then reduced which leads to a reduction of the Reynolds stress components. A frequency of actuation of 60 Hz induces a maximum shear layer size reduction (observed in the $\bar{v^2}$ Reynolds stress component). This actuation system of piezoelectric push-push mechanism has been identified in the

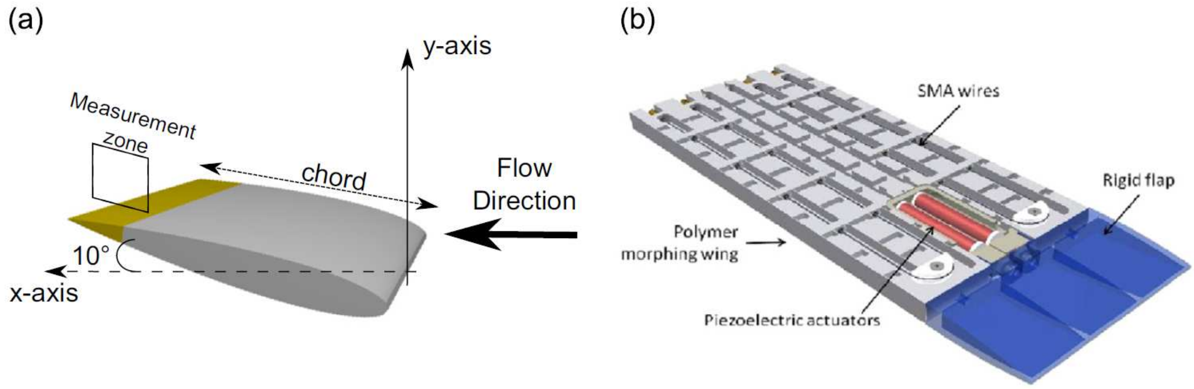

FIGURE 2.24: (a) descriptive sketches of wind tunnel mounted prototype setup. (b) 3D model design of the prototype (Scheller et al. (2015))

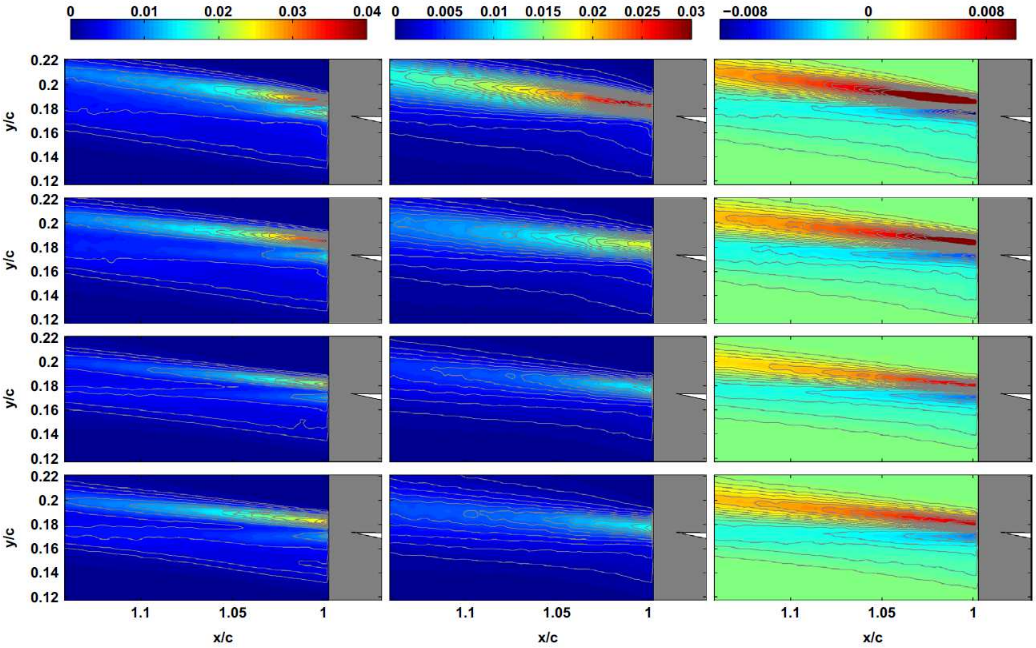

FIGURE 2.25: Iso-contours of time averaged Reynolds stressfield $\bar{u}^2/U_{\mathrm{inf}}$, $\bar{v}^2/U_{\mathrm{inf}}$ and $u\bar{v}^2/U_{\mathrm{inf}}$ from top to bottom actuations 0 Hz,30 Hz,60 Hz and 90 Hz (Scheller et al. (2015))

energy spectrum and can possibly attenuate the high-frequency Kelvin-Helmholtz vortices.

Hybrid morphing using SMA and MFC piezoelectric patches

The association of low-frequency high-deformation has been the fruit of this multidisciplinary collaboration between the two laboratories IMFT and LAPLACE and reported as "hybrid electroactive morphing", able to operate at different time and length scales of the turbulent motion (Chinaud et al. (2014)). This kind of morphing is partly bio-inspired from the large span hunting birds like the owl, able to simultaneously activate their feathers and large wings in order to increase performance and reduce the noise. (Scheller et al. (2015)) made an evidence of the hybrid electroactive morphing benefits for the first time in the literature, applied on a NACA4412 morphing wing. These activities had received a high distinction by the Royal Society inviting the multidisciplinary team in its annual exhibition under the theme of "Smart wing design through turbulence control" – Science Imitating Nature" in 2014 in collaboration with Imperial College, London[2], followed by the CNRS Journal "the wings of the future"[3]

Moreover, (Jodin et al. (2017)) constructed an A320 morphing prototype of 70 cm chord, able to camber its rear part beyond 60 % of the chord by an order of 15 % of the whole chord thanks to SMA operating at frequencies less than 1 Hz and simultaneously equipped by MFC (Macro-Fiber Composite) piezo-actuators in the near trailing edge region, able to vibrate from 30 to 500 Hz, thus ensuring increased capabilities of the hybrid electroactive morphing. They used Time-Resolved PIV (TRPIV) with data acquisition of an order of 6 KHz, pressure and aerodynamic forces measurements at higher-frequency-low-amplitude morphing effect in the trailing edge region and the near wake, as well as the camber control separately and finally the hybrid morphing. It was shown that this association of both classes of actuations is able to produce

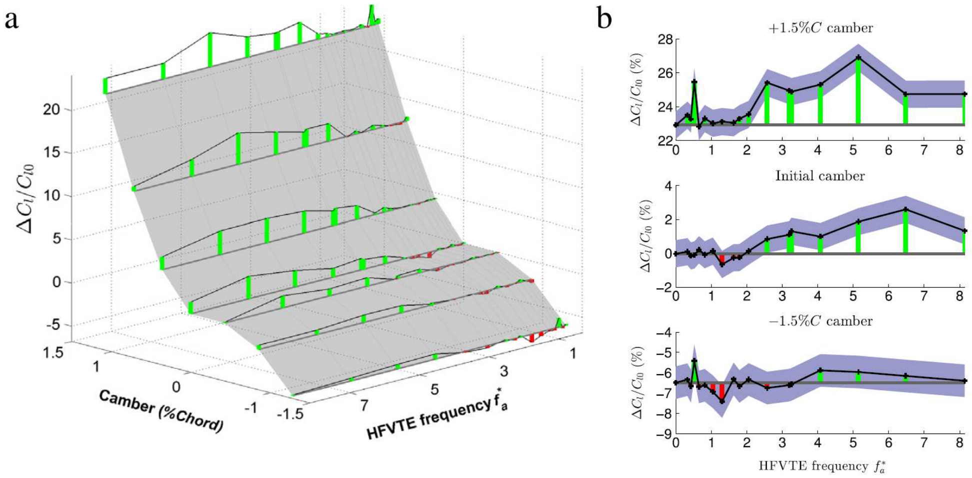

FIGURE 2.26: Measurement of the lift coefficient C_l gain as a funtion of camber control by means of SMA (-10 to 10 mm) and actuation frequencies using piezoelectric patches (0 - 250 Hz) and compared to the static case. (Jodin et al. (2017))

---

[2] http://sse.royalsociety.org/2014/smart-wing-design/

[3] https://lejournal.cnrs.fr/videos/les-ailes-du-futur

an order of 3 % more lift (see figure 2.26), than the only use of the camber control. By means of the Proper Orthogonal Decomposition (POD) and a frequency domain analysis, this study had shown the manipulation of the wake's turbulent structures, a vortex breakdown of the large coherent eddies and enhancement of smaller beneficial eddies thus producing an eddy-blocking effect through shear sheltering process, as explained in (Szubert et al. (2015)) and resulting in thinning the shear layers and the wake's width (see figure 2.27).

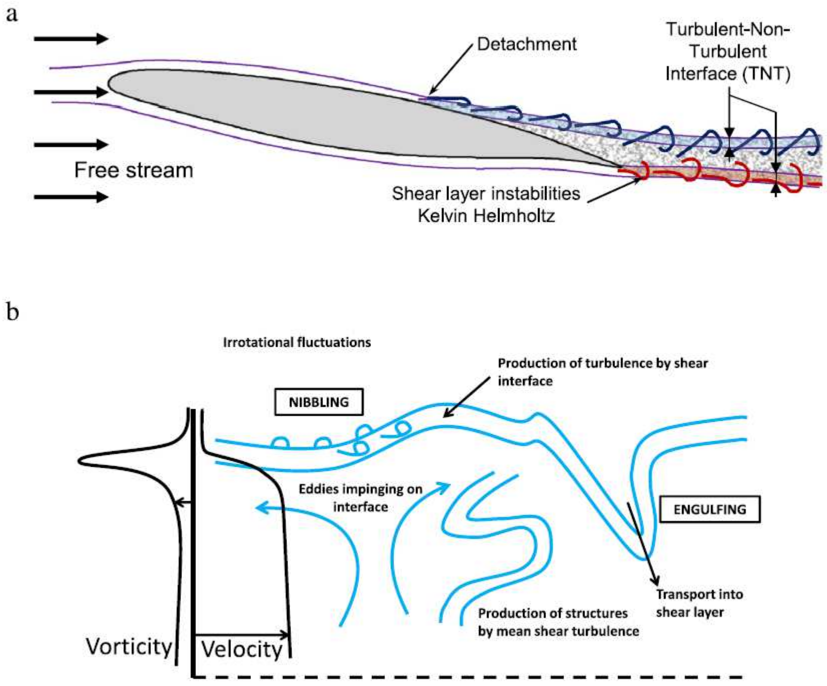

FIGURE 2.27: (a) Schematic description of the flow around A320 wing prototype, showing the detachment, shedding turbulences in the shear-layer. (b) Representation of the eddy-blocking effect between T/NT interface (Hunt et al. (2016)) with the vorticity and velocity evolution in this interface (Jodin et al. (2017))

Morphing in transonic regime at high Reynolds

Compressible flows around wing at high Reynolds have been widely investigated, in particular transonic regime. From a general point of view, it seems that the instabilities related to the compressibility observed at large Reynolds numbers are similar to those appearing for lower Reynolds numbers. Emission of vortices is formed in the wake after a separation of the boundary layer under the effect of the interaction with a shock wave or its thickening in the presence of an adverse pressure gradient. In the other part, oscillation of the supersonic regions can appear for certain ranges of coupled Reynolds number/Mach number.

Buffet appearance (unsteady quasi-periodic motion of the shock over the wing) occurs at a specific region of Mach number range (0.7 - 0.8) (McDevitt et al. (1976)), which corresponds to the cruise flight stage. It is therefore crucial to analyse the buffet dynamics because it may lead to critical conditions for an amplification of dip-flutter instability. The buffet instability appears due to a strong interaction and connection between the shock, the boundary layer, the separated shear layer and the wake instabilities formed in the near trailing edge region (Seegmiller et al. (1978), McDevitt et al. (1976), Jacquin et al. (2009)).

The amplitudes of the buffet increase in this region of Mach numbers. The interaction of the shear layer unsteadiness, of the shock vortex interaction and of the influence of the von Kármán instability on the buffet mode had been studied by numerical simulation by (Bouhadji and Braza (2003a,b)). This study contributed to highlight and understand the feedback effects from the near trailing edge and wake unsteadiness on the SWBLI and upstream region, exploited recently in the morphing concepts of the tRS prototype in the SMS project. The von Kármán mode persists up to Mach numbers 0.9 and the wall pressure is practically steady because of the progressive increase of the hyperbolic character of the flow with the Mach number increase. For higher Mach (0.9 - 0.95) the shock wave has moved in the wake acting as a barrier to the travelling of the wake instabilities upstream, therefore and the forces become steady.

More recently, (Szubert et al. (2015)) examined the transonic interaction between the buffet, the shear layer and the von Kármán vortices using the Organised Eddy Simulation, OES (Braza et al. (2006) and Bourguet et al. (2008)). By means of the wavelets and Proper Orthogonal Decomposition (POD) methods, the impact on the pressure and forces fluctuations have been detailed. The role of the high-order modes associated with lower energy in producing a shear sheltering effect in the separated shear layers past the SWBLI was analysed and used to create a stochastic forcing by re-injection of turbulence in these layers and the shock's shearing region, as source terms in the turbulence transport equations in the IOES (Improved OES) model. The forcing acts as an eddy-blocking effect which results in considerable thinning of the shear layers and of the wake's width.

Beyond the bio-inspired context, it is worthwhile noticing that the birds do not fly at transonic speeds corresponding to the cruise phase of a real aircraft. In these regimes,

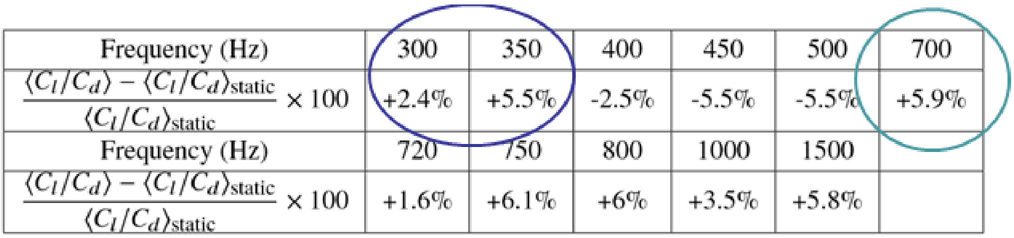

Frequency (Hz)	300	350	400	450	500	700
$\frac{\langle C_l/C_d\rangle - \langle C_l/C_d\rangle_{\text{static}}}{\langle C_l/C_d\rangle_{\text{static}}} \times 100$	+2.4%	+5.5%	-2.5%	-5.5%	-5.5%	+5.9%
Frequency (Hz)	720	750	800	1000	1500	
$\frac{\langle C_l/C_d\rangle - \langle C_l/C_d\rangle_{\text{static}}}{\langle C_l/C_d\rangle_{\text{static}}} \times 100$	+1.6%	+6.1%	+6%	+3.5%	+5.8%	

FIGURE 2.28: Relative gain (or loss if negative) of the averaged lift-to-drag ratio for different piezo-actuation frequencies compared to the static (non morphing) case

the numerical approach has proven essential for the design, prior to the experiments under way within the SMS project for this regime. In Tô et al. (2019) we investigated the electroactive morphing for an A320 type of wing in transonic regime (Mach number of 0.78, Reynolds number of order 3 Million), with the same turbulence modelling method as previously mentioned. The study revealed that a deformation with a slight upwards deflection of the trailing edge by 2 degrees associated with a trailing edge vibration of 300 Hz is able to attenuate the buffet instability and to enhance the lift-to-drag of the order of 6%. This is due to the feedback effects created from the trailing edge and the wake area towards the SWBLI (Shock Wave Boundary Layer Interaction) region, produced by an eddy-blocking within the shear layers, by means of the trailing edge vibration. This mechanism is similar to a shear sheltering one as in (Hunt et al. (2008)).

Our current numerical simulations in the SMS project concerning the transonic Reduced Scale (tRS) morphing prototype of an A320 wing have determined the optimal frequency ranges able to considerably increase the aerodynamic performance presented in figure 2.28 and 2.29, to decrease the buffet amplitude as well as the overall PSD level related to the noise. This results in a constriction of the shear layers and in an attenuation of the predominant frequencies of the shear-layers vortices as shown in figure 2.30. These numerical simulations are in strong synergy and contribute to

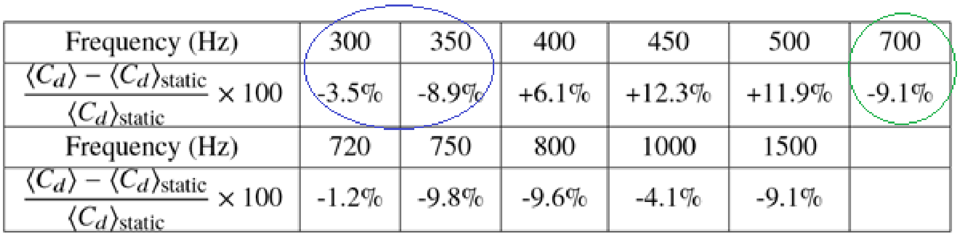

Frequency (Hz)	300	350	400	450	500	700
$\frac{\langle C_d\rangle - \langle C_d\rangle_{\text{static}}}{\langle C_d\rangle_{\text{static}}} \times 100$	-3.5%	-8.9%	+6.1%	+12.3%	+11.9%	-9.1%
Frequency (Hz)	720	750	800	1000	1500	
$\frac{\langle C_d\rangle - \langle C_d\rangle_{\text{static}}}{\langle C_d\rangle_{\text{static}}} \times 100$	-1.2%	-9.8%	-9.6%	-4.1%	-9.1%	

FIGURE 2.29: Relative gain (if negative in respect of drag reduction) or loss (if positive) of the averaged drag coefficient for different piezo-actuation frequencies comparing to the static case

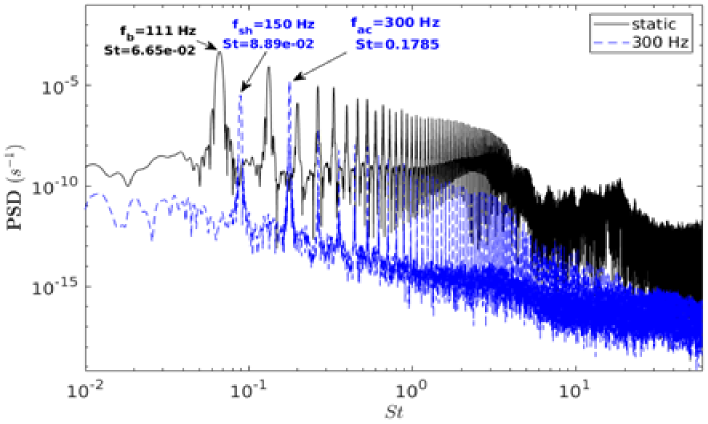

FIGURE 2.30: Attenuation of the buffet frequency f_b due to actuation and slight deformation of the trailing edge region in cruise phase, Mach=0.78, Re= 2.06 x 10^6. PSD of lift coefficient, transonic morphing prototype of A320 type

the experimental studies carried out in the SMS project concerning the design of the morphing prototype in cruise phase.

2.5 Conclusion

This chapter illustrates first bio-inspired flights back to history when human being tried to imitate the birds to fly. Then it represents an overview of some European and international projects related to industrial development of new wings. Electroactive morphing of future wings has been introduced and detailed using electroactive smart materials integrated in different scale wings able to control their shapes in order to have better efficiency. An overview of the phenomenology of the flow around bluff bodies has been proposed including different successive stages to the appearance of the instabilities and thus leading to a complicated flow dynamics. For moderate Reynolds numbers, it has been shown that when the boundary layer is laminar, these mechanisms are essentially based on the appearance of two-dimensional instabilities of von Kármán and Kelvin-Helmholtz or three-dimensionality as for instance the secondary instability which leads to vortex dislocations. At higher Reynolds numbers, different sources of instabilities interact in the near transitional and turbulent boundary layers with a pseudo-periodic character as for the flow around a wing placed at high angle of incidence. The energy spectrum is then filled with predominant frequencies related to the coherent organized structures and others created from a merging and interaction with different sources of instabilities. For flows with higher Mach numbers, some effects related to the compressibility have been highlighted as the SWBLI region which can lead under certain conditions to detachment of the boundary layer and appearance of the buffet phenomena.

A summary of most relevant studies that examined the morphing at higher Reynolds numbers in the subsonic speed were provided. The work started with a bending of a flat plate. Then, it was extended to a NACA aileron using electroactive materials. Afterwards, hybrid morphing was firstly introduced as an original concept. This allowed the association of piezoelectric MFC with SMA materials creating a unique partly bio-inspired reduced scale Airbus A320 wing. Theses studies have examined the flow in the wake and revealed a modification of the shear-layer instabilities and enhancement of aerodynamic performances. More recently, we studied electroactive morphing in the transonic regime through the trailing edge actuation and deflection which showed an attenuation of the buffet amplitude and a considerable reduction of the drag.

Chapter 3

Numerical methods and turbulence modelling

Contents

3.1 Governing equations of fluid dynamics

Fundamental laws of fluid dynamic motion are governed by : conservation of mass, momentum and the energy and expressed as ’conservation laws’. They describe the evolution of the conserved quantities in a certain domain through the transport equations. A continuous medium is supposed to treat the flow field of the governing equations of fluid dynamics. Therefore, the whole system can be investigated using continuum mechanics with a large number of fluid molecules within a small volume. Flow properties such as velocity, pressure, temperature, viscosity, etc. describe and reflect the statistical motion of the fluid molecules at each point of the flow field.

3.1.1 Navier-Stokes equations

In this section, the description of the three fundamental conservation laws (continuity, momentum and energy equation) is provided for a viscous flows, through the Navier-Stokes equations system. The structure of this section takes example of the PhD thesis of (Grossi (2014)) presenting a comprehensive review of the transport equations and their numerical treatment.

Continuity equation

Mass conservation principle in a fluid volume is expressed through the 'continuity equation', which defines the mass as a quantity that can not be created and destroyed in the system. The fluid density ρ (kg/m^3) which is a scalar field is the main transported quantity. The continuity equation does not present a diffusive flux term since there is no mass diffusion in a fluid at rest. The continuity equation can be expressed as :

$$\frac{\partial}{\partial t}\int_V \rho dV + \int_S \rho(\overrightarrow{v}.\overrightarrow{n})dS = 0 \tag{3.1}$$

The left-hand term in the equation 3.1 is the time rate of the mass change inside the volume control. The surface integral is the total mass flow across its boundaries. A net mass flux enters in the control volume when the mass flow has negative value while positive values corresponds to an outflow (exit). The continuity equation can be simplified by means of the 'Gauss' and 'Reynolds' theorems and expressed as :

$$\frac{\partial \rho}{\partial t} + \overrightarrow{\nabla}.(\rho\overrightarrow{v}) = 0 \tag{3.2}$$

For incompressible flow, ρ is constant in the equation 3.2.

Momentum equation

The equation comes from the fundamental principle of the second law of Newton which states in the variation of the momentum of an object is equal to the net force acting on its surface. The momentum equation expresses the conservation of momentum in the fluid system. It can be alternatively through three separated transport equations for the individual momentum components ρu, ρv and ρw.

$$\frac{\partial}{\partial t}\int_V \rho\overrightarrow{v} dV + \int_s \rho\overrightarrow{v}(\overrightarrow{v}.\overrightarrow{n})dS = \int_V \overrightarrow{Q_v} dV + \int_S \left(\overline{\overline{Q_s}}\,\overrightarrow{n}\right) dS \tag{3.3}$$

When the volume sources $\overrightarrow{Q_v}$ are all body forces per unit volume. The surface sources $\overline{\overline{Q_s}}$ are those that act over a fluid element : the surface (or internal) forces. In this group, there are the static pressure and the viscous stresses, which have a net effect only on the boundary of the volume. The pressure p exerted by the surroundings acts in the direction normal to S, pointing inwards the fluid element. Therefore, the surface sources can be computed as -p $\overline{\overline{I}}$, where $\overline{\overline{I}}$ is the unit tensor and $\overline{\overline{\sigma}}$ is the viscous stress tensor. In aerodynamics, the effect of the gravitational force on the fluid elements can be neglected and other volume sources are usually not present. Hence, the momentum equation becomes :

$$\frac{\partial}{\partial t}\int_V \rho\overrightarrow{v} dV + \int_s \rho\overrightarrow{v}(\overrightarrow{v}.\overrightarrow{n})dS = \int_S p\left(\overrightarrow{I}.\overrightarrow{n}\right) dS + \int_S \left(\overline{\overline{\sigma}}\,\overrightarrow{n}\right) dS \tag{3.4}$$

or in differential form

$$\frac{\partial\rho\overrightarrow{v}}{\partial t} + \overrightarrow{\nabla}.(\rho\overrightarrow{v}\, x\, \overrightarrow{v}) = -\overrightarrow{\nabla} p + \overrightarrow{\nabla}.\overline{\overline{\sigma}} \tag{3.5}$$

Since the air behaves as a Newtonian fluid, the shear stresses are proportional to the velocity gradients. Using tonsorial notation, the general form of the viscous stress tensor σ_{ij} reads

$$\sigma_{ij} = \mu\left(\frac{\partial u_j}{\partial x_i} + \frac{\partial u_i}{\partial x_j}\right) + \lambda\frac{\partial u_k}{\partial x_k}\delta_{ij} \tag{3.6}$$

where the first index in the subscript indicates the direction normal to the plane on which the stress is acting while the second one gives its direction. If $i = j$ the component is a 'normal stress' and otherwise, a 'shear stress'. Shear stresses are generated by the friction resulting from the relative motion of a body immersed in a fluid or of different fluid layers. In equation 3.6, μ is the dynamic viscosity and λ is the second viscosity of the fluid. A kinematic viscosity can also be defined as $\nu = \mu/\rho$. According to Stoke's hypothesis for a Newtonian fluid in local thermodynamic equilibrium

$$\lambda + \frac{2}{3}\mu = 0 \tag{3.7}$$

This relation is called 'bulk viscosity' and is a property of the fluid. It is responsible for the energy dissipation in a fluid of smooth temperature distribution submitted to expansion or compression (Schlichting and Gersten (2000)). So far, there is no experimental evidence that equation 3.7 does not hold except for extremely high temperatures or pressures (Blazek (2005)). Using relation 3.7, equation 3.6 becomes

$$\sigma_{ij} = \mu(\frac{\partial u_j}{\partial x_i} + \frac{\partial u_i}{\partial x_j}) - \frac{2\mu}{3}\frac{\partial u_k}{\partial x_k}\delta_{ij} \tag{3.8}$$

Although the viscous stresses are derived as being surface sources, they play the role of diffusive fluxes of momentum (thus requiring fluid motion), with the dynamic viscosity acting as the diffusion coefficient.

Energy equation

In fluid dynamics, the conservation law for energy is obtained from the application of the first law of thermodynamics to a control volume. It expresses the fact that the time variation of the total energy inside a control volume is obtained from the balance between the work of the external forces acting on the volume and the net heat flux into it. In the energy equation, the transported quantity is the total energy per unit volume ρE, where E is the total energy per mass unit. It is defined as the sum of the internal energy per unit mass e (a state variable) and the kinetic energy per unit mass $|v|^2/2$. The transport equation features a diffusive flux term which depends only on the gradient of e since, by definition, $\overrightarrow{v} = 0$ at rest. It accounts for the effects of thermal conduction related to molecular agitation and is given by $\overrightarrow{F}_D = -\gamma\rho\kappa\overrightarrow{\nabla}e$, where γ is the ratio of specific heat coefficients, $\gamma = c_p/c_v$. Since the internal energy can be expressed in terms of the static temperature T by $e = c_v T$, heat diffusion is more usually described using Fourrier's law

$$\overrightarrow{F}_D = \gamma\rho\kappa\overrightarrow{\nabla}e = -k\overrightarrow{\nabla}T \tag{3.9}$$

where k is the thermal conductivity coefficient ($k = c_p\rho\kappa$) and the negative sign accounts for the fact that heat is transferred from high- towards low-temperature regions.

Surface sources contribute to the energy equation through the work done by the pressure and viscous stresses (both normal and shear parts) acting on the boundaries of the fluid element $\overrightarrow{Q}_s = -p\overrightarrow{v} + (\overline{\overline{\sigma}}.\overrightarrow{v})$. Therefore, neglecting the work done by body forces as well as that of internal energy sources (e.g., radiation, chemical reactions, etc.), the integral form of the energy equation reads.

$$\frac{\partial}{\partial t}\int_V \rho E dV + \int_S \rho E(\overrightarrow{v}.\overrightarrow{n})dS = -\int_S p(\overrightarrow{v}.\overrightarrow{n})dS + \int_S (\overline{\overline{\sigma}}.\overrightarrow{v}).\overrightarrow{n}dS + \int_S k(\overrightarrow{\nabla}T.\overrightarrow{n})dS \tag{3.10}$$

which is also frequently written in terms of the total enthalpy

$$H = h + \frac{|\overrightarrow{v}|^2}{2} = E + \frac{p}{\rho} \tag{3.11}$$

where h is the enthalpy per unit mass. This yields

$$\frac{\partial}{\partial t}\int_V \rho E dV + \int_S \rho H(\overrightarrow{v}.\overrightarrow{n})dS = \int_S [(\overline{\overline{\sigma}}.\overrightarrow{v}).\overrightarrow{n}]dS + \int_S k(\overrightarrow{\nabla}T.\overrightarrow{n})dS \tag{3.12}$$

In differential form, equation 3.10 can be rewritten as

$$\frac{\partial \rho E}{\partial t} + \overrightarrow{\nabla}.\rho\overrightarrow{v}E = -\overrightarrow{\nabla}.p\overrightarrow{v} + \overrightarrow{\nabla}.(\overline{\overline{\sigma}}.\overrightarrow{v}) + \overrightarrow{\nabla}.(k\overrightarrow{\nabla}T) \tag{3.13}$$

Additional relations

To close the system of the Navier-Stokes equations, additional relations between the flow field variables are needed. In aerodynamics, the air is usually modelled as a perfect gas and therefore, a thermodynamic relation between the state variables p, ρ and T can be obtained by means of the equation of state

$$P = \rho R T \tag{3.14}$$

where $R = c_p - c_v$ is the gas constant per unit mass (for a perfect gas, c_p, c_v and thus γ and R are constants). In compressible viscous flow, heating due to high velocity gradients is responsible for variations in the fluid viscosity. To account for such effect, a common practice in aerodynamics is to adopt Sutherland's law (Sutherland (1893)), which expresses the dynamic viscosity μ of an ideal gas as a function of temperature only as

$$\frac{\mu}{\mu_{ref}} = (\frac{T}{T_{ref}})^{3/2}\frac{T_{ref} + S}{T + S} \tag{3.15}$$

μ_{ref} is a reference viscosity corresponding to the reference temperature T_{ref}, and the constant S is the Sutherland's parameter (or Sutherland's temperature). Values commonly used for air are μ_{ref} = 1.716 x 10^{-5} Pa.s, T_{ref} = 273.15 K and S = 110.4 K. Sutherland's Law gives reasonably good results at transonic and supersonic speeds. However, for hypersonic flows more elaborated formulas are usually employed.
The thermal conductivity coefficient k varies with temperature in a similar way to μ. For this reason, the Reynolds' analogy is frequently used to compute k, reading

$$k = c_p \frac{\mu}{P_r} \tag{3.16}$$

In the above equation, Pr is the Prandtl number, which is usually taken as 0.72 for air.

Final system of equations

In 3D Cartesian coordinates (x, y, z), the Unsteady Compressible Navier Stokes Equations can be expressed in conservative form as :

$$\frac{\partial}{\partial t}(W) + \frac{\partial}{\partial x}(f - f_v) + \frac{\partial}{\partial y}(g - g_v) + \frac{\partial}{\partial z}(h - h_v) = 0 \tag{3.17}$$

where t denotes the time. The state vector W is given by

$$\mathrm{W} = \begin{pmatrix} \rho \\ \rho u \\ \rho v \\ \rho w \\ \rho E \end{pmatrix} \tag{3.18}$$

and the convective fluxes are defined as

$$\mathrm{f} = \begin{pmatrix} \rho u \\ \rho u^2 + p \\ \rho u v \\ \rho u w \\ u(\rho E + p) \end{pmatrix}, \mathrm{g} = \begin{pmatrix} \rho v \\ \rho v u \\ \rho v^2 + p \\ \rho v w \\ v(\rho E + p) \end{pmatrix}, \mathrm{h} = \begin{pmatrix} \rho w \\ \rho w u \\ \rho w v \\ \rho w^2 + p \\ w(\rho E + p) \end{pmatrix} \tag{3.19}$$

$$\mathrm{f}_v = \begin{pmatrix} 0 \\ \tau_{xx} \\ \tau_{xy} \\ \tau_{xz} \\ (\tau U)_x - q_x \end{pmatrix}, g_v = \begin{pmatrix} 0 \\ \tau_{yx} \\ \tau_{yy} \\ \tau_{yz} \\ (\tau U)_y - q_y \end{pmatrix}, h_v = \begin{pmatrix} 0 \\ \tau_{zx} \\ \tau_{zy} \\ \tau_{zz} \\ (\tau U)_z - q_z \end{pmatrix} \tag{3.20}$$

with the shear stress tensor τ.

3.2 Turbulence modelling

3.2.1 The Reynolds-averaged Navier-Stokes equations

In turbulence, due to the high number of degrees of freedom related to the formation of different classes of vortices, there is a need to adopt a macroscopic approach and to resolve part of the physical motion, whereas the rest has to be modelled by taking into account appropriate phenomenological laws to describe the transfer mechanisms of this last part (unresolved turbulence or modelled part) towards the resolved turbulence and vice-versa. In this context, the definition of the *averaging* properties to be adopted is capital in respect of the separation and interaction between the two parts. According to *Morkovin's hypothesis*, the effect of density fluctuations on turbulence eddies in wall-bounded flows is insignificant provided that they remain small compared to the mean density. Indeed , this hypothesis is verified up to Mach numbers of about five (Blazek (2005)) and, therefore, a common approach in turbulence modelling is to apply Reynolds averaging (named also "statistical averaging" (Hinze (1987))) to the flow variables (otherwise one should use Favre averaging).

In Reynolds averaging, the flow variables are decomposed into two parts: a mean part and a fluctuating part. The velocity, for instance, is represented as $U = \bar{U} + U^{'}$, where $\bar{U}$ is it's mean value and $U^{'}$ it's instantaneous fluctuation. For stationary turbulent flow, $\bar{U}$ is normally statically computed using time-averaging, which is the most common Reynolds averaging procedure and is appropriate for a large number of engineering problems. Time-averaging can also be used. The statistical averaging can be equal to the time averaging, that had been widely adopted in experimental studies and in numerical studies afterwards, under the ergodicity hypothesis of the turbulence process, claiming that the statistical averaging does not depend on time, as well as its first and second order moments. In this case, the mean velocity is computed as :

$$\bar{U} = \lim_{N \to \infty} \frac{1}{N} \sum_{n=1}^{N} U_i(\vec{x}, t) \tag{3.21}$$

Also, by definition, the average of $U^{'}$ is zero. By considering the Reynolds decomposition in the Navier Stokes equations and by taking the mean, we obtain the RANS system of equations (Reynolds Averaged Navier Stokes). In case of time-dependent evolution of the U_{mean}, the system is the URANS (Unsteady Reynolds Averaged Navier Stokes) one. This system presents new unknowns, the second-order moments, $u_i u_j$ and therefore it is not closed. The ways of closing this system either by suitable phenomenological laws (Boussinesq approximation) or by additional transport equations for $u_i u_j$ had given access to the first and second-order moment closures in the URANS context since early 1970's. With the development and increased capacities of the computers, the URANS equations and their respective turbulence modelling gave rise to a multitude of turbulence modelling methods in the decades '80-90.

The passage (or extension) of RANS towards URANS adopted in a first step the same constants modelling the transfers between the resolved and unresolved turbulence. However, these constants had been derived for flows in *statistical equilibrium* where the Production is equal to the dissipation rate of the turbulence kinetic energy. A discussion on these aspects is also provided in a next section concerning *adapted* turbulence modelling able to capture non-equilibrium effects.

The simple extension of RANS to URANS with the inappropriate application of the modelling constants provided an excessive rate of turbulence diffusion and resulted in underprediction of the high Reynolds number effects for which these constants had been derived. Therefore, the majority of URANS modelling consisting of a simple extension of the RANS modelling by just adding the temporal term $d\bar{U}_i/dt$, provided an *over-prediction* of the drag coefficient for example, in case of high Reynolds number flows around bodies, as will be shown in the present thesis, by a simple URANS use of the k-ϵ model.

To recover these limitations of the standard URANS modelling, the definition of the averaging is of high importance. In this context, the LES (Large Eddy Simulation) was developed since '1985 and upgraded up to now, founded on the definition of a filtered averaging. From the middle of '1995, hybrid approaches associating URANS in the near-wall region and LES in the outer region have been developed.

In between URANS and LES, appropriate turbulence modelling based on *phase averaging or more generally ensemble averaging* was developed, coming from ideas of pioneering experiments on coherent structures (Cantwell and Coles (1983)), (Hussain and Reynolds (1970)), followed by more recent ones, (Perrin (2005)), in the Navier-Stokes equations by Reynolds-averaged ones and taking the average, obtains in differential form:

$$\frac{\partial \bar{\rho}}{\partial t} + \frac{\partial}{\partial x_i}(\bar{\rho}\bar{U}_i) = 0 \tag{3.22}$$

$$\frac{\partial}{\partial t}(\bar{\rho}\bar{U}_i) + \frac{\partial}{\partial x_j}(\bar{\rho}\bar{U}_i\bar{U}_j) = -\frac{\partial P}{\partial x_i} + \frac{\partial}{\partial x_j}(\bar{\sigma_{ij}} + \tau_{ij}) \tag{3.23}$$

$$\frac{\partial}{\partial t}(\bar{\rho}\bar{E}) + \frac{\partial}{\partial x_j}(\bar{\rho}\bar{U}_j\bar{E}) = -\frac{\partial P\bar{U}_j}{\partial x_i} + \frac{\partial}{\partial x_j}(\bar{\sigma_{ij}} + \tau_{ij}) + \frac{\partial}{\partial x_j}(k\frac{\partial \bar{T}}{\partial x_j} + q_j) \tag{3.24}$$

3.2.2 The eddy-viscosity assumption

The Reynolds-averaged Navier-Stokes equations were presented, the turbulent stress tensor τ_{ij} and the turbulent heat flux q_{tj} were introduced. The phenomenological law adopted to provide the needed additional equation for the $u_i u_j$ (τ_{ij}) tensor closing the system is inspired from the Boussinesq law for the Newtonian fluids, where the kinematic viscosity is replaced by the so-called "eddy viscosity":

$$\tau_{ij} = 2\mu_t S_{ij} - \frac{2}{3}\rho k \delta_{ij} \tag{3.25}$$

where μ_t is a scalar 'eddy viscosity' (also called turbulent viscosity) and S_{ij} is the mean strain-rate tensor.

$$S_{ij} = \frac{1}{2}(\frac{\partial u_i}{\partial x_j} + \frac{\partial u_j}{\partial x_i}) - \frac{1}{3}\frac{\partial u_k}{\partial x_k}\delta_{ij} \tag{3.26}$$

The Boussinesq hypothesis assumes that the principal axes of the turbulent stress and mean strain-rate tensors are collinear and is unable to capture anisotropy effects of the normal turbulent stresses (Bourguet (2008)). The Boussinesq approximation is though widely used in turbulence modelling where it provides satisfactory results concerning flows in statistical equilibrium, e.g. flows that do not develop unsteady coherent structures.

The eddy viscosity is evaluated by dimensional analysis through a turbulence length scale or through a turbulence kinetic energy and dissipation, yielding the introduction of two additional transport equations. This category of modelling is the so-called "two-equation" modelling in RANS or URANS. A detailed review of these considerations is presented in the PhD thesis of (Smaguina Laval (1998)), (Rodes (1999)), (Hoarau (2002)) and (El-Akoury (2007)). Based on the choice of the dimensional analysis variables, the k-ϵ and k-ω modelling has been derived. If additional transport equations for the $u_i u_j$ are considered, the new unknown appearing is the third-order moment tensor $u_i u_j u_k$, that need an additional phenomenological law itself for the closure of the system.

This class of turbulence modelling is the so-called *"second order moment closures"*, handled in the PhD theses of (Rodes (1999)), (Hoarau (2002)), (Bourguet (2008)). A detailed review of this class of models can be found in the PhD of (El-Akoury (2007)).

In presence of solid walls, due to the turbulent physics through the three classical layers, the viscous sublayer, the buffer region and the outer region (Hinze (1987)), the eddy viscosity concept has to respect this evolution and to tend to zero towards the wall.

The way of phenomenological laws (modelling) of this *turbulence dampening* is very important for the correct behaviour of a turbulence model and gave rise to a multitude of damping functions, f_μ multiplying the eddy viscosity and ensuring its progressive vanishing on the wall, by respecting the physics of these layers. This modelling gave access to the so-called "low Reynolds number turbulence modelling", (Patel et al. (1985)), where a multitude of damping functions had been studied in the context of the two-equation RANS modelling. It is worth noticing that "low Reynolds number modelling does not mean that the nominal Reynolds number of the flow is low. On the contrary, the validity of the closure schemes in RANS modelling (constants of the RANS transport equations) is based on the assumption of high Reynolds number of turbulence. Therefore the range of validity of the statistical modelling for a flow around a body is ideally of order 10^5 or higher.

Some of the applications in which the Boussinesq hypothesis fails are: flows with sudden changes in the mean strain, flows over curved surfaces, flows in rotating fluids and three-dimensional flows.

Based on the concept of eddy viscosity, the turbulent heat flux is then calculated by means of the 'Reynolds analogy'

$$qt_j = -k_t \frac{\partial T}{\partial x_j} = -c_p \frac{\mu_t}{Pr_t} \frac{\partial T}{\partial x_j} \tag{3.27}$$

where k_t is the turbulent thermal conductivity coefficient and Pr_t is the turbulent Prandtl number (which for air is 0.9).

3.2.3 Turbulence sustaining ambient terms

Turbulence models have been used with controlled decay (Spalart and Rumsey (2007)) turbulence sustaining ambient terms to prevent the free decay of the transported turbulence variables. The initial concept for controlled decay is simple: k and ϵ (or ω) are not allowed to drop below some preset values. It consists simply by adding source terms ϵ_{amb} and $C_{\epsilon 2}\epsilon_{amb}^2/k_{amb}$ to the right hand side of turbulent kinetic energy and dissipation equations as follows

$$\frac{Dk}{Dt} = P_k - \epsilon + \frac{\partial}{\partial x_j}[(\nu + \frac{\nu_t}{\sigma_k})\frac{\partial k}{\partial x_j}] + \epsilon_{amb} \tag{3.28}$$

$$\frac{D\epsilon}{Dt} = \frac{\epsilon}{k}(C_{\epsilon 1}P_k - C_{\epsilon 2}\epsilon) + \frac{\partial}{\partial x_j}[(\nu + \frac{\nu_t}{\sigma_\epsilon})\frac{\partial \epsilon}{\partial x_j}] + C_{\epsilon 2}\epsilon_{amb}^2/k_{amb} \tag{3.29}$$

with $\nu_t = C_\mu k^2/\epsilon$, and $C_\mu = 0.09$. The ambiant terms does not need to be disabled near the wall because k_{amb} and ϵ_{amb} are small enough.
For the K ω SST model, the addition of sustaining terms yields following equations :

$$\frac{Dk}{Dt} = P_k - \beta * \omega k + \frac{\partial}{\partial x_j}[(\nu + \frac{\nu_t}{\sigma_k})\frac{\partial k}{\partial x_j}] + \beta * \omega_{amb}k_{amb} \tag{3.30}$$

$$\frac{D\omega}{Dt} = \frac{\gamma}{\mu_t}Pk - \beta\omega^2 + \frac{\partial}{\partial x_j}[(\nu + \frac{\nu_t}{\sigma_\omega})\frac{\partial \omega}{\partial x_j}] + 2(1 - F_1)\frac{1}{\sigma_{\omega 2}\omega}\frac{\partial k}{\partial x_j}\frac{\partial \omega}{\partial x_j} + \beta\omega_{amb}^2 \tag{3.31}$$

The model in the equations 3.30 and 3.31 is identical to the classical Shear Stress Transport-k-ω model (SST) by (Menter (1994)) in every respect except for the addition of the sustaining terms $\beta * \omega_{amb}k_{amb}$ and $\beta\omega_{amb}^2$ respectively. If $k = k_{amb}$ and $\omega = \omega_{amb}$ then the destruction terms are cancelling. Generally these ambient sustaining terms inside the turbulent layer are of the order of magnitude smaller than the destruction terms at reasonable turbulence levels ($Tu = 1\%$ or less).

3.2.4 OES : Organized-Eddy Simulation

The Organised-Eddy Simulation (OES) approach is in-between the statistical and LES approach. It was derived from the highlights of the coherent structures development in turbulent shear flows including those around bodies, thanks to pioneering experimental studies starting in the middle of '70s: (Brown and Roshko (1974), Cantwell and Coles (1983), Hussain and Reynolds (1970)). Thanks to these studies, that made evidence of overly structures governing the turbulent shear flows was made and measured experimentally by appropriate averaging (the phase-averaging). This new insight has proven that turbulence is not just a chaotic process but has a dual character, where the chaotic structures are embedded in the coherent structures (figure 3.1):
The OES is used in the 2D configurations as well as in the 3D simulations of a supercritical airfoil. This method is described as follows: The statistical turbulence modelling offers robustness of the simulations in the region of high Reynolds numbers but it has proven a strong dissipative character that tends to dampen crucial instabilities occurring in turbulent flows around bodies, as for example low frequency modes (von Kármán instability, buffet or flutter phenomena). The OES approach offers an alternative that is robust and captures the above physical phenomena. In this method, the decomposition of a variable $u(x,t)$ is based on the phase ensemble - averaging of the flow as follows :

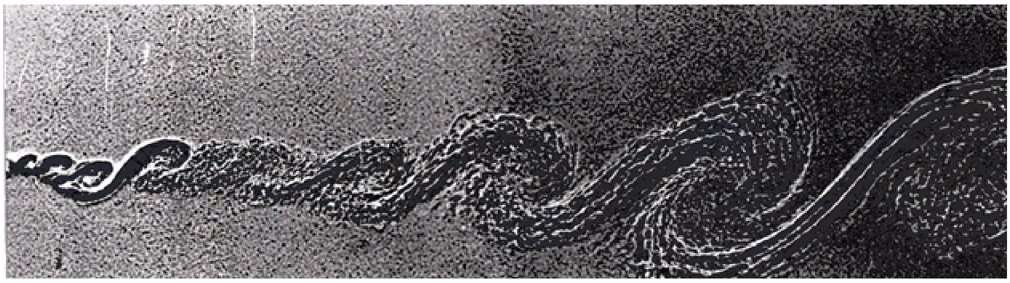

FIGURE 3.1: (Brown and Roshko (1974)), "On density effects and large structure in turbulent mixing layers", J. Fluid Mech. Vol. 64

$$u(x,t) =< u(x,t) > +u'(x,t) \tag{3.32}$$

where the $< u(x,t) > = \bar{u}(x) + u_c(x,t)$ the ensemble (phase) average calculated with the summation of the temporal mean $\bar{u}(x)$ and the resolved (coherent) fluctuations part $u_c(x,t)$. This results to a phase-averaging if only one periodicity is pronounced. This approach consists of splitting the energy spectrum in a first part that regroups the organised flow structures (resolved part) and a second part that includes the chaotic processes due to the random turbulence (to be modelled). In the time-domain, the spectrum splitting leads to phase-averaged Navier-Stokes equations (Jin and Braza (1994)). A schematic illustration of the OES approach is presented in the figure 3.2. The turbulence spectrum to be modelled is extended from high to low wave number range therefore statistical turbulence modelling considerations can be adopted inducing robustness properties.

However, the time and length scales of turbulence are modified in this part of the spectrum, because of modification of the energy transfers between the organised and chaotic turbulent motion. This yields non-equilibrium effects where the turbulence production is not equal to the dissipation. Experiments by TRPIV (Braza et al. (2006)) as well as by LDV (Djeridi et al. (2003)) quantified the difference in the form and the slope of the spectrum in the inertial range (figure 3.3). Furthermore, more recent TR-PIV experiments by (Perrin et al. (2008)) and by (Bourguet et al. (2007)) revealed and evaluated a strong mis-alignment in the principal axes of the stress and strain tensors in the near wake past a circular cylinder in high Reynolds number, under the coherent structures effects deviating the turbulence properties from those of equilibrium turbulence. This indicated the inadequacy of the (linear) Boussinesq law employed

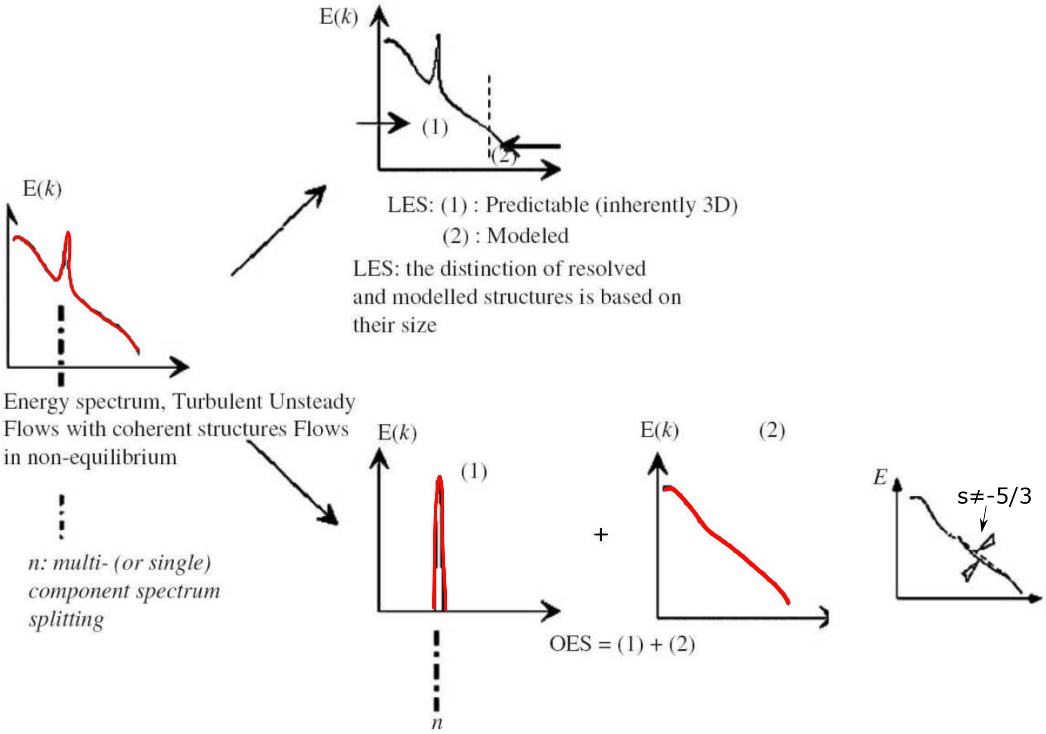

FIGURE 3.2: Representation of the spectral decomposition for OES and LES (Bourguet et al. (2008))

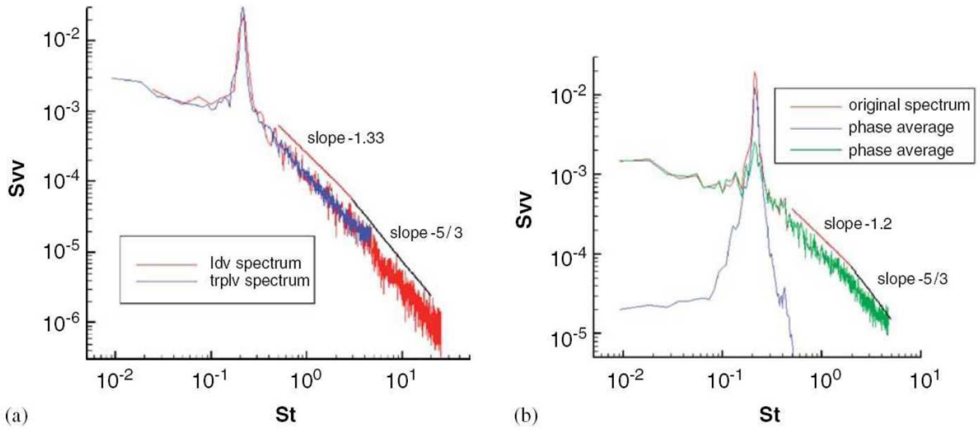

FIGURE 3.3: (a) Comparison of spectrum energie obtained from experimental data from PIV (Braza et al. (2006)) and LDV (Djeridi et al. (2003)). (b) Energy spectrum obtained from PIV before and after phase averaging. Measurement of the near cylinder wake at Re = 1.4 x 10^5

in standard URANS modelling that involves a scalar eddy-viscosity, thus leading to stress-strain alignment and can explain the need of taking into account the modification of the turbulent scales to capture the present non-equilibrium turbulence effects. Therefore the use of standard (U)RANS modelling is not sufficient in this case. In non-equilibrium turbulence, the inequality between turbulence production and dissipation rate modifies drastically the shape and slope of the turbulence spectrum in the inertial range (figure 3.2), comparing to the equilibrium turbulence, that obeys to the Kolmogorov's cascade (slope equals to 5/3). This modification has been quantified in experimental studies (figure 3.3). Therefore, the turbulence scales used in standard URANS modelling have to be reconsidered in OES, to capture the effects due to the non-linear interaction between the coherent structures and the random turbulence. In the context of the OES approach, a modification of the turbulence scales in two-equation models was achieved on the basis of the second-order moment closure (Bourdet et al. (2007)), to capture the stress-strain misalignment previously mentioned. By projecting the DRSM (Differential Reynolds Stress Modelling) equations on the principal directions of the strain rate, a transport equation is derived for the mis-alignment angle in three dimensions, deriving a *tensorial eddy-viscosity concept*, (Bourguet et al. (2008)). This yields to a directional eddy-diffusivity C_μ coefficient that tends to values of order 0.02 to 0.03 in the mis-alignment regions where it takes the classic value of 0.09 in the regions of alignment. This *anisotropic OES* modelling confirmed previous studies by (Rodes (1999)) and (Hoarau (2002)), that evaluated by DRSM and by DNS around a wing in high Reynolds number and strong incidence the

C_μ coefficient taking values of order 0.02 and quantified the deviation from equilibrium boundary layers (Bradshaw and Galea (1967)) that had evaluated the turbulence stress anisotropy uv/k to take a constant value along the boundary layer, from which had been derived the $C_\mu = 0.09$ by assuming the production equal to the dissipation and considering the classic Boussinesq law in (U)RANS. These facts suggested a simplified version of the OES modelling by considering a lower C_μ (order of 0.02) in the two equation modelling. Furthermore, the turbulence damping near the wall needed also to be revisited because of the different energy distribution between coherent and random processes in non-equilibrium near-wall regions.

The efficiency of the OES approach in 2D and 3D has been proven in a number of strongly detached high Reynolds number flows, especially around wings (Hoarau (2002)) and (Hoarau et al. (2006)), as well as in the context of DES (El-Akoury (2007)) as detailed in the next section, where the DES part near the body can be handled by the OES for a better capturing of the previously mentioned near wall non-equilibrium turbulence effects.

In the transport equations produced by means of the phase (ensemble) averaging where the Reynolds/Favre averages quantities are replaced by the phase averaged ones and the turbulent stresses are expressed as follows :

$$\tau_{ij} = 2\mu_t < S_{ij} > -\frac{2}{3}(\mu_t \frac{\partial < u_m >}{\partial x_m} \delta ij - \bar{\rho} K)\delta ij \tag{3.33}$$

This simplified form of the OES is adopted in the present study and it has been implemented based on Chien's K-ϵ model. The added value consists of a reconsideration of the closure constants and an adapted eddy-viscosity damping. A law with a less abrupt gradient than in equilibrium turbulence was suggested, (Jin and Braza (1994)) :

$$f_\mu = 1 - exp(-0.0002y^+ - 0.000064y^{+2}) \tag{3.34}$$

$$f_1 = 1 \text{ and } f_2 = \left(1 - 0.22e^{-\frac{Re_t^2}{36}}\right)$$
$$C_\mu = 0.02 - 0.04 \text{ , } C_{\epsilon 1} = 1.35 \text{ , } C_{\epsilon 2} = 1.8 \text{ , } \sigma_K = 1.0 \text{ and } \sigma_\epsilon = 1.3$$

It is worth noticing that the OES approach is *not intrinsically* three-dimensional as in case of the LES. This because main features of the coherent structures have a strong 2D character, as for example their frequency, based on a considerable number of experimental studies, including the ones previously mentioned. Therefore the OES allows carrying out a large and rich parametric study from which optimal ranges of the sensitive parameters (in the case of the present thesis the vibration frequency and amplitude of the actuators) can be detected and orienting the more detailed 3D study towards well focused and narrow parametric ranges. This offers a high potential comparing to other approaches needing 3D simulations only.

3.2.5 Delayed Detached Eddy Simulation DDES-OES

The Detached-Eddy Simulation(DES), is a hybrid RANS-LES method that was first introduced on the ideas of (Speziale (1998)). This approach aimed at associating the benefits of robustness and of the good physical description of turbulence in the near wall region and the benefits of LES in the outer (not wall-bounded) region around a body. Therefore, this approach removed the limitations of the LES to the low Reynolds number range and simultaneously permitted obtaining a more rich turbulence content than the simple URANS approaches by removing the excessive turbulence modelling diffusion in the high Reynolds number range around a body. The DES is therefore intended to model high Reynolds massively-separated flows around complex geometries and its repercussion has been great in the CFD community and in the industrial context, thanks to devoted federative European projects in aeronautics, as the projects : FLOMANIA (Flow Physics Modelling an integrated approach), DESIDER (Detached Eddy Simulation for Industrial Aerodynamics), ATAAC (Advanced Turbulence simulations for Aerodynamics Application Challenges), UFAST (Unsteady Effects in shock wave induced separation), TFAST (Transition location effects on shock wave boundary layer interaction), in which the research team of the present thesis participated with simulations and well focused experiments, as for example the "IMFT circular cylinder", (Haase et al. (2009)) that allowed validation of the present approach and its variant, the DDES: Delayed Detached Eddy Simulation", detailed in a next paragraph.

A recent review covering the DES and its later improvements is provided in Spalart (2009). A principal idea in the DES framework that highly increased its efficiency comparing to other hybrid RANS - LES methods is that the DES does not need imposing an interface between the RANS and LES regions. The only system of transport equations is the (U)RANS system in the framework of one or two-equation modelling, where the turbulence length scale is chosen as the minimum between the (U)RANS length scale and an LES-like length scale, equal to C_{DES}.max($\Delta x, \Delta y, \Delta z$) as following:

$$l_{DES} = min(l_{RANS}, C_{DES} \times \Delta) \tag{3.35}$$

Where Δ is the max$(\Delta x, \Delta y, \Delta z)$.
For one equation model Spalart-Allmaras model $l_{DES} = min(d_w, C_{DES} \times \Delta)$.
The augmentation of the dissipation term in the eddy-viscosity transport equation:

$$\frac{D\tilde{\nu}}{Dt} = C_{b1}(1 - f_{t2})\tilde{S}\tilde{\nu} + \frac{1}{\sigma}[\nabla.((\nu + \tilde{\nu})\nabla\tilde{\nu}) + c_{b2}(\nabla\tilde{\nu})^2] - \underbrace{(C_{w1}f_w - \frac{C_{b1}}{\kappa^2}f_{t2})(\frac{\tilde{\nu}}{l_{DES}})^2}_{Dissipation\ \ rate} \tag{3.36}$$

For the two-equation model K-ω model The augmentation of the dissipation term in the k transport equation :

$$\frac{D\bar{\rho}k}{Dt} = \tau_{ij}\frac{\partial U_j}{\partial x_i} - \underbrace{\frac{\rho k^{3/2}}{l_{DES}}}_{Dissipation\ \ rate} + \frac{\partial}{\partial x_j}[(\mu + \sigma^* \mu_t)\frac{\partial k}{\partial x_j}] \tag{3.37}$$

In the DES/OES approach; the improvement of l_{RANS} adopted from equilibrium turbulence within DES using l_{OES} in inertial regions where :

$$l_{OES} = \frac{k^{1/2}}{C_\mu \omega} \tag{3.38}$$

Typical DES grids normally have the grid spacing in the direction parallel to the surface Δx larger than the boundary layer thickness δ as illustrated on the top of figure 3.4 for a flat plate. In some cases, however, surface grids may become excessively refined to represent features of the geometry or for a proper resolution of a shock wave, for example. Furthermore, thick boundary layers can arise naturally as in high-incidence flows, near separation points or as a result of shock wave/boundary layer interactions. Such situations can derive Δx locally smaller than δ (figure 3.4), leading to a condition of 'ambiguous grid density' leading to a RANS computation, (see relation 3.35 for the l_{DES} length scale), whereas the grid on the right hand side would lead to approach the LES mode quite close towards the wall and yield spurious (unphysical) local separations. This inconvenient is well known as "the grey area of the DES", issued from the so-called "Modelled Stress Depletion", MSD, for which the Delayed Detached Eddy Simulation has been developed (Spalart et al. (2006)).

MSD may potentially reduce the skin-friction and in some cases even cause premature separation as reported by (Menter and Kuntz (2004)) who described the phenomenon as a 'grid-induced separation. The solution to the MSD problem via the DDES approach is detailed as follows, (Spalart et al. (2006)).

The improved DES approach detects and 'shields' attached boundary layers, thus delaying the activation of the LES mode too close to the wall. The modification of

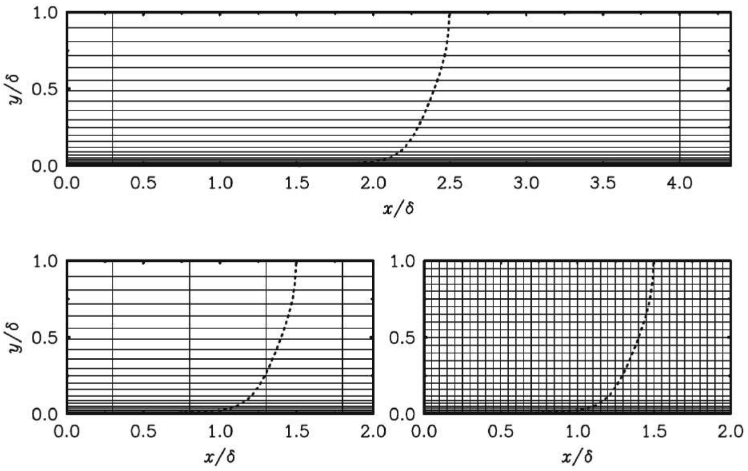

FIGURE 3.4: Typical grids for a boundary layer on a flat plate (from Spalart et al. (2006)). Top: DES grid ($\Delta x > \delta$). Left: ambiguous grid ($\Delta x < \delta$). Right: LES grid ($\Delta x \ll \delta$)

the turbulence length scale in DDES is done through the near-wall parameter r_d (see equation 3.39). This quantity can be easily implemented and extended to other eddy-viscosity models and serves as an indicator of whether a grid point is located inside a boundary layer.

$$r_d = \frac{\nu_t + \nu}{S\kappa^2 d^2}, \qquad where \qquad S = \sqrt{\frac{\partial u_i}{\partial x_j}\frac{\partial u_i}{\partial x_j}} \tag{3.39}$$

The subscript d stands for 'delayed'. r_d is equal to 1 in the logarithmic layer and goes to 0 as one approaches the boundary layer edge. The scalar S was chosen as the norm of the whole deformation tensor in order to gain in robustness in irrotational regions (Spalart et al. (2006)). The introduction of the molecular viscosity in the numerator allows keeping a significant value of r_d towards the wall, in respect of compensating the damping of the turbulence viscosity ν_t activated by the turbulence models.

The r_d parameter is used to design the delaying function f_d, which is capable of ensuring a sufficiently thick RANS region and activating the LES region not very close to the walls. This function is defined as:

$$f_d = 1 - tanh\left[(8r_d)^3\right] \tag{3.40}$$

and is equal to 1 in LES regions ($rd \ll 1$) and to 0 in all other zones. Finally, the $DDES$ length scale is computed by

$$l_{DDES} = l_{RANS} - f_d max(0, l_{RANS} - l_{LES}) \tag{3.41}$$

Taking the SA model as example, equation 3.41 becomes

$$l_{SA-DDES} = d - f_d max(0, d - C_{DES}\Delta) \tag{3.42}$$

Contrary to the *DES* (where the length scale depends only on the wall distance and on the grid size), in the *DDES* formulation the switching between RANS and LES also depends on the turbulence state by means of the eddy viscosity. Therefore, the effective turbulence length scale is influenced by the flow physics and can vary both in space and time. Furthermore, the transition between the two modes becomes more rapid, reducing the size of the gray area (Spalart et al. (2006)).
Compared to the DES method, tests for a boundary layer on a flat plate (Spalart et al. (2006)) showed that the DDES avoids undesired switching to LES when using ambiguous grids, keeping the eddy-viscosity levels comparable to RANS computations. In simulations involving coarse grids, the DDES provided results very similar to those from standard DES. A positive side effect of DDES is that the approach minimizes problems arising from inappropriate user intervention, although it does not eliminate them. For instance, proper grid design is still required. A detailed study showing the advantages of the DDES approach for the simulation of the transonic buffet over a supercritical wing, the so-called OAT wing in the context of the ATAAC European project is provided by Grossi et al. (2014), where a thorough investigation of the near wall area through the development of the f_d and μ_t is presented.

3.2.5.1 The OES approach within the DES and DDES

The OES approach can highly improve the DES and DDES, by reconsidering the turbulence length scale in the relation 3.41. In fact, in the near wall region, the flow is highly affected by the instabilities and the coherent structures development, even if these appear farther that the solid wall, due to the *elliptic character* of the flow enhancing the *feedback effects* in this low subsonic region near the wall (even in case of transonic or supersonic inlet Mach number). Therefore, this kind of boundary layer is in strong non-equilibrium and has to be handled by not simply URANS modelling. The OES method that is classified in-between URANS and LES, efficiently accounts on non equilibrium turbulence effects as detailed in section 3.2.4. It is therefore suitable for use in the near-region of the DES and DDES approaches. This is accomplished by considering the l_{DES} length scale according to the relation:

$l_{DES} = min(l_{OES}, C_{DES} \times max(\Delta x, \Delta y, \Delta z))$, where l_{OES} in case of using two-equation OES modelling is equal to $k^{3/2}/\epsilon$.

This introduction of OES in the DES framework allows a better physical representation of the near-region unsteadiness and of the turbulence transfers towards the LES region, thus ensuring a smooth and physical passage from the near region to the LES region.

This approach, called DES-OES and DDES-OES if the DDES length scale relation is adopted, provided significant results in a number of applications as follows: simulation of the flow around a circular cylinder at Reynolds number 1.4 x 10^5 by (Bourguet et al. (2008)) in a confined environment has been performed using the OES approach in the context of Detached Eddy Simulation shown in figure 3.5. Time averaged $\bar{U}$ and C_P obtained with DES-OES method were compared to the experimental results in figure 3.5 obtained by (Perrin (2005)) in the IMFT wind tunnel. In addition, the over prediction of the low pressure region (figure 3.5 (a)) upstream of the detachment ($\theta = 72°$) has been reduced compared to DES-SST method and the detached region is well captured. In figure 3.5 (b) the mean longitudinal velocity $\bar{U}$ has been compared with the PIV experiments. A good agreement has been reached. Moreover, a highly reliable prediction of the time-averaged aerodynamic forces has been achieved by the DES-OES where the drag is evaluated as $Cd = 1.43$ and the experimental results $Cd = 1.44$ (Perrin (2005)).

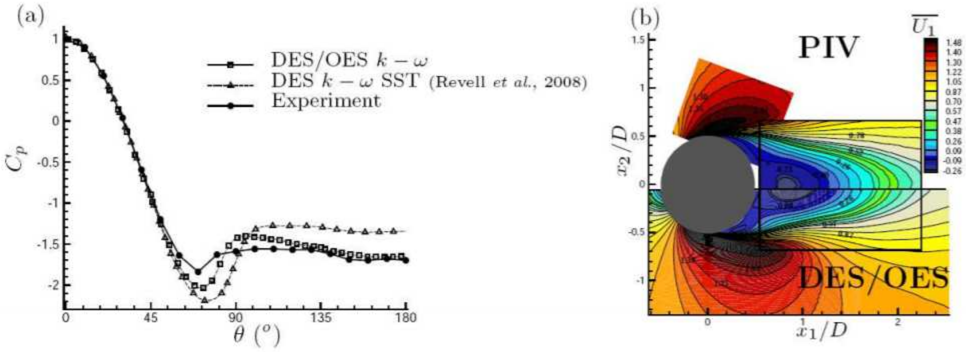

FIGURE 3.5: (a) Comparison between the experimental (Perrin (2005)) and numerical DES-SST and DES-OES time-averaged wall pressure coefficient, (b) comparison of time-averaged longitudinal velocity fields issued form TRPIV in the context of the "IMFT's circular cylinder" DESIDER - EU project test case, (El-Akoury (2007), Haase et al. (2009), Perrin (2005)) and from DES-OES approach, results in (Bourguet (2008))

The use of the OES approach in the statistical part of DES model allowed improving the prediction of strong detached turbulent flows around bluff bodies in the high

Reynolds number range. This has been accomplished due to the better coherence between the non-equilibrium RANS turbulence length scale and LES length scale in the interface URANS and LES, comparing to the classical standard DES model which uses only equilibrium turbulence RANS length scale.

The advantages of the DDES-OES have been shown in the prediction of a federative test-case for the hybrid methods concerning the of the flow around a tandem of cylinders, based on experiments by NASA - Langley (Jenkins et al. (2005)), widely used in the aeronautics community and particularly in the European project ATAAC, where participated our research team. The guest student **M. Gual-Skopek** in collaboration between Technical University Berlin (TUB) under the supervision of **Prof. Thiele** during his scientific stay in IMFT in the context of the ATAAC European project, was the winner of the 3rd Best student' award in AERODAYS 2011 organised by the European Commission, for his simulations with the DDES-OES for the tandem cylinders configuration, published in the RANS-LES Book (Skopek et al. (2012)). Moreover, In the article (Moussaed et al. (2016)), the DDES-OES approach has shown quite promising results for capturing the shear-layer instability and the related frequency modes past the downstream cylinder of the tandem cylinders, responsible for the landing-gear noise and provided a very good comparison of the mean field with the PIV data of NASA - Langley.

Furthermore, the study of our team by (Shinde et al. (2014)) provide quite good results for the Fluid-Structure interaction prediction of the vibrational instability developed in a cylinders array cooling configuration of a nuclear reactor, in collaboration with experiments by EDF (Electricité de France) and CEA (Commisariat d'Etudes Atomiques, in the context of the National ANR project BARESAFE ("Simulation of Safety Barrier Reliability") with participation of ICUBE and IMFT Institutes of research. Moreover, the introduction of the OES length scale in the simple DES approach highly improves it as shown in the PhD thesis of (Simiriotis (2020)) in the case of the transonic buffet simulation over the V2C wing designed by Dassault Aviation, in the context of the TFAST European project.

According to the previous sections, the OES approach has revealed quite promising results in many studies as well as when it is activated in the statistical part of the DDES. In the present thesis, we mainly focus on the OES and DDES-OES approaches to simulate the flow around morphing wings. As will be seen in the results, these modelling approaches are more reliable to well capture the unsteadiness, adverse pressure gradients, boundary layer detachment, main instabilities and coherent structures development in two and three dimensions.

The continuum hypothesis of the transport equations up to now needed to be reconsidered to solve numerically the system on a number of discrete unknowns derived from an appropriate grid. A huge variety of numerical methods (finite difference, finite volume, finite elements) had been developed in the last 40 years in order to discretise the Navier-Stokes system.

3.3 Navier Stokes Multi Block (NSMB) code

The numerical solver Navier-Stokes Multi-Block (NSMB) (Hoarau (2002), Hoarau et al. (2016), Vos et al. (1998)) is used in our study. This solver was a fruit of long developments from the beginning of ’90’s thanks to the first set of federative European Research programmes in Aeronautics, as the projects EUROVAL, and ECARP, regrouping main research Institutes as KTH (Stokholm), EPFL (Lausanne), VUB (Vrije Universitaer Brussels) in the FP2 and FP3 framework and later, through the EU projects of FP4 to FP7 framework, as : FLOMANIA, DESIDER, ATAAC, UFAST, TFAST, and more recently AFLONEXT (2nd generation of active wing), AGILE/AGILE4.0, RETALT, AFC4TR (within Cleansky2) and SMS, "Smart Morphing & Sensing for Aeronautical configurations. The partners of the NSMB consortium are : CFS Eng., Ruag Aerospace-Swiss, SMR Eng., ArianeGroup (AIRBUS & Safran) and the Institutes CERFACS, IMFT, ICUBE, Univ. of Karlsruhe, Ecole Polytechnique de Montréal, among other. The code is maintained by CFS-Engineering - Lausanne.
This code was adapted from the beginning for aeronautical configurations with emphasis on highly advective flows with a powerful set of numerical schemes and including also the equations for hypersonic flows. This code, based on structured finite volume architecture and parallel computing using MPI for the most powerful supercomputers, included CHIMERA grids (Deloze (2011)) able to handle very complex body configurations as well as coupling with the structural modes. More recently in the context of the SMS project, the NSMB code has been coupled with electroactive structural properties of the body, being the first code having this potentiality (Simiriotis (2020)).
The code solves the compressible form of the Navier-Stokes equations and uses structured grids. Furthermore, the development of CHIMERA grids allows treatment of complex geometries like those over a whole aircraft, as shown in the present thesis (Chapters 6 and 7). Well adapted for highly advective regimes including shock waves as well as suitable preconditioning methods permitting computation in very

low Mach number, practically incompressible regimes.

The NSMB code contains a considerable number of turbulence modelling closures in the context of LES, URANS and hybrid RANS-LES approaches. These developments can be found in (Hoarau (2002)) regarding URANS modelling for strongly detached flows (Martinat et al. (2008)), in the area of moving body configurations, (Barbut et al. (2010)) and (Grossi et al. (2014)) for Detached Eddy Simulation (Bourguet (2008)) concerning transition modelling and new developments in turbulence modelling by stochastic forcing coupling with electraoctively deformed structures (Simiriotis (2020)).

Nowadays the solver NSMB is mainly developed by the research institutes ICUBE in Strasbourg, IMFT in Toulouse, France and CFS Engineering and for several years, by interaction with the Ecole Polytechnique of Montreal.

In NSMB, the finite volume method is employed to solve the Navier-Stokes equations on multi-block structured grids, allowing massive parallel computing. Convective fluxes can be treated by central-differencing schemes with adaptive artificial dissipation (scalar or matrix formulations) or upwind schemes. For the latter, Total Variation Diminishing (TVD) schemes are available. In the present thesis, the version of Roe's third order upwind scheme (Harten (1997)) associated with the flux limiter "Monotonic Upstream-centered Scheme for Conservation Laws" (MUSCL) of van Leer (van Leer (1979)) are employed for the convective fluxes, as well as the 4th-order central scheme of Jameson for the diffusive terms. In addition, the "Advection Upstream Splitting Method" scheme (AUSM). is available (Liou and Steffen (1993)) as well as the Essentially Non Oscillating (ENO) (Harten et al. (1987)) and Weighted WENO (Liu et al. (1994)) high - order schemes are also available and used in current studies of our research team.

Time integration is handled in NSMB by means of the dual time stepping approach (Venkateswaran and Merkle (1995) and resolution of the derived linear systems using Lower-Upper Symmetric Gauss-Seidel (LU-SGS) or Lower-Upper Symmetric Successive OverRelaxation LU-SSOR. Time marching in explicit methodology employs the 4th - order Runge Kutta scheme.

3.4 Grid deformation for the morphing

A fast and reliable method for deforming the computational grid during each step of the time simulation is needed while maintaining a good mesh quality as the orthogonality and the smoothness. The remeshing algorithm implemented in the code NSMB combines the Volume Spline Interpolation (VSI) and Transfinite Interpolation (TFI) (Guillaume et al. (2011)). These methods collect at first the imposed displacement of the trailing-edge and creates a list of cell-vertex ensemble. The Volume Spline Coefficients calculation requires a matrix inversion of a full square matrix $N+1$ rows where N is the number of vertices on the configuration surface. Only moved block edges using VSI method are taken into account. This is one of the VSI method advantages that does not require all the coordinates. In the next step, the Trans Finite Interpolation is used to generate the displacement of block faces coordinates in two-dimensions or the volume in three-dimensions. Finally, the new deformed grid is computed based on the imposed deformation fixed as an input as presented in figure 3.6 showing the new computed grid after a deformation. These methods are used with a high success and they are able to compute high-quality mesh deformation allowing preservation of a good orthogonality whenever needed. In addition, the TFI method is quite fast since the computational effort and the number of volume grid points N_v are proportional.

3.4.1 Arbitrary Lagrangian Eulerian (ALE) method

In this section, basic theoretical concepts of the Arbitrary Lagrangian-Eulerian (Donea et al. (1982)) are presented. A brief discussion about the kinematics moving reference frames and derivation of ALE differential forms for the basic conservation equations of mass, momentum and energy are provided as in (Donea et al. (1982)).

The Arbitrary Lagrangian-Eulerian (ALE) method treats the computational grid such us a reference frame that could move with a imposed or arbitrary velocity w. When $w \neq v \neq 0$ the reference frame moves with a different velocity compared to the flow velocity. This frame is called Arbitrary Lagrangian-Eulerian and each point is identified by an instantaneous position vector ξ_i (mixed variable).

The fluid is still identified through its material coordinates a_i in the initial configuration of the continuum. The mixed position ξ_i is linked to the material variables (a_i,t)

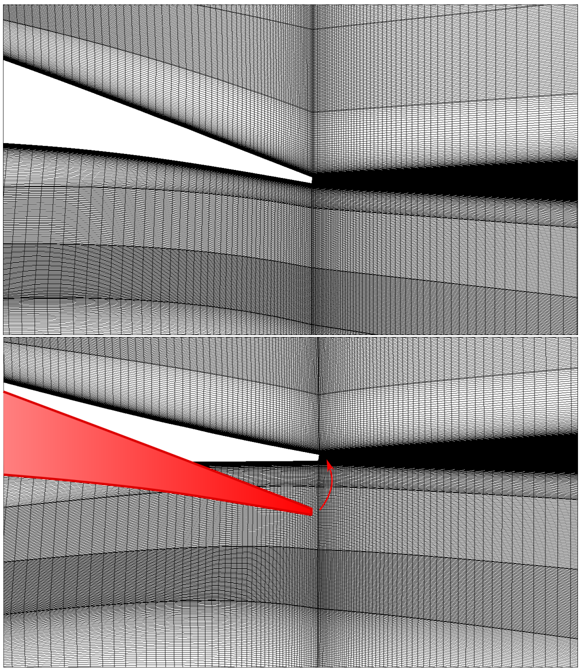

FIGURE 3.6: Left : A zoom of the static grid of the A320 near to the flap's trailing edge. Right : an upward dynamic deformation. The (red) area refers to the original position

by the law of motion of the reference frame as

$$\xi_i = f_i(a_i, t) \tag{3.43}$$

The ALE description can be viewed as a mapping of the initial configuration of the continuum into the current one of the reference frame, then Jacobian determinant can be expressed as

$$J = |\partial \xi_i / \partial a_j| \tag{3.44}$$

The conservation laws in the ALE description uses Cartesian tensor notation and neglects the viscous effects. The conservation of mass, momentum and energy can be expressed in their local form in a reference frame moving at an arbitrary velocity w as

$$\frac{\partial}{\partial t}(\rho J) = J \frac{\partial}{\partial x_j}(\rho(w_j - v_j)) \tag{3.45}$$

$$\frac{\partial}{\partial t}(\rho v_i J) = J \frac{\partial}{\partial x_j}(\rho v_i(w_j - v_j)) + J(\rho b_i - \frac{\partial p}{\partial x_i}) \tag{3.46}$$

$$\frac{\partial}{\partial t}(\rho e J) = J\frac{\partial}{\partial x_j}(\rho e(w_j - v_j)) + J(\rho v_j b_i - \frac{\partial p v_j}{\partial x_j}) \tag{3.47}$$

It is easily verified that the particular cases of purely Lagrangian ($w = v$) and purely Eulerian ($w = 0$) descriptions are contained in the above conservation relations.

3.5 The Proper Orthogonal Decomposition for the physical analysis of the unsteady flow fields

The proper orthogonal decomposition is an SVD (Singular Value Decomposition) able to split a dynamic system in its ingredients as an ensemble of orthogonal modes or Karhunen–Loewe decomposition, after maximisation of a scalar product representing a characteristic property of the flow. This is accomplished through evaluation of the Φ_i coefficients after an optimisation procedure. In fluid Mechanics, the POD has been used by adopting a *separation* of the space and time variables (the separable POD yielding the snapshots POD , (Sirovich (1987)) and (Berkooz et al. (1993))), according to the relation 3.48. The POD is used for a better understanding of the flow dynamics in the wake and for the reconstruction of the dynamic system by using a reduced number of only principal modes able to describe it.

The POD is efficient in both experimental and numerical context for identifying the dominant flow features as well as the impact of low energy modes involved in the chaotic turbulence processes. In addition, the POD is used in data reduction ROM (Reduced Order Modelling) in order to construct low-dimensional models (Bourguet et al. (2009, 2011)).

A flow velocity vector $U(x,t) = u_1, u_2, u_3$ following the 3 directions (x_1,x_2,x_3) is decomposed according to the separation of the time and space variables to:

$$U(\mathbf{x},t) = \sum_{i=1}^{N} \phi_i(\mathbf{x}) a_i(t) \tag{3.48}$$

Hence, the POD decomposes a set of instantaneous flow fields (velocity) into a series of orthonormal flow patterns (called POD modes) and the corresponding mode coefficients (temporal coefficients). The modes are rank-ordered by decreasing kinetic energy content, and the low-order, high-energy modes are interpreted as constituting the large-scale coherent structures of the flow.

$$u = (u_1, u_2, ..., u_{nc}); x = (x_1, x_2, ..., x_{nx}); t = (t_1, t_2, ..., t_{Nt}); N_x = n_x \times n_c \tag{3.49}$$

Given a set of instantaneous velocity fields n_c obtained via databases (saved snapshots) each t_i given as in the equation 3.49. The u_i are the vertical and streamwise velocities corresponding to the x_i directions. The snapshot matrix S can be constructed as given in the equation 3.50 :

$$S = \begin{pmatrix}
u_1(x_1, t_1) & u_1(x_1, t_2) & \cdots & u_1(x_1, t_{N_t-1}) & u_1(x_1, t_{N_t}) \\
u_2(x_1, t_1) & u_2(x_1, t_2) & \cdots & u_2(x_1, t_{N_t-1}) & u_2(x_1, t_{N_t}) \\
\vdots & \vdots & \vdots & \vdots & \vdots \\
u_{n_c}(x_1, t_1) & u_{n_c}((x_1, t_2) & \cdots & u_{n_c}((x_1, t_{N_t-1}) & u_{n_c}((x_1, t_{N_t}) \\
\vdots & \vdots & \vdots & \vdots & \vdots \\
u_1(x_2, t_1) & u_1(x_2, t_2) & \cdots & u_1(x_2, t_{N_t-1}) & u_1(x_2, t_{N_t}) \\
u_2(x_2, t_1) & u_2(x_2, t_2) & \cdots & u_2(x_2, t_{N_t-1}) & u_2(x_2, t_{N_t}) \\
\vdots & \vdots & \vdots & \vdots & \vdots \\
u_{n_c}(x_2, t_1) & u_{n_c}((x_2, t_2) & \cdots & u_{n_c}((x_2, t_{N_t-1}) & u_{n_c}((x_2, t_{N_t}) \\
\vdots & \vdots & \vdots & \vdots & \vdots \\
\vdots & \vdots & \vdots & \vdots & \vdots \\
u_1(x_{N_x}, t_1) & u_1(x_{N_x}, t_2) & \cdots & u_1(x_{N_x}, t_{N_t-1}) & u_1(x_{N_x}, t_{N_t}) \\
u_2(x_{N_x}, t_1) & u_2(x_{N_x}, t_2) & \cdots & u_2(x_{N_x}, t_{N_t-1}) & u_2(x_{N_x}, t_{N_t}) \\
\vdots & \vdots & \vdots & \vdots & \vdots \\
u_{n_c}(x_{N_x}, t_1) & u_{n_c}((x_{N_x}, t_2) & \cdots & u_{n_c}((x_{N_x}, t_{N_t-1}) & u_{n_c}((x_{N_x}, t_{N_t})
\end{pmatrix} \tag{3.50}$$

The correlation matrix R is required to compute the modal decomposition as :

$$R = \frac{1}{N}.S^T.S \tag{3.51}$$

and the corresponding eigenvalue problem as follows

$$RA = \lambda A \tag{3.52}$$

Where A is the eigenvectors matrix and λ the array of eigenvalues.
The calculated eigenvalues are arranged in the descending order as $\lambda_1 > \lambda_2 > ... > \lambda_N$=0. To calculate the spatial mode ϕ are computed from the matrix of eigenvectors A as follows :

$$\phi_i = \frac{\sum_{j=1}^{N} A_j^i u^j}{|| \sum_{j=1}^{N} A_j^i u^j ||}, i = 1, 2, ...N \tag{3.53}$$

ϕ_i being the i^{th} spatial mode. After computing spatial modes, the temporal modes are calculated directly :

$$a_i = \phi_i S \tag{3.54}$$

Both the temporal and spatial modes can now be used in order to reconstruct a snaphot u^n based on a fixed number of modes.

$$u^n = \sum_{i=1}^{N} a_i^n \phi_i \tag{3.55}$$

Chapter 4

Morphing of a reduced-scale airbus wing through electroactive trailing edge actuation

This chapter is a numerical investigation by means of high-fidelity simulation of the 2D and 3D flow around the SMS Reduced-Scale prototype actuated by MFC (Macro-Fiber Composite) piezoactuators vibrating along the span with the same frequency and amplitude. These patches produce also a slight deformation of the near trailing edge region, simulated as in the physical experiments carried at in the S4 wind tunnel of IMFT in the context of the PhD theses of ***G. Jodin*** *and* ***M. Carvalho****. This wing has a chord of 70 cm, an equal spanwise dimension and an incidence of 10°, corresponding to a typical take-off angle of attack, as suggested by AIRBUS - ETCT "Emerging Technologies and Concepts Toulouse", endorser in the SMS project. The numerical simulations take into account the presence of the upper and lower walls of the wind tunnel and have been accomplished in the Reynolds number range 500 000 - 1 Million, in agreement with the experiments. The numerical model is then validated using comparative study with experimental TR-PIV results.*

The morphing at high frequency low amplitudes of deformation are selected following the same behaviour as for the piezoelectric actuators embedded in the trailing edge of the wing. The study provides a fundamental understanding of how the actuations modify the coherent and turbulent vortex structures around the wing and in the wake, in interaction with the solid structure. By analysing these mechanisms, the influence of the morphing will be explained and its benefits enhanced. This results have been obtained by using the NSMB code with adapted turbulence modelling, the OES (Organised Eddy Simulation) approach, able to sensitise and keep up the coherent structures development, as well as its association in the hybrid turbulence modelling context through the DDES-OES method. The physical analysis has been accomplished by investigation of the time-dependent flow fields, spectral analysis and Proper Orthogonal Decomposition (POD).

Contents

4.1 Introduction

This study aims at identifying and to analysing the effects of the trailing edge vibration at high frequency (300 Hz) and slight deformation of the near trailing edge region of the A320 wing at a selected vibration frequency of 300 Hz and low amplitude by means of two-dimensional and three-dimensional numerical simulations, using the code NSMB. These values have been retained from a large 2D parametric study carried out prior to the 3D one, (Simiriotis et al. (2019)). The objectives of the present chapter are summarized as follows :

(a) To describe the flow properties in the static (non morphing) configuration and validation with experimental results obtained from the IMFT wind tunnel

(b) To illustrate the simulation strategy adopted for the numerical morphing of the Airbus A320 fixed span wing and the benefits of the 2D study that allowed finding the optimal ranges of the actuation frequency in respect of the aerodynamic performance improvement.

(c) To analyse the influence of the present dynamic morphing on the wake coherent and chaotic turbulent structures

(d) To analyse the organized modes under the morphing effects by a three-dimensional Proper Orthogonal Decomposition and reconstruction by retaining the most energetic modes and to explain the morphing benefits.

4.2 Summary of the physical and numerical parameters

The considered prototype is the Airbus-A320 RS wing at the clean configuration of 0.7 m chord and spanwise length mounted in wall-to-wall in the S4 wind tunnel of IMFT of a chord 0.7 m as in the figure 4.1 (a) and 4.1 (b). This last is equipped with High Frequency Vibrating Trailing Edge (HFVTE) actuators presented in figure 4.1 (c) (Jodin et al. (2017)). Theses piezoactuators are composed of Macro Fiber Composite (MFC) and assembled in series along the span direction. The trailing edge is able to deform at moderated amplitudes of order 1-5 mm. The vibration frequency can vary from 10 to 500 Hz. As will be shown, there is no need to go towards higher frequencies and amplitudes. In this present chapter, results from experimental measurement and

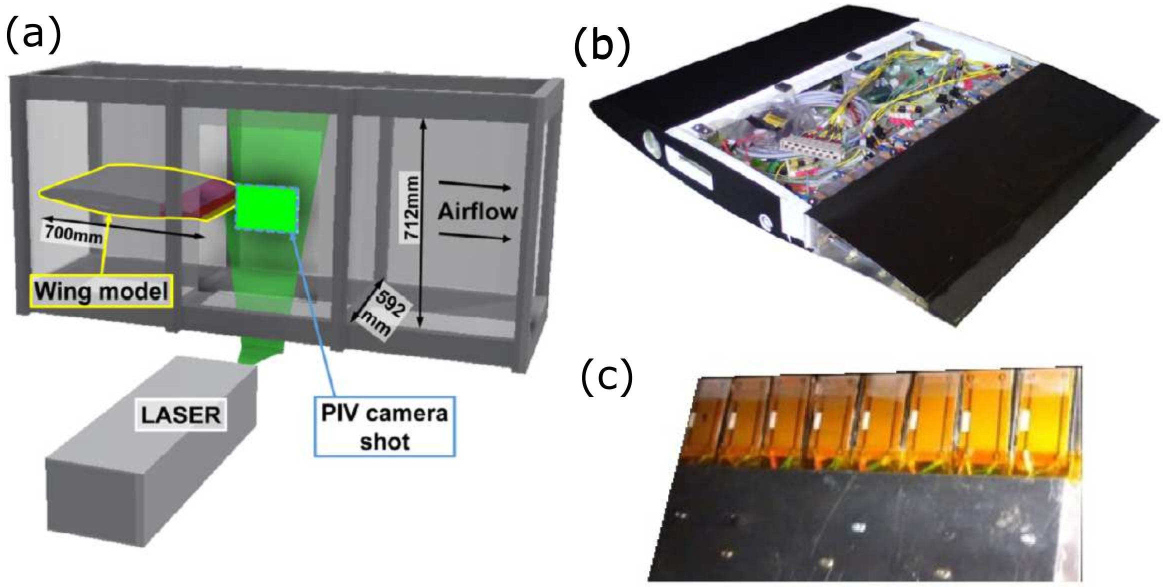

FIGURE 4.1: (a) : Experimental representation of the test section in the S4 wind tunnel of IMFT. (b) : The mounted Reduced-Scale Airbus-A320 wing. (c) : Piezoactuators embedded the trailing of the wing edge along the span direction

numerical simulations at Reynolds number of 1 million are compared as a first step. Beyond the comparison, this study provided for the experiments the optimal ranges of vibrations and amplitudes and accompanied the experimental study all over the SMS EU project, by analysing the physical mechanisms and enhancing the morphing benefits. Therefore, the objective is not just a "comparison" with the experiments but a strong synergy between the experimental and numerical study to provide the most improved design. The wing has been placed at an incidence angle of 10°. Time Resolved Particle Image Velocimetry (TRPIV) measurements (figure 4.1 (a)) in the near wake will be compared with those of the numerical computations.

Numerical simulations were carried out with the Navier-Stokes MultiBlock (NSMB) code. The numerical approach has been described in chapter 3.

The Computational grids were constructed following the experimental S4 wind tunnel in a similar way to the test section (figure 4.2(a)) in order to have more accurate solution compared to the experimental measurements. The grid sizes were selected after thorough numerical studies. The two-dimensional grid (figure 4.2(c)) contains 300 000 finite volume cells. The three-dimensional grid was extruded along the spanwise direction leading to a total size of 10 million. This grid includes 40 cells in the spanwise direction (0.59 m) which has been proven sufficient to capture the three-dimensionalities of the flow. The y^+ value corresponding to the first cell spacing

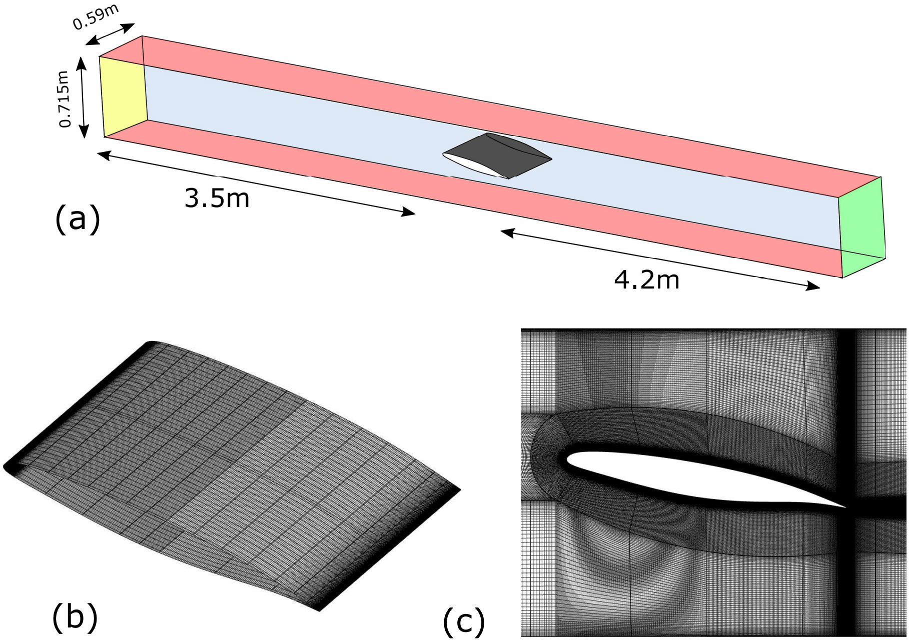

FIGURE 4.2: (a) : Computational domain of the multi-block grid. (b) : Three-dimensional surface grid of the A320 prototype. (c) : Two-dimensional near wing mesh

normal to the wall, was less than 1 which allows a correct capturing of the boundary layer dynamics and thickness, as well as the turbulence damping towards the wall. After a detailed investigation (Simiriotis et al. (2019)), a physical time step of 10 μs was selected and typical numbers of 60 and 150 of inner iterations have been used for the dual time stepping, allowing a good convergence of the solution in each outer time step for the two and three-dimensional cases.

Concerning the boundary conditions, the upper and lower walls of the tunnel were considered in two ways as non-slip (zero velocity at the wall) and slip (same velocity as in the inlet). After different tests, there were no considerable effects on the wake development. Symmetry boundary condition for the left and right edges of the span has been adopted. At the inlet section, a Dirichlet boundary condition has been imposed concerning the velocity, as well as a turbulence intensity of 1%. The turbulence intensity has been measured in the inlet section of the IMFT wind tunnel and was estimated at about 0.1 % of the free stream velocity. At the outlet boundary, non-reflective boundary conditions have been imposed, available in the NSMB solver.

Turbulence modelling

Based on the previous studies, the Organized Eddy Simulation (OES) Hoarau (2002), Bourguet et al. (2008) and Braza et al. (2006) captures quite well the near-wall turbulence stress anisotropy and the unsteadiness at the present angle of incidence at high Reynolds number, compared to the classical two equation modelling, as for example $k-\epsilon$ chien's model (Chien (1982)). This turbulence approach is able to produce the main flow instabilities as in the near trailing edge detachment of the boundary layer and a clear appearance of the shear layer instabilities, the Kelvin Helmholtz and the von Kármán vortices in the wake. Moreover, the OES approach is not intrinsically 3D like the LES and the DES and therefore allowed a quite rich parametric study that provided the first mechanisms investigation and the detection of the optimal ranges of the actuation (frequency, amplitude and patches length).

The predictive ability of various turbulence models have shown that the two-equation $k-\epsilon$ model (Chien (1982)) was not able to produce the instability and the unsteadiness at the present incidence value. The OES with the eddy-diffusion coefficient ($C_\mu = 0.03$) produced a physically correct flow detachment concerning the detachment of the boundary layer near to the trailing edge as shown in figure 4.3. In the present OES modelling, the ambient terms by (Spalart and Rumsey (2007)) have been activated (presented in chapter 3), to prevent a fast decay of turbulence kinetic energy from the inlet section towards the near-wall region. This technique in general allows a better establishment of the turbulent flow around the body. The OES modelling allowed development of the flow unsteadiness and the boundary layer detachment in figure 4.3 (b), comparing to the standard $k-\epsilon$ Chien's model in figure 4.3 (a). The flow separation occurs when the velocity at the wall is zero or negative. A positive or adverse pressure gradient occurs in the direction of the flow and creates the flow

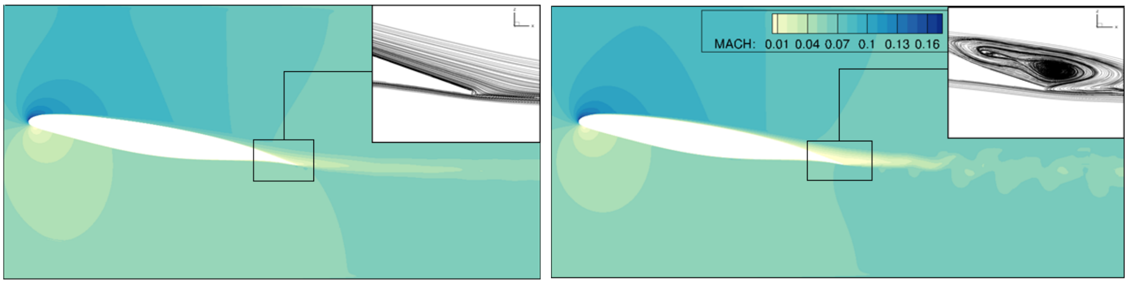

(A) The $k-\epsilon$ Chien model

(B) The OES model

FIGURE 4.3: Contours of Mach field and streamlines close to the trailing edge (detachment visible) .

detachment, see figure 4.4.

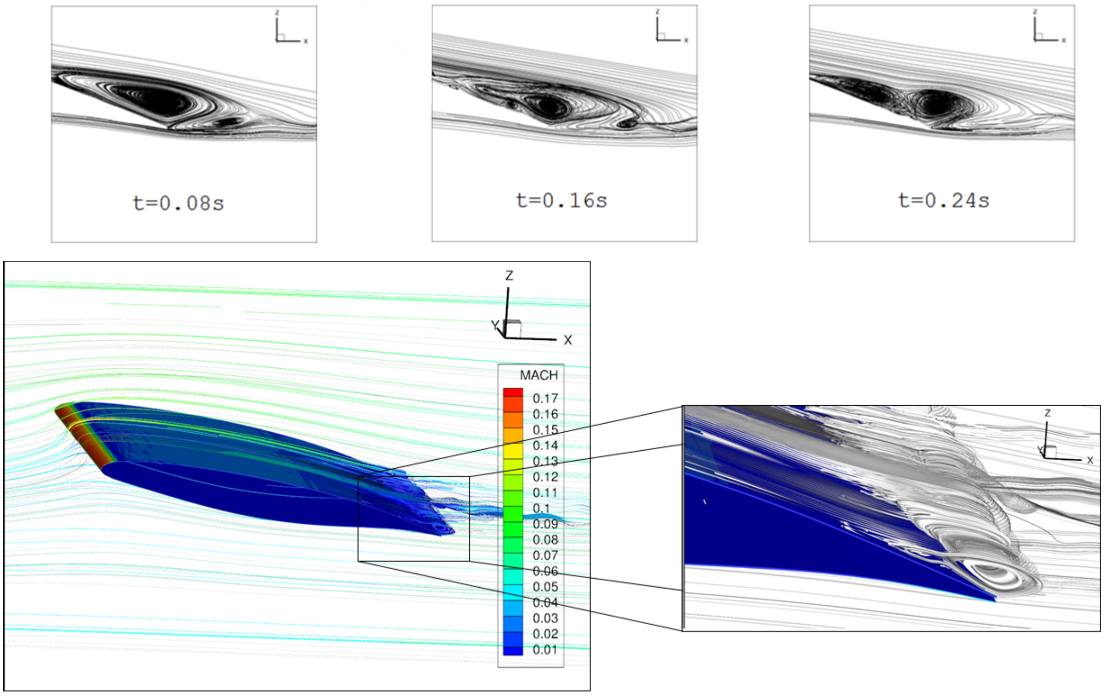

FIGURE 4.4: Streamlines around the trailing edge and the recirculation

The flow detachment is evident through streamlines visualization in figure 4.4 resulting to the unstable wake region. This detachment leads to a thicker effective bluff body which forms an unstable wake region. Upper and lower shear layer instabilities interact together at high velocity gradient that gives birth to an irregular alternating shedding further downstream and secondary three-dimensional instabilities as explained and studies by Hoarau et al. (2003) in low Reynolds numbers.

4.3 Static case: experimental and numerical results

In the following section both numerical and experimental results of the static case (non-morphing) are compared in order to validate the numerical model. A Reynolds number of 1 million has been fixed with an incoming velocity of 21.5 m/s. Experiment measurements were done at standard atmospheric parameters with a temperature (293 K) and reference pressure (101325 Pa). In numerical simulations higher value of turbulence intensity has been chosen (1%). In addition, the ambient sustaining terms are activated due to the significant decay of the turbulent kinetic energy has been observed from the inlet section up to the wing. Increasing the turbulence intensity in the freestream (inlet) allows a better representation of the numerical results comparing to the experiment measurements.

To further investigate the static configuration (no morphing), time averaged streamwise velocity U_{mean} has been extracted in selected positions located in the near wake

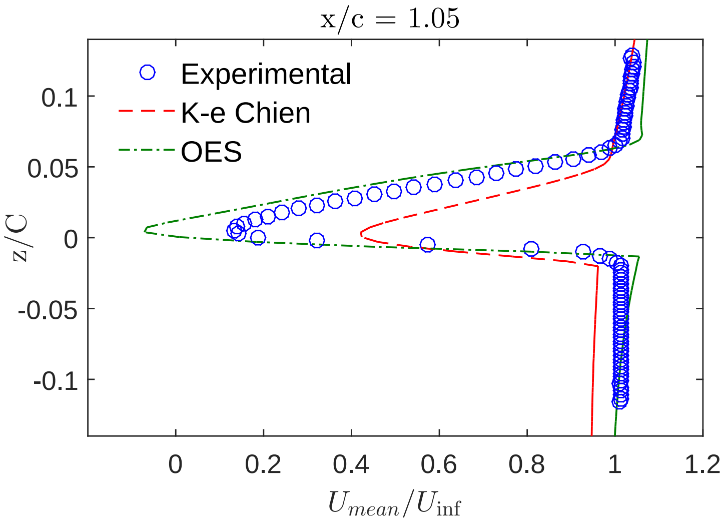

FIGURE 4.5: Comparison of the averaged dimensionless U mean velocity according to the OES and URANS/k-eps Chien models with TR-PIV experimental results (Jodin et al. (2017)) in IMF S4 wind tunnel.

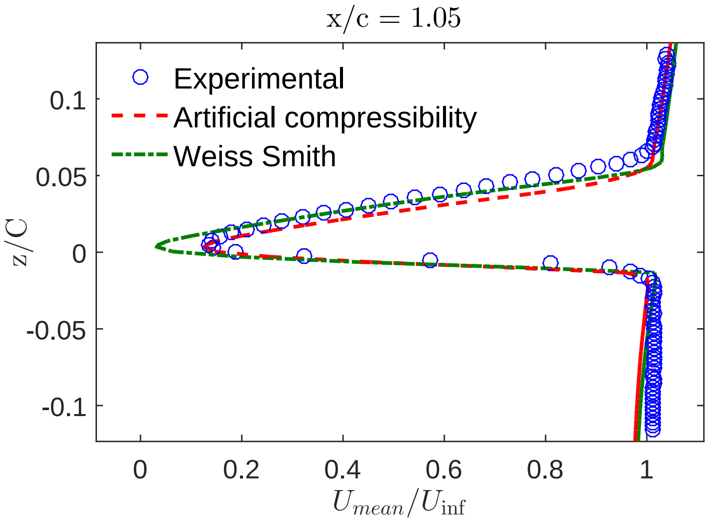

FIGURE 4.6: Comparison of the averaged non dimensional U velocity using different preconditioning methods

in figure 4.5. Both URANS $k-\epsilon$ Chien and OES models have been compared with experimental results. The $k-\epsilon$ Chien reveals less velocity deficit created by the wing. This is a consequence of its dampening character. In fact, the model was not able to capture the unsteadiness and the negative adverse pressure which produces the boundary layer detachment (experiments by (Jodin et al. (2017))). This fact underestimates the width of the wake and the velocity deficit. The *OES* produces a higher velocity deficit with a similar width. This can be explained due to the low subsonic speed range because the code NSMB solves the compressible Navier-Stokes equations (Mach numbers > 0.2). But in the present case the Mach number is estimated of 0.062. Local preconditioning techniques have been first introduced to enable the simulation of an incompressible flow. Two methods were tested : Weiss and Smith preconditioning (Weiss and Smith (1995)) and the Artificial Compressibility Method (Chorin (1967)) using the implicit dual time stepping LU-SGS method (Lower Upper Symmetric Gauss Seidel).

Artificial Compressibility shows less dissipation on the U_{mean}, figure 4.6 compared to the Weiss and Smith preconditioning method. Both methods are satisafactory in terms of the wake width (thickness) compared to the experimental results. However, the Artificial compressibility preconditioning provides a very good comparison of the velocity deficit with the experimental results and has been finally adopted for all the computations.

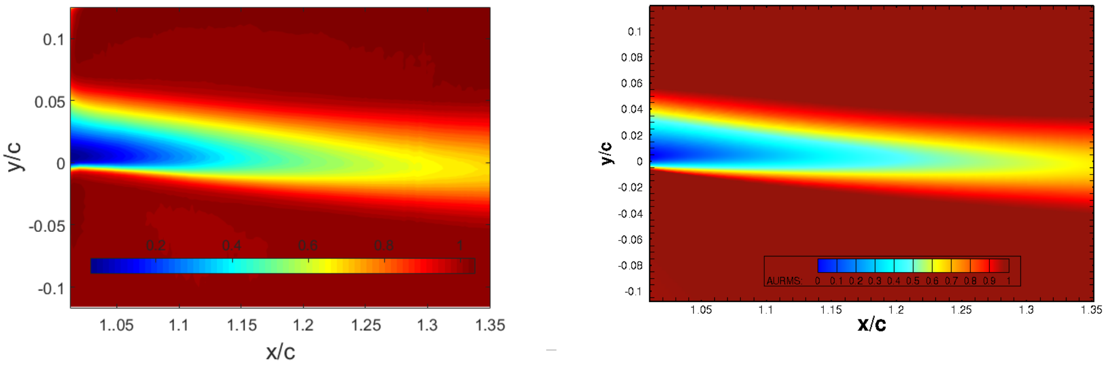

(A) Experimental (B) Numerical

FIGURE 4.7: Time-averaged of the stream-wise velocity component U_{mean} for the static case (no morphing). $(left)$: Experimental TRPIV measurement. $(right)$: Numerical results; $Re = 1.10^6$

Time-averaged of the velocity fields are extracted from the 3D numerical simulations (at middle of span y/c=50 %) and compared with TRPIV results. Figure 4.7 on the left presents the contours plot of time average stream-wise velocity for the static case in experiments and on the right 3D numerical simulation plotted in the near wake region. 3D simulations are in quite good agreement with the experiments, the wake thickness in the computation is slightly smaller in the upper shear-layer.

Velocity profiles are extracted for x/c equal to 1.05, 1.10, 1.15 and 1.20 and presented in figure 4.8. The values in each curve are normalised with the same dimensionless process in the simulations and the experiments. The wake expansion is accurately captured and only at the latest position the velocity deficit is slightly overestimated. Figure 4.9 represents a comparison of the PSD in the near wake region of 2D numerical simulations with experiments from IMFT. The width of the spectral bump due to the shear layer instability development past a morphing A320 wing is well captured in qualitative agreement with experiments carried out in IMFT (Simiriotis et al. (2019)). Spectral peaks underline the main instabilities in the wake, the vortex structure dynamics and their non-linear interactions. The OES model was able to predict more energetic coherent structures present in the wake and qualitatively more comparable to the experimentations.

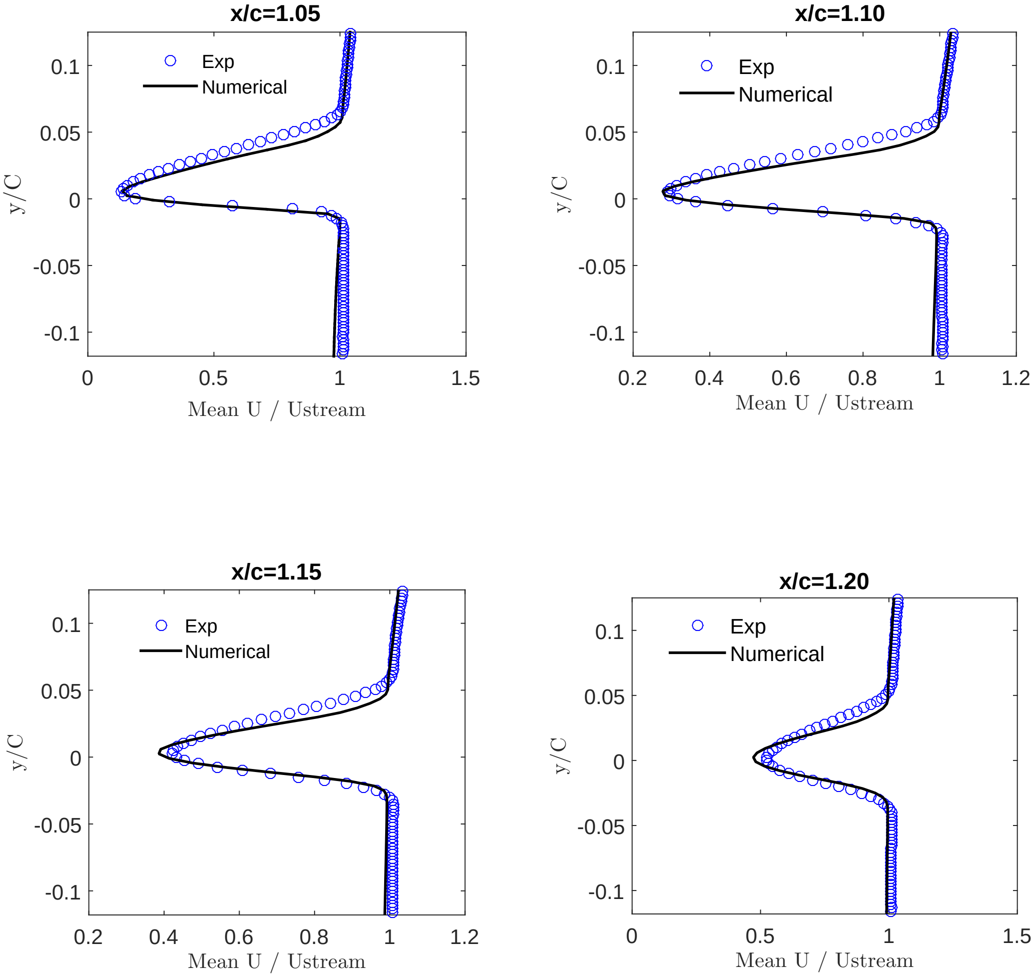

FIGURE 4.8: Comparison of U_{mean} profiles along the wake for $Re = 1$ M, angle of attack $\alpha^{\circ} = 10^{\circ}$; 3D computations tests compared with the TRPIV results.

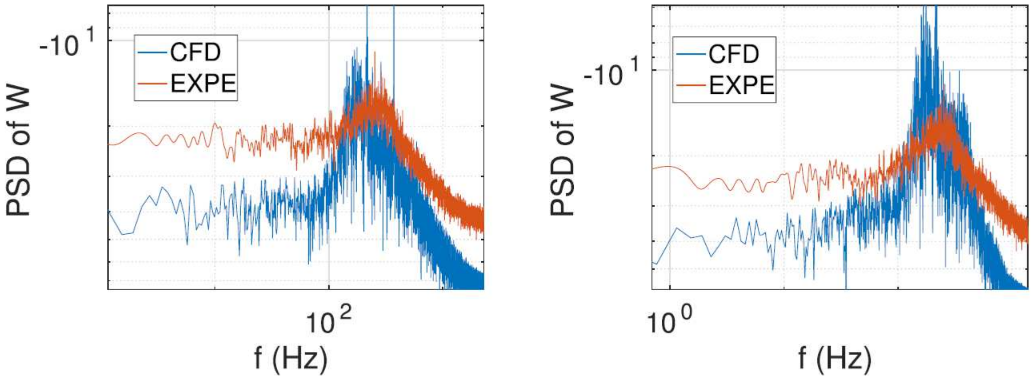

FIGURE 4.9: Spectral content of the near wake region, comparison between 2D computational results based on OES model and experiments from IMFT wind tunnel, Re = 1 M, angle of attack AOA = 10° for a reduced-scale Airbus A320 wing (Simiriotis et al. (2019)).

4.4 Morphing case : trailing edge displacement strategy

The Arbitrary Lagrangian-Eulerian (ALE) methodology Donea et al. (1982) (described in Chapter 3 has been utilized for the calculation of the applied displacement in the trailing edge region which follows exactly a second-order polynomial deformation at a frequency of actuation f_a and a fixed amplitude A_0 in a sinusoidal time variation. The dz increment calculated along the streamwise x direction (figure 4.10) is given in the following equation :

$$dz = \big(a(x - x_0)^2 + b(x - x_0)\big)sin(2\pi f_a t) \tag{4.1}$$

Where $a = 2/(3h_0)$ and $b = 1/(3h_0)$ are constants calculated from the maximum displacement h_0 which is the patch length and fixed to 3.5cm.

The maximum amplitude is located at the ending tip of the trailing edge as presented in figure 4.10. In fact aerodynamic forces on the vibrational behaviour of the piezoactuators were not taken into account since they have been evaluated to be negligible in the experimental measurements.

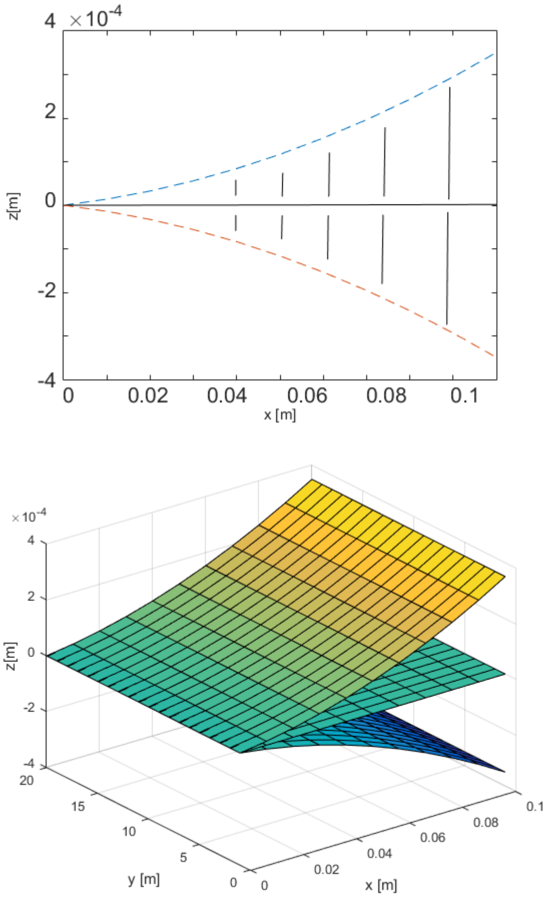

FIGURE 4.10: Schematic description of the displacement by means of the second order polynomial deformation in two and three-dimension

4.5 Dynamic case: trailing edge vibration and slight deformation: SMS project

4.5.1 Wake dynamics

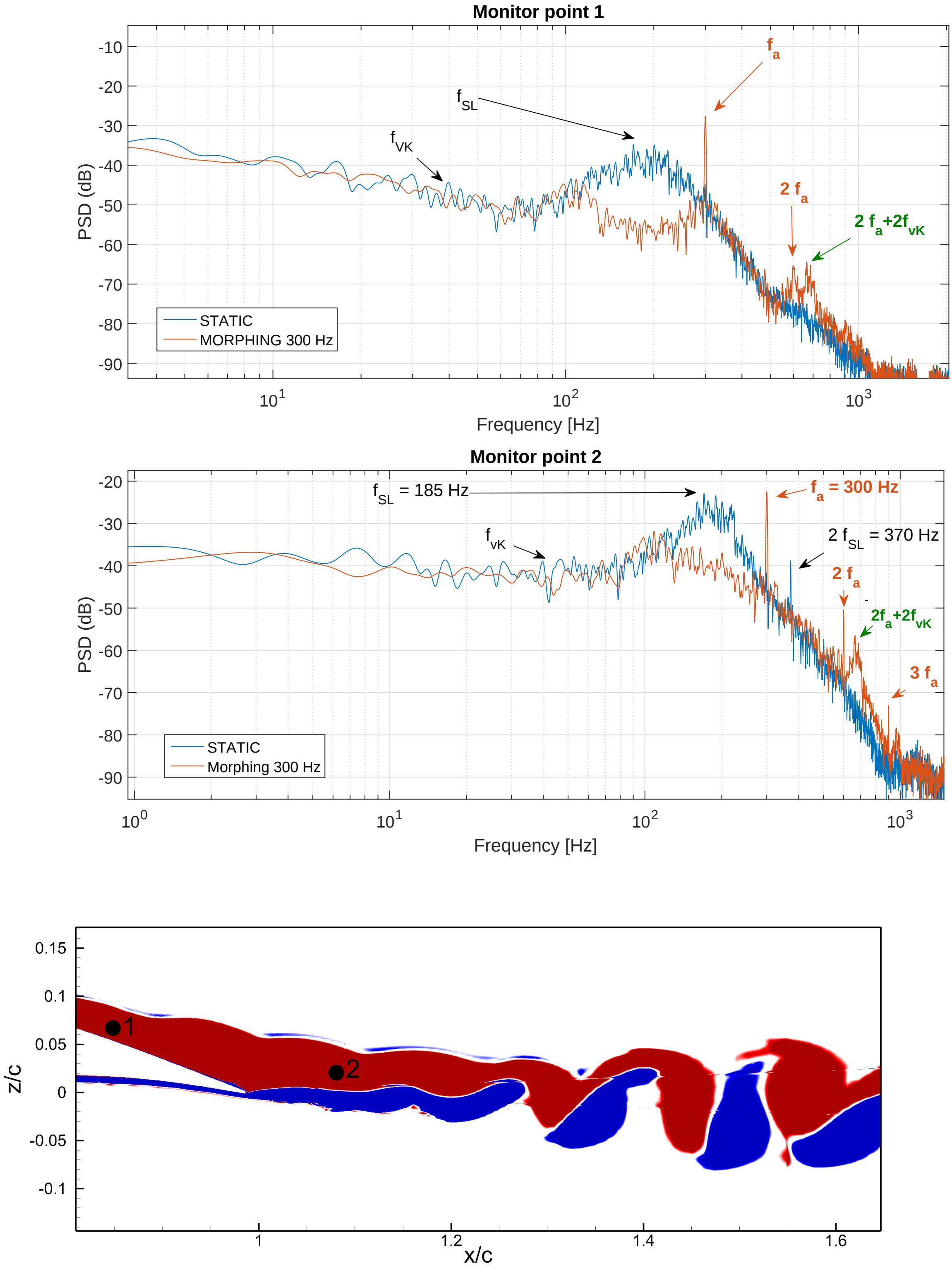

FIGURE 4.11: PSD of the vertical velocity component on the first two monitor points, from the static and morphing at 300 Hz configurations. (*last*) : presentation of the locations of extracted points within the converged signal of the vertical velocity

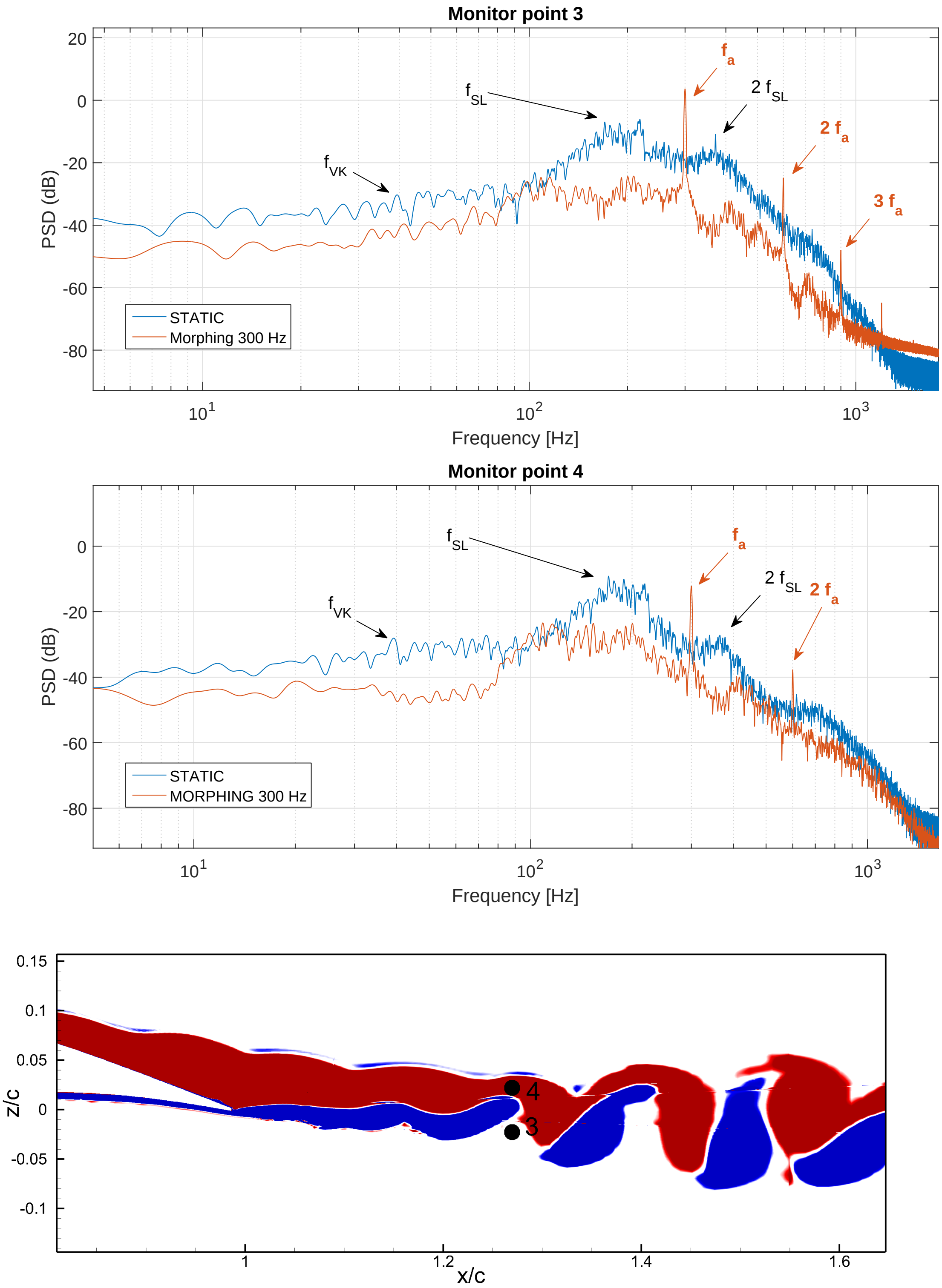

FIGURE 4.12: PSD of the vertical velocity component on the last two monitor points, from the static and morphing at 300 Hz configurations. (*last*) : presentation of the locations of extracted points within the converged signal of the vertical velocity

Figures 4.11 and 4.12 present respectively the selected monitor points and their locations in table 4.1. The PSD of the vertical velocity component was computed using the Welch's weighted overlapped segment averaging estimator (Welch (1967)) detailed in Appendix A for the static and the morphing configurations.

	MP 1	MP 2	MP 3	MP 4
x/C	0.8364	1.0758	1.2744	1.2748
z/C	0.0678	0.0294	-0.0214	0.0247

TABLE 4.1: Coordinates of the monitor points (MP) used for the spectral analysis

The understanding of vortex shedding mechanisms allows their control through morphing of trailing edge vibrations that modify and change the wake behaviour. These mechanisms are analysed through the turbulence spectra presented in figures 4.11 and 4.12. These figures show predominant frequencies interspersed among continuous frequency regions. The predominant peaks are due to the dynamics of coherent vortices and the continuous regions correspond to chaotic dynamics of the turbulence process. The upper and lower shear layers coming from both sides of the wing interact together and lead farther downstream to the von Kármán alternating mode. The lower shear layer is stronger due to the wing's incidence. The natural frequency of the corresponding shear layer vortices is of f_{SL} = 185 Hz. In the spectrum, the first harmonic of this frequency is also seen concerning the monitor points 2, 3 and 4. The shear layer vortices are the results of a Kelvin-Helmholtz instability developed in the separated shear layers and downstream. The von Kármán alternating mode, developed farther downstream through the interaction of both shear layers is characterised by a predominant frequency bump in the region f_{vK}=(40-50) Hz. The morphing of the trailing edge at the frequency of 300 Hz that had been proven optimal through the 2D parametric study has been applied in the present 3D simulations with an actuation's amplitude of 0.35 mm. The frequency and the amplitude of the morphing can have different effects on the flow behaviour (investigated in a previous work by Simiriotis et al. (2019)). When the frequency f_a is smaller than the predominant natural frequency of the wake f_{SL}, the effects in the wake are barely noticeable. Furthermore, when the f_a is closer to f_{SL} a lock-in phenomena of the shear layer frequency towards the actuation frequency has been observed. The shear layer instabilities and the von Kármán vortices are excited and oscillate with a larger amplitude. This could make the wake thicker and produce a loss in performances. However, when $f_a = 300$ Hz is higher than $f_{SL} = 185$ Hz (our case) it has been noticed in all the PSD that the

f_{SL} has been considerably attenuated up to (-25)dB, thus reducing the aerodynamic noise sources produced downstream of the trailing edge. In addition, the actuation frequency f_a and its harmonics are captured in the PSD due to the trailing edge vibrations. The PSD in MP 1 reveals effects of the vibrations on the wing as will be seen through the forces modification. These effects are related to the so called "eddy blocking" explained as follows.

The higher frequency vibrations induced by the piezo-actuation enhance smaller-scale structures injected directly in the shear-layer and producing an eddy-blocking effect, generating a shear sheltering process studied by (Hunt et al. (2008), Szubert et al. (2015), Jodin et al. (2017) and Simiriotis et al. (2019)). This effect is able to constrict the shear layers by reducing the turbulence diffusion and to produce thinner shearing regions through manipulation of the Turbulent-Non Turbulent (TNT) interfaces. An upscale energy transfer is enhanced by means of the vibrations towards the larger scale coherent eddies. The Eddy blocking effect consists on increasing the energy of non-coherent small structures and simultaneously on a vortex breakdown permitting an attenuation in energy as presented in PSD of the large coherent structures. Therefore, the morphing modifies the dynamics of the TNT interfaces and as a result, of the Turbulent-Turbulent (TT) interfaces both becoming thinner and leading to a reduction of the wake's width. These effects of turbulent structures manipulation instantaneously affect the pressure distribution all over the wing because of the elliptic character of the flow regime (low subsonic). As will be seen, the lock-in mechanism produced by the morphing enhances the vortices contributing to the circulation increase around the wing, thus increasing the lift and destroy harmful smaller-scale vortices influencing drag and noise.

4.5.2 Mean flow properties (3D)

The blue colored region on figures 4.16 corresponds to the detachment of the boundary layer and the recirculation of the flow which onsets the upper shear layer. The morphing case reveals that the blue region is reduced compared to the no actuation case. In order to examine in details , these effects streamlines calculated from mean flow velocities are highlighted in the figure 4.13.

The figure 4.13 compares the recirculation near the trailing edge in both cases. High frequency actuations appear to attenuate the width of the recirculation, this is caused by the movement of the trailing edge in the upward direction breaking the formed bubble. The boundary layer is reattached between $0.98 < x/C < 1$. Figure 4.14

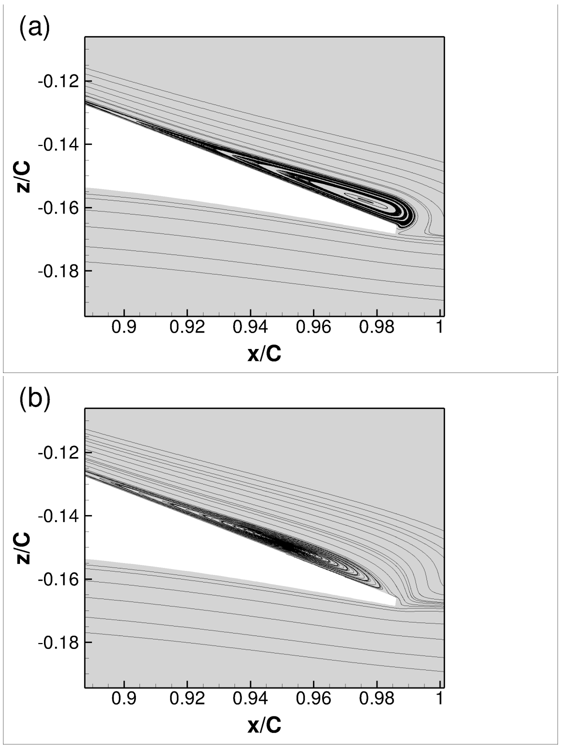

FIGURE 4.13: Streamlines calculated from the mean flow velocities streamwise and crossflow near the trailing edge of the wing highlighting the recirculation bubble. (a) The static case. (b) : Morphing case at 300 Hz

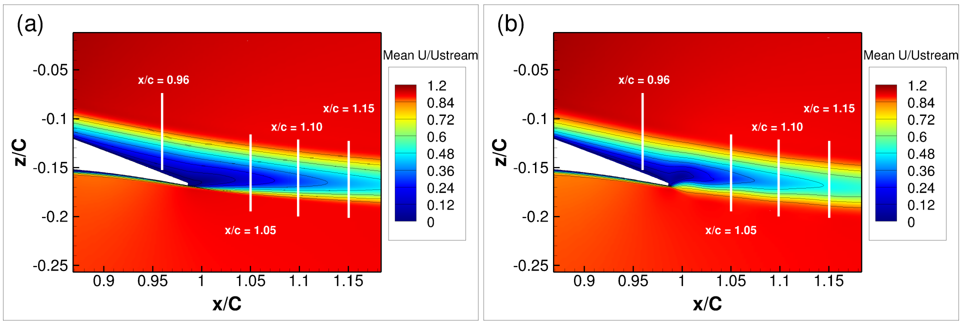

FIGURE 4.14: Time average streamwise velocity is represented in the wake region comprising the last 15 % of the wing chord. (a) represent the non morphing case. (b) presents the wake for the morphing case at 300 Hz

presents the mean streamwise velocities for both cases coloured with iso-surfaces. As it was observed in the previous section the velocity deficit (blue region) has been attenuated when the actuations are activated, this is related to the width thinning of the recirculation and the reattachment of the flow. The shearing becomes less stronger in the near wake. Figure 4.15 compares mean streamwise velocities from different extracted positions highlighted in the figure 4.14. The feedback effect of the actuation

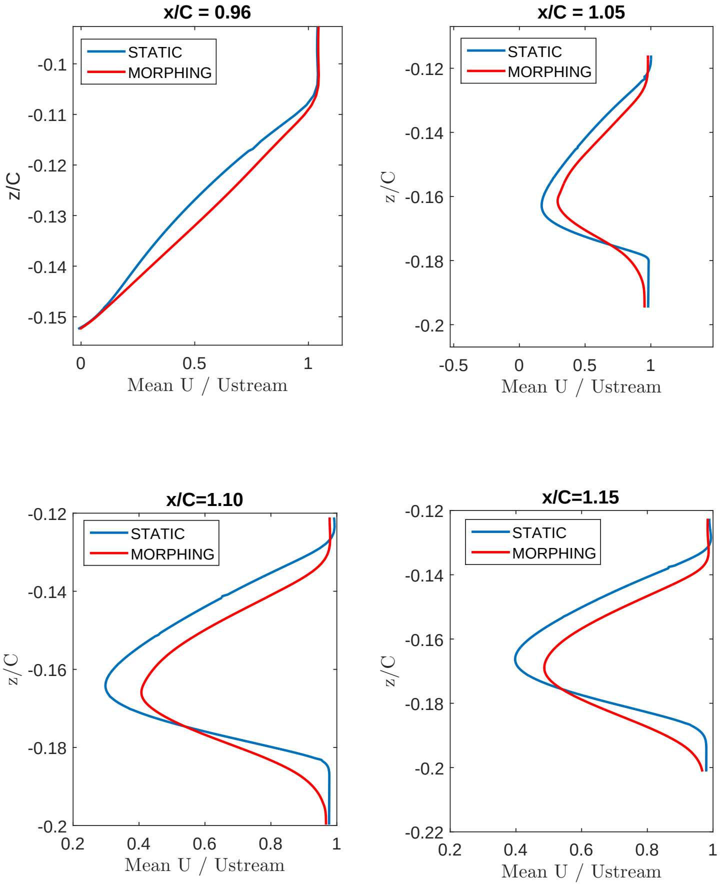

FIGURE 4.15: Comparison of time averages of streamwise velocity at different locations in the near-trailing region where the separation occurs for the static and morphing cases

is observed at the position $x/C = 0.96$ and the velocity deficit is less important in the morphing case, this is translated by an acceleration of the flow with more spread of the upper and lower shear-layers. In addition, from the positions $x/C = 1.05$, 1.10 and 1.15 the wake is oriented in the downward direction which enhances the aerodynamic performances. The TNT interfaces in upper and lower regions have been shifted downward also and a constriction of the TT region through the eddy blocking effect is observed. The wake width is then decreased.

4.5.3 Suppression of vortex dislocations

The wake is fully turbulent in the static case (no vibration), containing three-dimensional turbulent structures captured by the OES turbulence model. The three-dimensional transition to turbulence in the wake was discussed in Chapter 2, based on studies in the state of the art. At the present angle of incidence of 10 degrees the boundary layer is detached near the trailing edge of the wing at $x/C = 0.88$ and a separation bubble is formed. This induces higher lower and upper shearing due to the velocity gradient. The transition to three-dimensionality encounters physical mechanisms occurring as the Reynolds number increases. These mechanisms are trigged by the amplification of specific instabilities, mainly the shear layer and von Kármán instabilities as primary ones. Based on numerical studies by DNS in the low Reynolds number range (Persillon and Braza (1998)), the way the primary vortex rows are destabilised was studied. The transverse velocity component in the third direction progressively amplifies and forms "braid"-like structures between two von Kármán vortex rows. This

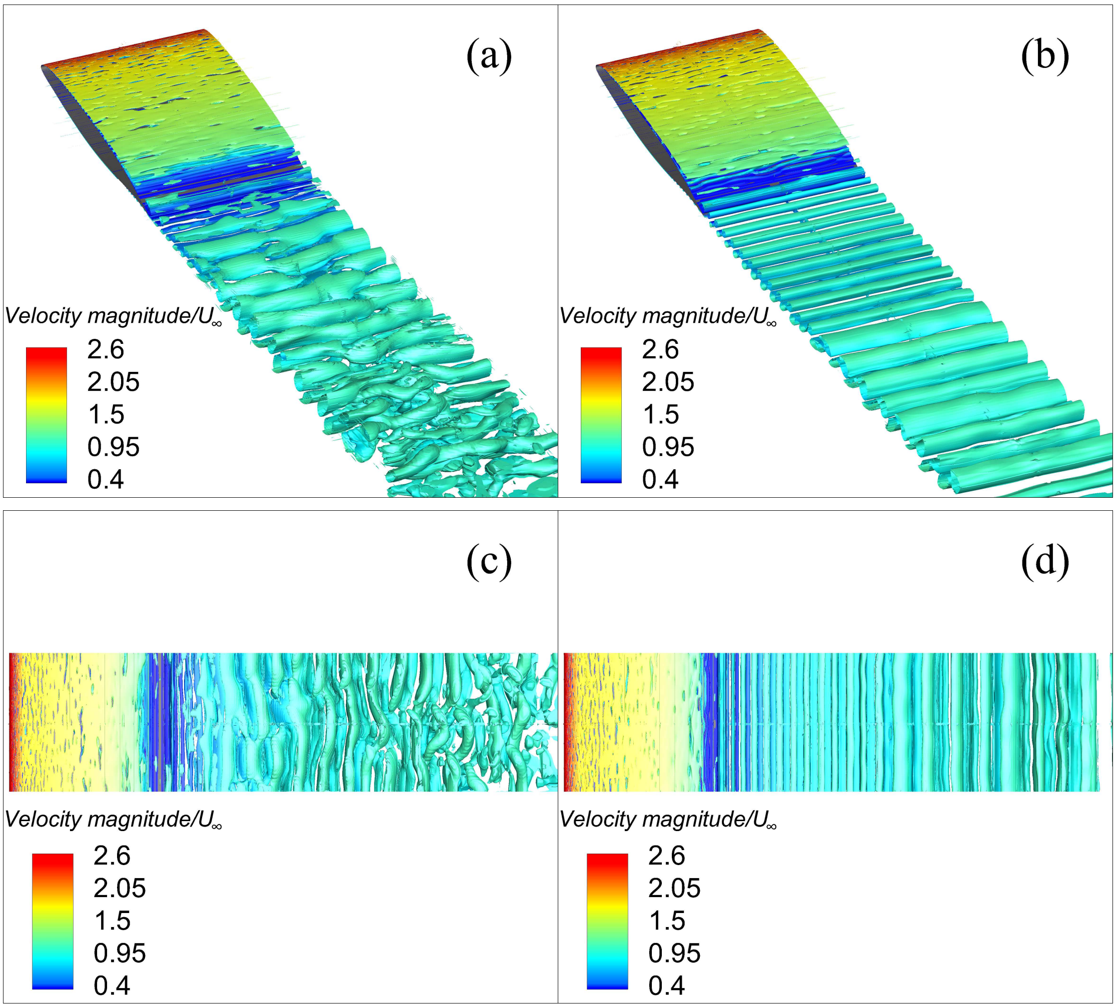

FIGURE 4.16: $Q - criterion$ (Q=1500) iso-surfaces colored by the Mach field, (a) and (c) static case (no vibration), (b) and (d) Morphing case (with vibration).

yields creation of longitudinal and vertical vorticity components, undergoing spanwise perturbation along the primary vortex rows. If the shearing mechanism is sufficiently high, these rows form a large-wavelength spanwise undulation (a "serpentine" pattern), known as *secondary instability*, whose amplification is derived by elliptic instability theory (Waleffe (1990)). Furthermore, under non-linearities in the shearing mechanism, the shedding of these undulated vortex rows display phase irregularities resulting in a break of the "spinal column" of the vortex row and formation of a junction with the next shed vortex row. This junction, due to local spanwise irregularity of the shedding velocity is known as vortex dislocation pattern, studied in detail by DNS (Braza et al. (2001)) and observed in low Reynolds number experiments by (Williamson (1992)). In the present study, vortex dislocations are revealed through the Q criterion iso-surfaces and coloured by the non-dimensional velocity magnitude (figure 4.16) to better show the turbulent structures. Furthermore, shear-layer instabilities vortices of smaller size are formed through fine scale three-dimensional turbulence and their presence is associated with energetic frequency peaks in the PSD (figures 4.11 and 4.12).

Figures 4.16 (b) and 4.16 (d) show the modification of the vortex pattern due to the morphing by applying the 300 Hz vibration along the span with an amplitude of oscillations of 0.35 mm and a length of the piezo-actuator patches of 3.5 cm. A suppression of the three-dimensionality is obtained.

This significant morphing effect is due to the modification of the shearing distribution due to the vibration, which produces a different form in the "ellipses" displayed by a 2D cut-off of the primary vortex rows.

The development of the spanwise undulation of the alternating vortex rows can also be analysed by the elliptic stability theory as in (Waleffe (1990), Bayly (1986), Landman and Saffman (1987)). According to this theory, an initially bi-dimensional vortex row submitted to spanwisely periodic small perturbations becomes unstable and develops a spanwise undulation with a large, regular wavelength when the ratio of the axes of the elliptic shape of the 2D section of this vortex becomes higher than a critical value. (Landman and Saffman (1987)) evaluated this critical regime and the growth rate of the secondary instability. Braza et al. (2001) analysed from this theory the appearance of the secondary instability through DNS around a circular cylinder in the low Reynolds number range. Regarding of the secondary instability growth, an ensemble of parameters govern its development, as the inclinations θ for the wavenumber k for which the wave-vector of the perturbations grows. Among these θ values, there exists an angle θ_{max} corresponding to the maximum growth rate.

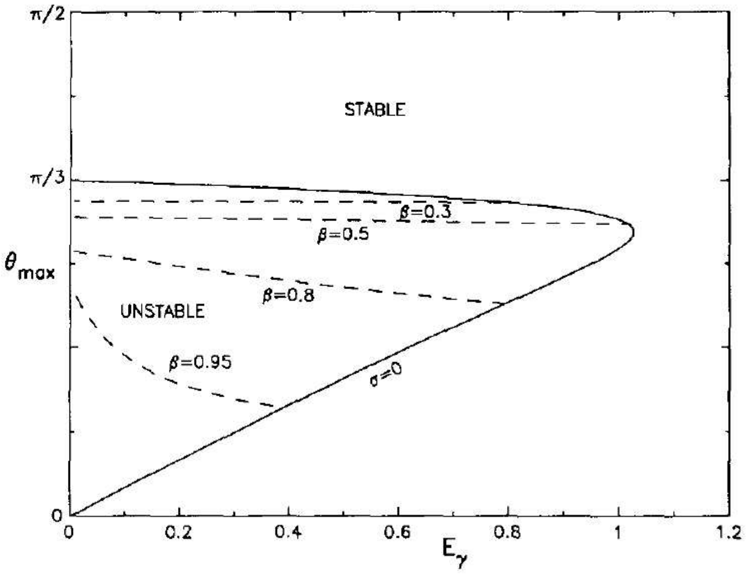

FIGURE 4.17: Most unstable wavenumber inclination versus Ekman number for various streamline eccentricities β (Landman and Saffman (1987))

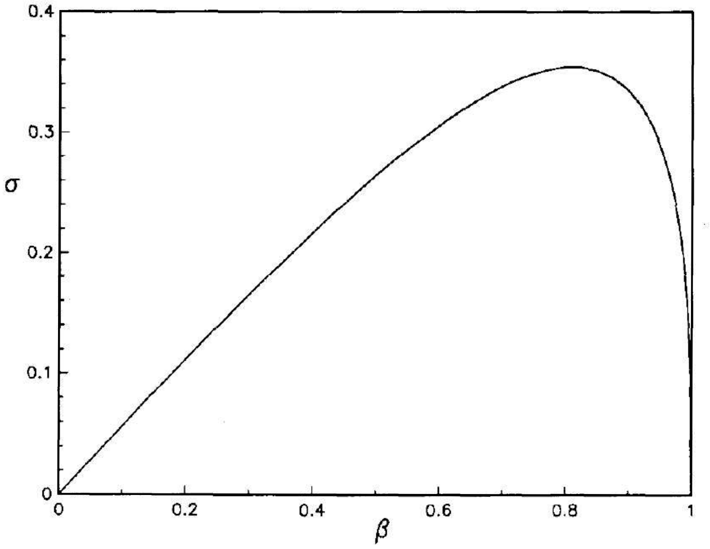

FIGURE 4.18: Maximum growth rate σ as function of the eccentricity parameter β (Landman and Saffman (1987))

The variation of the Eckman number $E_\gamma = 2\pi\nu k_0^2/g$ (k_0 is a constant of integration), is evaluated by (Landman and Saffman (1987)). This variation has been used for this study concerning the static and the morphing cases and presented in figure 4.17. At a fixed viscosity ν and vorticity $2\gamma = 2\omega_y$, β can be determined for a given strain field ϵ, or by the parameter α which defines the ellipsis ratio, $\beta = \epsilon/\gamma = (\alpha^2 - 1)/(\alpha^2 + 1)$. In the static case, we found in figure 4.19 that $3.11 < \alpha < 4.5$, hence $0.81 < \beta < 0.9$. However, for the morphing case $2.07 < \alpha < 2.14$ and hence $0.62 < \beta < 0.688$ is decreased. The necessary and sufficient condition to have an elliptic flow is fulfilled when $0 < \beta < 1$. Figure 4.18 allows the evaluation the maximum growth rate σ as a function of the calculated eccentricity β. The morphing *reduces the eccentricity*, thus producing less maximum growth rate than the static case. This results to a disappearance of the three-dimensional structures because the growth rate of the secondary instability has been reduced.

As a summary, the present actuation introduces a global modification of the wake though the longitudinal, vertical and spanwise directions. The shear-layer is affected by the new formed vortices and as a result, the von Kármán vortices are less expanded, delayed and more organised.

4.5.4 Coherent structures dynamics

Iso-vorticity ω_y surfaces are shown on the median spanwise section (figure 4.19). In figure 4.19 (a) the interaction between the upper (in yellow) and the lower (in blue) shear layers is highlighted. Von Kármán vortices are rolled up from $x/C = 1.85$ and expanded in the vertical and downstream directions. In figure 4.19 (b), the actuation at 300 Hz coupled with a low amplitude of 0.35 mm causes an increase of the shearing rate in the trailing edge region, because the lower boundary layer is still attached to

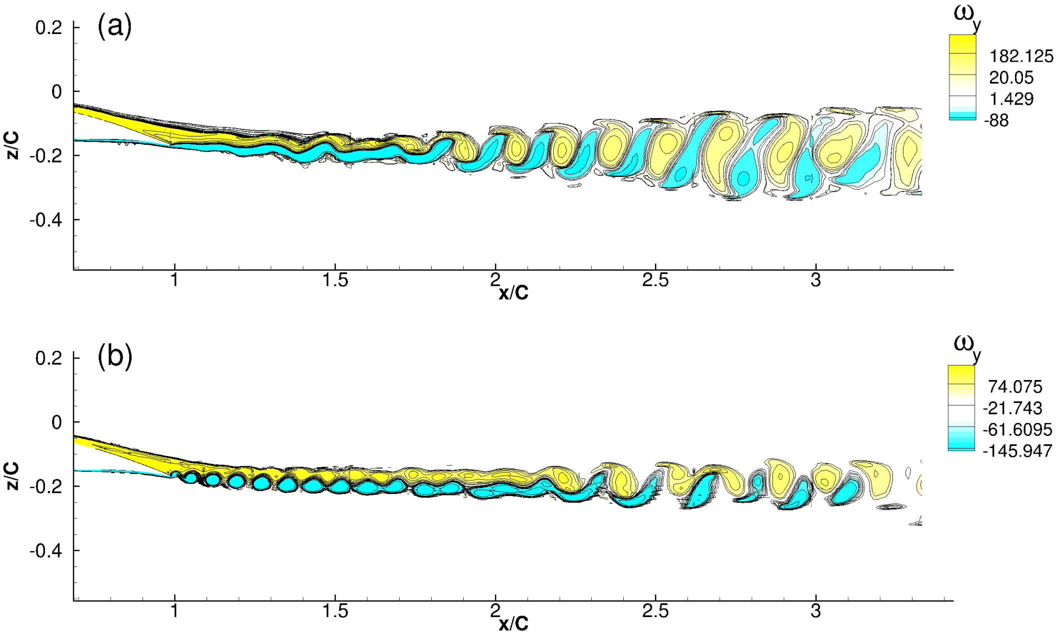

FIGURE 4.19: Spanwise vorticity ω_y at middle span. (a) : Static case. (b) : Morphing case at 300 Hz

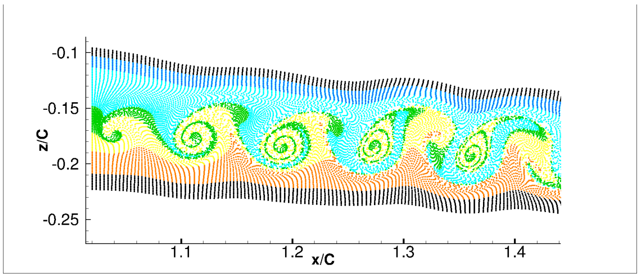

FIGURE 4.20: Streaklines visualization of the near trailing edge wake of the morphing case highlighting the modification of the shear-layer

the wall when the trailing edge moves downwards.

Streaklines have been injected downstream (see figure 4.20) to better illustrate the vortex dynamics. A formation of new anticlockwise vortices is more pronounced than clockwise ones due to the separation of the upper boundary layer. Theses mechanisms manipulate the wake's coherent structures resulting in a delay for the formation of the von Kármán vortices with less expansion in the vertical direction through their merging between $1.6 < x/C < 1.85$. In figure 4.21, the injected streaklines

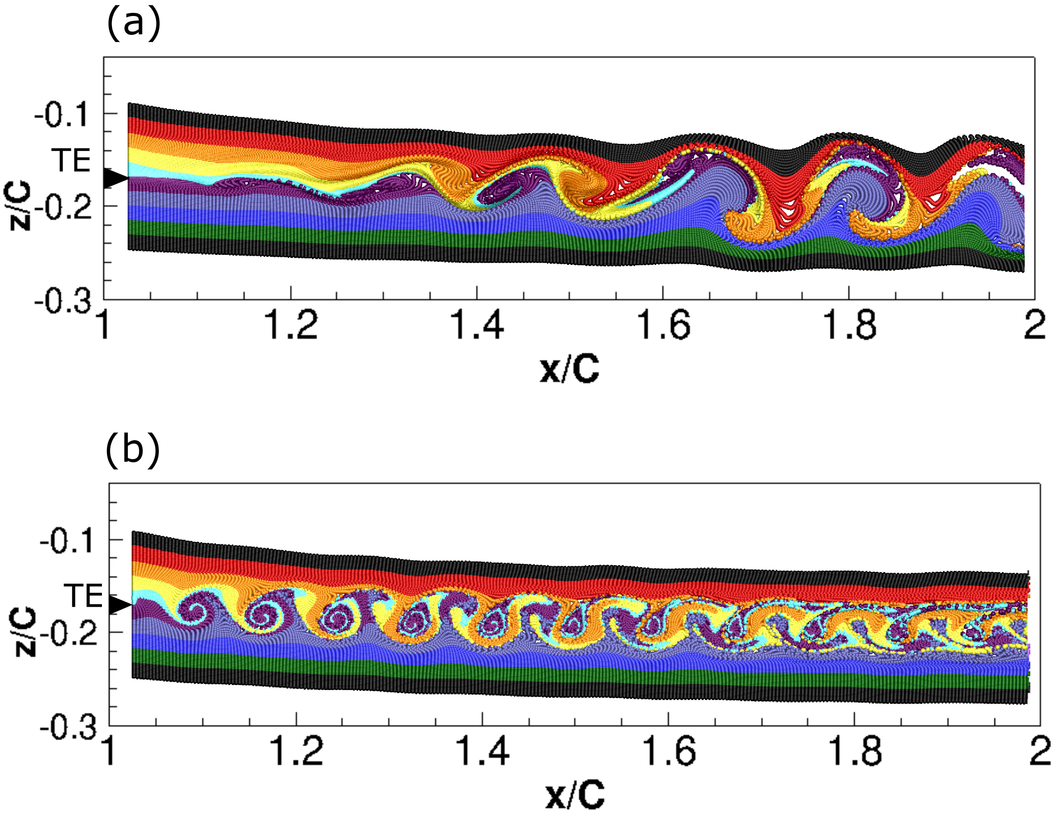

FIGURE 4.21: Visualization of the wake turbulent structures with streaklines and comparing (a) static with (b) morphing case

illustrate the far wake modification. The morphing in figure 4.21 (b) reduces the interaction between these layers illustrated with different colors: the upper shear layer in the red region and the lower shear layer violet and blue regions. These regions are transformed to practically Non-Turbulent regions. Compared to the static case in 4.21 (a), these regions are mixed inside the Turbulent-Turbulent region and this helps to the onset of the von Kármán vortices farther downstream.
In next section, we focus on the temporal and spatial evolution of the spanwise velocity due to its role on the amplification of the secondary instability.

4.5.5 Spanwise Velocity analysis

The onset of the three-dimensional transition through successive steps was studied by (Persillon and Braza (1998)) and (Hoarau et al. (2003)). The spanwise velocity component is amplified as function of time according to three successive steps: a linear growth, a non-linear evolution followed by a saturation state. As a consequence, after an establishment time, this velocity component is organised according to counter-rotating cells and the streamwise ω_x vorticity displays "braid" (e.g. "fer à cheval") structures along the span. Based on the previous discussion, under these conditions, the development of the secondary instability occurs as a regular spanwise undulation associated to these "braid" structures (mode A, experimentally studied by Williamson (1988)), modifying the initially 2D von Kármán vortex rows. As Reynolds number increases, the wavelength of the spanwise undulation decreases and the "braid" form is deformed (mode B). In our present case of high Reynolds number, the regime corresponds to mode B. To analyse the morphing effect, the instantaneous spanwise velocity component is extracted from different vertical slices as presented in figure

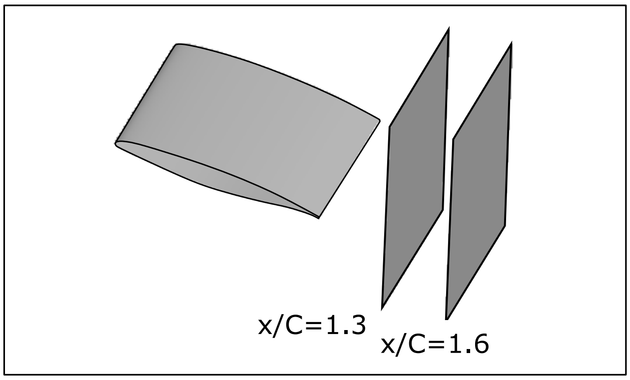

FIGURE 4.22: Positions of the extracted slices of the spanwise velocity

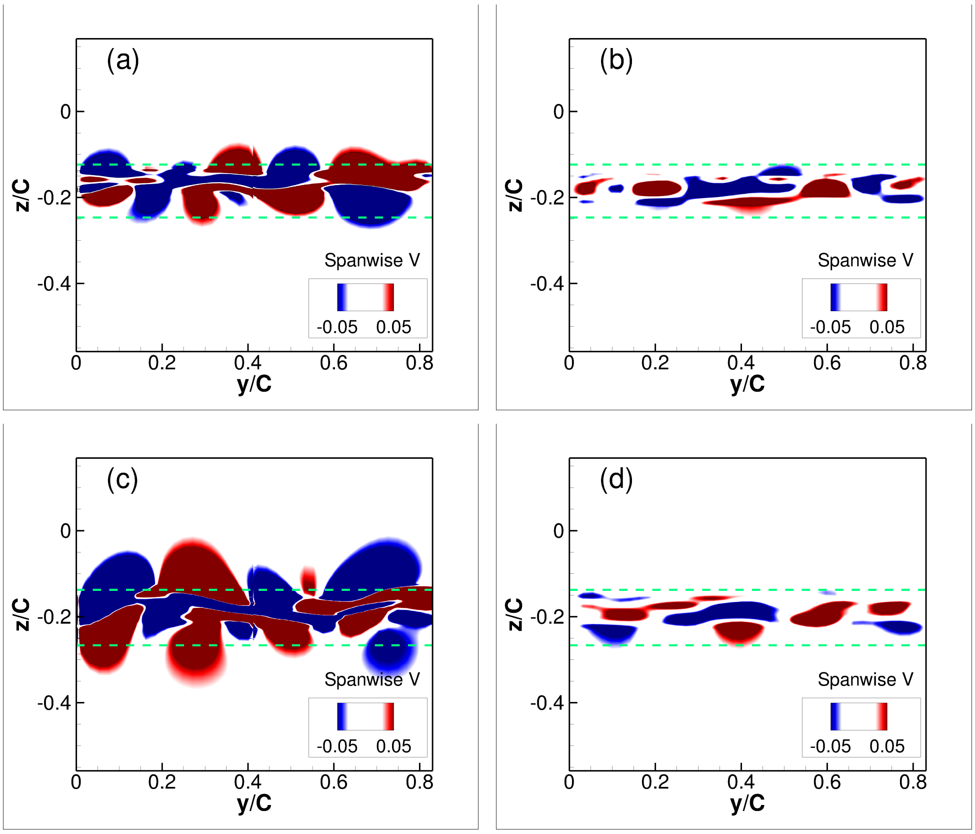

FIGURE 4.23: Spanwise velocity extracted from slices at different wake positions in left the static case and in the right the morphing. (a) and $(b) : x/C = 1.3$; (c) and $(d) : x/C = 1.6$

4.22. Figure 4.23 presents the spatial evolution of the instantaneous spanwise velocity component at two different positions in the wake ($x/C = 1.3$ and $x/C = 1.6$). This velocity in the static case is of a high magnitude due to the fully turbulent flow at the present high Reynolds number coupled with the relatively high angle of incidence which causes the appearance of the three dimensionality as in figures 4.23(a) and 4.23(c). In the morphing case (figures 4.23(b) and 4.23(d)), a drastic attenuation of the spanwise velocity occurs, where the green dashed lines present the maximum variation of the spanwise velocity. This is directly related to the complete suppression of the three-dimensionality

Figures 4.24(a) and 4.24(b) illustrate same velocity component extracted from different transverse lines along the span. These lines are located inside the Turbulent-Turbulent (TT) region same as in figure 4.23. The spanwise velocity is completely suppressed in the Turbulent-Non-Turbulent (TNT) interfaces at $z/C = -0.12$ and $z/C = -0.24$ for the morphing case. In the Turbulent-Turbulent (TT) region where

$-0.2 < z/C < -0.16$, the spanwise velocity is attenuated but not completely because of the dynamic movement of the trailing edge that injects new rows of two-dimensional vortices. Farther downstream, the spanwise velocity in figure 4.24(b) is more important than in the previous position. This is due to the growth of the von Kármán vortices. It appears that the morphing attenuates and stops the evolution of the spanwise velocity even in the far wake.

The spanwise velocity is extracted along a longitudinal line in the spanwise direction in the near wake, which is located at positions $x/C = 1.143, z/C = -0.167$ and stored at a selected time interval of simulation (0-0.05sec). At 0 sec the solution is fully converged and contains developed three-dimensional wake (unsteady static case). Afterwards, the trailing edge actuations are activated presented in figure 4.25. A considerable attenuation of the spanwise velocity under the actuations is observed.

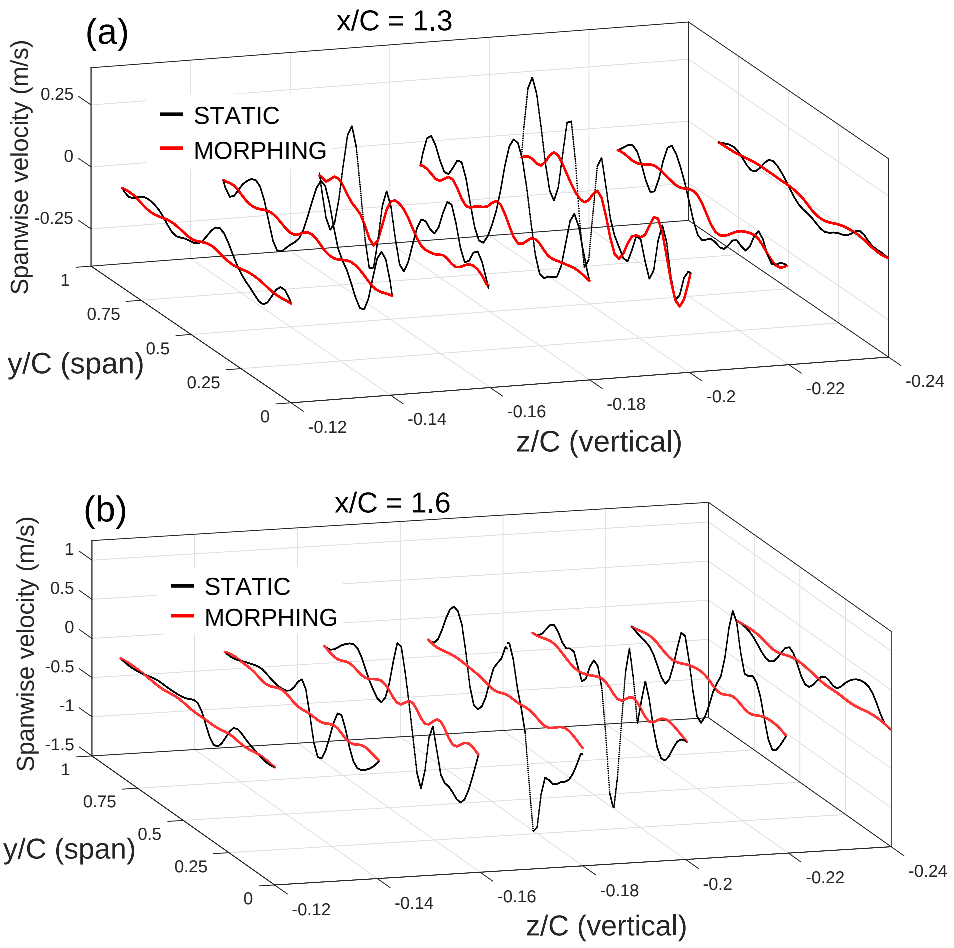

FIGURE 4.24: Spanwise velocity extracted from vertical slices in the z/C direction. (a) at the position $x/C = 1.3$; (b) at the position $x/C = 1.6$ for both static and morphing cases.

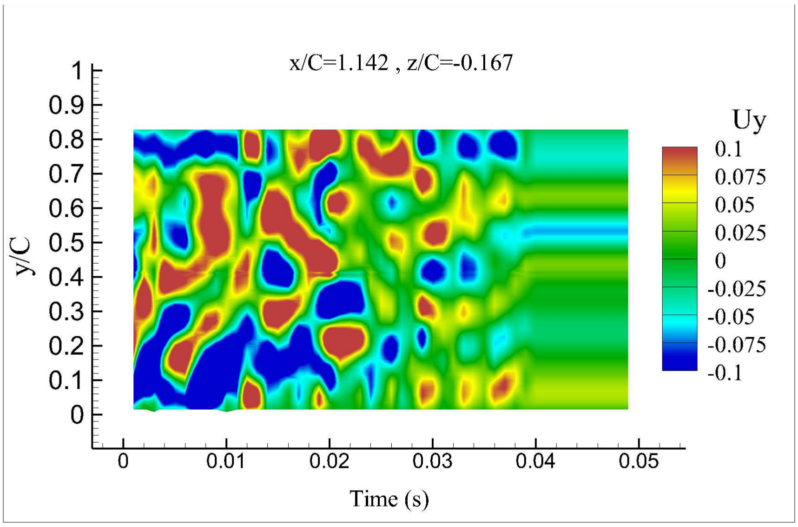

FIGURE 4.25: Space-time evolution of the spanwise velocity component at $x/C = 1.142, z/C = -0.167$ along the span for a morphing configuration

The effect appears after 0.026 sec. This time was necessary for the convection of the information to travel from the position $x/C = 1$ to towards $x/C = 1.143$.

In the time range (0.04 - 0.05 sec) a complete disappearing of the spanwise velocity followed by the suppression of the three-dimensional signature of the wake is found. A two-dimensional wake is then created thanks to the morphing though injecting new rows of vortices that interact with the existing coherent structures through the mechanisms analysed and render the flow practically two-dimensional.

4.5.6 Proper Orthogonal Decomposition

The three-dimensional analysis of the coherent patterns in the wake is carried out with the Proper Orthogonal Decomposition (POD). This allows decomposition of the flow according to a significant number of orthogonal modes extended form high energy (low order modes) towards to low energy (higher order modes) and reconstruction of the physical variables according to a selected number of these modes. The POD decomposes the velocity components $U(x,y,z,t)$ into N spatial $\phi_i(x,y,z)$ and temporal modes $\alpha_i(t)$ according to the amount of energy that they contain, according to the SVD approach (Berkooz et al. (1993)), where $U(x,y,z,t) = \sum_{i=1}^{N} \phi_i(x,y,z).\alpha_i(t)$, "separable POD" in respect of the space and time (Sirovich (1987)). This methods considers that the shape modes $\phi_i(x,y,z)$ are spatial variables only, whereas the coefficients $\alpha_i(t)$ depend on the time only. This application of the separable POD consists of

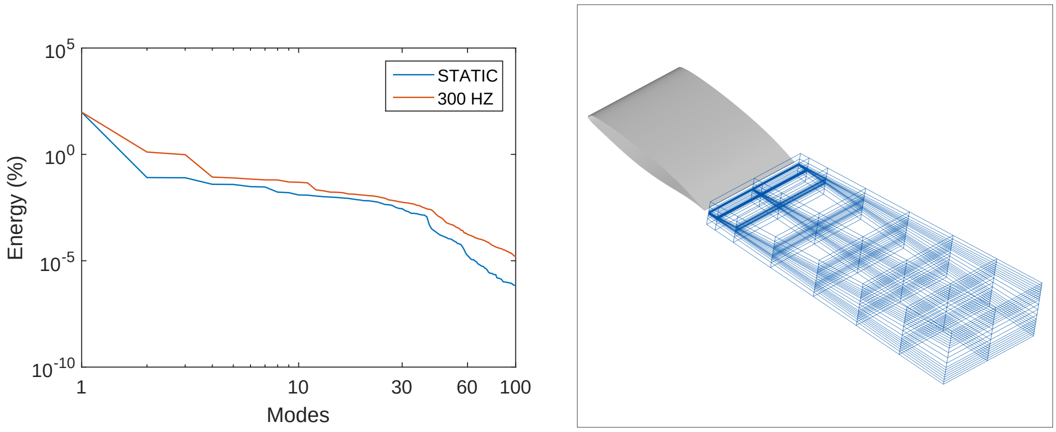

FIGURE 4.26: Energy diagram of the POD modes. (a) energy contribution of the first 100 modes. (b) POD domain extracted from the initial 3D grid

considering a significant number of successive snapshots describing in detail the time and space evolution of the flow system from the High-Fidelity approach (the CFD in the present case). The POD maximises a scalar product through a suitable correlation matrix evaluation. This application of POD is also called more recently "the snapshots method", suitable for numerical and experimental results. In the present study a subdomain of 224 x 360 x 40 cells in the wake presented in the figure 4.26(b) is stored each 10^{-4} s and 500 successive instantaneous vertical velocity fields are selected to cover more than 6 periods of the vortex shedding. The space and time-dependent domain is sufficient to capture three-dimensionality and the morphing effects in wake dynamics. Figure 4.26(a) illustrates the energy diagram of 100 modes. The total energy in the morphing case is $+2.77\%$ more than the static case. This energy is distributed over higher and lower modes. Through the actuations the morphing enhances the formation of smaller scale turbulent structures and injects them inside the Turbulent-Turbulent (TT) region.

The spatial and temporal modes are significantly different in both cases. The spatial modes components streamwise, spanwise and vertical directions are denoted u_n, v_n and w_n respectively, where n is the order of the modes. The iso-surfaces of the $Q-criterion$ of the mode components is selected at a fixed value and coloured with the velocity magnitude (figures 4.27 and 4.28).

A spectral analysis of the respective temporal modes is also presented to complete to the frequency analysis previously preceded and to identify the predominant effects.

In the static (no morphing) (figures 4.27 and 4.28), mode 2 is coupled with mode 3 and mode 8 is coupled with mode 9 because they contain the same amount of the energy level. It is noticeable that the first 10 modes contain the highest energy distribution

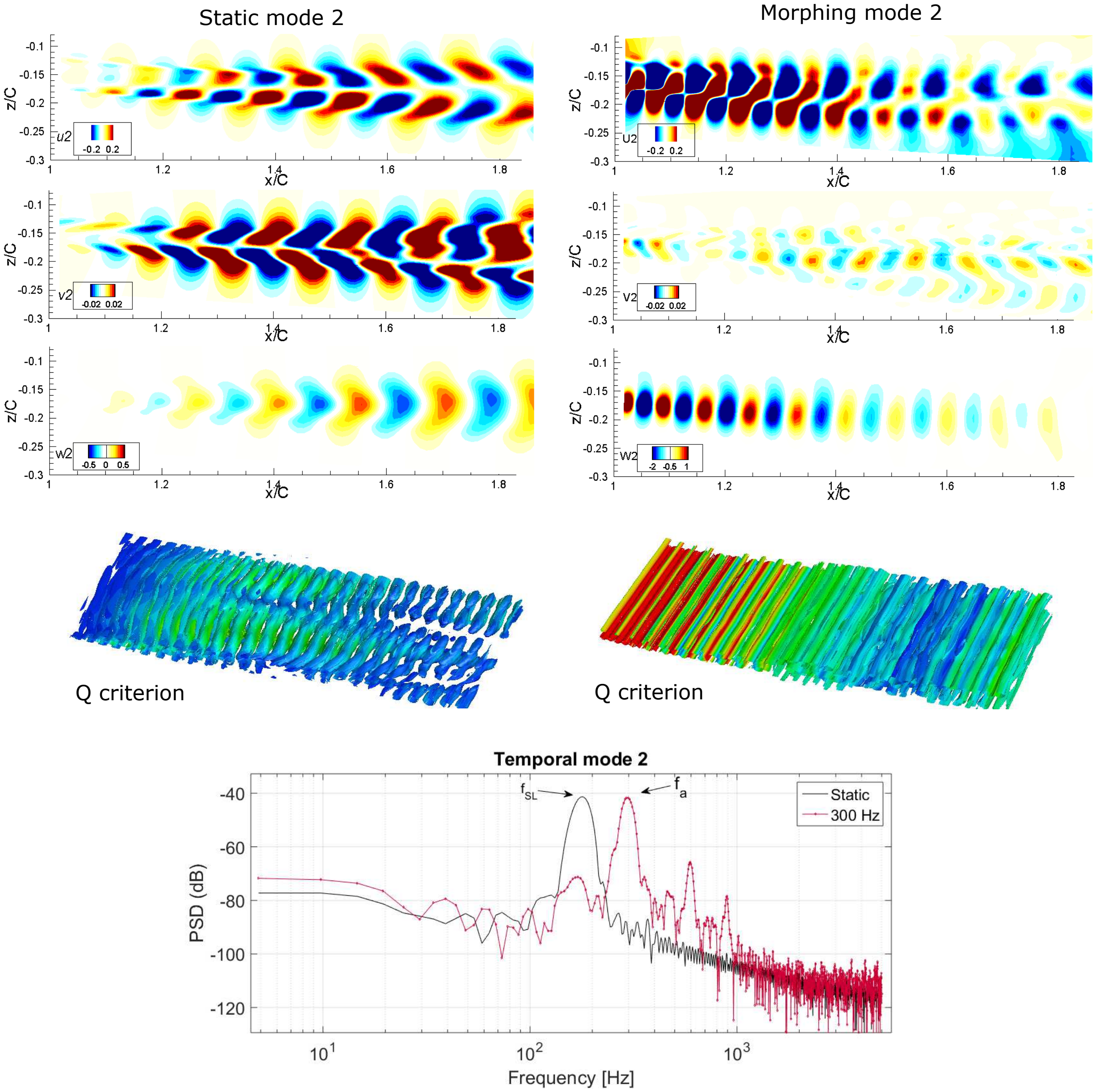

FIGURE 4.27: Energy diagram of the POD modes. (*a*) energy contribution of the first 100 modes. (*b*) Comparison of the first 30 modes of the morphing and the static cases

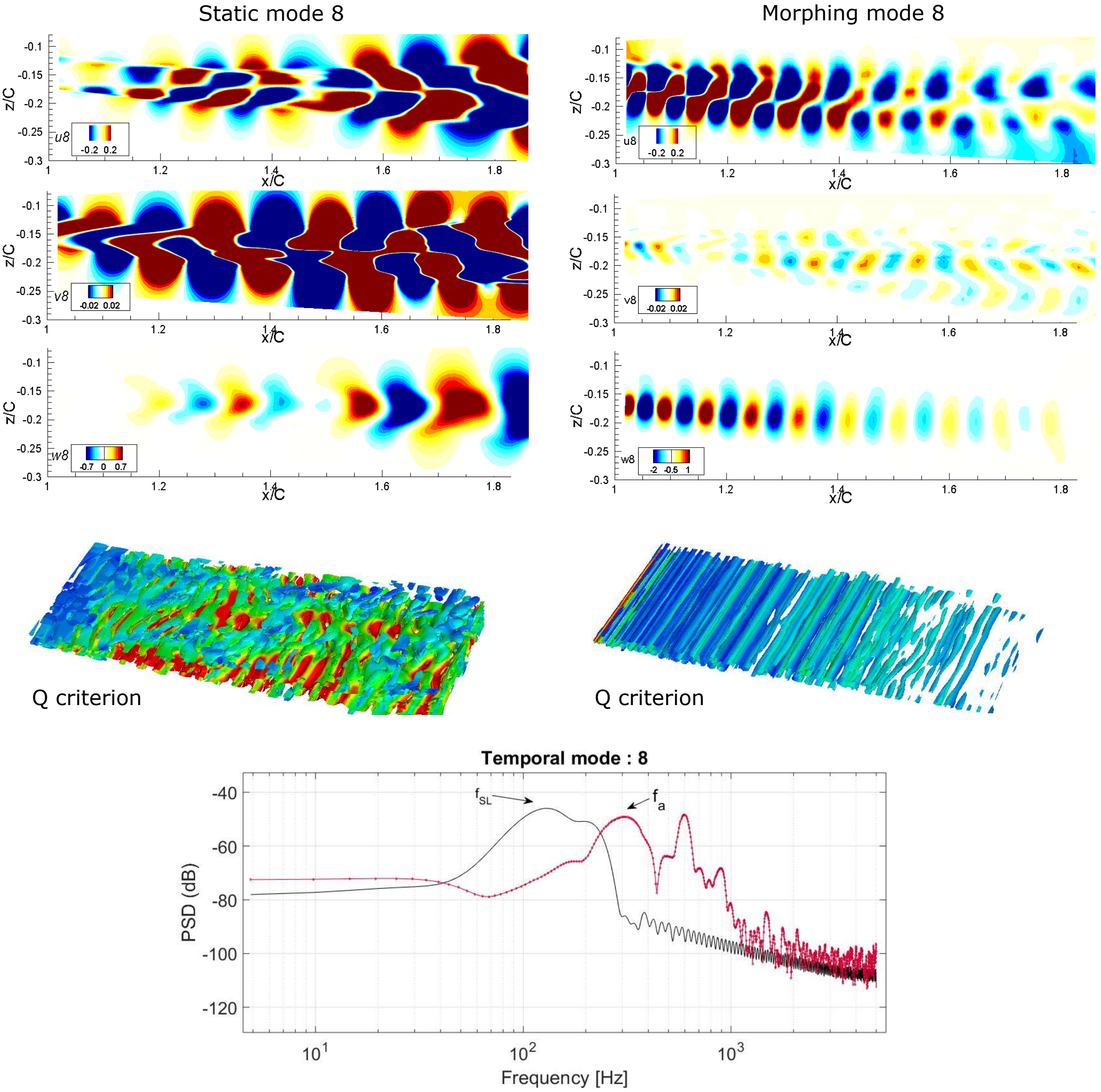

FIGURE 4.28: Energy diagram of the POD modes. (a) energy contribution of the first 100 modes. (b) Comparison of the first 30 modes of the morphing and the static cases

of the POD. High order modes with less energy represent the chaotic part of the flow. Our principal interest will remain only on low order modes at high energy. The higher order modes effect will be also discussed. Modes 2 and 8 are mainly associated with the alternating vortex pattern issued from the two shear layers as evaluated from the spectral analysis where the bump of f_{SL} is present , as well as the von Kármán bump. In addition, the *Qcriterion* illustrates the formation of the 3D wake including the onset of different vortex dislocations located farther in the wake.

Considering the morphing case in the same figures, the following modifications are noticed. Mode 2 corresponds to the reinforced shear layer close to the trailing edge. The streamwise velocity of the mode 2 (u_2) is more energetic through the flow acceleration related to the velocity deficit reduction. The vertical w_2 exhibits high energy concentration near the trailing edge because of the injected vortices from the actuations. The spanwise velocity component v_2 is drastically reduced because the vortex rows are less sensitive to the secondary instability and remain practically two-dimensional. The temporal coefficients contain the actuation frequency signature as a dominant bump that replaces the shear layer frequency f_{SL}. The energy of mode 8 is found considerably reduced and this mode is now more affected by the chaotic motions. A drastic diminution of all mode components u_8 , v_8 and w_8 compared to the static is observed.

Previous studies, El-Akoury et al. (2008) had shown that a reconstruction needs 11 to 19 modes to reveal the flow pattern with a good representation of the shear layer and von Kármán dynamics..

A reconstruction of the first 10, 20 and 30 modes has been investigated. It is found that the main dynamics are quite well captured as well as the modification of the flow due to the trailing edge actuation. In figure 4.29 the solution has been reconstructed and is similar to the initial solution. The morphing introduces an enhanced vorticity component ω_y through the modification of the vertical W velocity, which is merged with the instantaneous vorticity distribution and reinforces the vorticity component in the y-direction. Consequently, the von Kármán vortex rows become less sensitive to small spanwise perturbations and to the secondary instability, thus more stable. These effects suppress the three-dimensionality.

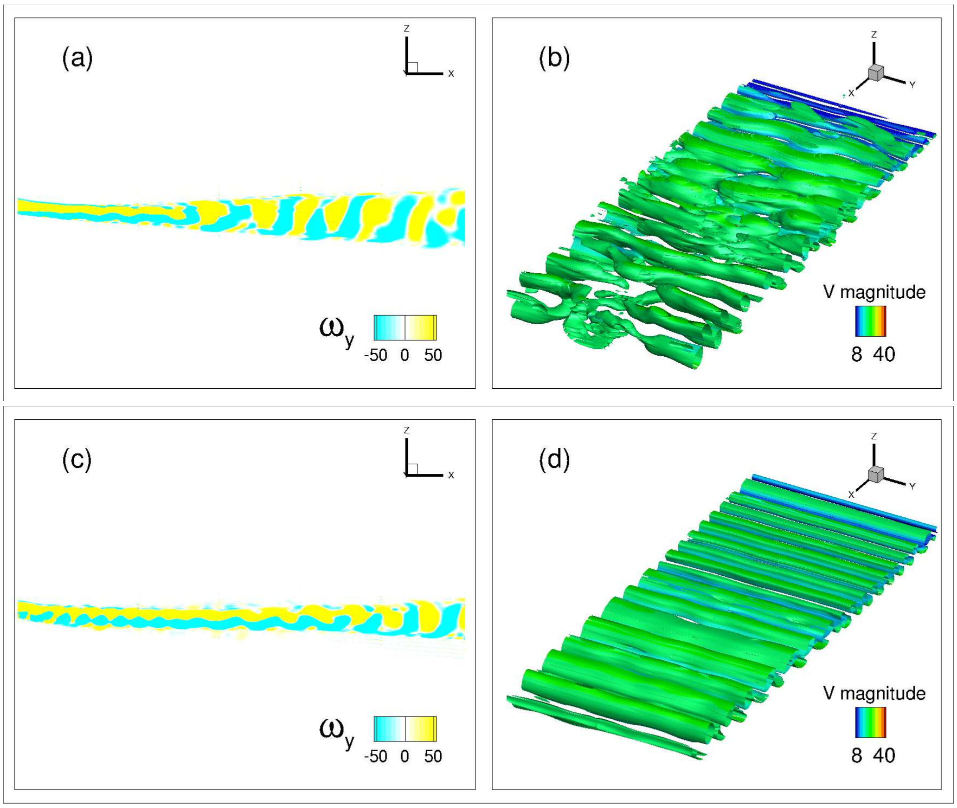

FIGURE 4.29: Reconstruction from 30 first POD modes presenting the vorticity ω_y (left) and $Q - criterion$ (Q=1500) colored by the velocity magnitude (right) for the static case (a) and (b) and morphing at 300 Hz (c) and (d)

4.5.7 Reconstruction of low energy modes

In (Szubert et al. (2015)) a stochastic forcing by means of POD modes has been examined through a transonic analysis. The shear layer and the shock's motion area (due to the buffet phenomenon) are filled by smaller-scale structures. In order to maintain the TNT interfaces thin and to limit the diffusion effect, a small amount of kinetic energy reconstructed from the higher order POD modes was added in the transport equations of K and ϵ equations by using this stochastic forcing, the thickness of the shear layers and of the wake's width were considerably reduced thanks to the action of this forcing, that enhances the eddy blocking effect. This forcing reproduces a similar blocking and thinning effect as shown by DNS within the boundary layer by (Ishihara et al. (2015)) regarding these interfaces.

The morphing appears having the same effects as in the stochastic forcing. In figure 4.30 the reconstruction of the streamwise velocity u through low energy modes is produced. Smaller-scale structures are more energetic in the morphing (figure 4.30(b))

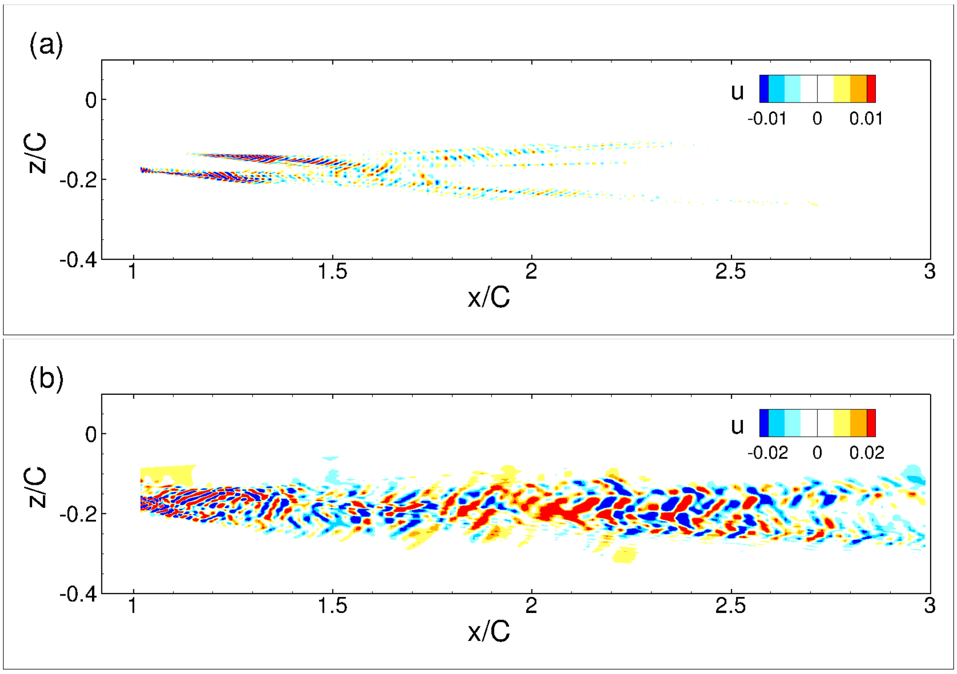

FIGURE 4.30: The streamwise u velocity through a reconstruction of the last 10 modes (90 - 99). (a) static case. (b) morphing case at 300 Hz

compared to the static case (figure 4.30(a)). The actuation injects more energy in the shear layers through the smaller-scale chaotic structures. This small amount of energy is indirectly added to the transport equations which maintains the TNT thinner and limits the turbulent diffusion. This produces an eddy blocking effect same as in the stochastic forcing which is consistent with a wake thinning induced by the morphing and examined in the previous section (mean flow properties).

4.6 DDES-OES simulations

Additional simulations were conducted thanks to the PRACE - FWING project N° 2017174208 allocation of 15 million hours of CPU computing in the Supercomputing Centre TGCC (Irène Skylake MPI processors of 1656 fine nodes composed of bi-processors Intel Xeon 8168 (SKL) at 2,7 GHz with 24 cores. A grid of 60 million cells has been used for the simulations, the grid has been carefully studied to be efficiently adapted to hybrid turbulence modelling. In fact, the current issue regarding Hybrid RANS-LES simulations to avoid that the Δ-span length be systematically chosen to evaluate the DDES length scale (see chapter 3, equation 3.42). To this end, the longitudinal Δx and vertical Δz refinements have to be carefully studied in respect of the

Δz.

It has a significant refinement in a wide extended region around the wing and along 2 chords in the wake as shown in figure 4.31. The time step has been also carefully studied in respect of the grid refinement, to ensure the time-dependent evolution of smaller-scale vortex structures, providing an appropriate CFL. The value of $\Delta t = 5\mu$ sec has been retained, giving a CFL of 0.1. The rest of parameters are remained the same as for the grid of 10 million cells. The DDES approach uses in its URANS part for the near region the OES model in the so called DDES-OES method. Thus, the non-equilibrium turbulence effects in the boundary layer and in the near wall region take into account to highly inhomogeneous turbulent flow.

Figure 4.32 provides a global view of the turbulent structures existing in the wake

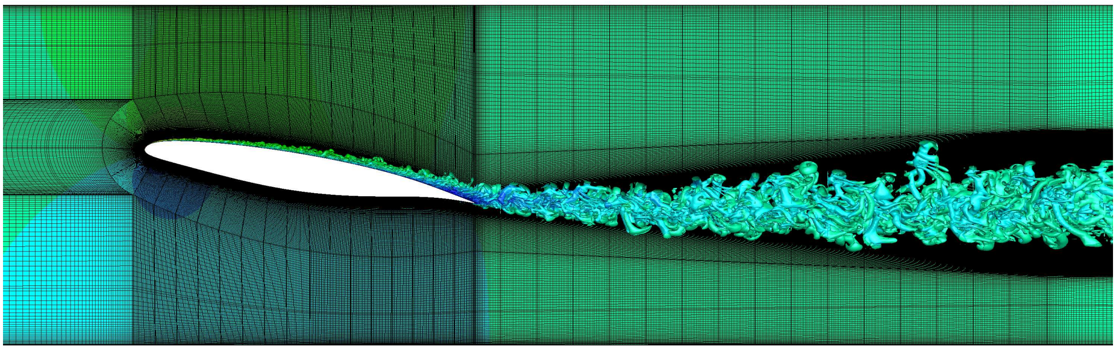

FIGURE 4.31: Iso-contours of the $Q - criterion$ (Q=1500) coloured by the dimensionless velocity magnitude superimposed on the grid, in the mid-span plane of the A320 morphing wing

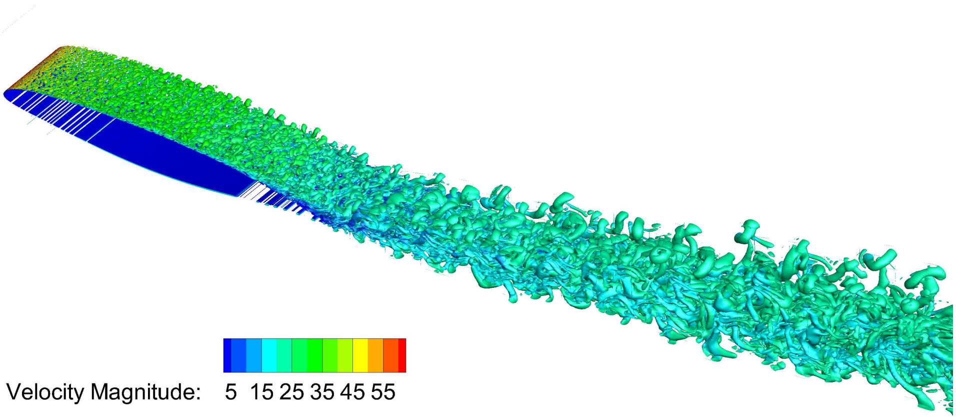

FIGURE 4.32: $Q - criterion$ (Q=1500) colored by the non-dimensional velocity magnitude on the wing's surface and the wake region (static case)

and the fully turbulent boundary layer in the upper surface of the wing. The boundary layer is detached and the recirculation near the trailing edge is formed similarly as in the 10 million grid case. Downstream in the wake, the shear layer and wake instabilities related to the coherent vortices are well pronounced with more small-scale structures thanks to the DDES approach, that provides an LES simulation in the outer region. The von Kármán vortices are associated to a considerable extension of the wake width in the vertical direction. In figure 4.33, the lower shear layer is quite pronounced because the morphing effects are more visible due to the high shearing. A formation of two-dimensional uniform vortex rows appears along with small braid structures in the morphing case (figure 4.33(b)). The vortex rows are more organised and injected continuously through the trailing edge actuation, compared to a more chaotic behaviour in the static case (figure 4.33(a)). These results are consistent with those obtained previously with a coarser mesh based the OES approach.

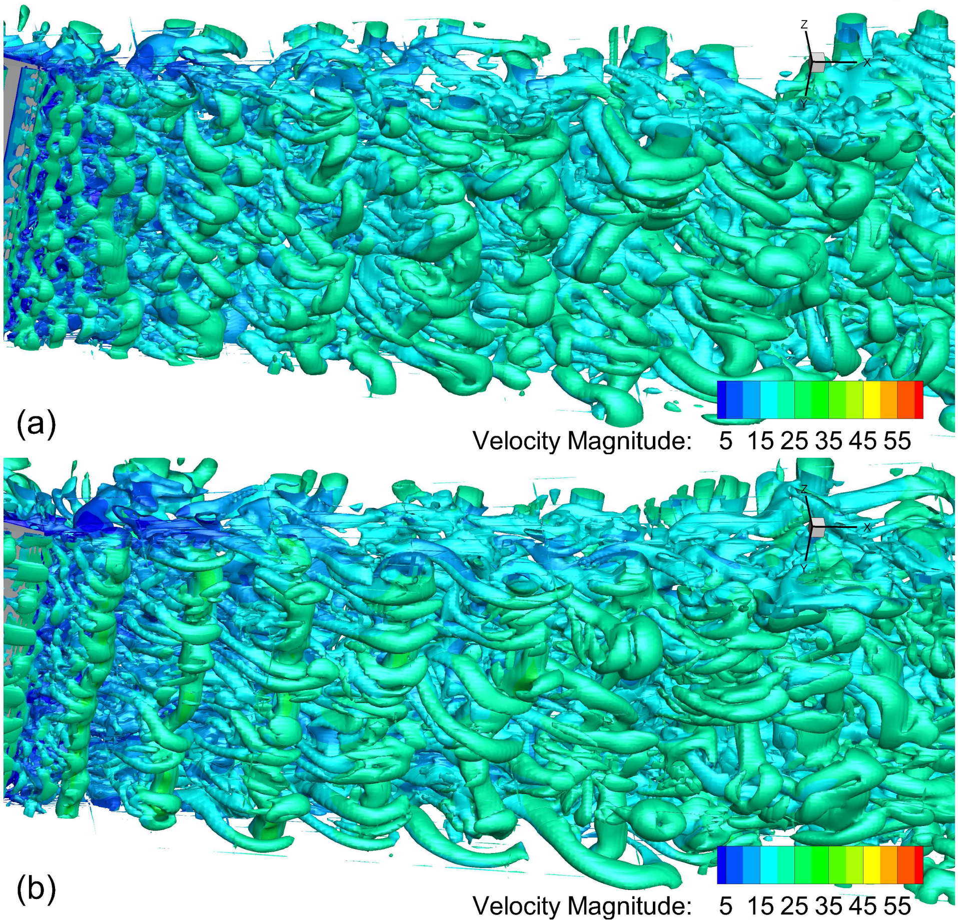

FIGURE 4.33: Q_c*riterion* (Q=1500) colored by the velocity magnitude.
(a) : Static case (no vibration). (a) : Morphing 300 Hz

$\frac{\langle Cl\rangle - \langle Cl\rangle_{static}}{\langle Cl\rangle_{static}}$ x 100	+ 4.2870
$\frac{\langle Cd\rangle - \langle Cd\rangle_{static}}{\langle Cd\rangle_{static}}$ x 100	+ 2.6263
$\frac{\langle Cl/Cd\rangle - \langle Cl/Cd\rangle_{static}}{\langle Cl/Cd\rangle_{static}}$ x 100	+ 1.6182

TABLE 4.2: Relative modification of lift, drag and lift-to-drag coefficients between the static and the morphing case at an actuation frequency of 300 Hz

4.7 Aerodynamic performances

The actuation at the frequency of 300 Hz such a frequency as found to increase the relative changes of the averaged aerodynamic forces as the lift, drag and lift-to-drag ratio presented in table 4.2. More pronounced enhancement of the lift can be noted compared to the static case, which produces high lift-to-drag ratio around this frequency.

The increase of the lift-to-drag ratio is explained through the change of the wake behaviour as its orientation (towards a slight lower inclination), thinning and reinforced two-dimensional character. The recirculation area reduction allowed a decrease of the velocity deficit and moves the wake in the downward direction.

4.8 Conclusion

This chapter presents a numerical study of the electroactive morphing effects by means of Macro-Fiber Composite (MFC) piezoelectric patches mounted along the span of a Reduced-Scale Airbus A320 prototype wing. Numerical results are in good agreement with experimental TR-PIV results. The morphing at an optimal vibration frequency of 300 Hz (higher than the natural frequency) coupled with a slight deformation of 0.35mm of the piezoelectric patches has been examined in details in respect of the aerodynamic performance increase and the main flow characteristics. The wake dynamics are affected by the actuations. Compared to the static configuration (no morphing) significant changes have been underlined as following :

- Suppression of the three-dimensionality and of the secondary instability through the injection of small-scale structures which reinforce the attenuation of the secondary (3D) instabilities an produce a practically 2D wake.
- Increase of regularity of the shear layer mode farther downstream, becoming more prominent than the von Kármán mode. This is due to the fact that the actuation frequency is close to the natural shear layer frequency, thus rendering the wake more regular around the shear layer mode.
- The POD reconstruction through low energy modes allowed understanding of the eddy-blocking effect produced by the vibrations and similarly as a stochastic forcing.
- The actuations attenuate the maximum growth of the secondary instability, explained by elliptic instability analysis, thus suppressing the vortex dislocations and the 3D effects in general.
- Reduction of the recirculation area (flow reattachment) near the trailing edge region and of the velocity deficit, leading to wake thinning.
- An aerodynamic noise sources reduction of -20 dB in the wake obtained by means of spectral analysis. This is related to the attenuation of the shear-layer and von-Kármán natural frequencies of two-dimensional simulations.
- The present actuation frequency and amplitude choice produced an enhancement of the mean lift force +4.28 % and an improvement of the aerodynamic performance lift-to-drag of +1.61 % by manipulating the near and far wake turbulent structures.

Chapter 5

Morphing of high-lift system using trailing edge actuations

This chapter investigates the morphing effects concerning the LS A320 prototype of the SMS project. This consists of a two-element high-lift configuration with the airfoil-flap in take-off position. The flow around the airfoil-flap and the near wake is analysed and validated through experimental unsteady dynamic pressure measurements in the S1 wind tunnel of IMFT in collaboration with CEMENTYS co-partner in the SMS project.
A parametric study of frequency of vibration and amplitude of deformation is performed for different morphing cases. This new concept, revealed an attenuation of the predominant natural shear-layer frequency and to considerably decrease the width of the von Kármán vortices with a simultaneous increase of aerodynamic performances.

Contents

5.1 Introduction

The aerodynamic design of high-lift configurations needs to fulfil specific targets for take-off and landing configurations. In addition, this system needs to have a minimum complexity of mechanical structure for less weight and cost. Flaps and slats are used to increase aerodynamic performances specially the lift force. During take-off or landing the flap is translated and deflected from its initial position in the airplane. The increase of the wing surface and the camber helps to increase the pressure distribution over it and to improve the lift. A considerable number of studies aimed at investigating the flow around high-lift configurations, as for example in the European project ATAAC[1], where the LEISA three-element wing had been selected and tested experimentally and numerically with a considerable number of CFD codes, involving hybrid RANS-LES turbulence modelling. Synthetic turbulence had been injected in the slat, the flap and the rear part of the wing to predict the flow detachment. The studies of (Soulat et al. (2016)) on shape optimisation for a multi-element device test-case aimed to maximize the lift and minimize the drag. By choosing two different optimizations and using only geometrical parameters (geometrical optimization) or the angle of attack and the Mach number (total optimization), they have found for both optimizations quite similar optimal geometric positions : a flap rotation to increase the lift and an upward slat rotation to reduce the drag. In another aerodynamic multi-objective optimization, the study of (LU et al. (2017)), proposed a flexible variable camber trailing edge of the flap for a two-element airfoil-flap able to camber its shape smoothly at the take-off and landing conditions. They have found that a variable camber of the flap of 50 % of its chord can increase the lift coefficient by about 8 % and the lift-to-drag ratio by 7 % for the take-off configuration and improve the lift coefficient at a stall angle of attack by 1.3 %. A recent study of (Abdessemed et al. (2018a)) proposed to use dynamic meshing to perform numerical simulation of static and time-dependent morphing of a NACA 0012. Their work revealed an increase of the average aerodynamic efficiency CL/CD of 6.5% with a maximum deflection (5 % chord). A considerable number of studies treated shape optimization, static cambering and leading edge with a droop nose aiming at improving aerodynamic performances in order to increase lift, decrease of drag or increase of the stall angle. To our knowledge, there is a lack of experimental and numerical studies investigating a dynamic morphing of a high-lift configuration in respect to the wake dynamics understanding in the high Reynolds number range.

---

[1] http://cfd.mace.manchester.ac.uk/ATAAC/WebHome

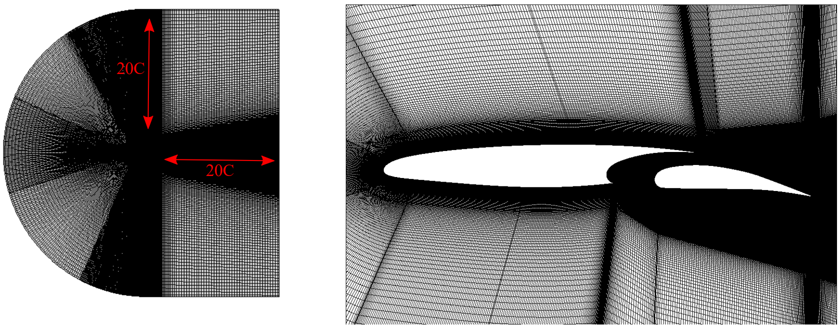

FIGURE 5.1: Computation grid of the high-lift LS configuration of the A320 in the take-off position

This is the originality of the present study which is part of the H2020 'Smart Morphing and Sensing' (SMS) European project (`http://smartwing.org/SMS/EU`) aiming at improving aerodynamic performances as increasing the lift, decreasing the drag and to attenuate the aerodynamic noise by means of novel electroactive morphing concepts. Instead of the classical high-lift system, a morphed flap is installed, able to change its shape dynamically to adapt it to different flight configurations as take-off, cruise and landing.

The present numerical study focuses on the morphing by means of MFC (piezoactuators) near the trailing edge region at low-amplitudes with frequencies in the range 60 - 400 Hz, applied on the high lift configuration having a chord of 2.40 m and a flap's chord of 1 m at the take-off position for a Reynolds number of 2.25×10^6. This corresponds to a near scale 1 configuration of the A320's flap, in the context of the so-called Large Scale (LS) prototype of the European research programme SMS, for which the camber control has been designed experimentally by (Jodin et al. (2018)).

The present numerical study first focuses on the investigation of the morphing effects in the clean configuration of the LS prototype, providing also a validation of the numerical results for this configuration and secondly, the investigation of the morphing effects in the case of the two-element at the take-off configuration (airfoil-gap-flap). The flow dynamics around the A320 airfoil-gap-flap is analysed in detail concerning the static and morphing cases. The shear layer, wake instabilities and dynamics past the airfoil and the flap are discussed. An explanation of the dynamic morphing is provided regarding the understanding of the modified physical mechanisms when a specific vibration and slight deformation of the flap's trailing edge are added, depending on a fixed actuation frequency. To illustrate the morphing effect over the time-dependent signals of the velocity, spectral analysis of suitably chosen monitor positions was performed and compared with the static case (no vibration) taken as

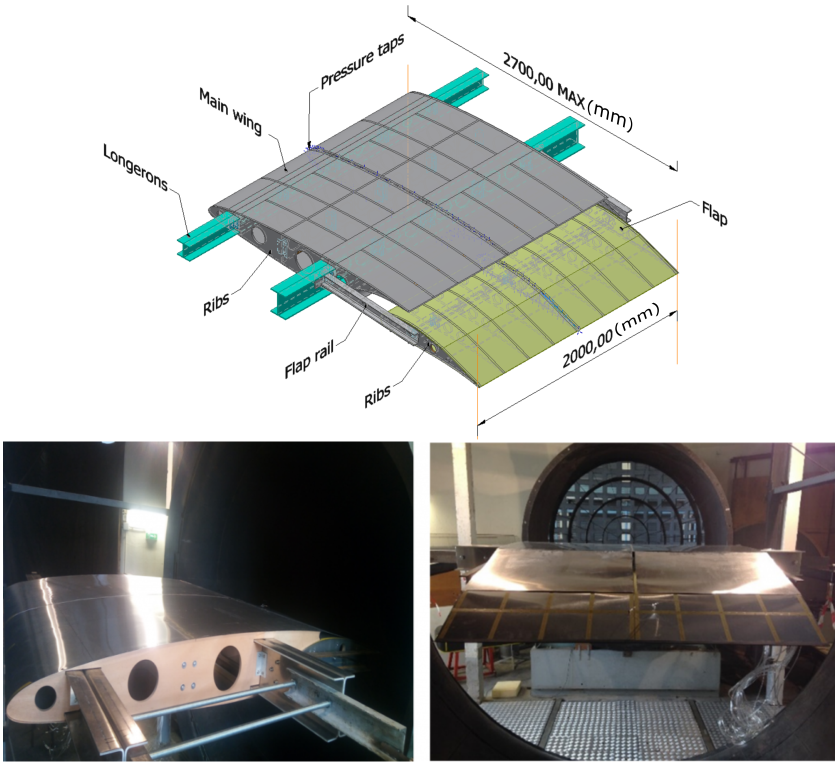

FIGURE 5.2: The CAD prototype and the experimental high-lift LS prototype mounted in the IMFT wind tunnel

reference. Finally, the influence of the morphing configuration on the aerodynamic lift and drag coefficients is presented and discussed in relation with the modification of the pressure distribution over the airfoil and the flap due to the morphing. A map of amplitude, frequency and lift coefficient is presented showing the optimal regions of the morphing actuation.

5.2 Numerical and experimental configurations

The numerical flow domain around the airfoil-flap system is considered in this study with farfield boundary conditions at 20 chords from the inlet, outlet, top and bottom as presented in the figure 5.1. The flap is detached from the airfoil, translated from its initial position and deflected with 10° of incidence corresponding to the take-off position for an A320 wing. The resulting total chord of the airfoil and the flap in the take-off is about 2.72m. The corresponding Reynolds number is around 2.25×10^6 and standard air properties have been chosen.

The numerical grid has multiblock structure and it has a CH topology and a size of

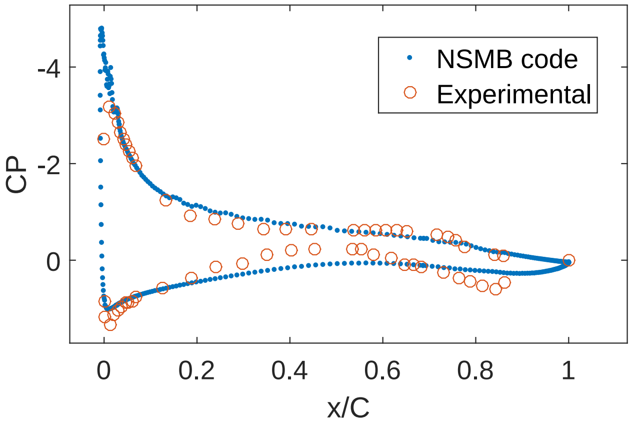

FIGURE 5.3: Comparison of the mean wall pressure coefficient in the clean configuration of numerical and experimental results : the flap is attached to the wing.

0.6 million cells approximately. The mesh has been tested with the numerical solver Navier-Stokes Multi-Block (NSMB) (Hoarau et al. (2016)). In this work, a preconditioning method was selected based on the artificial compressibility in our compressible solver NSMB in the implicit dual time stepping method with Lower Upper Symmetric Gauss Seidel (LU-SGS). The y+ value provided by this grid is smaller than 0.5 in the whole near wall domain, thus ensuring an optimal behaviour of the near-wall turbulence modelling with the appropriate damping for the eddy viscosity adopting a modified damping function regarding the Chien's k-ϵ model, (Jin and Braza (1994)), according to the Organised Eddy Simulation (OES) approach, (Bourguet et al. (2008)). A study of the time step has been carried out for the 2D simulations. A $dt = 10^{-5}$ second was found to be sufficient after a detailed investigation and was able to better capture the physics for the morphing at high frequency vibrations. A typical number between 60 and 100 inner steps was sufficient for the convergence in the dual time process. A comparison of the numerical results of the pressure coefficients with the experimental results obtained from the IMFT wind tunnel (see figure 5.2) is presented in the figure 5.3.

Based on previous studies in our research group which examined the predictive ability of various turbulence models, (Bourguet et al. (2008), Jin and Braza (1994), Szubert et al. (2015)), it was shown that the standard two-equation k-ϵ Chien model, Chien (1982) was not able to produce the main flow instabilities and the unsteadiness at the present values of incidence and Reynolds number. However, the Organised-Eddy Simulation (OES) model, (Bourguet et al. (2008), Braza et al. (2006)) provides quite well the dynamics of the flow detachment dynamics including the separated shear layers and the wake instabilities. Furthermore, the OES approach is not intrinsically 3D and provides quite a good for 2D evaluation of the main flow instabilities, thus allowing a rich parametric study of the morphing actuations before selecting a reduced number of cases for a 3D investigation. In the present chapter, this turbulence modelling approach has been used and shows a clear appearance of low frequency instabilities as the von Kármán vortices past the trailing edge on the two-element configuration involving a large gap between the main wing and the flap, these aspects are crucial for the modification of the flow dynamics and are well captured by the present approach. The refined grid has around 300 cells on the airfoil and the flap and minimum cell size less than 1 mm near the flap's trailing edge to capture the detachment of the boundary layer near the trailing edge. This grid showed its ability to capture the real flow modification in the wake region when the morphing is activated.

The experimental prototype consists of a high-lift A320 LS prototype with two elements presented in the figure 5.2, containing a wing and a flap. In the IMFT large subsonic wind tunnel S1, an aerodynamic evaluation has been investigated for two configurations (Clean and take-off) with several degrees of incidence and different Reynolds numbers in the range [1-4] Million. This wind tunnel is an Eiffel type, which consists of a cylindrical central building containing the experimental chamber, the assembly and modification space, as well as the measuring equipment. The section of the collector decreases gradually to a diameter of D = 2.40 m to the outlet. However, at the entrance the diameter is 6 m. This manifold is made of sheet steel 3 mm thick. The inlet section includes two filters in the desired weight to suppress the vortex movements of the air that must be without the operation of the blower. The diffuser consists of a frustoconical section of 11.50 m, with an apex angle slightly lower than 8°, an entrance diameter of 2.70 m. This wind tunnel has a contraction section upstream of the test section with a double level of honeycombs ensuring a low turbulence intensity of order 1 %, as well as end plates attenuating the extremity effects and ensuring a most uniform flow with low turbulence level, to provide uniform low turbulent flow.

Experimental and numerical results are provided in the figure 5.3 of the pressure coefficient (C_P) for the LS prototype at 0° angle of attack and a Reynolds number of 1x10^6 in the clean configuration (the flap is attached to the wing). There is a difference of C_P in the pressure depression located in the leading edge of the wing between the numerical simulations by the NSMB solver and the experimental results from the wind tunnel. The numerical approach is affected by the 2D approximation previously mentioned which was performed with farfield conditions and does not consider the

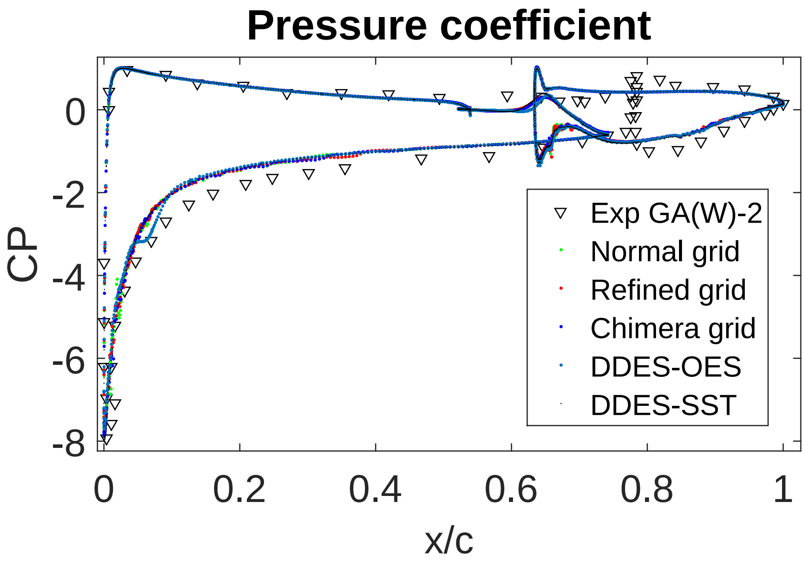

FIGURE 5.4: Pressure coefficient of the wing-flap LS configuration for different grid

confinement with the presence of the upper, lower and sided walls. In addition, grid dependency has been examined through two-dimensional normal, refined, chimera (overset) grids and three-dimensional mesh based on hybrid turbulence modelling as the DDES-SST and DDES-OES. These results are compared with (LU et al. (2017)) results of GA (w) 2 wing-flap and the A320 at the same flow configuration and speed in figure 5.4 was tested. Numerical simulations show a good approximation to GA (w) 2 in CP distribution around the wing, but there is a small change in the upper surface of the wing due to the difference of shape. Notice that in GA (w) 2 flap is smaller than the A320 which explains the reason of the difference in the pressure distribution. Even though we still have a good agreement between both configurations.

More detailed experimental tests of unsteady pressure measurements were carried out in the wind tunnel and are provided by means of piezo resistive pressure transducer placed at 72% of the chord on the upper surface of the flap and near the trailing edge in the take-off position to capture the near wake instabilities (predominant frequencies). These results are discussed with those obtained by the numerical model. Power Spectral Density (PSD) of converged signals is computed for both cases. Converged experimental signal of 210 seconds is stored each 10^{-4} second (see figure 5.5b for the signal sample) and compared to a numerical signal of 2 seconds stored each 10^{-5} second in the figure 5.5a. The PSD in the figures 5.5c and 5.5d revealed the existence of several predominant frequencies (f_1, $f_1 + f_2$, f_2 and f_3) quite similar in both configurations. The frequency f_1 corresponds to the von Kármán instability bump formed in the range of 10-30 Hz in the numerical PSD. A similar bump formation

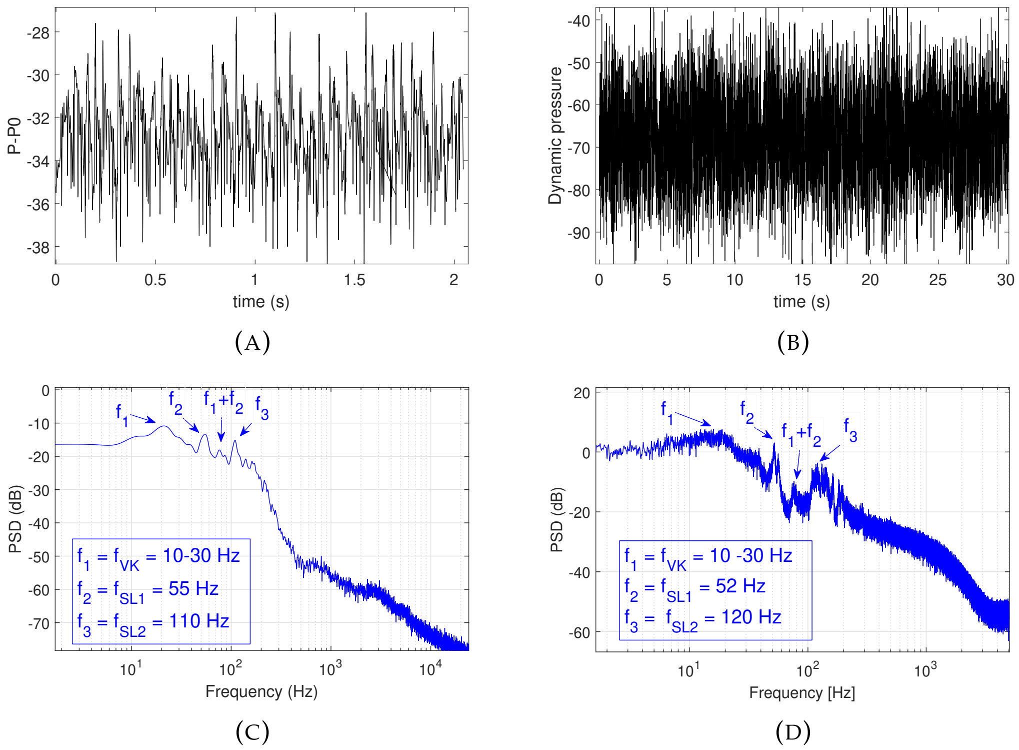

(A) (B)

(C) (D)

FIGURE 5.5: Pressure signal at 72% of the chord in the suction side of the flap. (A) : numerical $\Delta P = P - P0$, (B) : experimental dynamic pressure (sensors). (C) : PSD of the numerical signal. (D) : PSD of the experimental signal

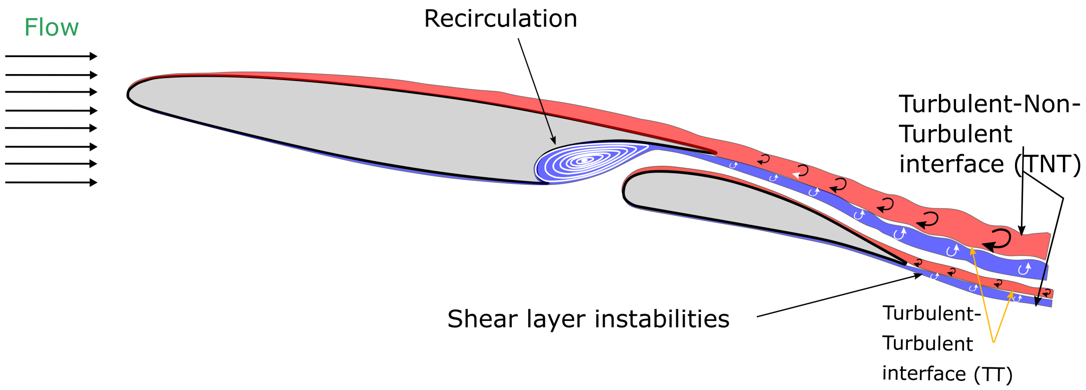

FIGURE 5.6: Sketch of the wake dynamics. The recirculation area and shear layer instabilities appearing just downstream of the trailing edge of the wing and the flap in between TNT and TT interfaces

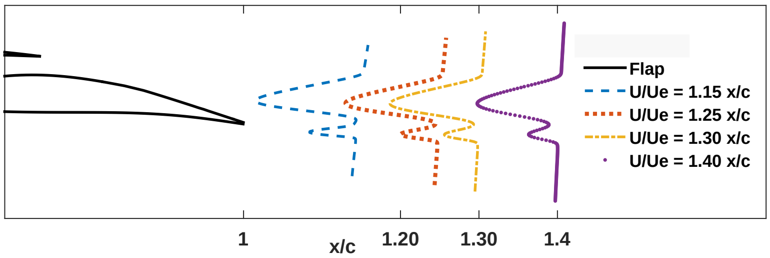

FIGURE 5.7: Mean non-dimensional streamflow velocity extracted from different position in the wake

is obtained in the experimental PSD in the figure 5.5d. The frequency f_1 is near 15 Hz in both cases and the bump formation is due to the interaction with smaller-scale turbulent chaotic motion present at this high Reynolds number. Then, a predominant frequency f_2 is also found, corresponding to the coherent vortices shedding in the upper shear layer and to their interaction with the von Kármán mode (highlighted by the streaklines in the next sections). The interaction between both instabilities generates new predominant frequencies as for example $f_1 + f_2$ found in the figures 5.5c and 5.5d. The predominant frequency f_3 is associated to the lower shear layer and its smaller vortices in the formation region past the flap's trailing edge.
Furthermore, another comparison of these results can be made with the study conducted by (Jodin et al. (2017)) on the same prototype but in a smaller scale with a single element of chord C=0.7m at Re=0.5 million (U=10.5 m/s). It was found that the Strouhal number $St = 3$ ($fr = 46$ Hz) corresponds to the von Kármán instability. The results of the Large-Scale prototype ($C = 2.72$m) at Re=2.25 million (U=12.47 m/s) are in good qualitative agreement with these results. The von Kármán instabilities have a St of 3.27 ($fr = 15$ Hz).

5.3 Flow Characteristics

The flow around the high-lift configuration is investigated numerically to understand the physics, the wake behavior and the reasons of the appearance of the turbulent instabilities during the take-off position. This could help us to find out an optimal morphing region with a specific vibration frequency at a certain deformation. The flow around the two-element airfoil-flap can be decomposed into three different regions :

- Airfoil region : Starting from the airfoil and presenting a high axial velocity deficit in the near wake figure 5.7. The airfoil acts as a dominant bluff body in the flow at this angle of attack. The velocity deficit reaches critical values, which introduces the appearance of the wake instabilities and the wake first shear layer highlighted in figure 5.6.
- Flap region : Starting from the flap and presenting a smaller velocity deficit than the airfoil (figure 5.7) due to the presence of the airfoil. A second shear layer is created downstream of the flap's trailing edge (figure 5.6).
- Separating region : There is a considerable vertical distance between the end of the airfoil and the leading-edge of the flap called the gap, which splits the velocity deficit into two parts (see figure 5.7). Consequently this separates the shearing of the airfoil and the flap in the wake. The C form at the end of the airfoil produces a recirculation region governed by an anticlockwise vortex.

There exists an interaction between these 3 regions in the wake and the flow in the wake is the result of a non-linear interaction between the lower and upper shear layers of the airfoil and the flap at this Reynolds number of $2.25\text{x}10^6$ and 8° of angle of attack. The difference in the velocities between the upper and the lower shear layer is much higher in the airfoil's region than around the flap. This leads to creation of unstable waves which are amplified when they propagate further in the wake. Beyond critical state of the shearing mechanism, formation of von Kármán vortices presented in figure 5.8 occurs from x/C=1.25 to x/C=1.8. These vortices are shed with a predominant frequency between 10 - 30 Hz (see figure 5.12) and are not fully formed. Further in the wake for x/C > 2 these shear layers produce the full formation of the von Kármán vortex street. Near the flap, small disturbances in the mixing layer create a wavy deformation but this does not roll up to create von Kármán vortices because of a smaller velocity deficit.

5.4 Morphing through near trailing edge vibration and slight deformation

The trailing edge of the flap is deformed as a function of time in numerical simulations, according to the dynamics of MFC piezoactuators instrumented experimentally

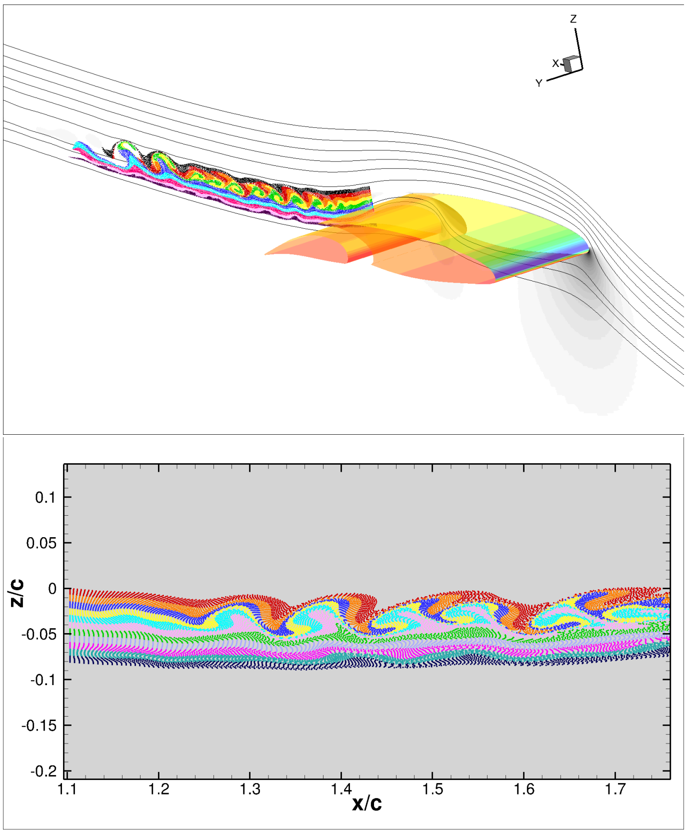

FIGURE 5.8: Visualisation of the wake instabilities by mean of streaklines in the static case (no vibration)

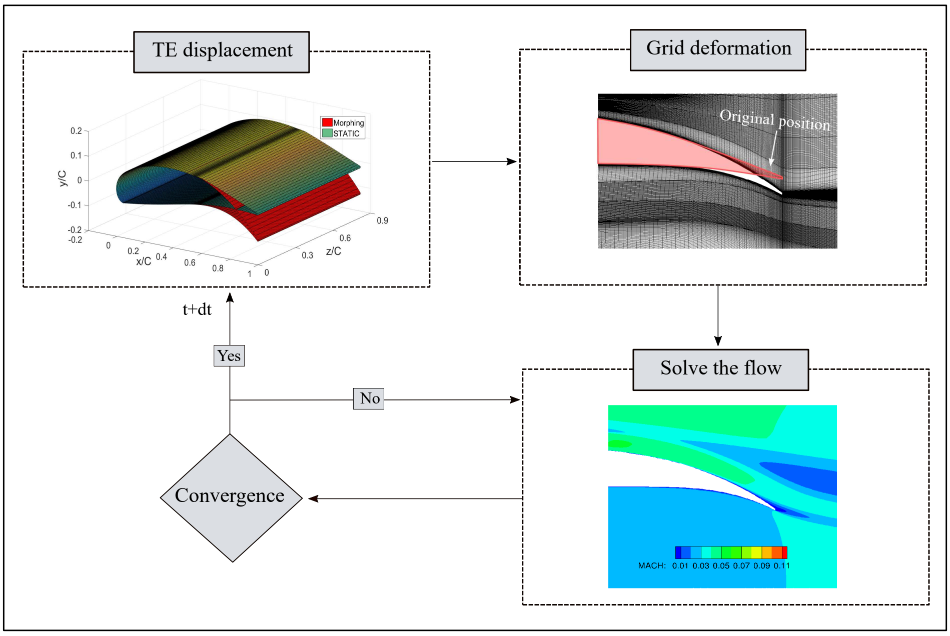

FIGURE 5.9: Dynamic grid deformation implemented in the NSMB solver to simulate the time-dependent morphing

in the morphing prototypes of previously mentioned studies. The unsteady movement and the slight deformation of these patches are introduced in the numerical model in the same way as in the experiments by (Jodin et al. (2017)) and (Scheller et al. (2015)), by using Arbitrary Lagrangian Eulerian (ALE) method (Donea et al. (1982)) and a second order polynomial equation similar to the MFC patches deformation.

The displacement of the flap geometry is imposed at first, then the new deformed grid is computed by means of Volume Spline Interpolation (VSI) and Trans-Finite Interpolation as used by(Guillaume et al. (2011)) remeshing methods. Next, the NSMB code solves the momentum equation and the pressure correction for the new grid in a convergence loop. Once the convergence is achieved, new time step $t + dt$ will be calculated as presented in the figure 5.9. These methods are well adapted for small deformations to preserve good quality of the mesh as the orthogonality. The OES approach is used concerning the turbulence modelling.

The frequency of the trailing edge actuations and amplitude of deformations values have been the object of a detailed parametric study as in the clean configuration in order to evaluate the morphing effects on the flow dynamics and the aerodynamic performances. The vibration of the flap introduces either an undulation in low frequency lower than 200 Hz or a new anticlockwise vortex in the case where the frequency is higher as in figure 5.10. These morphing effects interact with the existing wake instabilities and modify the wake behavior. In order to understand the modification produced by the vibration, an area is selected close to the flap's trailing edge and snapshots were saved for a time interval of 10^{-4} second to better analyse the effects of the dynamic morphing.

The angle of attack is more significant when the trailing edge deformation is oriented to the pressure side. This configuration acts as a dominant bluff body. The air particles are submitted to an important shearing in the lower region past the trailing edge. At the same time, air particles located in the suction side of the trailing edge are dropped behind the trailing edge and split into two parts: the first creates a small recirculating vortex and the second part is mixed with the particles coming from the lower shear layer. This creates new anticlockwise vortices which were not present in the static case, which have specific properties as an elliptic vortex shape with (β, α) parameters. The distance between two vortices corresponds to $L = U/(c.f_a)$, where f_a is the actuation frequency. These new introduced vortices modify the flow further in the wake and affect the formation of the von Kármán instability, thus producing an eddy-blocking effect (Szubert et al. (2015)), resulting to a constriction of the shear layers and a thinning of the wake's width. The injected vortices are dissipated over $0.2C$, which will be analysed in the next section.

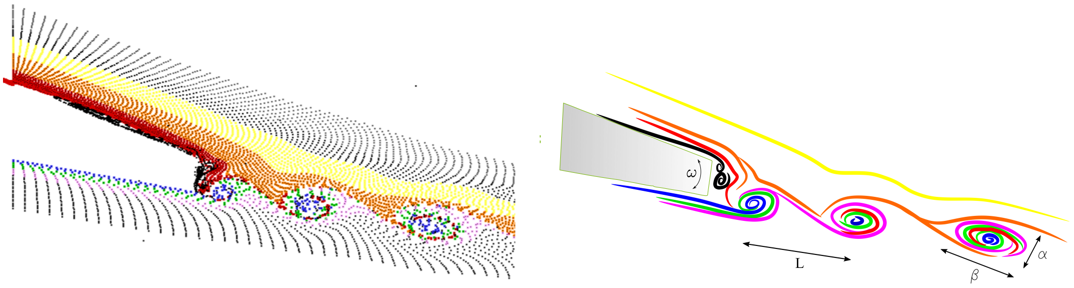

FIGURE 5.10: Zoom showing the near region of the flap's trailing edge with coloured streaklines visualisation and schematic description of high frequency morphing actuation at 300 Hz

Calculated streaklines are useful to understand the real flow dynamics in the wake and its modification. 2D numerical results are compared to 3D experimentation of TR-PIV at a Reynolds number of 5.10^5 and angle of incidence of 10° for a reduced scale prototype on the clean (one element) configuration of chord $C = 0.7m$. These experimentation were carried out with a morphing frequency of 220 Hz for a same actuation amplitude. Despite the fact that the numerical and the experimental configurations are not the same but surprisingly with the vibration a good consistency of the morphing is obtained between both results. Different colors were chosen to identify the wake structures, the particles coloured in blue are placed in the pressure side

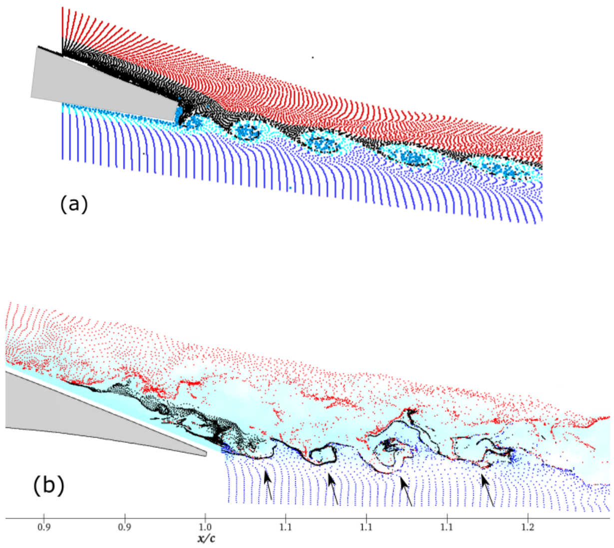

FIGURE 5.11: Morphing Streakline technique visualization. (a) : Numerical simulation of the two-element wing-flap A320 with actuation frequency $f_a = 300$Hz. (b) : TRPIV of a single wing A320 with an actuation frequency $f_a = 220$Hz

(intrados) of the wing, the red particles in the suction side (extrados), these two layers are separated with black streaklines near to the trailing edge and the separation of the boundary layer. Effects of the morphing are visible, the vibration introduces constantly new smaller spaced vortices in both configurations presented in figure 5.11. The arrows in the figure 5.11 (b) show the re-circulation of the black particles which is highly visible also in the figure 5.11 (a). The 2D simulations captures the coherent structures and filters smaller scale structures, on the other hand, in the experimentation, three-dimensional interaction and TRPIV captures all the physics with smaller and larger turbulent structures. However, morphing effects are visible and these new vortices separate the lower and the upper shear-layer and present an eddy blocking effect.

5.4.1 Influence of the actuation frequency

Several simulations are tested for the two-element airfoil-flap in the morphing configuration and compared to the static case (no vibration) taken as reference case. The purpose is to analyze the influence on the wake behaviour, aerodynamic forces and energy distribution. A certain range of vibrations from low to high frequencies range of the order (30 Hz – 400Hz) at a fixed small deformation amplitude of 0.35 mm were tested to show an optimal configuration allowing the attenuation or suppression of the wake instabilities and leading to an improved aerodynamic performance through the trailing edge dynamic control.

The frequency effects are visible in the wake. These effects from low to higher frequency ranges are shown in figure 5.12, which illustrate a streaklines visualization injected in different coloured layers to reveal the exact modification of the flow. At a low frequency of 30 Hz in figure 5.12a, the shear layer instabilities are excited due to a resonance phenomenon produced by the morphing in the wake. The flap shear layer frequency is forced at 30 Hz vibration mode through the morphing and the natural frequency in the wake of the von Kármán is between 30 Hz and 40 Hz. The anticlockwise vortices interact with the upper formed von Kármán and expand them in the vertical direction. The actuation near to the natural frequency leads to a considerable amplification of the turbulent structures in the wake for the morphing compared to static configuration. Thus, the need to investigate frequencies of actuation f_a greater than the natural frequency is important to analyze the wake response to higher vibration actuations. When the morphing frequency is in a medium range, in the figure 5.12b (60 Hz) and figure 5.12c (100 Hz), this produces an undulation of the flap's shear layer which has a direct effect on the von Kármán and induces breakdown of the first von Kármán vortex in into two smaller von Kármán vortices for the 60 Hz actuation. In figure 5.12c the 100 Hz actuation shows an attenuation of the von Kármán vortices from x/c = 1.2 to x/c = 1.4. The undulation interacts with the airfoil's shear-layer and prohibits the formation of the instabilities.

Higher frequencies are investigated up to 400 Hz. At 200 Hz, the undulation noticed in low frequency actuations is transformed into small anticlockwise vortices that were presented in the previous section (with a zoomed near trailing edge area), this global view of the wake cannot exhibit them. The higher frequency have better effects than lower or medium frequencies. The figure 5.12d, 5.12e and 5.12f present respectively 200 Hz, 300 Hz and 400 Hz frequencies of actuation. A considerable attenuation of the von Kármán vortices and the shear-layers instabilities occurs when the frequency actuation increases. In the figure 5.12e, the 300 Hz frequency shows an optimal attenuation of these vortices and a complete disappearing of the instability from x/c=1.1 to x/c=1.7 compared to the static configuration. The morphing injects and creates new vortices in the flow which are smaller and more energetic. These lasts interact with the upper and lower shear layers of the wing and prohibit the von Kármán vortices to form. Above this optimal frequency, in the figure 5.12f the 400 Hz frequency gives

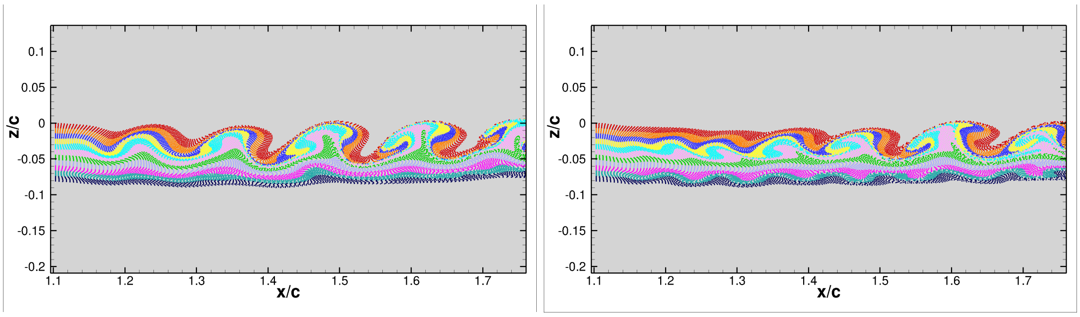

(A) f_a=30 Hz (B) f_a=60 Hz

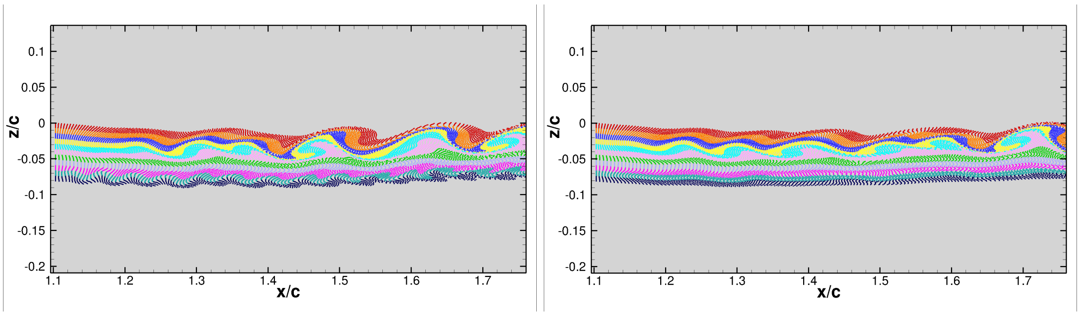

(C) f_a=100 Hz (D) f_a=200 Hz

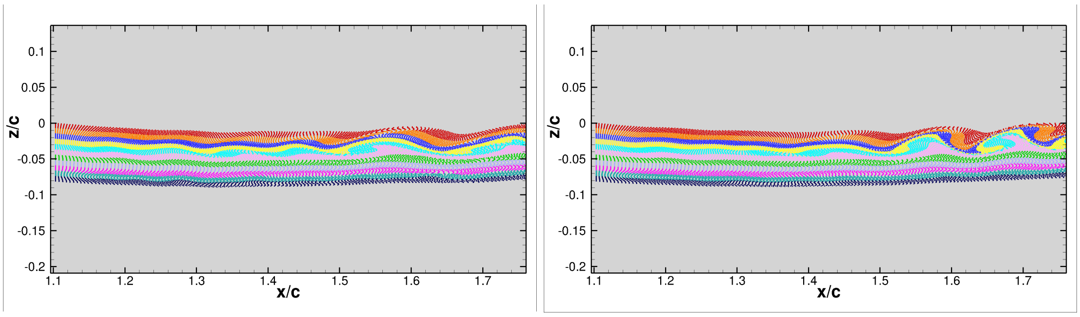

(E) f_a=300 Hz (F) f_a=400 Hz

FIGURE 5.12: Streaklines visualisation for different actuation frequencies at a fixed slight deformation of 0.35mm

again birth to these vortices. Consequently, a vibration at an optimal frequency suppresses and delays this kind of instabilities. This is related directly to a decrease of the predominant modes in the energy spectrum, which are the sources of the aerodynamic noise in the wake, as described in the frequency domain analysis detailed in the next section.

5.4.1.1 Predominant wake frequencies

To study the flow characteristics, a considerable number of snapshots has been saved each at a sampling rate of 10^{-3} second, to investigate the velocity signals at different positions in the near and farther wake. Monitor points in different specific coordinates at x/c = 0.95, x/c = 1.25 and x/c = 1.47 were stored for the static case and different morphing cases at high frequencies aiming to capture the motion of the low frequency instabilities like the von Kármán existing in the wake and their modification due to the vibration. A Power Spectral Density (PSD) is computed for this monitor points signals by means of the Welch's weighted overlapped segment averaging estimator, using Hamming windows with 50 % overlap and zero padding (Welch (1967)) and (Appendix A). Based on our research, this method shows the energy in a frequency domain and exhibits high energy modes related to the predominant instabilities created in the wake.

As previously analysed, a natural predominant frequency f_1 in the range of 10 Hz

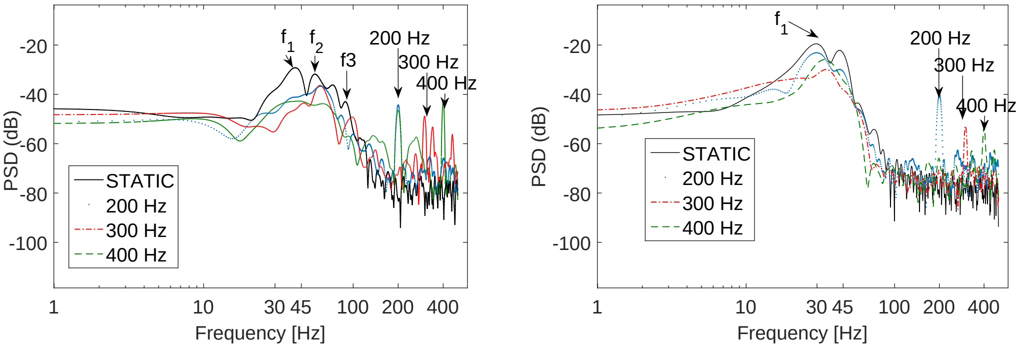

(A) x/C=0.95, z/C=0; (B) x/C=1.25, z/C=0.04

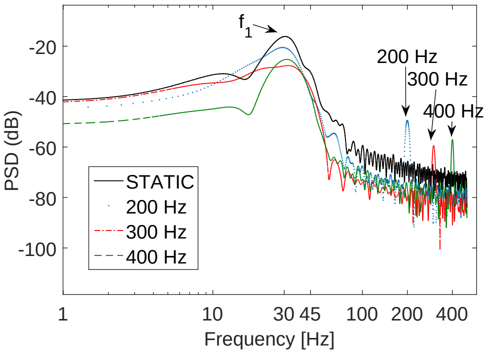

(C) x/C=1.47, $z/C = 0.04$

FIGURE 5.13: Power spectral density of the crossflow velocity for different high frequency actuation cases in the wake.

to 30 Hz was noticed and corresponds to the von Kármán vortex motion presented in figure 5.8. The PSD method illustrates the principal bumps related to this instability and in addition it is followed by f_2 and f_3 corresponding to the shear-layers instabilities in the static case (see figure 5.13a). The morphing at high frequencies of 200 Hz, 300 Hz and 400 Hz with a low amplitude deformation, reveals a diminution of the von Kármán and the shear-layers bumps of the predominant natural frequencies in the 3 positions in the figure 5.13a, 5.13b and 5.13c. Furthermore, peaks at 200 Hz, 300 Hz and 400 Hz are visible and correspond to the frequencies of the trailing edge actuation.

The morphing at higher frequency range introduces new smaller vortices which replace the existing instabilities by means of an eddy blocking effect and consequently generates a reduction and a delay in the formation of the von Kármán vortices. Further in the wake at the position x/c = 1.47 in the figure 5.13c the von Kármán vortices are fully developed and expanded to roll up into a von Kármán vortex street. Hence, the vibrations provide a considerable diminution of von Kármán vortices frequency peaks compared to the static (no vibration) case.

The 300 Hz case at a 0.35 mm amplitude of deformation causes a better decrease of the spectral energy peaks compared to 200 Hz and 400 Hz and can achieve between -10 dB to -15 dB related to the aerodynamic noise. These results match with those in figure 5.12, where the 300 Hz produces a complete disappearance of these instabilities better than the other frequencies and even further in the wake.

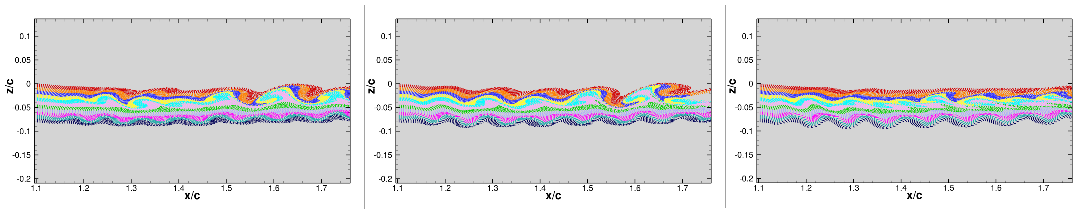

(A) A_m=0.5 mm (B) A_m=1 mm (C) A_m=1.5 mm

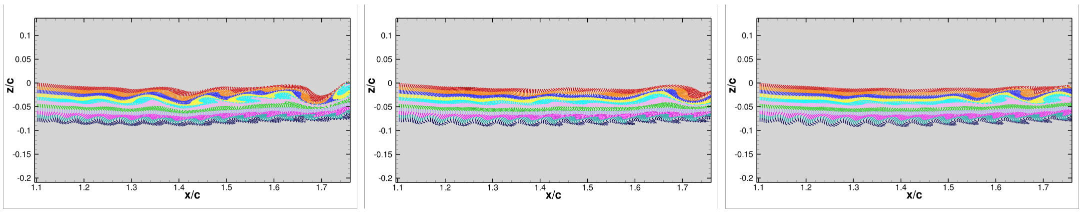

(D) A_m=0.5 mm (E) A_m=1 mm (F) A_m=1.5 mm

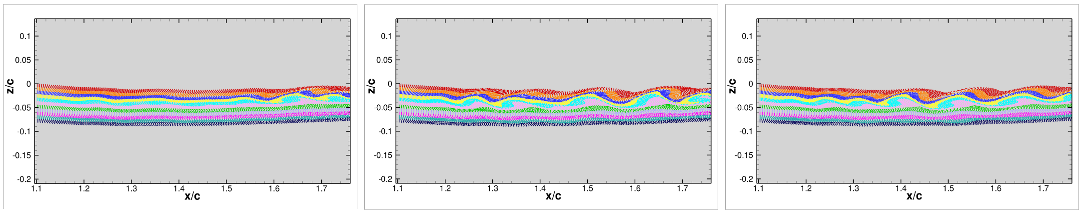

(G) A_m=0.5 mm (H) A_m=1 mm (I) A_m=1.5 mm

FIGURE 5.14: Streaklines visualisation for different actuation amplitudes and frequencies. (*A*), (*B*) and (*C*) f_a=60 Hz; (*D*), (*E*) and (*F*) f_a=100 Hz; (*G*), (*H*) and (*I*) f_a=300 Hz

5.4.2 Influence of the amplitude

The effects of the amplitude are investigated in this section. A matrix of amplitude frequency was necessary to draw the different effects of the trailing edge morphing. A range of higher amplitudes compared to the previous case presented (with 0.35mm) has been selected with actuation frequencies from a lower to a higher range. The figure 5.14 illustrates the 3x3 matrix of amplitude-frequency, where amplitudes of 0.5 mm, 1 mm and 1.5 mm were chosen and frequencies of 60 Hz, 100 Hz and 300 Hz. As mentioned in the previous section, an undulation of the flap's shear-layer is created due to the morphing at lower frequencies than 200 Hz.

In figure 5.14a, 5.14b and 5.14c at a fixed actuation of 60 Hz, when the morphing amplitude increases, the undulation in the flap's shear layer becomes higher and expands in the vertical and horizontal directions. The width of the von Kármán vortices is diminished compared to the static case in the figure 5.8. Furthermore, it is shown in figure 5.14d, 5.14e and 5.14g, that for an actuation frequency of 100 Hz, it appears that the undulation becomes smaller than the previous case, due to a higher trailing edge vibration when increasing the angular velocity. The von Kármán vortices have been moved farther downstream. This is due to the interaction of the airfoil's shear-layer with the von Kármán vortices, and as a consequence their formation and expansion are refrained comparing to the static case. This undulation is formed in the lower shear-layer of the flap and interacts with the upper Turbulent-Non-Turbulent (TNT) interface (Szubert et al. (2015)). The undulation and the TNT interface enclose the von Kármán vortices and decrease their width until they make them disappear.

The morphing undulation dominates the von Kármán vortices in the wake for a higher amplitude case and lower or medium frequencies such as 60 Hz and 100 Hz. However, contrary to the figure 5.14g, 5.14h and 5.14i when the frequency is set at 300 Hz, an increase of the amplitude more than 1 mm reveals the return of the formation of smaller von Kármán vortices.

This investigation of frequency-amplitude helped highlighting optimal behaviours of the flap's trailing edge vibration and its amplitude. when the morphing of the flap's trailing edge has optimal configurations. It can be noted from figures 5.14c, 5.14e and 5.14g are the best cases. As a result, low frequency-high amplitude, medium frequency-medium amplitude and high frequency-low amplitude are the most optimal configurations to suppress the wake instabilities.

5.4.3 Proper Orthogonal Decomposition

The POD of the vertical velocity is computed, the modification of the flow is highlighted when comparing high to low energy modes of the static case in figures 5.15, 5.16 and 5.17 to the cases at an actuation frequency of 200 Hz, it has been shown that the most prominent effects are located in the wake. The time step of the sampling is 10^{-3} sec which is sufficient to capture more than 6 periods of the shear-layer and von Kármán vortices. A constant number of snapshots (300) were used to construct the POD correlation matrix.

The spatial mode 3 (figure 5.15 (a)) and mode 18 (figure 5.16 (a)) of the static case corresponds to the shedding of the von Kármán mode and observed in the PSD of the temporal coefficient (figure 5.15 (c) and 5.16 (c)). The trailing edge vibrations at higher frequency modify the wake and create new modes (figure 5.15 (b)) and (figure 5.16 (b)). The actuations attenuate the von Kármán mode and increases the energy of the chaotic structures (detailed in Chapter 4) which breaks the low frequency turbulent structures through injection of smaller scale structures and produces the eddy blocking effect.

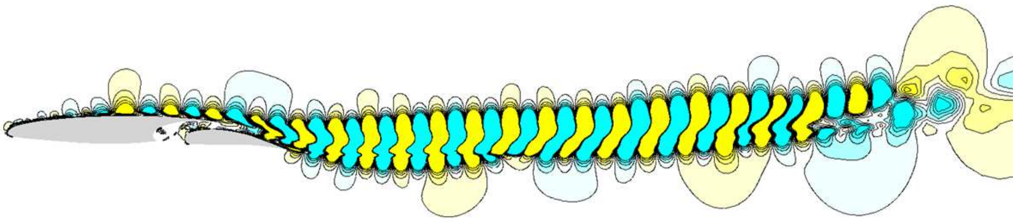

(a) : *w3*

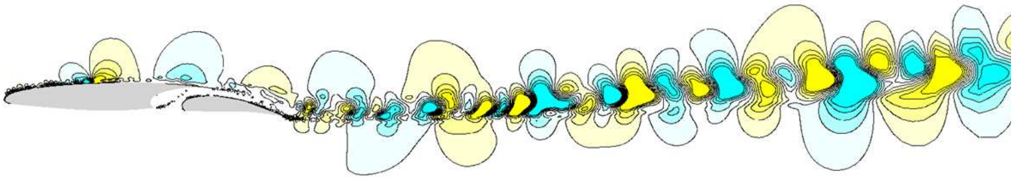

(b) : *w3*

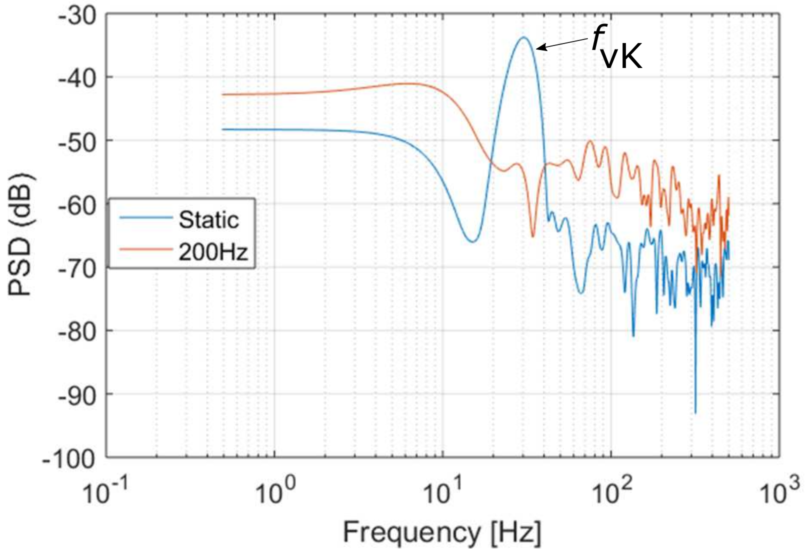

(c) : $\alpha 3$

FIGURE 5.15: POD of the vertical velocity (mode 3). (a) : spatial mode for the static case, (b) : spatial mode for the morphing at 200 Hz, (c) : PSD for the temporal modes

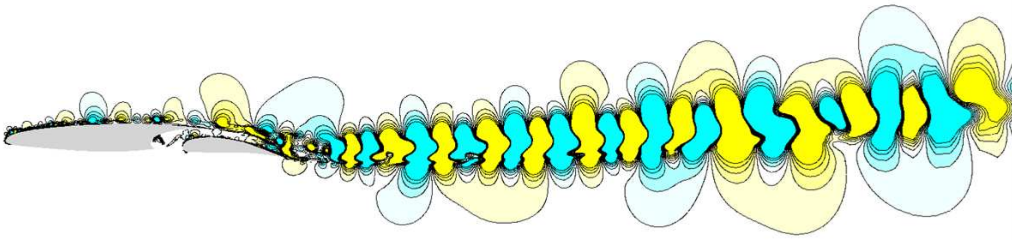

(a) : *w18*

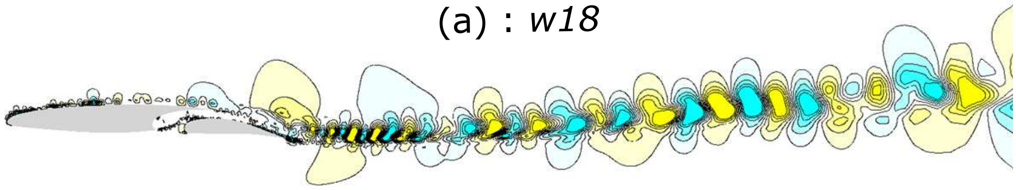

(b) : *w18*

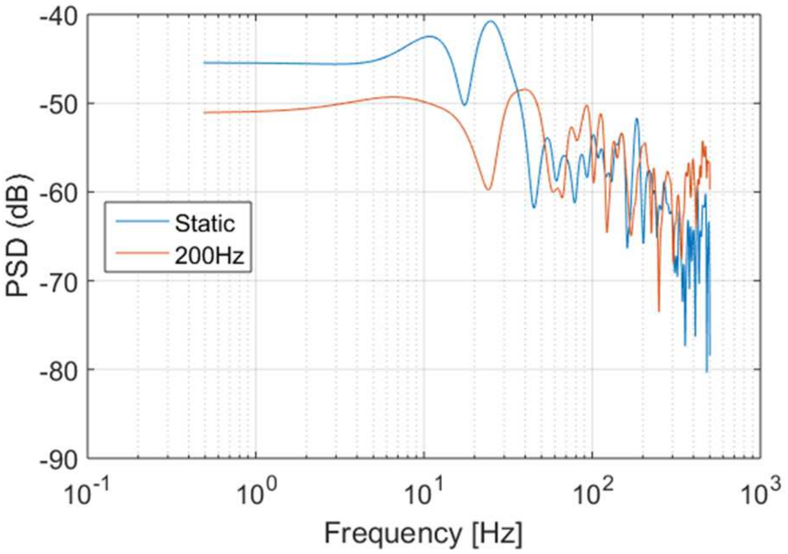

(c) : $\alpha 18$

FIGURE 5.16: POD of the vertical velocity (mode 18). (a) : spatial mode for the static case, (b) : spatial mode for the morphing at 200 Hz, (c) : PSD for the temporal modes

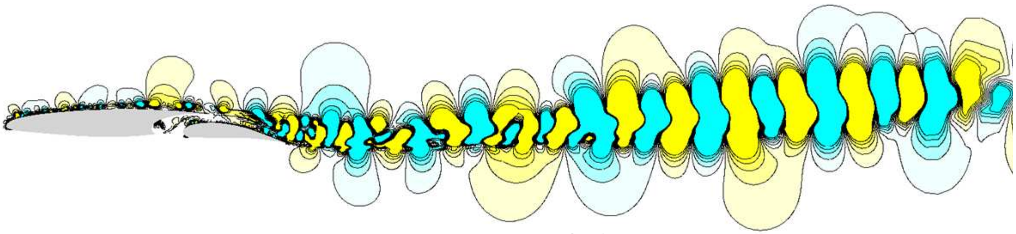

(a) : *w27*

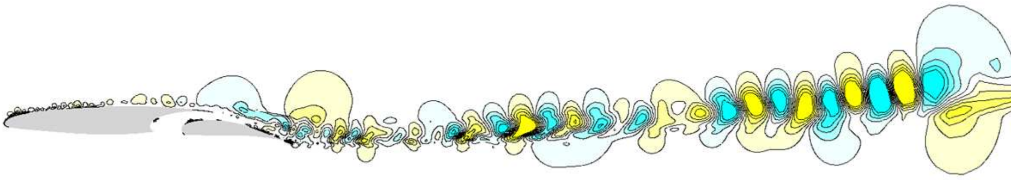

(b) : *w27*

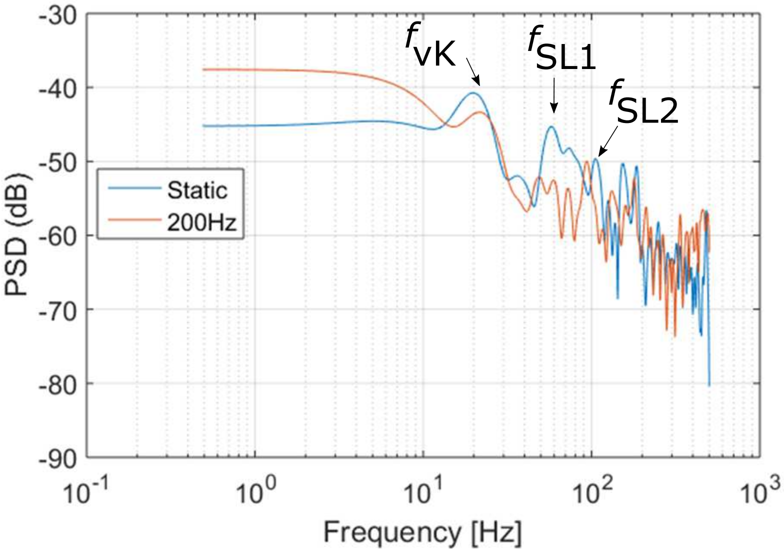

(c) : $\alpha 27$

FIGURE 5.17: POD of the vertical velocity (mode 27). (a) : spatial mode for the static case, (b) : spatial mode for the morphing at 200 Hz, (c) : PSD for the temporal modes

As a consequence, the coherent structures are attenuated and the wake width is reduced. The spatial mode 27 (figure 5.17 (a)) of the static case corresponds to the von Kármán mode and both the wing and the flap shear layers, highlighted in the PSD of the temporal coefficient (figure 5.17 (c)). The morphing interacts with low and high frequencies and attenuates the natural frequencies f_{vK}, f_{SL1} and f_{SL2}.

5.4.4 Effects of the morphing on the aerodynamic forces

An investigation is carried out in order to analyze the morphing effects on the local aerodynamic loads over the wing-flap system. The simulations are performed at the same Reynolds number and angle of attack for the take-off position. The lift and drag forces are computed by means of an integration of the pressure and viscous forces over a wing-flap surfaces. To ensure the statistical convergence of the numerical simulations an acquisition time of 1 s is employed for 100 000 stored points in a converged signal. The figure 5.18a displays the drag coefficient signal from static (no vibration) configuration. The signal corresponds to a chaotic regime due to the high

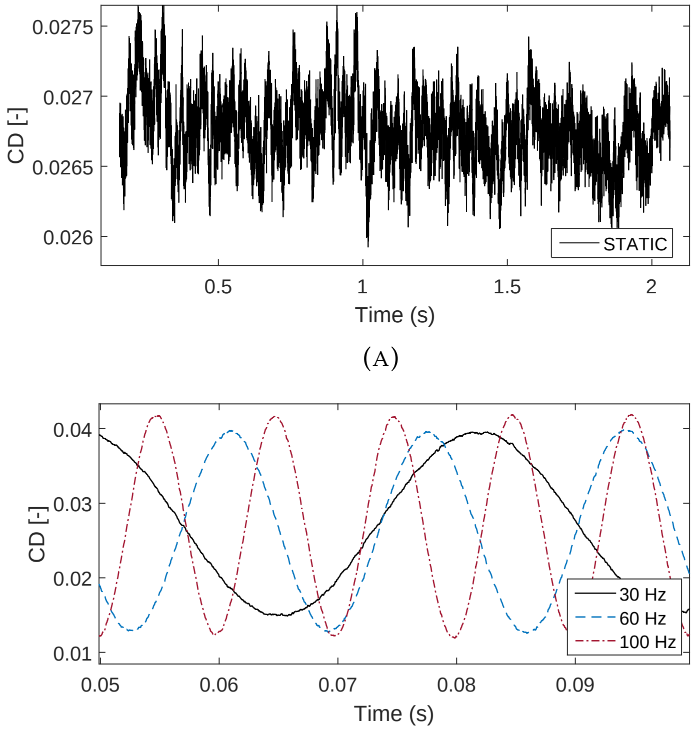

(A)

(B)

FIGURE 5.18: Time series of the drag coefficient. (A) converged static case; (B) morphing at different actuation frequencies

Reynolds number. Irregular fluctuations are captured by the refined grid in the static case where the local minimum cell size is less than 1 mm. However, the morphing in figure 5.18b shows only sinusoidal harmonic actuation frequencies. When the flap's trailing edge is vibrating at a fixed frequency, a lock-in phenomenon appears concerning the natural frequency trained by the actuation frequency. The effects appear on the pressure signal and modifies the mean values of the drag and lift forces.
The morphing introduced either a new undulation of the shear layers or small vortices which replace the existing instabilities and add kinetic energy into the shear-layer which produces a breakdown of the low frequency instabilities, reduces the thickness of the wake and consequently reduce the total drag. The vortex shedding loses its coherence due to the disorganization of the structures in the wake. Through the morphing, this mode is practically suppressed and replaced by a new mode, where the instabilities are attenuated in the upper and lower shear-layers in the case of higher frequency actuations (order of 300 Hz) near the trailing edge of the flap.

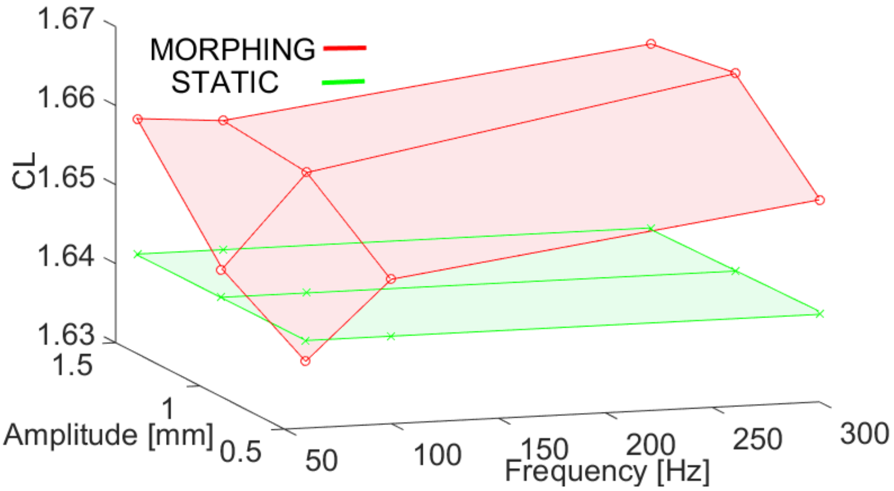

FIGURE 5.19: Mean lift coefficient at the take-off position as a function of different actuation frequencies and amplitudes compared to the static case

TABLE 5.1: Aerodynamic coefficients of the morphing configuration for difference frequency actuations

Frequency of actuation (Hz)	60	100	200	300	400
$\frac{(CD-CD_{static})}{CD_{static}}$ x 100	-1.7971	+0.7532	+1.0664	+2.8859	+1.1857
$\frac{(CL-CL_{static})}{CL_{static}}$ x 100	-0.2918	+0.5797	+0.3465	+0.5529	+0.2557

Compared to the static configuration, the injection of beneficial vortices influences the pressure distribution over the flap and even over the airfoil by means of feedback effect. The lift coefficient CL variation as a function of the frequency in the range of (60 Hz – 300 Hz) and the amplitude actuation in a range of (0.5mm – 1.5mm) is presented in figure 5.19. The best CL is in the higher frequency/higher amplitude range. The effect of high frequencies has already been discussed. The actuation at high amplitudes that means smaller cambering at 1.5 mm corresponds to an increase of the angle of attack of the flap's trailing edge. This can explain the lift increase. An increase of the signal's amplitude has been also noticed together with a higher regularity of the signal's temporal evolution. Another significant effect is that the drag coefficient CD has a small increase when the frequency and amplitudes are higher.

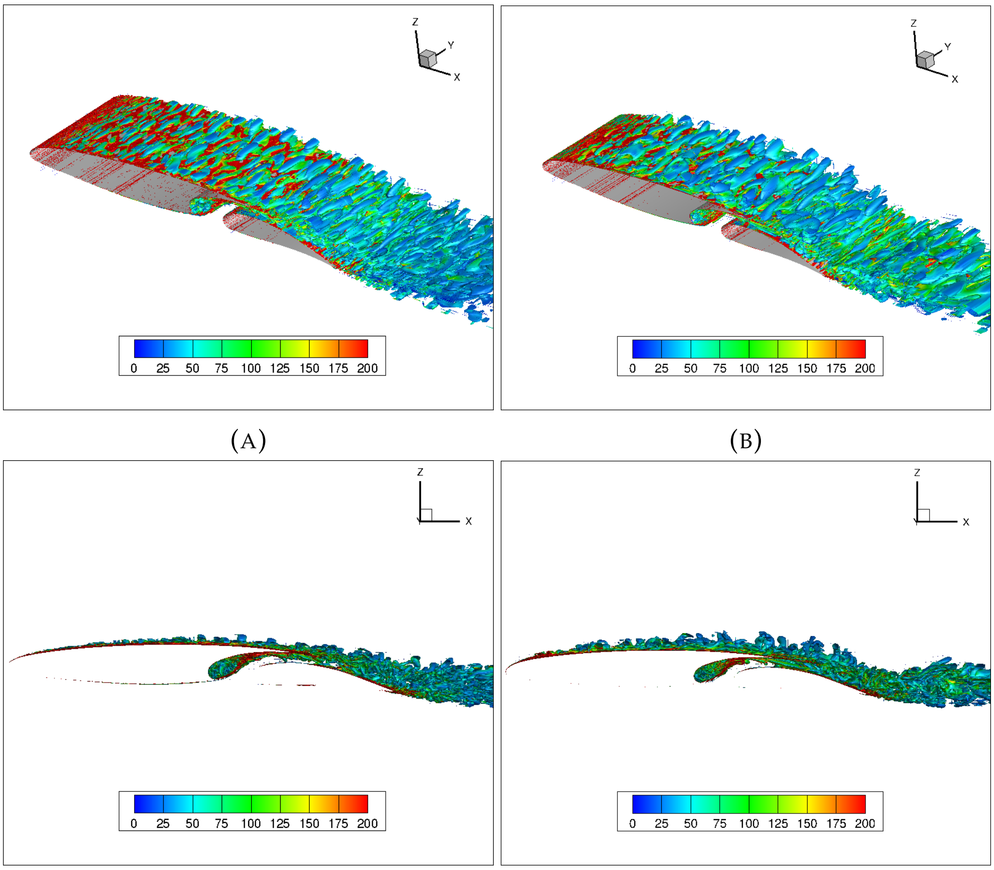

(A) (B)

(C) (D)

FIGURE 5.20: Q criterion (Q=1000) iso-contours, coloured by the velocity magnitude, (A) and (C) : DDES-k- ω SST. (B) and (D) DDES-k- ϵ OES. 3D perspetive view and (x,z) plane taken from the middle section towards the span edge

5.5 DDES-OES Simulations

The design of the DDES grid around the airfoil-flap requires a homogenous local grid cells with $\Delta x \approx \Delta y \approx \Delta z$ in order to ensure a correct evaluation of the l_{DDES} scale and to provide a physically appropriate passage from the URANS towards the LES region. It is worth mentioning that in case of large Δy, the choice of the C_{DES}.max(Δx, Δy, Δz) length scale used in the LES region (see Chapter 3), would be systematically chosen as a function of the Δy and this would result to a "DNS-like" computation everywhere. Two different hybrid models DDES-SST and DDES-OES have been chosen to simulate the flow around the LS wing-flap configuration (figure, 5.20) using a grid of 30 million cells approximately with a spanwise of 0.11C (40 cells in the span direction).

To illustrate the flow regions, figure 5.20 provides a view of the turbulence structures visualized by the iso-surfaces of the Q criterion coloured by the dimensional velocity magnitude above the wing and in the wake by means of the DDES-SST and DDES-OES. The DDES-SST shows less solved turbulent structures compared to the DDES-OES which generates relatively large structures. This is caused by the modification of the constant C_μ for the OES model in the URANS region which predicts the behaviour of the boundary layer detachment. In addition, (Bourguet (2008)) have shown also that a DES based on the OES revealed better approximation to experimental results around a cylinder than a DES based on the SST model (explained in chapter 3).

Figure 5.21 presents the static and the morphing configurations for the three-dimensional simulation using the OES-DDES hybrid model. The Q criterion fixed at the value of 1000 and coloured by the velocity magnitude contours represents small scale turbulent structures captured by the LES model highlighted in global 3D view in figure 5.21 (a). The formation of three-dimensional wake structures of the flow is presented through the spanwise in figure 5.21 (b) near the flap's trailing edge. The spanwise velocity is amplified when the Reynolds number is higher, this leads to the appearance of the secondary instability of the vortex rows. Moreover, vortex dislocations are formed illustrated by a junction of the 'spinal column' (of two adjacent vortex as has been studied by DNS in (Braza et al. (2001)) in the low Reynolds number range). However, the high-frequency low-deformation morphing modifies the flow behaviour in the same region. It is found that an actuation at 300 Hz and amplitude of 0.7 mm practically suppresses the secondary instability and the vortex dislocations due to the same reasons analysed through elliptic instability theory for the clean configuration

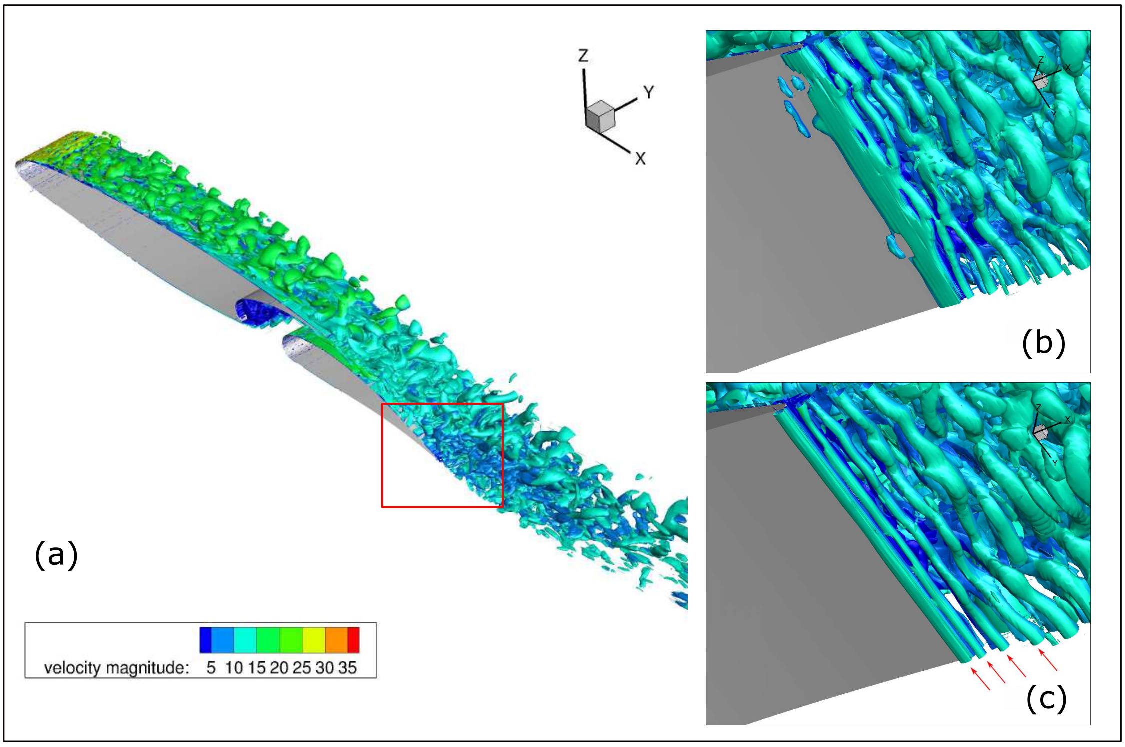

FIGURE 5.21: Q criterion (Q=1000) coloured by the velocity magnitude for the Large-Scale prototype at the take-off position using the OES-DDES turbulence model. (a) Three-dimensional view of the static. (b) static, illustrating coherent vortex rows with vortex dislocations. (c) morphing with 300 Hz vibration and slight trailing edge deformation: attenuation of the vortex dislocations and of the three-dimensional effects in the morphing configuration

of the RS prototype (Chapter 4, Section 4.5.3), resulting to a considerable wake thinning in figure 5.21 (c). The generated smaller vortex rows created by the vibration interact with the shear-layer and create an eddy blocking effect, which helps to make a thinner wake. Moreover, it contributes to attenuate the noise sources in the energy spectrum in figure 5.13 through the attenuation or diminution of the shear layer instabilities and modification of the pressure distribution over the flap by feedback effects. This leads to a considerable modification on the aerodynamics loads with significant benefits, this expects considerable benefits in the performances as presented in the previous section. The time of the computations prevented us from calculation of these benefits during a significant observation time.

5.6 Conclusion

This chapter highlights the morphing effects on the wake dynamics and the aerodynamic forces of a fixed span A320 high lift configuration containing two-elements wing and flap. The numerical simulations of the Large-Scale (LS) prototype of the SMS European project have been investigated and discussed with respect to experimental data of IMFT in the clean and the take-off configurations for $Re = 1 \times 10^6$, 2.25×10^6 and angles of attack of $0°$, $8°$. Afterwards, the numerical configuration was set in the take-off position to investigate the morphing effects for a high-lift wing-flap configuration. A detailed examination of the flow around the wing-flap system and a wake analysis of the turbulent structures is provided. The morphing is then activated in the flap's trailing edge actuating at high frequency vibration-low amplitude deformation. Effects of the dynamic vibration reveal a suppression and delaying of the von Kármán vortices formation in the wake after a detailed investigation of a frequency and amplitude of actuation domains. In addition, the spectral analysis revealed a significant reduction of low frequencies instabilities and obtained approximately 15 dB of noise reduction in the predominant frequency peak. Finally, the dynamic morphing improves the aerodynamic lift compared to the classical static system through a vortex breakdown of largest coherent structures and enhancement of good vortices. The aerodynamic lift is increased up to +0.55% for high frequency actuations with a total gain obtained in CL/CD efficiency of **+2%**

F

Chapter 6

Morphing of the high-lift system using cambered flap

This chapter presents the efficiency of morphing based on cambering of the flap. Novel optimal shapes are studied in respect of the aerodynamic performance increase. The cambering shapes are the same as in the experiments and the dynamic cambering follows a similar camber control law as in the experiments of the SMS project. Series of Electro-Mechanical Actuators EMA implemented inside the flap to achieve high amplitudes of deformations at low frequencies. Quasi-static and dynamic cambering are investigated based on a parametric study of Reynolds numbers, angles of attack and different camber positions.

FIGURE 6.1: $(left)$: morphing flap assembling structure in the workshop laboratory of INPT/IMFT $(right)$: detailed CAD view of the EMA

Contents

6.1 Introduction

Observing how birds can fly has been the subject of scientific interests for many decades bio-inspired design to improve performances and reduce the noise of the wing devices. An interesting study (Lawley et al. (2019)) aimed at characterising the structure of real owls flying and the near wake dynamics by means of long-duration PIV in a wind tunnel at a speed of 8 m/s. The study revealed that the near wake of the owl compared to other birds did not exhibit any apparent shedding of organized vortices but more chaotic patterns. The owl manipulates the near wake dynamics and suppresses the aeroacoustic signal through the control of small scale vortices (this was investigated in chapters 4 and 5). More recently, the same research group has regrouped the shapes of kinematics of the owl during the flight and implemented a numerical model in their CFD house code with the same behaviour as a real owl. Owl dynamics was investigated through their CFD analysis. It was shown that the lift signal is periodic and increases when the wing of the owl is cambered while the drag is maintained fixed instead of increasing, despite the more bluff body of the wing's configuration, thanks to an optimal cambering shape. This allows an increase of the aerodynamic efficiency. The wing leading-edge is oriented smoothly downwards allowing a better attachment of the boundary layer and the trailing edge region is cambered in order to decrease the pressure. This mechanism shows that owls have the ability to increase their aerodynamic performances with appropriate cambering and simultaneously to not produce aerodynamic noise as other birds.

However, One should take into account that birds can not fly at the same speed as airplanes. There is a need to find a new technology in a similar way as the owl wings in order to increase aerodynamic efficiency, simultaneously decrease the aerodynamic noise and designed for high speed flying.

As known, the Airbus A320 high lift flap is not deformable. Thanks to an hydromechanical system that comes out from the clean configuration at a specific deflection angle, thus creating a "cambered" overall shape with a gap, comparing to the clean configuration.

In the present study, a new morphing design is introduced through optimal cambering of the flap in static and dynamic operation. The present chapter analyses the benefits in the aerodynamic performance obtained through this new design.

The morphing flap is based on an articulated rib where actuators control the rotations of the elements around the hinges (Jodin et al. (2018)). The proposed concept is presented in figure 6.2.

This concept is based on articulated ribs that have to resist to aerodynamic forces, hinges allowing the rotation of the articulated ribs, the actuators responsible for the shape control and finally the skins or covering devices ensure a smooth shape during the cambering.

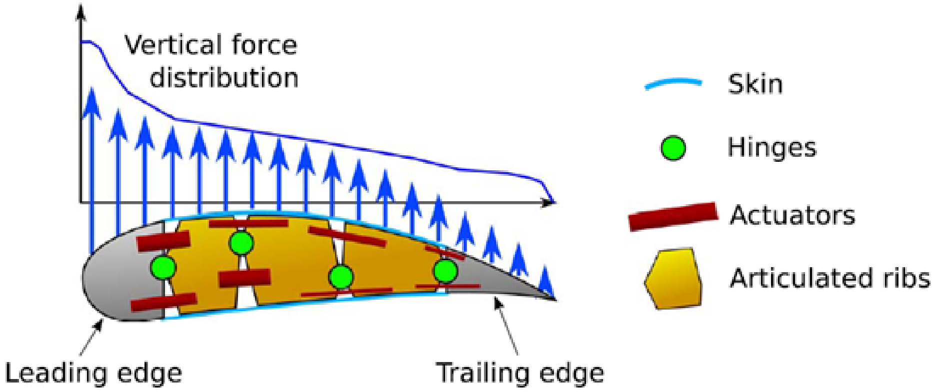

FIGURE 6.2: Mechanism of the articulated flap (Jodin et al. (2018))

A flap was designed and constructed based on a new mechanism of dynamic cambering of the LS prototype (Giraud et al. (2019)) using innovative Electro-Mechanical Actuators (EMA) in the context of the SMS project (`http://smartwing.org/SMS/EU/`). Series of these actuators were interconnected to achieve high cambered position in synergy with the numerical simulations. The model was designed and constructed in a real flap by (Bmegaptche et al. (2019)) in the workshop of IMFT, in collaboration IMFT-LAPLACE Laboratories with the contribution of *D.Harribey*. The EMA were studied from the electrostructural point of view by (Giraud et al. (2019)) in NOVATEM Company, partner of the SMS project. A first set of experiments has been carried out in the S1 wind tunnel of IMFT. Unsteady pressure measurements were conducted using new piezoresistive pressure transducers with sampling rate (order of 2-5 KHz) acquisition allowing the measurement of pressure fluctuations. In chapter 5, we compared through spectral analysis the experimental and numerical signals and found a good agreement in terms of predominant frequencies.

The objective of this chapter is to investigate the aerodynamic performances concerning the LS prototype of the SMS project, the computations have been done in 2D in a first step, followed by simulations over the Airbus A320 real configuration in a second step. The NSMB solver is used for all the computations. The dynamic camber is handled through the ALE (Donea et al. (1982)). The numerical cambering does not take into-account the electro-mechanical properties but considers the shapes as boundary conditions for the CFD computations. The final deformation of different cambered positions is similar as in the experiments (figure 6.3), thus achieving

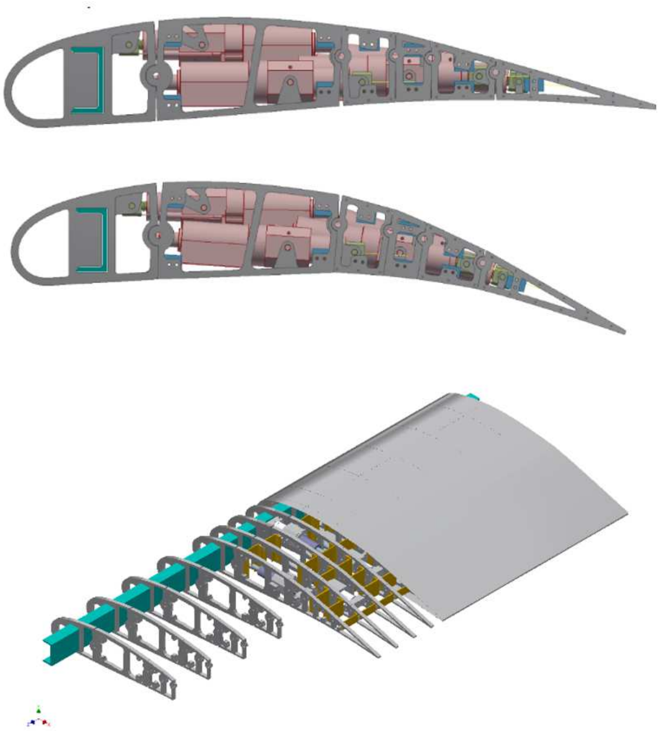

FIGURE 6.3: The proposed design of the real scale A320 flap including the Electro-Mechanical Actuators for the camber deformation

static and dynamic camber deformation of the flap, whose trailing edge reaches 10 cm downwards. A first set of 2D simulations was selected to investigate the optimal behaviours and then extended to the 3D A320 airplane containing different parts.

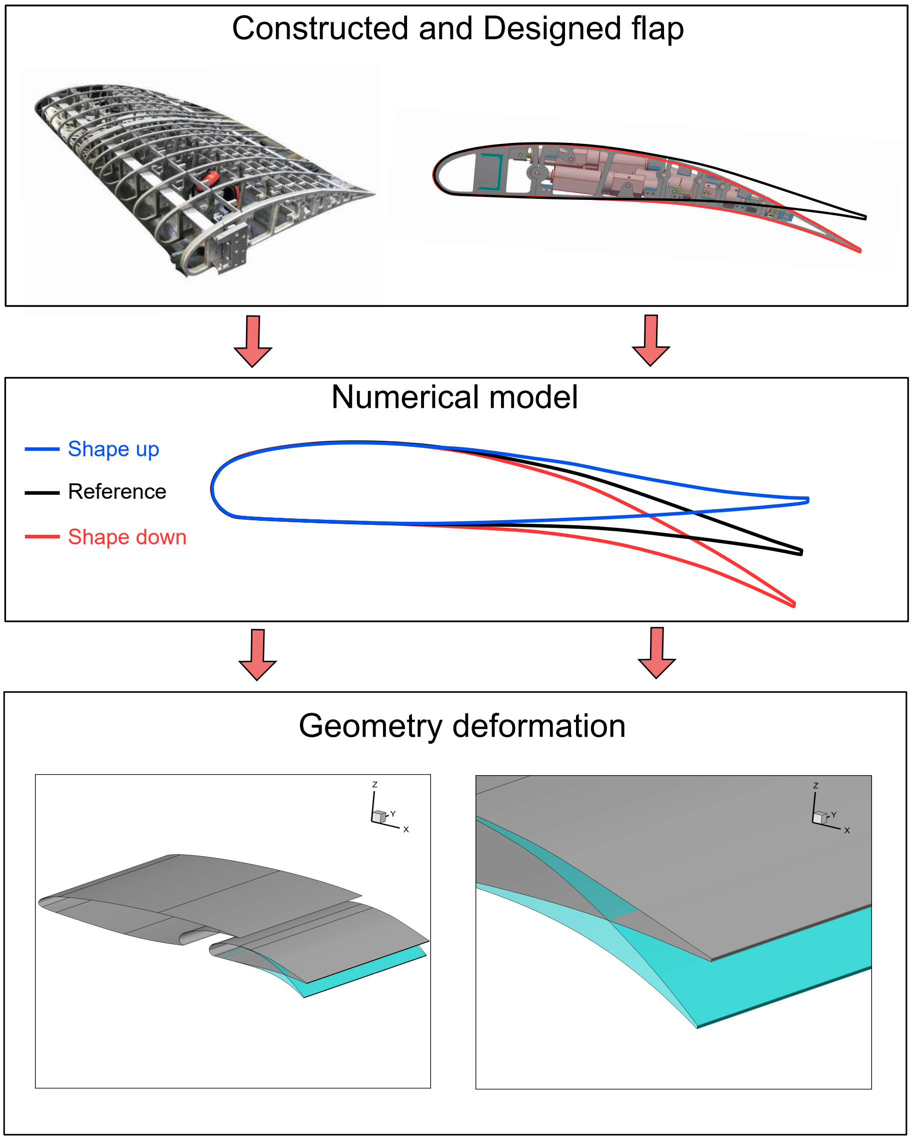

FIGURE 6.4: Quasi-static camber control of the A320 flap similar to the EMA behaviour

6.2 2D simulations of the LS prototype

6.2.1 Numerical model of cambering

The experimental configuration is based on an innovative concept of a morphing flap *near full scale* during the take-off and landing flight phases. The flap has 1 m chord in a wing-flap configuration of 2.40 m total chord. In take-off position, the overall chord is 2.72 m. The spanwise length is of 4 m and 2 m regarding two different wind tunnels, the one at Polytechnic of Milano and the other, the S1 wind tunnel of IMFT, respectively. The flap, having a 2 m span, contains a series of EMA able to make a dynamic camber control. This achieves high deformations up to 10 % of the flap's chord in the downward and upward directions with 85 % deformation from the trailing edge to the leading edge of the flap. This high-lift system has proven to be able to resist the aerodynamic pressure forces in different camber positions. The LS wing-flap system is tested in the $POLIMI$ and $IMFT$ wind tunnels using PIV and forces measurements.

In figure 6.4 the experimental and designed shapes of the cambered flap are extracted, implemented in the numerical model and successfully tested for the flap of the LS prototype. In the context of the SMS project only downward cambering has been investigated and will be presented in the next section. In figure 6.5, different cambered positions from low to high deformations are computed and compared to the reference flap. The maximum deformation reaches 10 cm. The main objective is to identify the optimal shapes of deformation in order to increase the aerodynamic efficiency.

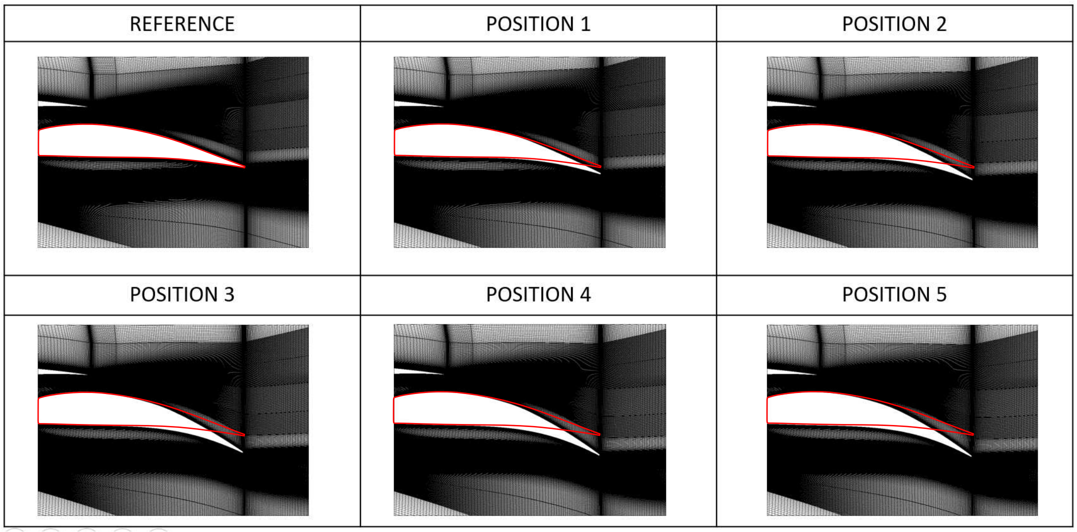
REFERENCE
POSITION 1
POSITION 2
POSITION 3
POSITION 4
POSITION 5

FIGURE 6.5: Different quasi-static cambered positions of the flap

6.2.2 Numerical and physical parameters

The simulations were carried out with the NSMB solver. The same numerical parameters as previously are considered because of the same flight stage in the take-off phase at low Mach number (as in the chapter 5). Far-field boundary conditions using Riemann Invariants have been selected in 2D simulations. Different Reynolds numbers and angles of attack associated with multiple cambered positions were selected following table 6.1 corresponding to the take-off configuration.

The OES modelling has been used for the 2D simulations to better capture and analyse the wake instabilities with emphasis to the coherent structure dynamics.

-	Re	α	Camber positions
2D	2.25M, 7M	0°, 2°,4°,6°,8°	P1, P2, P3, P4

TABLE 6.1: Set of different physical parameters employed in the numerical study

6.2.3 Dynamic cambering model

The numerical model implemented in the NSMB code allows a flap's deformation very close to the experimental configuration by using a 3rd order polynomial equation. This study allows determining the best optimized cases concerning the deformation in order to obtain an increased aerodynamic efficiency.

The algorithm for the wing's deformation and grid cells displacement was explained previously (chapters 4 and 5) by using dynamic trailing edge vibrations following a sinusoidal law, adapted in the case of the MFC piezoelectric patches. A new algorithm is used for the EMA in the flap. The deformation will achieve a desired cambered position then stops in a smooth way.

To avoid numerical perturbations on the aerodynamic forces, the Newton method is used to calculate the incremented displacement dz following an exponential law in equation 6.1.

$$\begin{cases} If \quad x > x_c & ; \dfrac{dz}{dt} = -f(z).K.e^{-2.\pi.K.t} \end{cases} \tag{6.1}$$

X_c is the coordinate where the cambering starts, $f(z)$ is the 3rd order polynomial and K is a camber accelerator coefficient that controls the speed of deformation.

This method ensures a smooth and small displacement that is computed at each time step. This is well adapted to the deformation and similar to the experimental control law for the cambering of the LS prototype, developed by the ONERA in the context of the SMS project. The numerical cambering in the present study is accomplished in 2 sec of simulations compared to the experimental cambering where the time scale is of 1 min (30 times slower than the simulations). The objective in this work is to study the physical mechanisms leading to the increase aerodynamic performances within reasonable simulation times before to go towards full time-scale cambering for the simulations too.

6.2.4 Results

6.2.4.1 Numerical and experimental results

Numerical results of the dimensionless velocity magnitude are compared with experimental PIV results obtained by POLIMI in the SMS project. The LS prototype is mounted in the POLIMI wind tunnel (presented in chapter 2, figure 2.11), where a matrix of parameters has been set for both take-off and landing configurations. In parallel, a new model has been developed to obtain approximate results as in the experimental environment.

Different speeds have been tested in experimental measurement. A velocity of 34 m/s is selected to compare the mean fields of results. The PIV window is located at the end of the flap and starts at 85%, to capture the cambering effects, the boundary layer separation and the near trailing edge dynamics. The same conditions are chosen for the 2D numerical computations. In figure 6.6, three different angles of attack 4°, 6° and 8° were compared for the reference case in the take-off position. The velocity behaviour is similar in both numerical and experimental results, the velocity is decreased in the wing and the flap shear layers and the deficit is approximately the same. The dimensionless velocity reaches 1.15 in the suction side of the flap where the flow is accelerated. In the flap shear layer, the velocity deficit is very close in both configurations for all angles of attack. The numerical model predicts very well the near trailing edge region. The blue region in figure 6.6 (f) corresponds to the separation of the boundary layer due to the higher angle of attack in experiments. In numerics, the flow appears less separated due to several reasons.

The experimentations are 3D contrary to 2D simulations. The flap has 2 m of span and the wing has 4 m, there is an existence of discontinuities between them. A longitudinal recirculation is then created and observed in a similar study of (Abdessemed et al. (2018b)). This last modifies the thickness of the boundary layer and may lead to

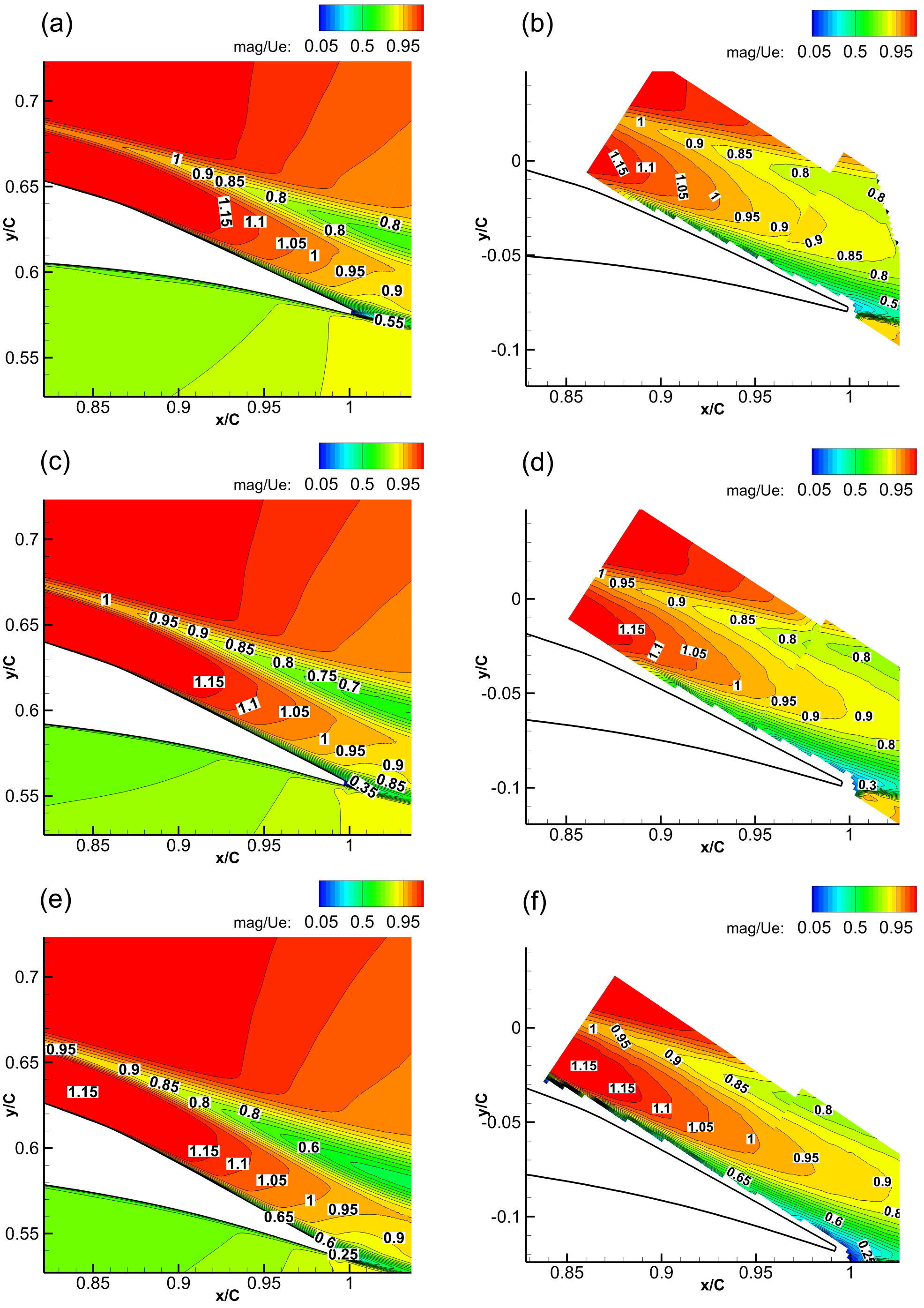

FIGURE 6.6: Dimensionless velocity magnitude of numerical and experimental PIV results for different angles of attack. $(left)$: numerical. $(right)$: experimental. (a) and (b) : 4°, (c) and (d) : 6°, (e) and (f) : 8°

the separation at an earlier stage. In addition, in 2D simulations a smooth surface is considered that induce a thinner boundary layer compared a the real flap which has some roughness.

Figure 6.7 presents a comparison of numerical and experimental results at a camber position 1 (3 cm of downward deformation) at two different angles of attack 4° and 8°. The dimensionless velocity achieves 1.15 in all the cases as a maximum value and its variation is almost the same in all the locations. The wing and flap shear layers are well represented by the numerical model. The velocity deficit in the flap's shear layer is approximately the same in both configurations. However, the boundary layer is separated near the trailing-edge in the experimental measurements in figure 6.7 (*d*) due to higher angle of attack 8° coupled with the camber position 1 in the downward direction which increases the deflection angle of the flap.

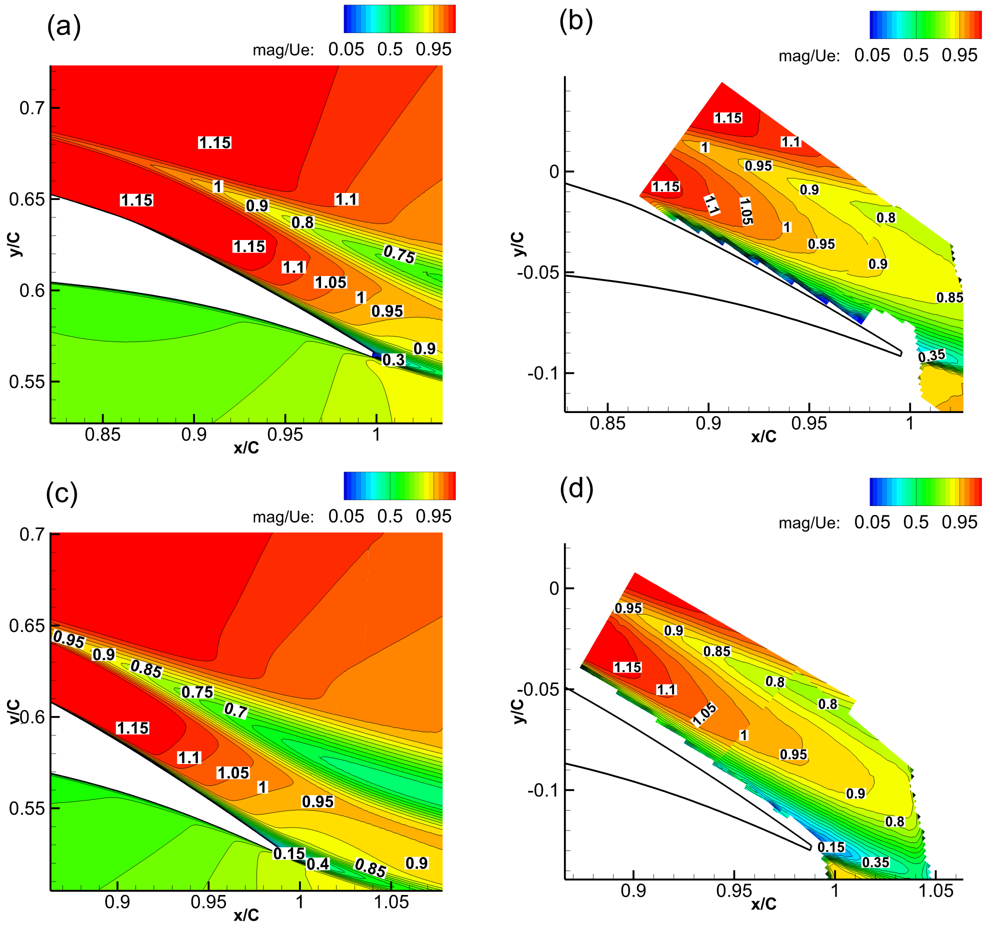

FIGURE 6.7: Dimensionless velocity magnitude of numerical and experimental PIV results for different angles of attack at camber position 1. (*left*) : numerical. (*right*) : experimental. (*a*) and (*b*) : 4°, (*c*) and (*d*) : 8°

Shape-measurements due to the fluid-structure interaction were conducted in POLIMI to evaluate the displacement of the flap surface as a function of the speed with respect to the zero-displacement condition at zero velocity. A maximum load case is considered in the take-off configuration at 8° with camber of 10 cm. The results have shown the displacement of the flap along the span is negligible and only the cases of maximum aerodynamic load reports that deformations are quite small in the vertical and longitudinal directions. Based on these results, the numerical model is simplified and does not take into account the electro-mechanical properties of the EMA.

6.2.4.2 Quasi-static approach

A quasi-static approach is used applying the different cambered positions derived from (Jodin et al. (2018)) in the range of [1-10] cm concerning the downwards trailing edge location in 2D simulations for the LS prototype in take-off configuration in the SMS European project. This approach allows a fast and physical analysis of the cambering effects for different Reynolds numbers and angles of attack. Two different Reynolds numbers of 2.25 and 7 Million in a range of angles of attack [0° - 4°] have been selected. The grid of 0.6 M points presented in zoom in figure 6.5 provides y+ values less than one. This ensures a correct behaviour of the turbulence damping towards the wall through the modified f_μ damping function according to the OES k-ϵ modelling (chapter 3 , equation 3.34). As will be discussed in the results, this modelling method together with the present grid and numerical parameters (time step, size of the domain) ensure a correct development of the flow unsteadiness, of the boundary layer and separated shear layers development.

Figure 6.8 shows the averaged wall CP coefficient related to the different cambered

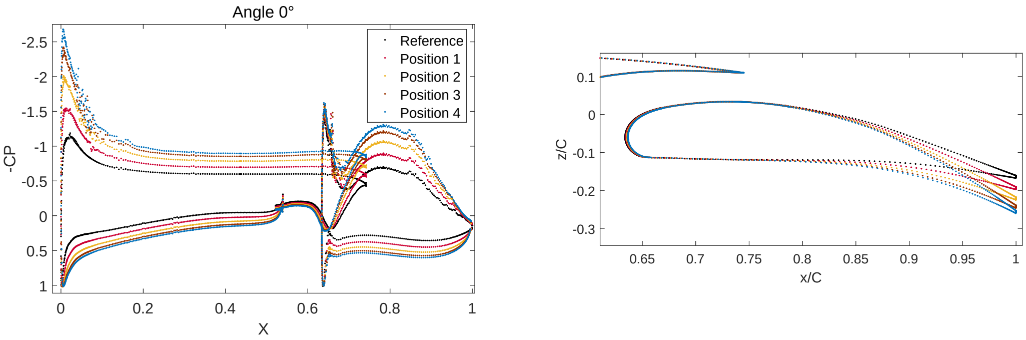

FIGURE 6.8: Pressure coefficient of different quasi-static positions of the flap compared to the reference baseline configuration

positions of the flap at 0° angle of attack. The cambering increases the deflection angle of the flap that leads to an increase of the pressure difference. The flap is not the only

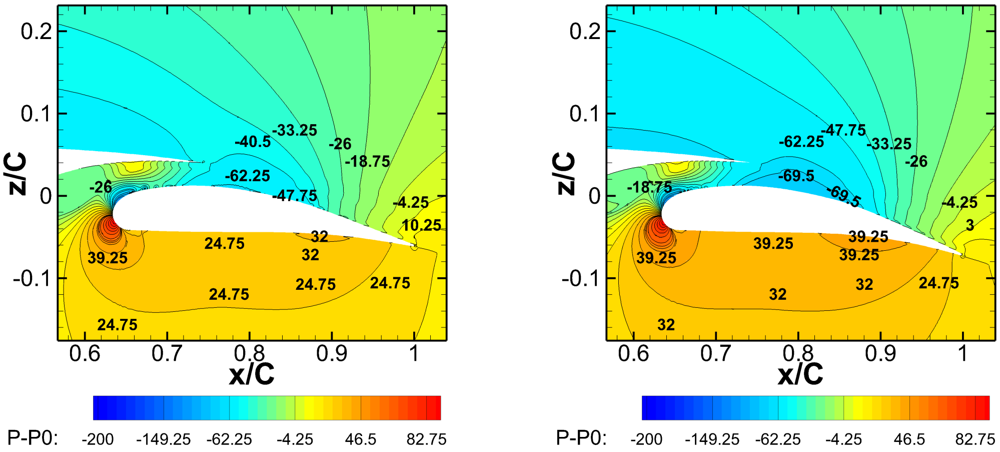

(A) Pref (B) P1

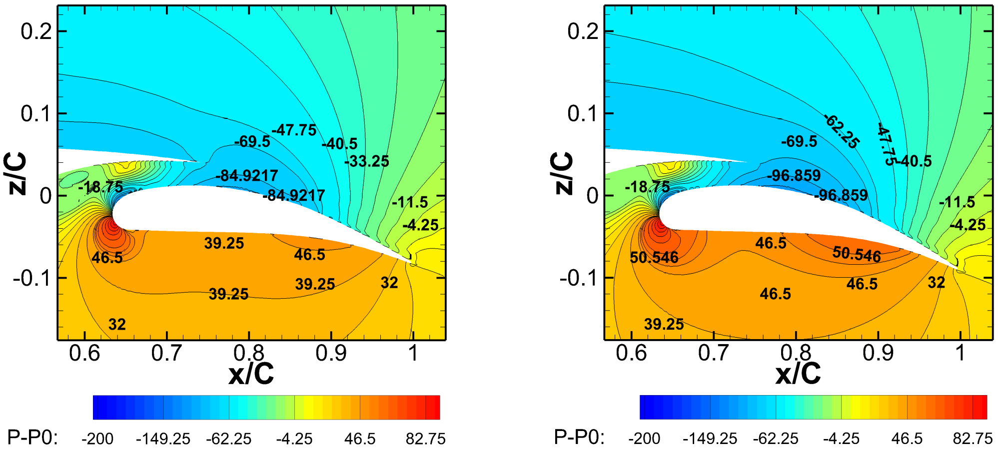

(C) P2 (D) P3

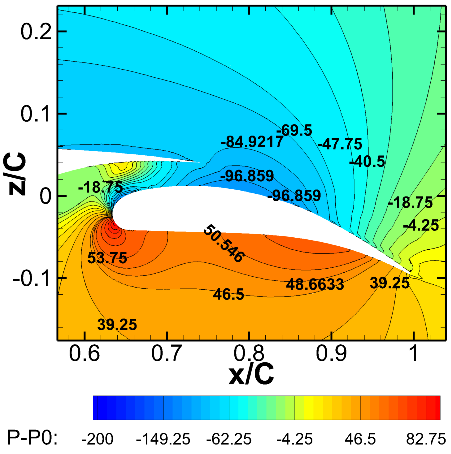

(E) P4

FIGURE 6.9: Pressure distribution of the flap in different camber positions

affected through this modification, but also a feedback is noticed in the wing surfaces up to the leading-edge. A considerable increase of the pressure difference is created between the section and the pressure sides of both the wing and the flap.

Figure 6.9 corresponds to the different camber positions and compares the pressure difference $p - p_0$, where p_0 is the standard pressure of the air to the reference case in figure 6.9 (a). The $p - p_0$ increases gradually from the leading edge to the trailing edge in the pressure side when the flap is cambered downward. Simultaneously, in the suction side the pressure decrease varies gradually from -62.25 Pa in the reference position up to -96.859 Pa in the position P4.

The increase of ΔP corresponds to an increase of the produced lift force around the flap surface. The mean aerodynamic forces for the different cambered positions are calculated for the selected angles of attacks corresponding to the take-off configuration. It is recalled that in this case, the fixed part of the wing has the incidence of 8° and the flap in the conventional design (e.g. without cambering) takes deflection of 10°.

Table 6.2 and 6.3 shows the relative gain (%) on the lift-to-drag ratio for different cambered positions between 0° and 6° degrees for Reynolds numbers 2.25 Million and 7 Million. Associating the cambering in the flap leads up to 24% gain on the aerodynamic performances. It has been found that for the case of Re=2.25 M regarding position 2 at angle of attack 4°, the cambering leads to a loss, whereas at Re=7 M it gives better lift-to-drag ratio. Higher cambered positions associated with high angles

α	P1 = 30%	P2 = 60 %	P3 = 85 %	P4=100 %
0°	+12.79	+20.00	+24.51	+24.25
2°	+ 5.79	+ 8.10	+ 8.03	+ 5.0211
4°	+ 0.88	-2.466	-6.01	-9.33
6°	- 4.36	-12.16	-15.69	-19.28

TABLE 6.2: Lift-to-drag ratio gain in (%) of different cambered positions compared to the reference baseline at a Re = 2.25M

α	P1 = 30%	P2 = 60 %	P3 = 85 %	P4=100 %
0°	+13.76	+20.67	+22.67	+22.74
2°	+7.97	+10.35	+10.79	+10.41
4°	+3.26	+2.63	+1.21	+ 0.21
6°	- 1.00	-3.32	-7.03	-10.73

TABLE 6.3: lift-to-drag ratio gain in (%) of different cambered positions compared to the reference baseline at a Re = 7M

of attack lead to a separation of the boundary layer inducing a recirculation near the trailing edge. This increases the shearing between the lower surface of the flap and the flow and enhances the formation of more predominant shear-layer instabilities as the Kelvin-Helmholtz and von Kármán vortices. A considerable increase of the drag was observed in these configurations due to the increase of the wake thickness which explains the loss in the lift-to-drag ratio.

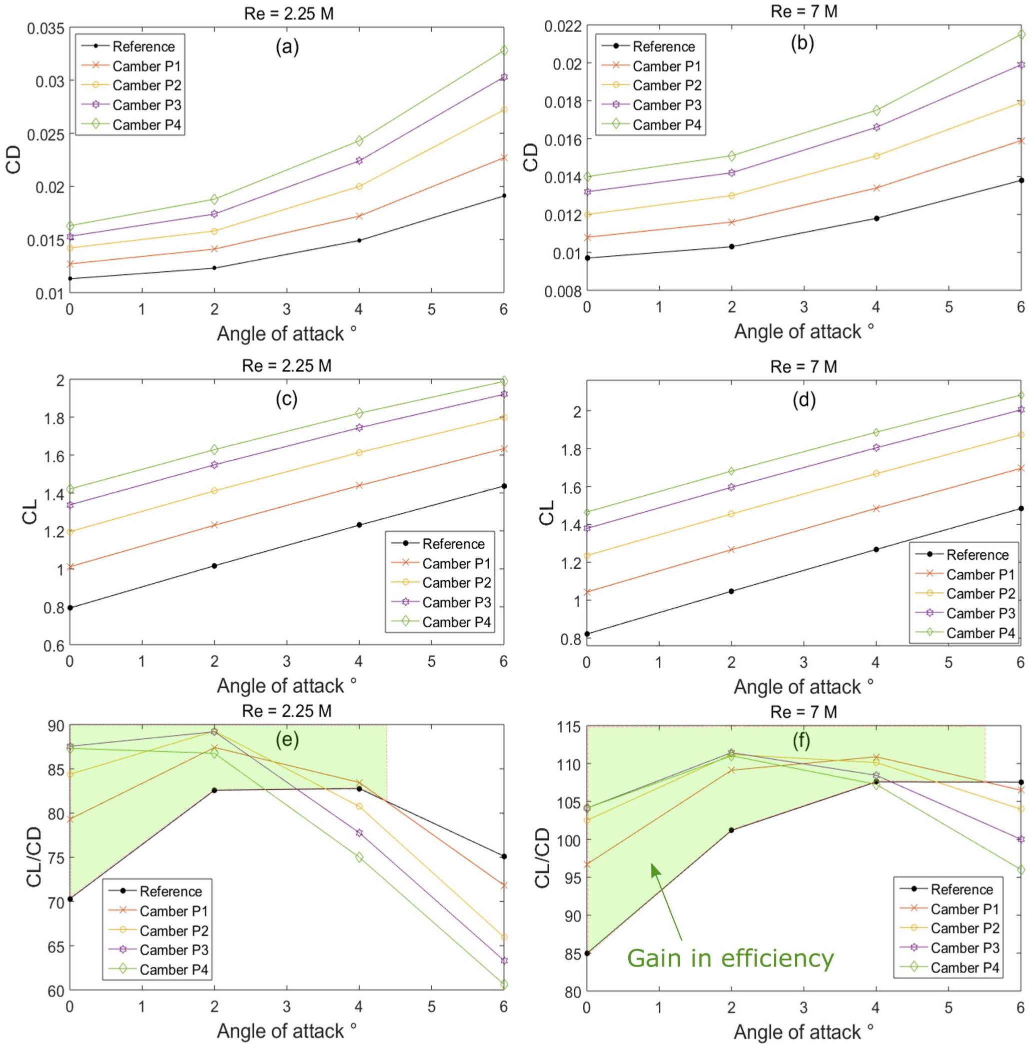

FIGURE 6.10: Comparison of the lift-to-drag ratio of the first cambered position at 4° with the reference baseline at 8°

For higher Reynolds numbers, the boundary layer is more turbulent and more energetic because of the supercritical regime. This prevents or delays the flow detachment near the flap's trailing edge when the flap is cambered at high positions and set at high angles of attack. The drag is less sensitive to the cambering at high Reynolds numbers which leads to improve the lift-to-drag ratio as seen in table. 6.3.

In figure 6.10 the drag, lift and lift-to-drag ratio are presented for both Reynolds numbers and the selected cambered positions. The drag increases for high cambered positions and for high angles of attack. It follows a non linear growth when the angle of attack is higher in particular for 6 ° as in figures 6.10 (a) and 6.10 (b). For higher Reynolds the drag is maintained less than 0.022 for all the cases. But for lower Reynolds, the drag increases towards 0.0325. In the other hand, the lift shows a linear evolution with the cambering and the angle of attack in both Reynolds numbers (figures 6.10 (c) and 6.10 (d)). An improvement of the lift is obtained for all the cambered cases. In figures 6.10 (e) and 6.10 (f), the aerodynamic efficiency CL/CD is presented. The green colored area presents the gain of the cambering when the angle of attack is increased. For high Reynolds number this area is larger, which means that gain in efficiency is better.

Moreover, the cambered position P1 downwards improves the lift-to-drag ratio and provides a better aerodynamic performance compared to the conventional wing-flap system at higher angle of 8° at Re of 7 Million. A small cambering has considerable effects over the aerodynamic efficiency as presented in figure 6.11.

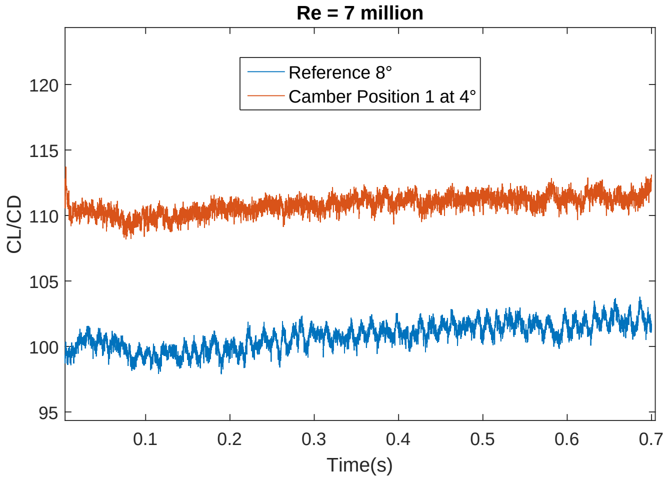

FIGURE 6.11: Comparison of the lift-to-drag ratio of the first cambered position at 4° with the reference baseline at 8°

6.2.4.3 Dynamic cambering approach

In this section, a dynamic motion of the cambered model (see section 6.2.3) is analysed. The applied deformation on the grid uses a similar control law as the experimental prototype. The real prototype's flap reaches a maximum cambered position of 10 cm within a duration of 1 min. The numerical model would be very time consuming to reach the same time-scale. The model used in the present study reaches the maximum cambered position within 2 seconds.

(Chinaud et al., 2014) investigated a flat plate pending for and compared the quasi-static approach with the dynamic pending. The maximum displacement was obtained in 1 second. The comparison was performed for phase-averaged fields velocity and Reynolds stresses. It was found that the recirculation was formed in the dynamic case at small pending position compared to the static from the velocity iso-contours. The dynamic pending increases the shear in the mixing-layer near the plat trailing edge and a change in the topology of the shear-layer. They concluded that the

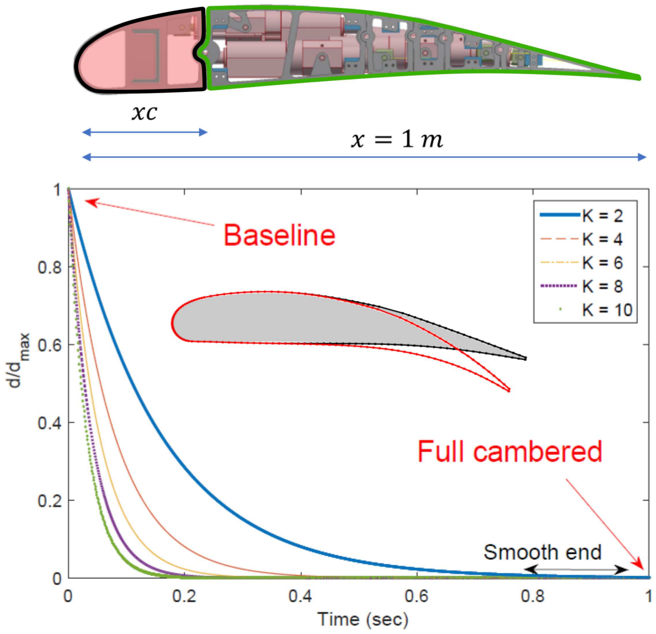

FIGURE 6.12: Dynamic control law of the camber motion using different accelerator coefficients with a smooth stop

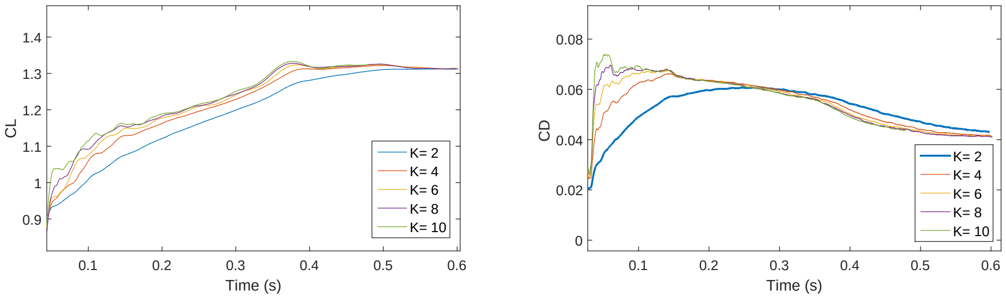

FIGURE 6.13: Time evolution of the lift and drag coefficient using different camber accelerator coeffiecients

comparison between the dynamic case and selected static cases reveals a qualitative similarities. Based on their study, a model has been developed using different actuations speeds to better understand the transition period. In figure 6.12 demonstrates the deformation law through different accelerators coefficients going from the baseline to the fully cambered position. The displacement is incremented continuously in different ways, the best repartition is found for low speeds of cambering (K accelerators). A smooth stop is defined between 0.8 and 1 second in order to avoid numerical perturbations over the wall pressure. This impacts directly the aerodynamic forces.

The unsteady transition of the cambering affects the aerodynamic forces and the drag which appears more sensitive than the lift force as illustrated in figure 6.13. Different K acceleration coefficients were tested in order to evaluate the influence over the transition phase. When the cambering is accelerated, it impacts more the drag. This last reaches higher values with a very high slope. After that, the signal converges to the same value for the all the acceleration factors investigated. The lift increases smoothly while increasing the K and reaches the same values.

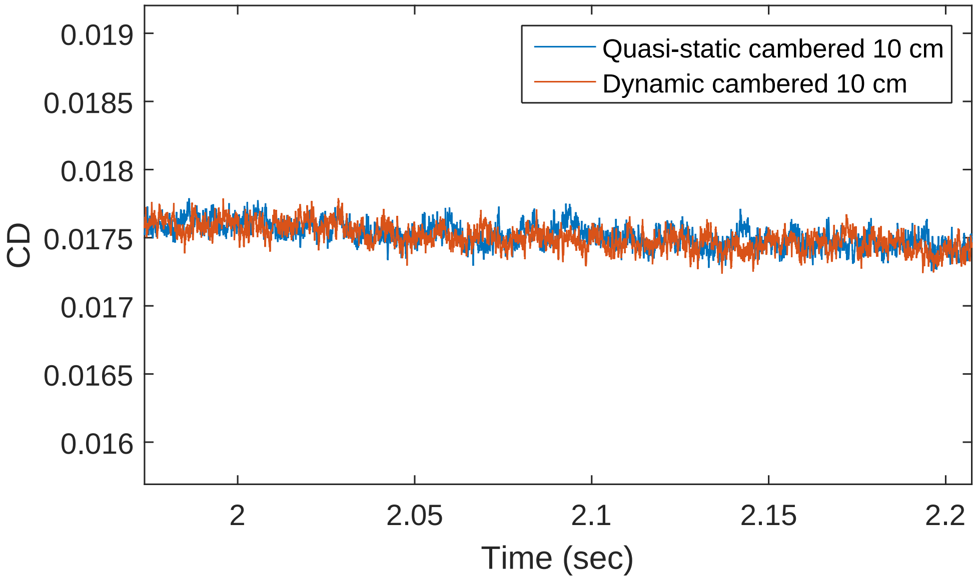

FIGURE 6.14: Comparison of dynamic and quasi-static approaches in terms of aerodynamic drag coefficient signal

The quasi-static assumption helped reaching rapidly unsteady converged solutions and identifying optimized regions of the cambered flap in two-dimensional simulations. However, the effects of the dynamic cambering and the transition on the aerodynamic forces need to be investigated and clarified.

In figure 6.14 the dynamic and quasi-static approaches are compared in terms of the drag force because it appears more sensitive to the transition. A maximum cambered position at 10 cm at an angle of attack of 4° degrees are taken into account. After the dynamic cambering has reached convergence and the flap has stopped, it has been compared to the quasi-static case. It appears that both signals are superimposed and transition from the dynamic case does not have effects on the final converged solution.

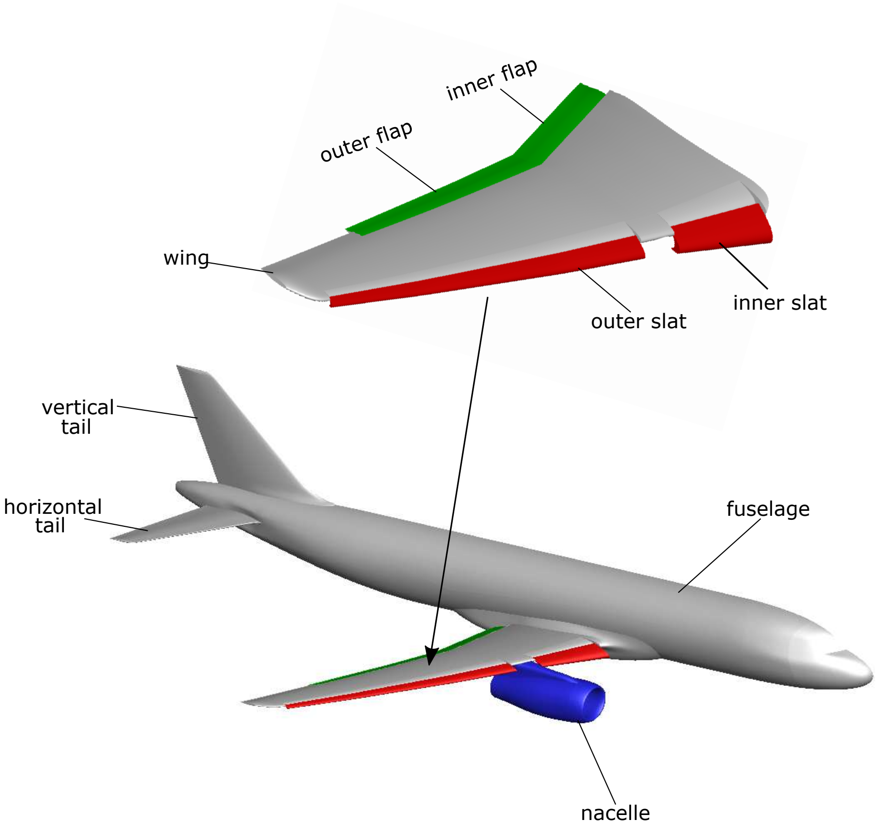

FIGURE 6.15: Schematic description of the of Airbus A320 airplane with different components used for the numerical simulations

6.3 Airbus A320 aircraft

Concerning the Airbus A320 aircraft, the deformation is applied along the spanwise direction including the variation of the flap's chord and its orientation. A patched grid was implemented in the code thanks to the Chimera approach developed in NSMB by (Deloze (2011)) to efficiently take into account the deformation in the vertical direction regarding the flap's chord. The cambering deformation includes the inner and outer flaps, presented in figure 6.15. A uniform downward cambering is considered.

6.3.1 Numerical and physical parameters

The $P1$ cambering position was found the optimal configuration for 2D simulations in increasing the aerodynamic efficiency CL/CD. The inner and outer flaps are cambered according to this position. The Airbus A320 aircraft is set into two angles of attack. The angle 4° corresponds to the best efficiency obtained with the cambering position $P1$ and the angle of 8° is the standard angle for the take-off conditions (table 6.4). Furthermore, the URANS Spalart Almaras (SA) one equation model (Spalart and Allmaras (1992)) was selected for the three-dimensional Airbus A320 airplane simulations, in order to shorten the computational time concerning the complexity of the full aircraft's geometry and facilitate the convergence.

-	Re	α	Camber positions
3D	11M	$4^\circ, 8^\circ$	P1

TABLE 6.4: Set of different physical parameters employed in the 3D numerical study

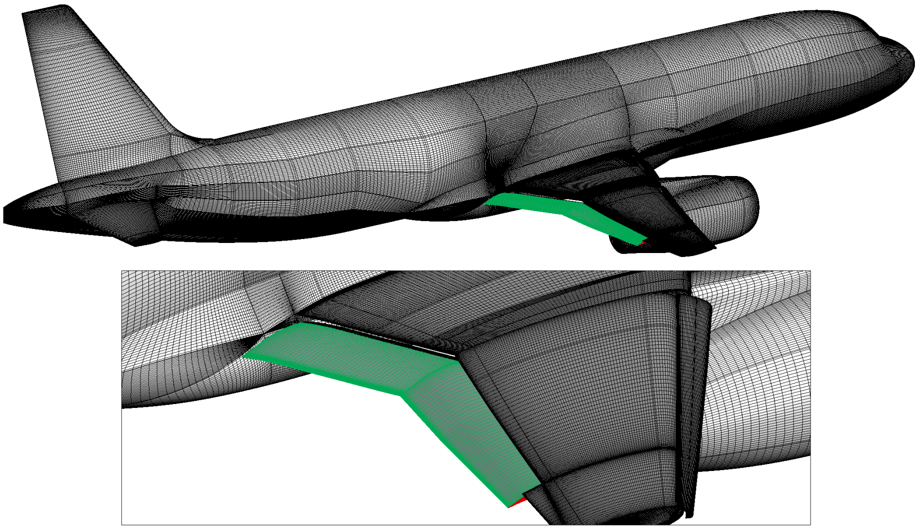

FIGURE 6.16: Computational grid over the Airbus A320 airplane with the flap placed at the take-off position

6.3.2 Grid generation and validation

3D structured grid whose size is presented in table 6.5 have been created in order to investigate the morphing effects of a real scale A320 airplane containing a fuselage, high-lift system (slats, flaps and wing), horizontal and vertical tails and a nacelle. A

-	Type	cells number
3D	Coarse airplane (G1)	10M
3D	Finer airplane (G2)	50M

TABLE 6.5: Computational grids used for the numerical simulations

Chimera grid has been selected to generate different independent grids for the different parts in the 3D airplane (figure 6.16) thanks to CFS Engineering. This allows having good quality of grids over these complex geometries and capturing the physics near the walls such as the boundary layer development and detachment. The grid

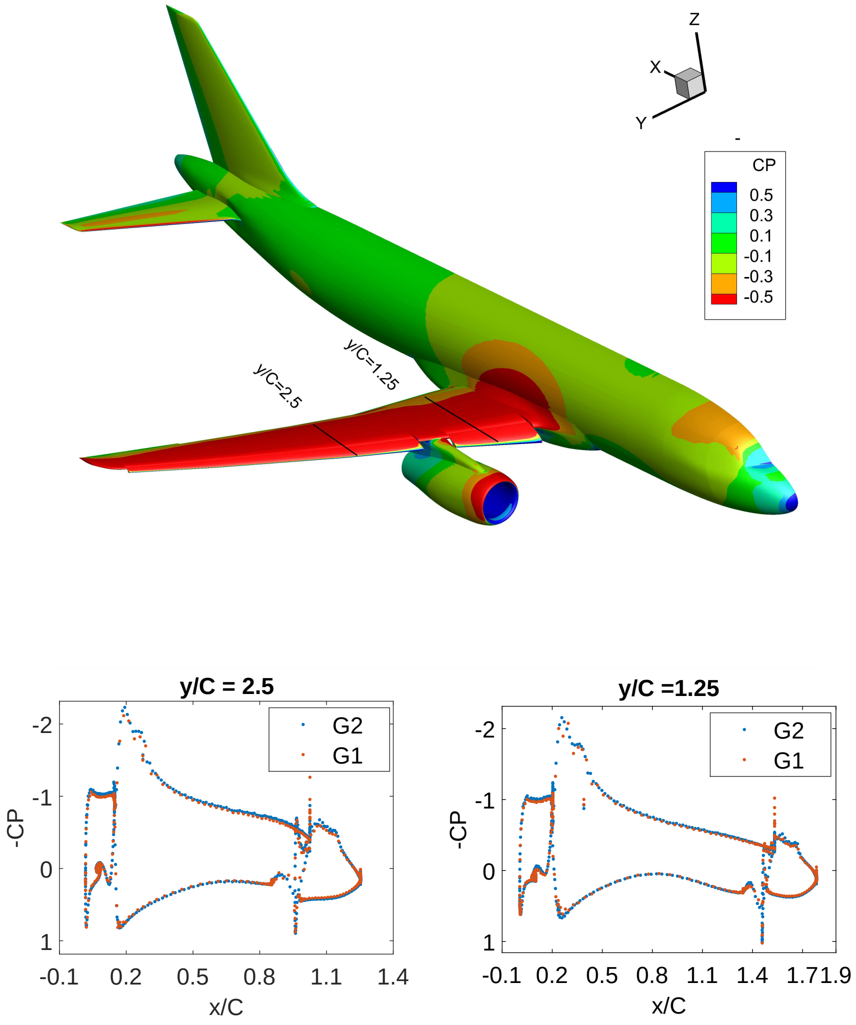

FIGURE 6.17: CP iso-surfaces around the Airbus airplane with extracted slice along the spanwise wise comparing normal and refined grids

around the flaps and slats is an overset mesh (Chimera) in order to compute dynamic camber based on the EMA actuators during the simulations as presented in the previous section.

The deformation of the computational domain and the flap geometry uses the ALE method in the NSMB solver which is an efficient method to impose displacements and adapt the mesh deformation in respect on the morphing configuration.

Figure 6.17 presents iso-surfaces of the pressure coefficient on the Airbus airplane using the G1 and G2 grids. Two different slices are extracted along the span in order to examine the grid independence. The C_P at the position $y/C = 1.25$ is deduced from the inner slat and flap and in the position $y/C = 2.5$ for the outer slat and flap. The results are in a good compromise for both grids, the G1 of 10 M cells and the more refined grid G2 of 50 M cells. All the simulations were continued with the G1 grid in order to facilitate the analysis of the aerodynamic performances using the best camber position studied in section 6.2.4.2 from the 2D simulations.

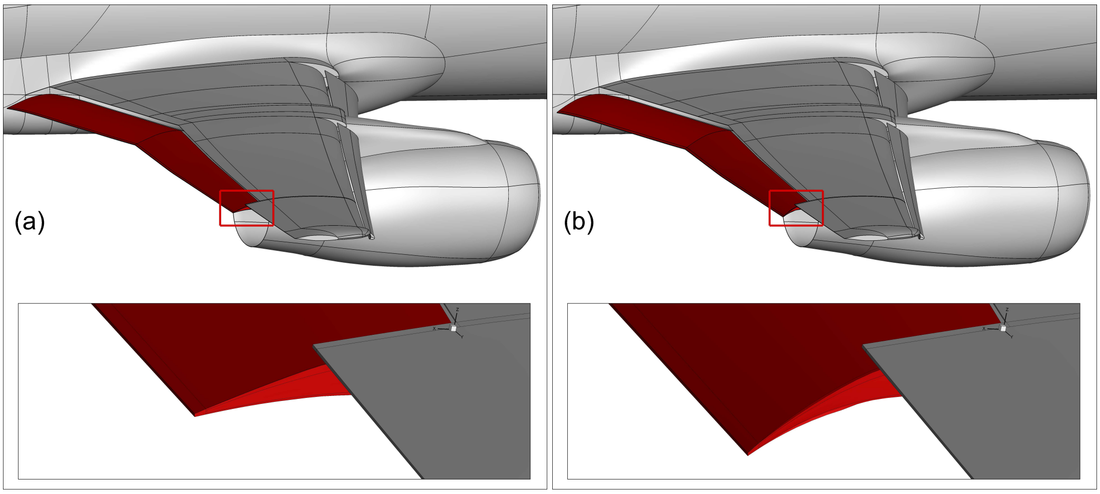

FIGURE 6.18: Zoom on the downward cambered inner and outer flaps compared to the reference baseline at the take-off position

6.3.3 Results: Airbus A320 quasi-static approach

To evaluate the effects of the flap cambering on the Airbus aircraft, a full-scale A320 airplane is considered during a real take-off configuration. This allows obtaining more representative gain percentages on the lift-to-drag aerodynamic performance.

Figure 6.18 shows the deformation of the inner and outer flaps with a camber control using the EMA model of order of 10 cm downwards concerning the trailing edge and following the same cambering as for two-dimensional simulations.

Based on different tests conducted for the two-dimensional simulations, a defined cambered position P1 was computed for the inner and the outer flaps regarding optimal two-dimensional results at a medium chosen angle of attack of 4°. This is compared first with the conventional configuration at the same angle, as presented in figure 6.19. This figure shows that the pressure difference $P - P0$ to increase over the flaps upper surfaces with a simultaneous feedback on the pressure distribution over the wing and up to its leading-edge. Same effects have been observed in the two-dimensional simulations (figure 6.8) where the CP was presented. In addition, the pressure is continuously increased in a considerable part of the fuselage-wing junction (figure 6.19). This increase allows reaching better aerodynamic efficiency than the standard configuration and the 2D simulations.

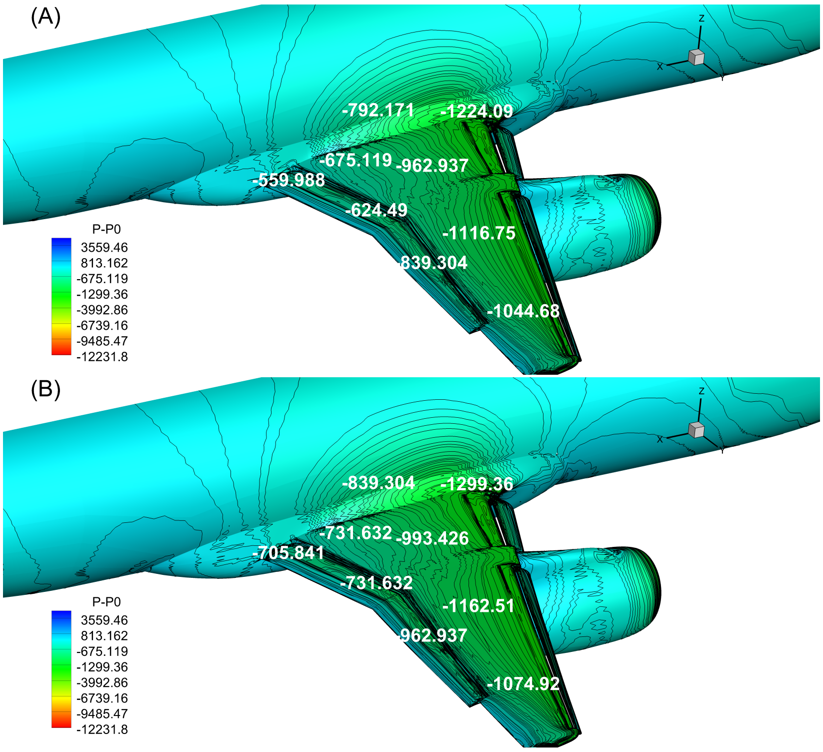

FIGURE 6.19: iso-surfaces of dimensional pressure difference of the Airbus A320 airplane angle of attack 4°. (A) : reference baseline, (B) : cambered position P1

The relative gain in lift-to-drag ratio $\frac{(\frac{CL}{CD} - (\frac{CL}{CD})_{ref})}{(\frac{CL}{CD})_{ref})}$ of +0.81 % is presented in figure 6.20 and compared to the reference case at the same angle of attack. The cambered flap increases the lift-to-drag of the Airbus airplane. This is shown through the pressure modification in the wing and the fuselage. In addition, figure 6.21 shows comparison of one cambered position at 4° with the reference case at standard takeoff conditions of 8°. An increase of +2.24% lift-to-drag ratio is obtained regarding the position P1.

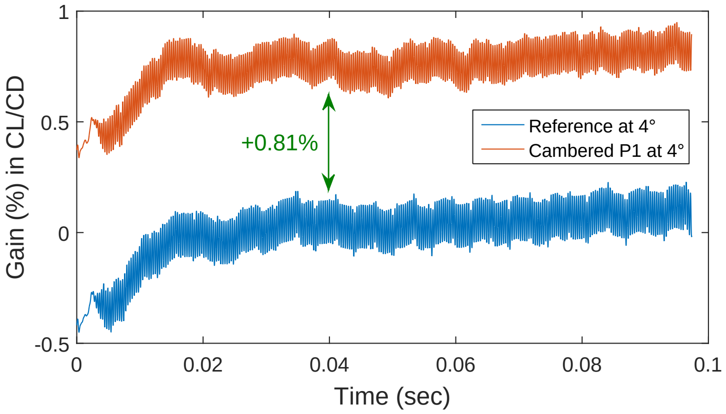

FIGURE 6.20: Total gain of lift-to-drag ratio of the airplane with cambered flap at position P1 at an angle of attack 4°

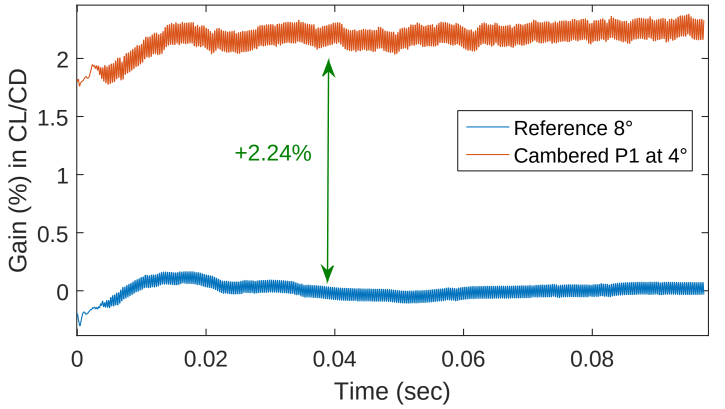

FIGURE 6.21: Total gain of lift-to-drag ratio of the airplane with cambered flap at position P1 at angle of attack 4° compared with reference at 8°

6.4 Cambering in the upward direction

An internal project held by Airbus with a collaboration of INPT, IMFT and LAPLACE aims to build a real drone (UAV) with 3D printed technology. The Clark wing profile has been selected for the wing design because of the facility of printing. Two internal and external flaps (are not presented due to confidentiality) are equipped with the SMA control to ensure the flaps to camber in the downward and upward positions. The aim of this section is to investigate the upward cambering near the stall configuration (downward cambering effects have been examined previously).

Two-dimensional grid has been created around the Clark airfoil (chord = 1 m) as presented in figure 6.22 using a far-field boundary conditions of length 20 chords to

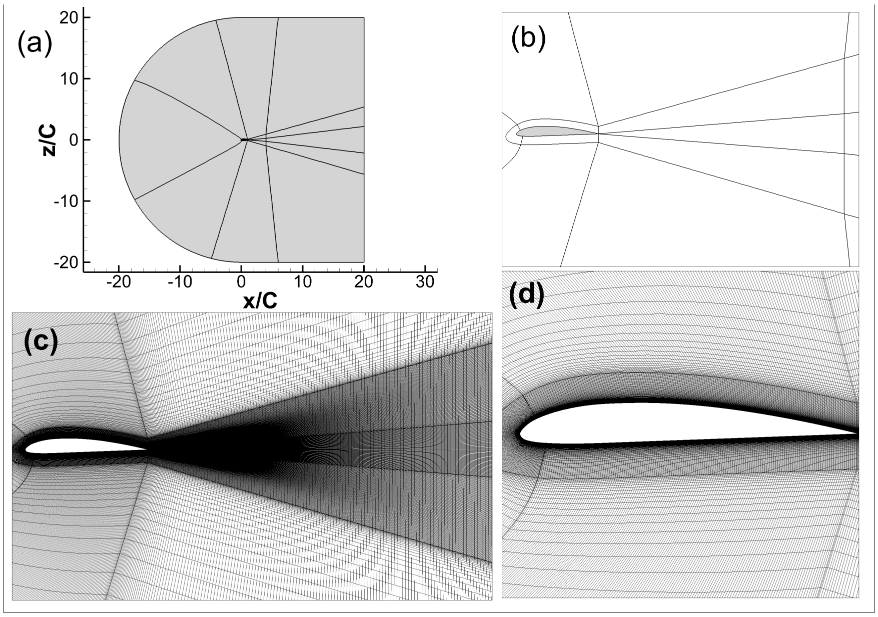

FIGURE 6.22: Two-dimensional grid around the Clark airfoil and representation of the refined wake region using multi-blocks analysis

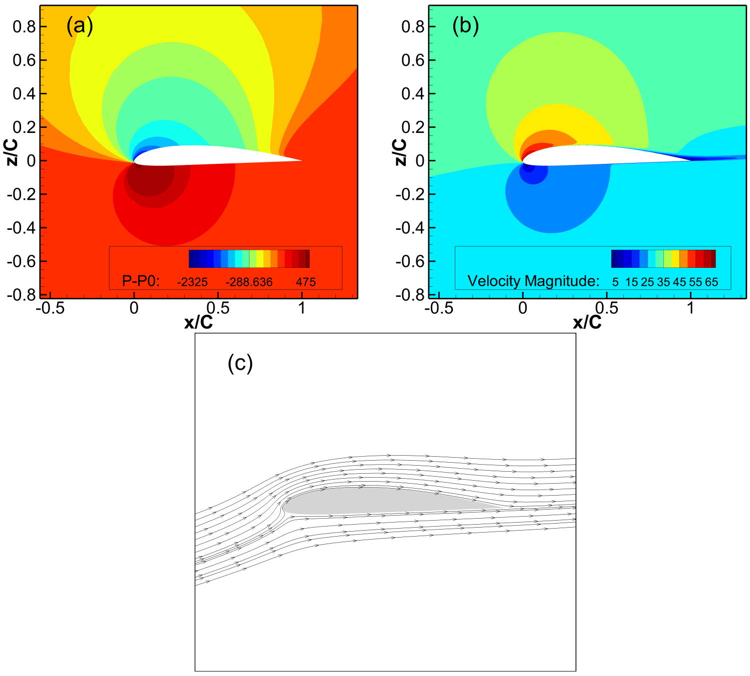

FIGURE 6.23: Fields of solution around the Clark airfoil at an angle of attack 10°. (a) : Pressure difference P-P0 distribution. (b) : Velocity magnitude contours. (c) : Streamlines around the upper and lower airfoil surfaces

avoid feed-back effects. The mesh has 170 000 cells mostly distributed around the airfoil and the wake. It has been split into 16 blocks having approximate cell numbers in order to faster the simulations (figure 6.22 *b*). The wake is refined along 2 chords (150 cells in the longitudinal direction) to avoid the coherent structures dissipations (figure 6.22 *c*) and the cells are kept orthogonal with $Y+ < 1$ in order to capture the sub-viscous layer in the boundary layer (figure 6.22 *d*).

The Reynolds number has been fixed at 2 million (U = 34 m/s) which corresponds to the mean speed used in different flight stages. the solution has been investigated at a first at an angle of attack of 10°. Because of the lack of experimental data, same numerical parameters are considered as in the previous chapters because the flow remains subsonic at this range of speed (Mach = 0.1). The OES turbulence model has been used in this study.

The figure 6.23 highlights the reference baseline fluid flow around the Clark airfoil. Pressure difference is created through the upper and the lower surfaces of the airfoil in figure 6.23 (a) and the fluid flow is accelerated in the upper surface near the leading-edge (figure 6.23 (b)). The boundary layer is fully turbulent at this Reynolds number. The Clark is not a supercritical airfoil (does not include a curvature in its intrados but a line), this helps having less shearing between the upper and the lower shear layers due to its small thickness and as consequently wake instabilities are less pronounced at this angle of attack (10°). Streamlines are aligned with the airfoil surface (figure 6.23 (c)).

Three different angles of attack 16, 18 and 20 degrees near the stall region are selected in order to compute an upward camber deformation of 10 cm. The same control law used for the LS prototype is used for the dynamic cambering in this configuration.

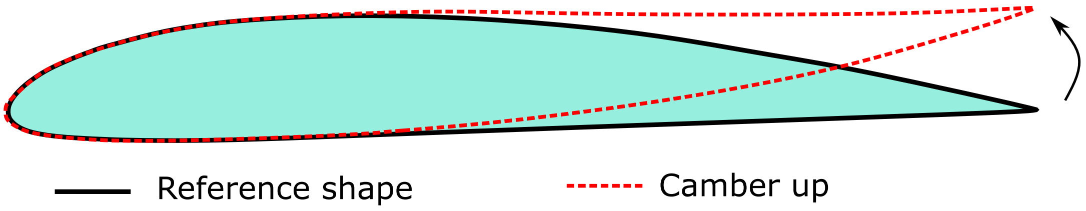

FIGURE 6.24: Schematic description of Clark airfoil cambering in the upward direction with a deformation of 10 cm

In figure 6.24 the baseline reference Clark airfoil and its final cambered position are presented. The trailing edge moves in the upward direction and stops smoothly to avoid numerical perturbations on the aerodynamic forces.

Increasing the angle of attack induces a formation of trailing edge vortices (recirculation) due to the separation of the boundary layer which moves towards the leading edge generating a shear layer which origins follows the separation point. Near

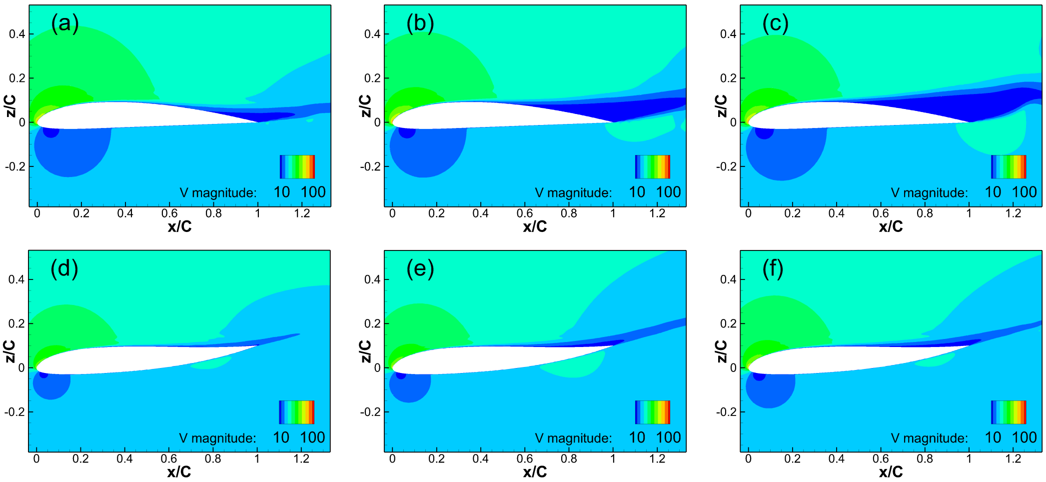

FIGURE 6.25: Velocity magnitude contours around the Clark airfoil at different angles of attack. Baseline (reference) : (a) 16 °; (b) 18 °; (c) 20 °. Camber up ((10cm) : (d) 16 °; (e) 18 °; (f) 20 °

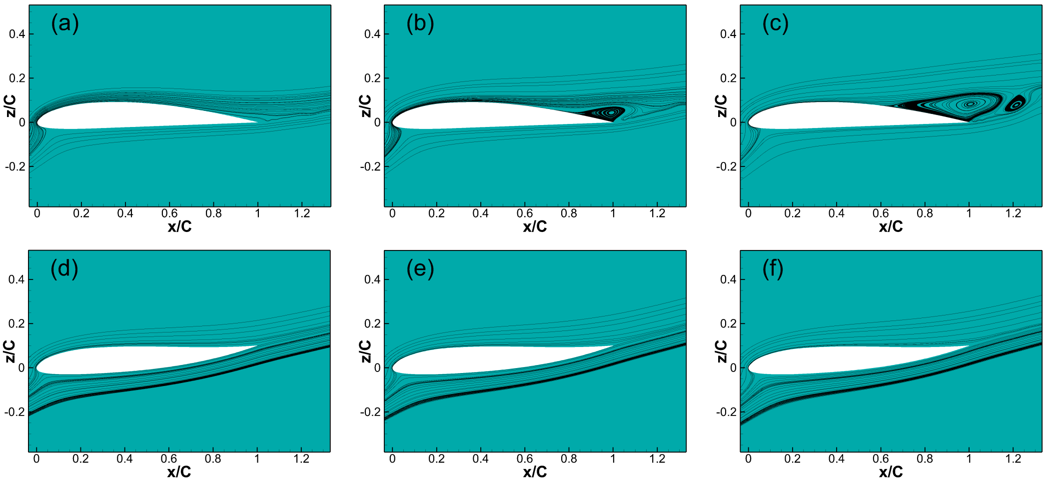

FIGURE 6.26: Streamlines visualization around the Clark airfoil at different angles of attack. Baseline (reference) : (a) 16 °; (b) 18 °; (c) 20 °. Camber up (10cm) : (d) 16 °; (e) 18 °; (f) 20 °

stall conditions the separation line approaches the leading-edge region and produces a fully detachment of the boundary layer and a considerable loss in the lift forces followed by an increase of the drag. This phenomena can be avoided by using the upward camber. In figure 6.25 fields of velocity magnitude are presented for different angles of attack near the stall conditions. The non-cambered airfoil is presented in figures 6.25 (a), (b) and (c) for different angles of attack 16 °, 18°, and 20° respectively. The separation point moves towards the leading edge when the angle of attack increases. At 20° the separation is formed at $x/C = 0.351$, for 18° is approximately at $x/C = 0.528$ and for 16° it moves near the trailing edge at $x/C = 0.782$ that was observed in a zoomed view of the figure 6.26. The camber suppresses completely the separation at all tested angles of attack (figure 6.26) streamlines are reattached to the upper surface of the airfoil. The upper boundary layer is then re-attached and follows continuously the new cambered shape. The velocity gradient dU/dY inside the shear layer is then decreased through the re-attachment of the upper shear layer and the interaction of both upper and lower shear-layers becomes less critical and hence suppresses all the wake instabilities. In figure 6.27, the voritcity provides an overview of global wake instabilities for the non cambered configuration and full cambered one. For the reference cases, when the angle of attack is increased the von Kármán vortex shedding is more pronounced and the wake becomes thicker due the high shearing produced by the angle of attack and the recirculation (figures 6.27 (a), (b) and (c)).

It is found that the camber attenuates and suppresses completely the von Kármán vortices for all the angles of attack (figure 6.27). A thinner wake is formed in all cambered configuration. Mean aerodynamic forces are further investigated for the case of 20°. The mean drag has been reduced because of the wake thinning and the mean lift also appears to decrease because the cambering decelerates the flow through its feedback to the leading-edge thus producing less pressure difference. However a gain of +108% has been observed on the aerodynamic efficiency lift-to-drag ratio as presented in the table 6.6

-	Baseline	camber up	gain/loss
CD	0.047	0.017	-176.47 %
CL	0.830	0.625	-24.69 %
CL/CD	17.66	36.76	$+108$ %

TABLE 6.6: Representation of drag, lift, lift-to-drag ratio for the reference and cambered configurations with the gain or loss in (%) at the angle 20 °

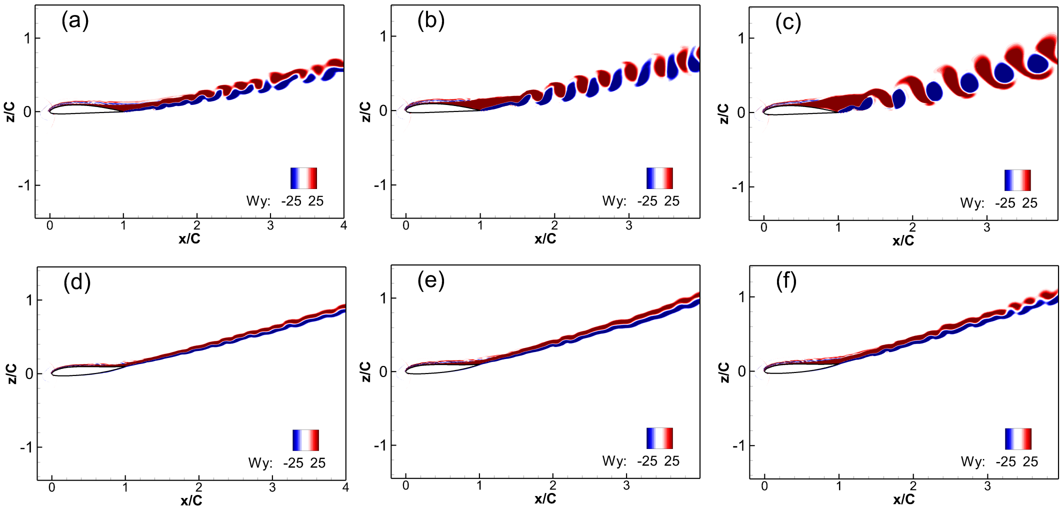

FIGURE 6.27: Spanwise vorticity around the Clark airfoil at different angles of attack. Baseline (reference) : (a) 16 °; (b) 18 °; (c) 20 °. Camber up (10cm) : (d) 16 °; (e) 18 °; (f) 20 °

6.5 Conclusion

This chapter investigates Hi-Fi simulations of morphing based on cambering and ensured by EMA actuators. This is applied on the LS prototype, the Airbus Airbus A320 airplane and the Clark airfoil. The morphing flap is able to dynamically camber allowing achieving an improved lift-to-drag efficiency compared with the standard (non-morphing) configuration. These facts have taken benefit from a parametric study involving a number of quasi-static cambered positions investigated by means of 2D simulations. This investigation allowed optimising the regions where the cambering is more effective.

Furthermore, this study makes evidence of considerable benefits from feedback effects of the cambering, which produces high pressure in the wing and fuselage-wing junction and thus increases the total lift to-drag up to +2.24 % more than the reference configuration.

An additional cambering in the upward direction using the one element Clark airfoil in two-dimensional simulations was found to re-attach the flow in the upper boundary layer and suppress the recirculation at high angles of attack. As consequently, von Kármán vortex shedding disappeared and a thinner wake has been formed following the new geometry. Mean aerodynamic performances have been increased up to +108%. The upward cambering helps to avoid stall phenomena that leads to a fully detachment of the boundary layer and a considerable loss in efficiency.

This study shows that the most highly cambered positions can not be coupled with high angles of attack due to the boundary layer separation leading to a loss in efficiency caused by the drag increase. Hybrid morphing using the cambering and the trailing edge actuations would be the most appropriate solution, because the motion of the trailing edge induces a vortex breakdown of the coherent structures through the injection of smaller scale vortices able to attenuate the drag increase. This benefits from a hybrid morphing effect has been proven and investigated in another part of our studies (chapter 7).

Chapter 7

Electroactive hybrid morphing of the Airbus A320 during Takeoff

This chapter represents the last part of the results core. It examines the hybrid electroactive morphing. This latter brings together both high frequency low amplitudes of deformation of the trailing-edge (ensured by the piezoelectric actuators) and high amplitudes of deformation low frequency (ensured by the EMA actuators) and mounted on the real flap of the Airbus A320 airplane at the real take-off conditions. The association of trailing-edge vibrations and the cambering revealed an increase of the lift-to-drag ratio compared to the reference case and the only use of the cambering.

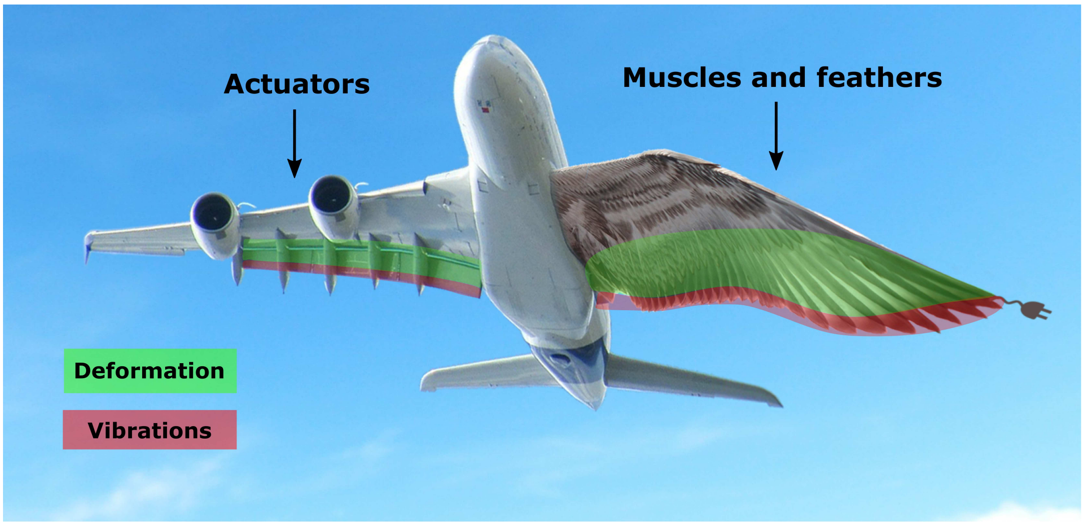

FIGURE 7.1: Hybrid electroactive morphing (courtesy of G. Jodin)

Contents

7.1 Concept of hybrid morphing at a real scale

The work of (Scheller et al. (2015)) firstly proposed the hybrid concept and developed a small fixed span wing prototype (NACA4412). A hybrid morphing wing contains both series of SMAs (able to make deforamtions +/- 10 % of the chord in a limited frequency < 1Hz) and piezoelectric fiber actuators (small deformations order of mm coupled with higher frequencies < 100 Hz). The study showed a reduction of the wake energy which leads to an improvement in aerodynamic performance. (Jodin et al. (2017)) improved this system and implemented it in a Reduced-Scale Airbus A320 wing prototype with frequencies in the range [100, 450] Hz for trailing-edge actuations. A reduction in pressure drag (approximately -5 %) and an increase in lift (enhancement +2%) were obtained only for high frequency low amplitude vibrations. In this chapter, we propose an innovative solution to couple the camber control with

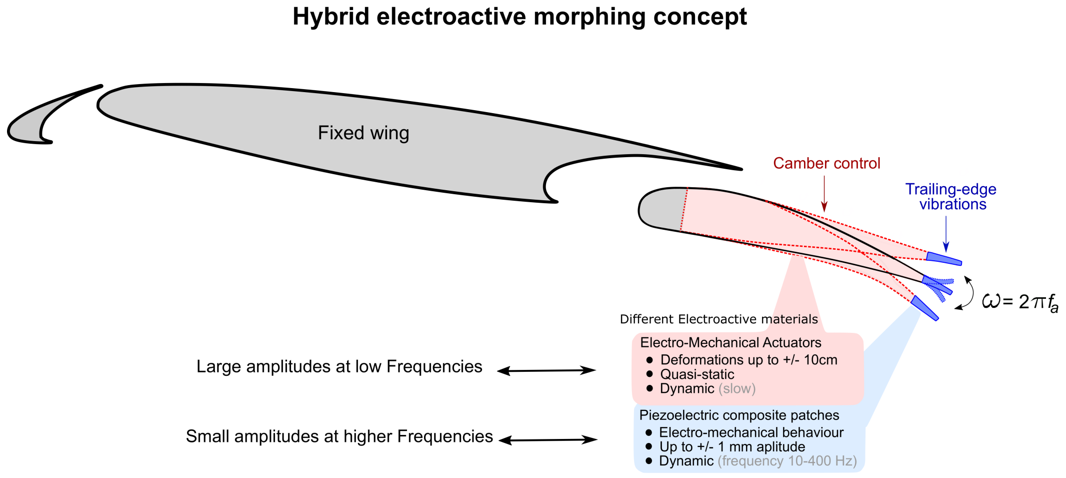

FIGURE 7.2: Illustration of the maximum deformed shapes of the airfoil. The red superimposed profiles depict the effect of the camber control using Electro-Mechanical Actuators, the blue parts represent the vibrating trailing edge using piezoelectric patches.

the piezoelectric patches applied for the Airbus A320 airplane in the take-off configuration. The cambering is achieved using the Electro-Mechanical Actuators (detailed in chapter 6) and trailing edge actuations (detailed in chapters 4 and 5). Figure 7.2 demonstrates the concept of hybrid morphing used in the simulations. The wing and the slat are maintained as fixed bodies and the internal and external flaps embed the electroactive hybrid morphing.

The camber through the EMAs allows an increase of the aerodynamic lift and lift-to-drag ratio. The piezoactuators implemented in the trailing edge region as presented in the figure 7.3 are able to manipulate the wake turbulent structures allowing an improvement of the aerodynamic efficiency.

In figure 7.4 the flaps surfaces are deformed following different laws. Figures 7.4 (a) and 7.4 (b) illustrate only the cambering in downward direction and figures 7.4 (c) and 7.4 (d) represent a zoom in the trailing edge region where the movement of the piezoelectric patches is simulated.

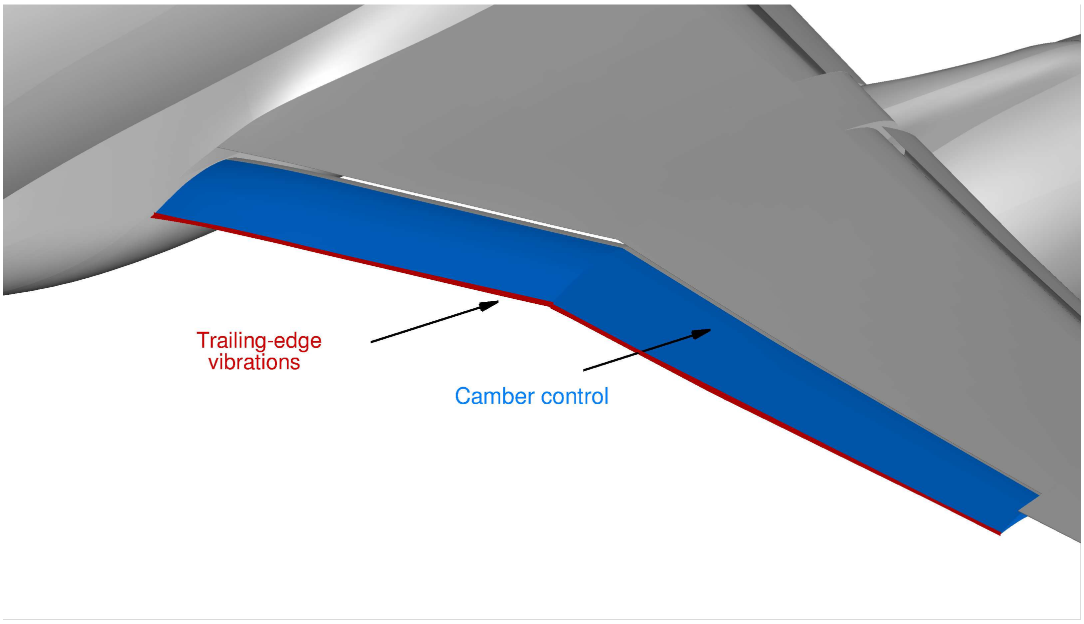

FIGURE 7.3: Presentation of hybrid morphing flaps mounted in the Airbus A320 airplane

Trailing edge actuations at a frequency of 300 Hz with small amplitude of vibrations order of 0.35 mm revealed optimality in manipulation of wake turbulent structures as thinning of its width, suppression of its three-dimensional character and increase of aerodynamic efficiency (in chapter 4 and 5). In addition, camber position $P1 = 3$ cm in the downward position have shown best increase of lift-to-drag ratio in low and medium angles of attack compared to higher cambering positions due to higher

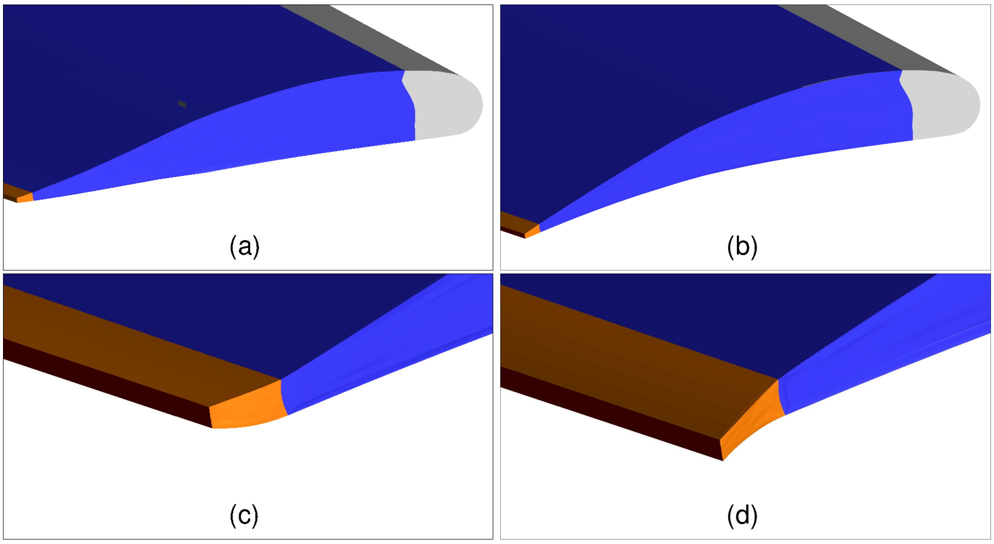

FIGURE 7.4: Deformation of the flap surfaces using EMA actuators for cambering and trailing edge vibrations using MFC piezoelectric patches. (a) and (b) camber deformation. (c) and (d) trailing edge vibrations

increase of drag related to more bluff body domination (in chapter 4 and 6).
A similar domain and grid (G1) around the Airbus A320 airplane at the take-off position (flap deflection 10 °) has been considered for this study and was detailed in the previous chapter. We defined only the patch boundary condition used for the trailing edge deformations in addition to the cambering.
The physical parameters are selected the same as in the previous work (Re = 11M, Ma=0.15 and α in the range [0° - 8°] degrees). The Spalart Almaras (SA) one equation model Spalart and Rumsey (2007) has been used as a turbulence model to facilitate the convergence on this coarser grid (10 million cells).

7.2 Aerodynamic evaluation

A first set of mean aerodynamic forces is presented in figure 7.5 and table 7.1 where the mean drag is plotted for different configurations as following: the reference case (static), only cambered flap and the camber with trailing edge vibrations (hybrid morphing). Different angles of attack are considered in order to evaluate the drag gain or loss in every case. The camber was found to increase the drag for all the angles of attack due to the more dominant bluff body. Trailing edge vibrations decreases the drag through the vortex breakdown of the coherent structures and thinning of the

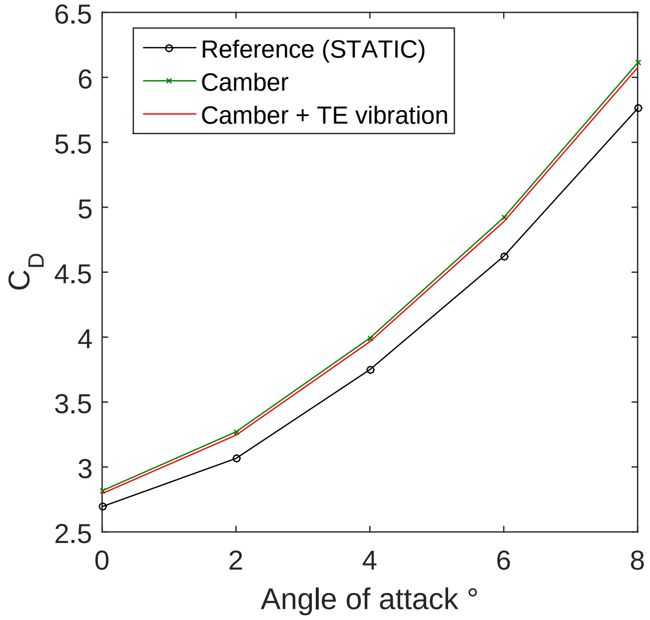

FIGURE 7.5: Mean aerodynamic drag comparison of the reference case (static), camber and camber with trailing edge vibrations

	0°	2°	4°	6°	8°
$\frac{<Cd>_{CAMB} - <Cd>_{REF}}{<Cd>_{REF}}$ x 100	+4.54	+6.68	+6.49	+6.45	+6.10
$\frac{<Cd>_{HYB} - <Cd>_{REF}}{<Cd>_{REF}}$ x 100	+3.75	+5.84	+5.74	+5.76	+5.47
$\frac{<Cd_{HYB}> - <Cd_{CAMB}>}{<Cd_{CAMB}>}$ x 100	-0.76	-0.78	-0.71	-0.65	-0.60

TABLE 7.1: Aerodynamic drag gain/loss for both cambered flap and camber with trailing edge vibrations

wake compared to the only camber configuration. The hybrid morphing maintains the drag smaller with a -0.6 % to -0.78 % for all the angles of attack. These small percentages are explained through the effects of the piezoelectric patches length and amplitude applied to the reduced-scale wing prototype of chord 0.7 m which are the same for the full scale Airbus A320 airplane with a real chord 3.2 m. The length and amplitude should be rescaled and investigated in further details.

The mean lift forces are presented in the figure 7.6 and table 7.3. The camber and

	0°	2°	4°	6°	8°
$\frac{<Cl>_{CAMB}-<Cl>_{REF}}{<Cl>_{REF}}$ x 100	+15.40	+10.19	+7.34	+5.79	+4.76
$\frac{<Cl>_{HYB}-<Cl>_{REF}}{<Cl>_{REF}}$ x 100	+14.90	+9.85	+7.11	+5.61	+4.60
$\frac{<Cl>_{HYB}-<Cl>_{CAMB}}{<Cl>_{CAMB}}$ x 100	-0.44	-0.31	-0.21	-0.17	-0.15

TABLE 7.2: Aerodynamic lift gain/loss for both cambered flap and camber with trailing edge vibrations

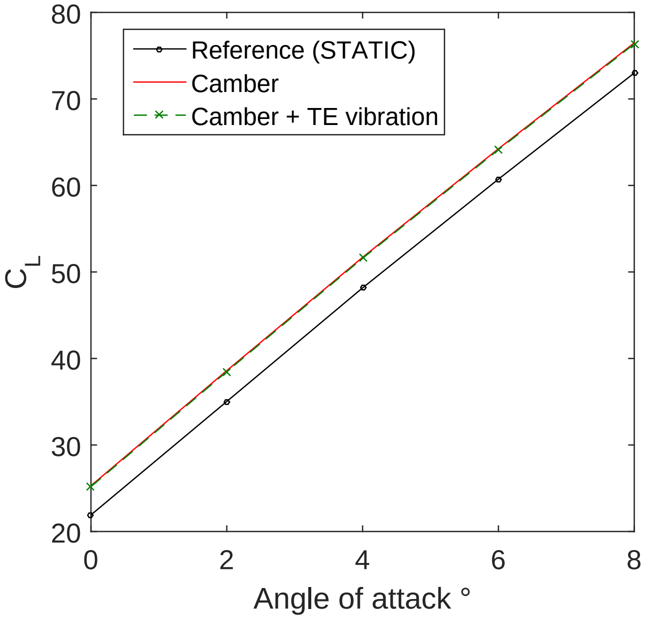

FIGURE 7.6: Mean aerodynamic lift comparison of the reference case (static), camber and camber with trailing edge vibrations

hybrid morphing improve the lift compared to the reference (static) case up to +4.76 % when the angle of attack is 8 degrees. The trailing edge vibrations effects are barely seen compared to the only cambered flap, a very small decrease is noticed. To better quantify the effects of the hybrid morphing the aerodynamic efficiency lift-to-drag is highlighted in figure 7.7 and table 7.3. The lift-to-drag ratio is increased in the interval $0 \leq \alpha < 6$ of angles of attack. When $\alpha \geq 6$ a loss in efficiency is observed due the boundary layer detachment near the trailing edge when the flap is cambered.

The trailing edge vibrations are found to increase better the lift-to-drag ratio compared to the only cambered flap because of the drag decrease thanks to the hybrid morphing concept. The gain in the efficiency is better when the angle of attack is increased because the instabilities are more pronounced and as a consequence the wake width is larger. The trailing edge actuations manipulate these vortices through the

	0°	2°	4°	6°	8°
$\frac{<Cl/Cd>_{CAMB}-<Cl/Cd>_{REF}}{<Cl/Cd>_{REF}}$ x 100	+10.37	+3.29	+0.793	-0.627	-1.267
$\frac{<Cl/Cd>_{HYB}-<Cl/Cd>_{REF}}{<Cl/Cd>_{REF}}$ x 100	+10.744	+3.788	+1.30	-0.141	-0.8191
$\frac{<Cl/Cd>_{HYB}-<Cl/Cd>_{CAMB}}{<Cl/Cd>_{CAMB}}$ x 100	+0.33	+0.48	+0.50	+0.49	+0.45

TABLE 7.3: Aerodynamic gain/loss for both cambered flap and camber with trailing edge vibrations

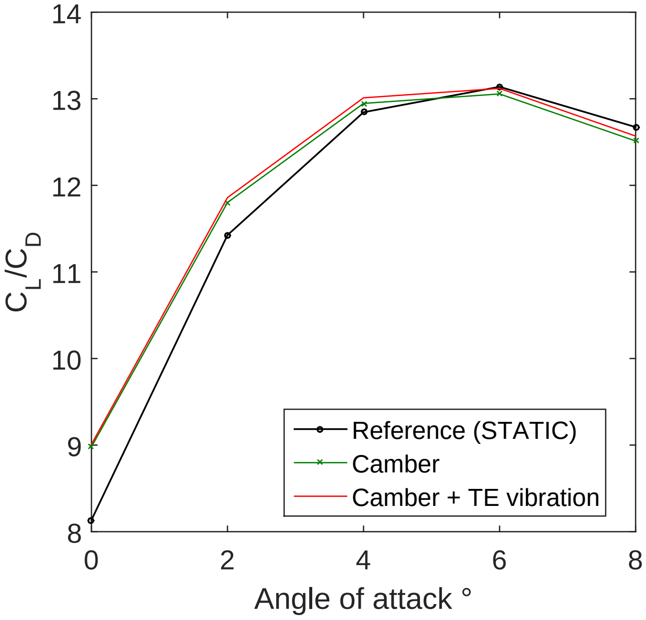

FIGURE 7.7: Mean aerodynamic performances efficiency lift-to-drag ratio comparison of the reference case (static), camber and camber with trailing edge vibrations

eddy blocking effects allowing a transfer to an upward energy scaling (Szubert et al. (2015)) which reduces the width of the wake and decreases the drag.

7.3 Conclusion

This chapter proposes a numerical analysis of hybrid electroactive morphing using Electro Mechanical Actuators (EMA) for the cambering and Macro Fiber Composite (MFC) piezoelectric patches for trailing edge vibrations embedded in a real scale flap mounted in the Airbus A320 airplane at the take-off position. The numerical model uses patched boundary conditions in order to compute different deformations normal to the surface due to the span variation of the the internal and external flaps (swept wings). Trailing edge vibrations at a frequency of 300 Hz with a slight deformation of 0.35 mm coupled with a cambering at P1 (3 cm) revealed that the hybrid morphing can improve the aerodynamic efficiency better than the only flap cambering. The trailing edge vibrations decrease the drag by manipulating the wake instabilities and inducing a vortex breakdown of the coherent vortices. An increase of the aerodynamic performance lift-to-drag ratio from +1.30 % up to 10.744 % is obtained using the hybrid morphing flap. But, for higher angles of attack the coupling between camber and trailing edge vibration was not able to increase the efficiency. For such configurations, only trailing edge vibrations have better effects in improving the aerodynamic efficiency (detailed in chapter 4 and 5).

Chapter 8

General conclusions

8.1 Conclusions

The present thesis investigated morphing concepts for an A320 wing in reduced scale and near scale one by means of High Fidelity numerical simulation involving adapted turbulence modelling in high Reynolds number.

The morphing concepts investigated are based on electroactive devices embedded in the prototypes of the H2020 N° 723402 European Research project SMS, "Smart Morphing and Sensing for aeronautical configurations (`http://smartwing.org/SMS/EU/`)", coordinated by INPT (Toulouse Institut National Polytechnique).

Two different electroactive morphing wings have been studied, from a reduced scale of chord 70 cm towards real scale application for the Airbus A320 airplane.

The originality of the proposed electroactive morphing is to link fundamental understanding through the manipulation of turbulence vortices near the trailing edge region and in the wake, in different time and length scales as those governing the turbulence spectrum. These concepts are bio-inspired from the way the large span hunting birds camber the main wings, their ailerons and feathers, simultaneously realising lift increase, drag reduction and aerodynamic noise reduction. Part of this thesis is devoted to the association of the low frequency/high deformation with higher frequency/low deformation actuations, in the so called by the multidisciplinary team IMFT-LAPLACE *the hybrid electroactive morphing* ©.

It is worth mentioning that the present thesis has been carried out in synergy with the experiments of the SMS project for which the numerical studies helped to define the optimal ranges of the actuation parameters and optimal shapes to attain, that allowed the experiments to confirm the aerodynamic performance increase indicated by the present simulations. The present thesis offered an understanding of the morphing

effects that helped to find out the optimal concepts and parametric ranges, thus providing the best benefits.
Different morphing concepts are examined in this thesis :

- The first part of the study investigated the electroactive morphing on the so-called "Reduced Scale", RS prototype of the SMS project (chord = 0.7 m) using Macro-Fiber Composite (MFC) piezoelectric actuators implemented near the trailing edge and along the span on the RS prototype by the LAPLACE Laboratory. A first set of the numerical results has proven the good agreement between the numerical approach and the experiments carried out by TRPIV in the S4 wind tunnel of IMFT for the same Reynolds number range (1 Million). The numerical results highlighted the morphing benefits on a wide range of actuation parameters, the vibrations, amplitudes and length of the piezo-patches. The simulations have been done by means of the NSMB (Navier Stokes Multi Block) code, using the Organised Eddy Simulation (OES), that ensured a physically correct development of the flow instabilities and coherent structures. The fact that this approach is not intrinsically 3D, allowed performing a rich parametric study in 2D, that specified the main areas of interest concerning the morphing parameters, then performing a 3D study in well focused, optimal narrow ranges of the parametric space. The frequency of 300 Hz with a slight deformation of 0.35 mm using a patch length of 3.5 cm is found an optimal set of parameters, thus the present numerical study contributed to the experiments that have focused in more detail around this range of parameters.
- The second part concerns the study of high frequency/low amplitude of deformations using piezoelectric patches and low frequency/high deformation by means of EMA actuators on the so called Large Scale (LS) prototype of the SMS project. This configuration consists of a two-element A320 wing and its high-lift flap of 2.72 m chord and flap's chord of 1 m. The spectral analysis of unsteady pressure signals revealed same predominant natural frequencies related to the shear-layers and von Kármán instabilities for both numerical and experimental tests for the Large-Scale two-element wing-flap. The morphing effects on the Airbus A320 airplane through cambering of the high-lift flaps has been investigated in detail.
- Finally the hybrid morphing concept applied to a real scale flap mounted on an Airbus A320 airplane has been examined. This morphing concept simultaneously associates the cambering at low frequency/high deformation (ensured by

the EMA actuators) and high frequency/low deformation vibration in the near trailing edge region (ensured by the piezoelectric actuators).

The present work makes evidence of considerable benefits from the morphing concepts, partly bio-inspired through the injection of beneficial turbulent structures able to manipulate the surrounding turbulence and the wake's wake coherent structures. The actuations studied numerically in the present thesis are independent on the kind of the morphing actuators. The high cambering can be realised by Shape Memory Alloys (SMA), as in other parts of the SMS project and different kinds of piezo-actuators (other than MFCs) can be employed to realise the higher-frequency vibrations, as for example push-push actuator systems concerning other prototypes of the related teams beyond the SMS project (Scheller (2015)). Therefore, the benefits evaluated by this thesis have a more general character.
The major outcomes of the trailing edge actuations are highlighted as follows :

- Suppression of the three-dimensionality and vortex dislocations in the wake and attenuation of the secondary instability growth. Reduction of the recirculation area near the trailing edge leads and considerable wake thinning due to the injection of smaller scale vortices at a frequency close to the natural frequency of the shear layer instability, enhancing a lock-in effect and a thinning of the shear layer, as well as moving the von Kármán vortices farther downstream.
- Upward energy transfer in POD modes leads to an eddy-blocking effects and contribute to the observed thinning of the wake.
- Spectral analysis in the RS prototype revealed an attenuation in the aerodynamic noise sources of -20 dB and in the case of the LS, -15 dB due to the lock-in, thinning of the shear-layer vortices and the attenuation of the von Kármán natural frequency in the wake.
- Enhancement of the mean force lift of $+4.28$ % and lift-to-drag efficiency of $+1.61$ % in the 3D Reduced Scale, while an enhancement of lift of $+0.55$ % and $+2\%$ in lift-to-drag for the LS prototype is observed.

The principal outcomes on the LS prototype (involving near scale one cambered flap) are underlined as following :

- The numerical results are in good agreement with the experiments concerning the spectra of the fluctuating pressure, that reveal the main frequency modes and their interactions governing the wing/flap. Additional PIV results obtained from POLIMI are in good agreement with the numerical results.

- Associating downward cambering in the flap (camber 1) leads up to + 3.26 % gain on the aerodynamic performances on the Large-Scale prototype.
- Increase of the lift-to-drag ratio up to +2.24 % more than the conventional, by means of the cambered flap for the Airbus A320 in take-off condition using a cambered flap more than the conventional configuration.
- Upward cambering at high angles of attack was found to reattach the flow, suppress the recirculation and reduce the wake thickness. Consequently, the drag is considerably reduced and lift-to-drag ratio is improved up to +108 % of course these benefits are indicative and would suggest good trends in case of manoeuvring needs (gusts modifying abruptly the incidence of the inflow for example), where such high angles of attack would occur for short flight phases.

Finally the hybrid morphing benefits are summarised as follows :

- Successfully implemented and simulated the hybrid morphing for a real Airbus A320 airplane within the NSMB code simultaneously coupling the best cambering and the best trailing edge vibration from the previous steps.
- The Aerodynamic performances are more improved using the hybrid morphing on the Airbus A320 airplane than the only camber control or only trailing edge vibration. A decrease of the drag of -0.78% and an increase of the lift-to-drag ratio from +0.50 % are achieved compared to the only use of cambering.

A main feature associated to all the morphing concepts analysed in the present thesis is the huge benefit coming from the feedback effects from the morphing manipulating turbulence in the rear part and optimally redistribute the pressure along all the wing's surface, thanks to the interaction with the separated shear layers and the wake. Therefore, we used the unsteadiness to cut-off harmful vortices and to enhance beneficial ones, partly like the large-span hunting birds do. This main idea of *"Smart wing design through Turbulence Control - Science imitating Nature"*, coming from the last decade studies of the multidisciplinary team IMFT-LAPLACE (see the dedicated film of the CNRS Journal, `https://lejournal.cnrs.fr/videos/the-wings-of-the-future` has been verified, confirmed and further developed by the present thesis in the context of the SMS EU project, `www.smartwing.org/SMS/EU`.

This thesis led to a number of publications and participation in international dissemination activities in section RELATED PUBLICATIONS AND CONTRIBUTIONS 8.3

8.2 Perspectives

8.2.1 Airbus project for a free flight morphing testing on the UAV THOR

The continuation of the morphing and realisation towards real flight is under investigation in the context of the MINOTHOR ("Morphing in THOR") Airbus project that followed the Smart Morphing and Sensing European project. This project is held by Emerging Technologies & Concepts, part of the Airbus R & T group and Airbus Hamburg with a collaboration of the IMFT and LAPLACE laboratories. It aims at demonstrating the benefits of these novel morphing concepts in real flight concerning the technology in the improvement of aerodynamic and structural performances where new morphing high lift flaps are mounted on an Unmanned Aerial Vehicle (UAV) with wings span of 1.9 m. The Hybrid morphing of the high-lift flaps under way consists of camber control through SMAs and trailing edge vibrations using piezoelectric actuators embedded into two internal and external flaps. In parallel, 3D simulations are carried out around the full drone allowing the evaluation of the optimal parametric ranges the optimal regions of this hybrid morphing in order to increase the aerodynamic efficiency, decrease the noise into real flight conditions. A first set of simulations have been provided according to the same approaches used in the present thesis, that helped the definition of a first set of the flying testing parameters.

This is a valuable opportunity to finally evaluate the real effects of hybrid morphing into a real flight configuration, preparing a future use in real aircraft's wings.

8.2.2 Morphing wings at transonic speed

The methos developed in the present thesis contributed in the SMS project's studies of the cruise phase of flight, in collaboration with other PhD students of the research team IMFT-LAPLACE with the contribution of ICUBE. The buffet dynamics strongly interact with the shear layer and the wake instabilities. This latter modifies the thickness of the separated region due to the shock's motion along the upper surface of the A320 wing. This motion is quantified by a well defined predominant frequency f_b tracked in the drag, lift and pressure signals. The near trailing edge vibrations morphing actuations can produce a lock-in of this frequency when the trailing edge is actuated near this natural frequency.

Innovative morphing concepts can be adopted based on the present thesis results.

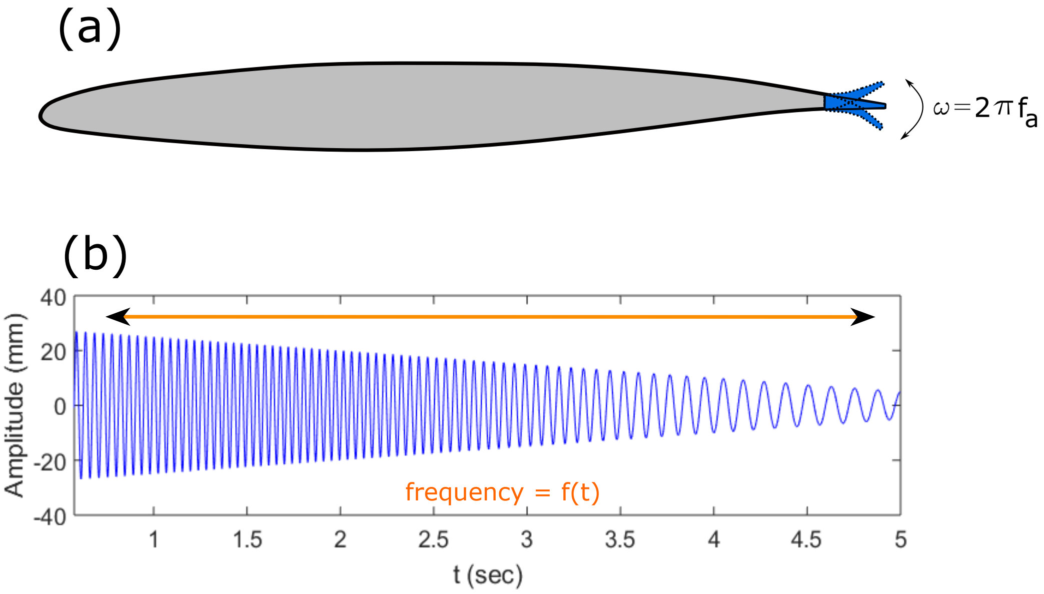

FIGURE 8.1: Trailing edge vibrations with a variable frequency and amplitude in time

By actuating the trailing edge vibration at a f_a close to f_b, a lock-in of the buffet frequency can be created. Afterwards, f_a amplitude decreases in the simulations as a function of time, in a similar way as by reducing the electrical intensity in the hardware as presented in figure 8.1. It is supposed that the buffet frequency will follow the same behaviour as in the actuation frequency because of the lock-in phenomenon. This could help to decrease and maintain the shock motion at lower frequencies (attenuation of the buffet mode). As a result, this would lead to reduce the separation region and enhance the aerodynamic performances.

8.2.3 Electro-active skin design

Bioinspiration from shark-like skins and birds feathers can lead to an electroactive skin design with multiple degrees of freedom. This could be implemented on the suction side of the wing and able to manipulate small eddies in a similar way as in the present thesis in order to enhance the beneficial ones playing an important role in the performances. This multiple-degree of freedom live skin, far beyond classic "drag reduction", will act along the wake in 3D and by feedback will simultaneously be able to increase lift and reduce noise. The concept can take example from the manta ray and jelly moon. The originality of the concepts developed in the thesis contribute to design electroactively controlled fringes (able to change their form) to manipulate the Turbulent-Turbulent and Turbulent-Non-Turbulent interfaces at higher Reynolds numbers (real flight conditions) and to enhance the aerodynamic performance increase.

8.3 RELATED PUBLICATIONS AND CONTRIBUTIONS

The following section presents a list of my contributions : awards and recognition, scientific popularization and publications.

JOURNAL PUBLICATIONS

1. **A. Marouf**, Y. Bmegaptche Tekap, N. Simiriotis, J.-B.Tô, Y. Hoarau, J.F Rouchon, M. Braza. Numerical and experimental investigation of frequency and amplitude effects of a Morphing wing in one/two element configurations at high Reynolds number, International Journal of Numerical Methods for Heat & Fluid Flow. `https://doi.org/10.1108/HFF-07-2019-0559`
2. N. Simiriotis, G. Jodin, **A. Marouf**, P. Elyakime, Y. Hoarau, J.C. Hunt, J.F. Rouchon, M. Braza. Morphing of a supercritical wing by means of trailing edge deformation and vibration at high Reynolds numbers: experimental and numerical investigation, Journal of Fluids and Structures `https://doi.org/10.1016/j.jfluidstructs.2019.06.016`
3. J-B. Tô, N. Simiriotis, **A. Marouf**, D. Szubert, I. Asproulias, D.M Zilli, Y. Hoarau, J. C. R. Hunt, M. Braza. Effects of vibrating and deformed trailing edge of a morphing supercritical airfoil in transonic regime by numerical simulation at high Reynolds number, Journal of Fluids and Structures 04/2019; `DOI:10.1016/j.jfluidstructs.2019.02.011`

ARTICLES IN BOOKS

1. **A. Marouf**, N. Simiriotis, J-B. Tô, Y. Bmegaptche, Y. Hoarau, M. Braza : DDES and OES Simulations of a Morphing Airbus A320 Wing and Flap in Different Scales at High Reynolds, In book: Progress in Hybrid RANS-LES Modelling. January 2020, ISBN : 978-3-030-27607-2, `https://doi.org/10.1007/978-3-030-27607-2_20`
2. G. Jodin, N. Simiriotis, A. Aalilija, **A. Marouf**, Y. Hoarau, G. Harran, J. F. Rouchon, M. Braza: Fluid-Structure Interaction and Control Around Vibrating and Morphing Configurations at High Reynolds Number, Fluid-Structure-Sound Interactions and Control, 01/2019: pages 199-206; , ISBN: 978-981-10-7541-4, `DOI:10.1007/978-981-10-7542-1_30`

ARTICLES IN LEARNED SOCIETIES

1. **A. Marouf**, N. Simiriotis, J-B. To, J-F. Rouchon, Y. Hoarau and M. Braza. Morphing for Smart Wing Design through RANS/LES Methods, Progress in RANS-based Scale-Resolving Flow Simulation Methods II, S. Jakirlic et al. ERCOFTAC Bulletin N° 121, December 2019. `https://www.ercoftac.org/publications/ercoftac_bulletin/bulletin-122/`

INDEXED CONFERENCE PROCEEDINGS

1. **A. Marouf**, Y. Hoarau, J. Vos, D. Charbonnier, Y. Bmegaptche Tekap, M. Braza. Evaluation of the aerodynamic performance increase thanks to a morphing A320 wing with high-lift flap by means of CFD Hi-Fi approaches, American Institute of Aeronautics and Astronautics AIAA, Aviation Forum, invited SMS Session, Dallas 17-21 June 2019 `https://doi.org/10.2514/6.2019-2912`
2. Y. Bmegaptche Tekap, A. Giraud, G. Jodin, C. Nadal, **A. Marouf**, I.G. Martinez, D. Harribey, B. Nogarede, J-F. Rouchon, M. Braza. Design of a Large-Scale High-Lift Morphing A320 Wing Based on Electro-Mechanical Actuators and Shape Memory Alloys, American Institute of Aeronautics and Astronautics AIAA, Aviation Forum, invited SMS Session, Dallas 17-21 June 2019 `https://doi.org/10.2514/6.2019-2908`

3. N. Simiriotis, K. Diakakis, G. Jodin, F. Kramer, **A. Marouf**, Y. Hoarau, J-F Rouchon, G. Tzabiras, M. Braza. Synthesis on High-Fidelity Numerical simulation of a morphing A320 wing in subsonic speeds and sensitivity evaluation, American Institute of Aeronautics and Astronautics AIAA, Aviation Forum, invited SMS Session, Dallas 17-21 June 2019 `https://doi.org/10.2514/6.2019-2911`
4. J-B Tô, P. Flaszynski, N. Simiriotis, **A. Marouf**, R. Szwaba, P. Doerffer, M. Braza. Aerodynamic performance of a bio-inspired A320 morphing wing in the transonic regime, American Institute of Aeronautics and Astronautics AIAA, Aviation Forum, invited SMS Session, Dallas 17-21 June 2019 `https://doi.org/10.2514/6.2019-2909`

INTERNATIONAL CONFERENCES

1. **A. Marouf**, Y. Bmegaptche Tekap, N. Simiriotis, J-B. Tô, J.-F. Rouchon, Y. Hoarau, M. Braza. Numerical and experimental investigation of frequency and amplitude effects of a morphing wing in one/two element configurations at high Reynolds number, 54th 3AF International Conference on Applied Aerodynamics, Paris - France; 03/2019 `http://3af-aerodynamics2019.com/wp-content/uploads/AERO2019_PROGRAMME_22032019.pdf`
2. **A. Marouf**, Y. Bmegaptche Tekap, N. Simiriotis, J.-B. Tô, J.-F. Rouchon, Y. Hoarau, M. Braza. Predictive numerical study of cambered morphing A320 high-lift configuration based on Electro-Mechanical Actuators, 5th Symposium on Fluid-Structure-Sound Interactions and Control, 27-30 August 2019, Crete island, Greece, `http://smartwing.org/FSSIC2019`
3. **A. Marouf**, Y. Bmegaptche Tekap, N. Simiriotis, J.-B. Tô, J.-F. Rouchon, Y. Hoarau, M. Braza. Aerodynamic performance increase of a morphing A320 wing with high-lift flap by means of Hi-Fi CFD approache, 9th EASN International Conference on Innovation in Aviation & Space, Invited SMS Session, 2019, Athens, Greece `https://easnconference.eu/sites/default/files/9th_EASN_Final_Agenda.pdf`
4. **A. Marouf**, N. Simiriotis, J-B. Tô, Y. Bmegaptche Tekap, Y. Hoarau, M. Braza. Numerical investigation of one and two element wing-flap with a morphing flap at high Reynolds numbers using hybrid models. 7th Symposium on Hybrid RANS-LES Methods, Berlin - Germany; 09/2018 `https://hrlm7.sciencesconf.org/218303`

5. **A. Marouf**, N. Simiriotis, J.B Tô, Y. Bmegaptche Tekap, Y. Hoarau, J.-F. Rouchon, M. Braza. Numerical study of trailing-edge dynamics of a two element airfoil-flap with morphing flap at high Reynolds number, IUTAM 2018, "Critical flow dynamics involving moving/deformable structures with design applications", 18-22 June 2018, Santorini island, Greece, `http://smartwing.org/IUTAM`
6. P. Flaszynski, R. Szwaba, P. Doerffer, J-B. To, N. Simiriotis, **A. Marouf**, J.F. Rouchon, M. Braza. Aerodynamic Performance of an A320 type morphing wing in the transonic regime, 9th EASN International Conference on Innovation in Aviation & Space, Invited SMS Session, Invited SMS Session, 2019, Athens, Greece
7. N. Simiriotis, **A. Marouf**, K. Diakakis, G. Tzabiras, F. Kramer, F. Thiele, M. Braza. High-Fidelity Numerical simulation of a morphing A320 wing in subsonic speeds and sensitivity evaluation. 9th EASN International Conference on Innovation in Aviation & Space, Invited SMS Session, Invited SMS Session, 2019, Athens, Greece
8. G. Jodin, N. Simiriotis, **A. Marouf**, J-B. Tô, J-F. Rouchon, M. Braza. Electroactive morphing for the wings of the future design through turbulent wakes manipulation, International colloquium on bluff body flows. 4 - 5 July 2019 Strasbourg, France
9. Y. Bmegaptche Tekap, G. Jodin, **A. Marouf**, J.B Tô, G. Harran, J.-F. Rouchon, M. Braza. Wind tunnel experimental investigation of an electroactive morphing high-lift flap on a two-element wing in subsonic speeds. IUTAM 2018, "Critical flow dynamics involving moving/deformable structures with design applications", 18-22 June 2018, Santorini island, Greece
10. J.B Tô, D.M ZILLI, N. Simiriotis, **A. Marouf**, Y. Hoarau, M. Braza. Numerical simulation and modelling of a morphing supercritical airfoil in a transonic flow at high Reynolds numbers. IUTAM 2018, "Critical flow dynamics involving moving/deformable structures with design applications", Santorini, Greece; 06/2018
11. N. Simiriotis, G. Jodin, **A. Marouf**, Y. Hoarau, J.-F. Rouchon, M. Braza. Experimental and Numerical Investigation of Electro-Active Morphing on a supercritical wing in high Reynolds numbers. IUTAM 2018, "Critical flow dynamics involving moving/deformable structures with design applications", Santorini, Greece; 06/2018

12. N. Simiriotis, G. Jodin, **A. Marouf**, Y. Hoarau, J.-F. Rouchon, M. Braza. Electroactive morphing on a supercritical wing targeting improved aerodynamic performance and flow control in high Reynolds numbers, 53rd 3AF International Conference on Applied Aerodynamics 26 – 28 March 2018, Salon de Provence Paris – France, ; 03/2018 `http://3af-aerodynamics2018.com/wp-content/uploads/AERO2018_PROGRAMME_VF_20032018.pdf`
13. G. Jodin, N Simiriotis, A Aalilija, **A. Marouf**, Y Hoarau, G Harran, J F Rouchon, M Braza. Fluid-Structure Interaction and Control around vibrating and morphing configurations at high Reynolds number. Fluid-Structure Interaction and Control around vibrating and morphing configurations at high Reynolds number, Tokyo-Japan 08/2017 `http://www.fssic.com/2017conference/FSSIC2017_Programme.pdf`
14. J.B. Vos , D. Charbonnier , A. Jungo, **A. Marouf** , N. Simiriotis , M. Braza. CFD Simulations on Morphing Wings and Aircraft in the frame of the European funded H2020 SMS Project, 5th Symposium on Fluid-Structure-Sound Interactions and Control 27-30 August 2019, Crete island, Greece
15. Y. Bmegaptche Tekap, A. Giraud, **A. Marouf**, C. Nadal, G. Harran, J-F. Rouchon, M. Braza. Design and structural analysis of a320 large scale morphing flap based on electro-mechanical actuators, 5th Symposium on Fluid-Structure-Sound Interactions and Control 27-30 August 2019, Crete island, Greece
16. J.-B. Tô 1, N. Simiriotis, **A. Marouf**, Y. Hoarau, J.-F. Rouchon, C. Nadal AND M. Braza. Manipulation of a shock-wave/boundary-layer interaction in the transonic regime around a supercritical morphing wing, 5th Symposium on Fluid-Structure-Sound Interactions and Control 27-30 August 2019, Crete island, Greece
17. N. Simiriotis, **A. Marouf**, G. Jodin, Y. Hoarau, J.C.R. Hunt, J.F. Rouchon and M. Braza. High-Fidelity Numerical simulation of morphing and the suppression of the 3D instabilities. Hybrid morphing for highlift configuration 5th Symposium on Fluid-Structure-Sound Interactions and Control 27-30 August 2019, Crete island, Greece

AWARDS AND RECOGNITIONS

- **Best communication award 2018** in the 53th International Conference on Applied Aerodynamics 3AF – Salon de Provence, March 2018, France mentioned in the N° 39 of the Journal "Lettre 3AF", of the "Association d' Aéronautique et d' Astronautique de France". `https://www.3af.fr/sites/default/files/lettre-3af-39-110919-preview-2.pdf`

- **Best poster award 2018** in the competition of PhD students in the doctoral school ED MSII 269 Strasbourg (compétition des doctorants).

- **Best conference poster award (two finalists)** in the International Union of Theoretical and Applied Mechanics IUTAM conference 18-2 June, Santorini, Greece: Wind tunnel experimental design of an electroactive morphing high-lift flap on a two-element wing in subsonic speeds. Y. Bmegaptche, G. Jodin, A. Marouf, J.B. Tô, G. Harran, J.F. Rouchon & M. Braza. `http://smartwing.org/iutam/?q=best_poster_award`

LARGE PUBLIC DISSEMINATION ACTIVITIES

- Creation and maintenance of the official web site of the SMS EU project: `http://smartwing.org/SMS/EU/`

- Creation and maintenance of the official site of the IUTAM Symposium "Critical flow dynamics involving moving/deformable structures with design applications", `http://smartwing.org/iutam/`, Santorini island, Greece, 18-22 June, 2018 and contribution to the final editing of the Symposium proceedings - Publisher Springer.

- Creation and maintenance of the official site of the FSSIC Symposium "5th Symposium on Fluid-Structure-Sound Interactions and Control", `hhttp://smartwing.org/FSSIC2019/`, 27-30 August 2019, Chania, Crete island, Greece and contribution to the final editing of the Symposium proceedings - Publisher Springer.

- **The European Researchers' Night (La Nuit européenne des Chercheurs)-Toulouse** : participation in the stand of INPT/CNRS/IMFT/LAPLACE Laboratories at the European Researchers' Night (Nuit Européenne des Chercheurs) on 29th September 2017 at the "Quai des Savoirs", in Toulouse, France. `http://smartwing.org/SMS/EU/the-researchers-night-la-nuit-des-chercheurs/`

- **The day of science (Fête de la science) in France, 15 October 2017** : Participation in IMFT's open morphing Laboratory and visit of the wind tunnels S1, S4 to a large people's audience showing them the studies that carried and visits of wind tunnels and specially the bio-inspired electroactive morphing of wings in the SMS project.

- **Aeroscopia Museum, Toulouse - Blagnac, October 2017**: Participation in the visit of the SMS stand displaying the bio-inspired electroactive morphing wings. `http://smartwing.org/SMS/EU/aeroscopia/`

- Participation in EuroScience Open Forum – ESOF 2018 Toulouse, video link : `http://smartwing.org/SMS/EU/2018/07/10/euroscience-open-forum-esof-2018-toulouse/`

- Results of the present thesis were presented in the SMS stands hosted by INEA of the European Commission at the "Innovation and Leadership in Aerospace" ILA Berlin 25 - 29 April 2018, Germany and in the 7th Transport Research Arena (TRA) by the EU Commission Vienna 16-19 April 2018, Austria.

Appendix A

Power Spectral Density (PSD)

The PSD is applied on a signal $x(t)$ of a specific physical flow property extracted from the Hi-Fi numerical simulation in the present thesis. The signal could be the drag or lift versus time, the velocity components (u_1,u_2,u_3) and pressure. This method contributes to investigate the turbulence spectrum obtained through the simulations and composed of predominant frequency peaks and of a continuous part extended from the low to the high frequency range.

In the following chapters, the role of the signal processing is major in our study. The purpose is to identify and understand the flow behaviour around and behind in the wake of the A320 prototypes and to analyse its modification when dynamic morphing is applied near the trailing edge area.

There are two main methods of power spectral density estimation presented in figure A.1 : non-parametric and parametric methods.

Non-parametric methods are less computational complex than the parametric models. Moreover, these methods are divided into two categories : Periodograms and Correlograms. Periodograms refer to direct methods because they use a direct transformation of the signal. Correlograms are known as indirect methods. These methods are based on computing the Fourier transform of some sort of estimate of the autocorrelation sequence. Due to a high amount of variance associated with higher order lags (in case where a small amount of data samples are used in the correlations), windowing is used. The Blackman-Tukey method generalizes the correlogram methods.

In the next chapters, the PSD estimation is based on the non-parametric periodogram and a splitting of the signal into a number of subsets along which the PSD is evaluated according to Welch method (Welch (1967)). This method reduces the spectral noise level whenever the size of the chosen windows is optimal ("slipping FFT"). It

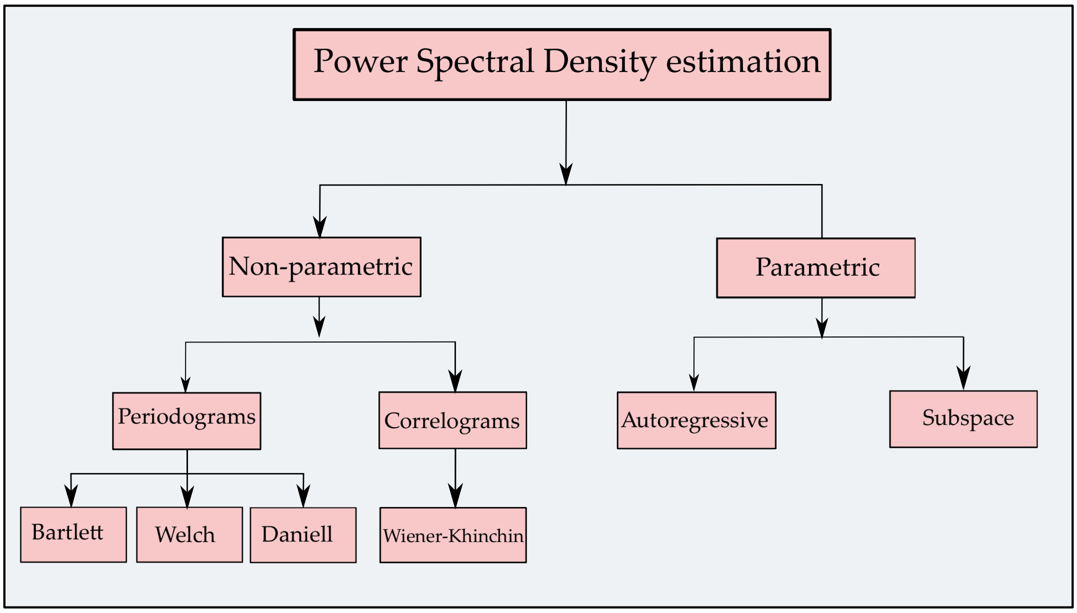

FIGURE A.1: Overview of the PSD estimations methods used in signal processing.

generalizes the Bartlett's method (Babtlett (1948)) by using overlaping and windowing PSD "samples".

To describe the Welch method in a mathematical form (Stoica and Moses (2005)), let :

$$y_j(t) = y((j-1)K + t), \quad t = 1, ..., M, \quad j = 1, ..., S \tag{A.1}$$

denote the j^{th} data segment. In A.2, $(j-1)K$ is the starting point for the j^{th} sequence of observations. K = M, then the sequences do not overlap (but are contiguous) and we get the sample splitting used by the Bartlett method with data sub-samples. However, the value recommended for K in the Welch method (Welch (1967)) is K = M/2 (with 50 % overlap between successive segments that could be obtained.

The windowed periodogram corresponding to $y_j(t)$ is computed as :

$$\phi_j(\omega) = \frac{1}{MP} |\sum_{t=1}^{M} v(t) y_j(t) e^{-i\omega t}|^2 \tag{A.2}$$

Where P denotes the "power" of the temporal window $v(t)$:

$$P = \frac{1}{M} \sum_{t=1}^{M} |v(t)|^2 \tag{A.3}$$

The Welch estimate of PSD is determined by averaging the windowed periodograms in A.2

$$\phi_W(\omega) = \frac{1}{S}\sum_{j=1}^{S} \phi_j(\omega) \tag{A.4}$$

The modifications made over the Bartlett method are made to allow the overlap between the data segments and to get more perdiogorams to be averaged in order to to decrease the variance of the estimated PSD.
The Welch estimator is related to the Blackman-Tukey (Blackman and Tukey (1958)) spectral estimator by a straightforward calculation, same as in the Bartlett method by inserting A.2 in A.4 :

$$\phi_W(\omega) = \frac{1}{S}\sum_{j=1}^{S} \frac{1}{MP}\sum_{t=1}^{M}\sum_{k=1}^{M} v(t)v^*(k)y_j(t)y_j^*(k)e^{-i\omega(t-k)} \tag{A.5}$$

We assume for the covariance r that the sum does not depend on both t and K, but only on their difference $(t-k)$, as following :

$$\tilde{r}(t,k) = \frac{1}{S}\sum_{j=1}^{S} y(t)y_j^*(k) \approx \tilde{r}(t-k) \tag{A.6}$$

Putting A.6 in A.5 and after several steps and having $\tau = t - k$:

$$\phi_W(\omega) \approx \sum_{\tau=-(M-1)}^{M-1} w(\tau)\tilde{r}(\tau)e^{-i\omega\tau} \tag{A.7}$$

To summarize, the Welch estimator has been shown to approximate a Blackman-Tukey estimator for the estimated covariance sequence A.6 which may be expected to have finite-sample properties different from those of $\hat{r}(k)$.
The Welch method of estimation can be efficiently computed via the FFT, and is one of the most frequently used PSD estimation methods. The usual covariance $\hat{r}(k)$ can be replaced in the Blackman-Tukey estimator by other sample covariances in the purpose to reducing the computational CPU cost and improving the statistical accuracy.
To obtain important information from experimental or numerical signals based on pressure or velocity measurements, different parameters of the Welch method have been examined such as the window type, which can be Hanning, Rectangular, Gaussian or Hamming windows. The Hamming window revealed the predominant frequencies present in the wake compared to other windows. This last has been chosen for the computation of Power Spectral Density in our studies. Different window lengths have been tested and demonstrated in the figure (A.2), which shows a PSD of

an experimental signal of instantaneous static pressure obtained from piezo-resistive sensors placed in a two-element wing-flap configuration (at 72 % of the flap's chord) and tested at the IMFT wind tunnel. Reducing the window length up to 10 % of the total length of the signal revealed small bumps (see figure A.2 (c)) between 50 Hz and 100 Hz that were hidden in larger windows due to the noise and bad averaging for the windowing. Small windows are able to attenuate the random noise and show up predominant frequencies related to the coherent structures present in the wake such as the shear-layer instabilities.

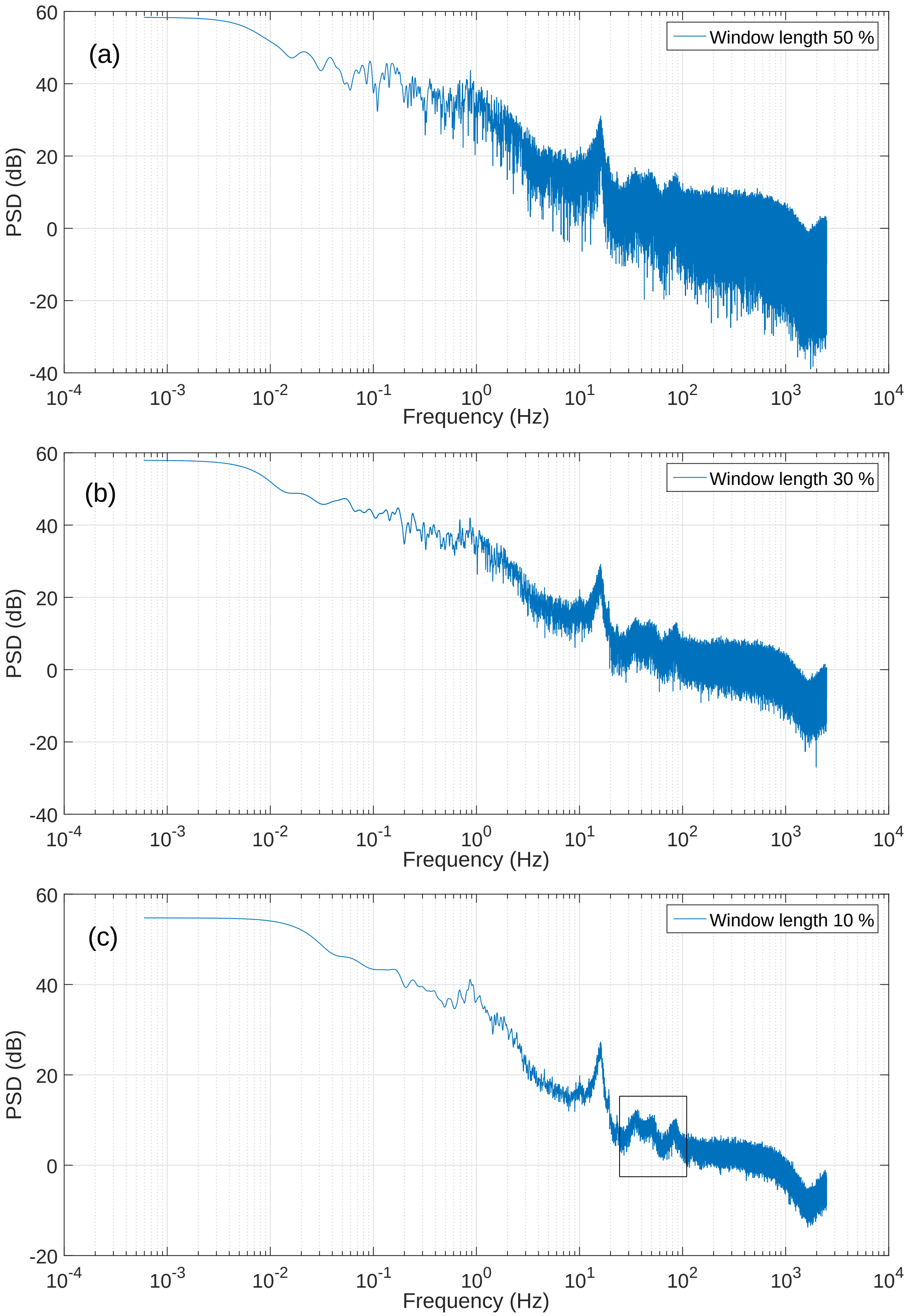

FIGURE A.2: Comparison of different window lengths using the Hamming window in the Welch method. (a) : 50 %. (b) : 30 %. (c) : 10 %

Bibliography

C. Abdessemed, Y. Yao, A. Bouferrouk, and P. Narayan. Morphing airfoils analysis using dynamic meshing. *International Journal of Numerical Methods for Heat & Fluid Flow*, pages 00–00, April 2018a. URL `https://doi.org/10.1108/hff-06-2017-0261`.

C. Abdessemed, Y. Yao, A. Bouferrouk, and P. Narayan. Analysis of a 3d unsteady morphing wing with seamless side-edge transition. In *2018 Applied Aerodynamics Conference*. American Institute of Aeronautics and Astronautics, June 2018b. URL `https://doi.org/10.2514/6.2018-3178`.

J. Allain. *Analyse physique des mécanismes de transition tri-dimensionnelle dans le sillage d'un cylindre circulaire par simulation directe*. PhD thesis, 1999. URL `hhttp://www.theses.fr/1999INPT021H`. Thèse de Doctorat, Institut National Polytechnique de Toulouse.

M. S. Babtlett. Smoothing periodograms from time-series with continuous spectra. *Nature*, 161(4096):686–687, May 1948. URL `https://doi.org/10.1038/161686a0`.

G. Barbut, M. Braza, Y. Hoarau, G. Barakos, A. Sévrain, and J. B. Vos. Prediction of transonic buffet around a wing with flap. In *Progress in Hybrid RANS-LES Modelling*, pages 191–204. Springer Berlin Heidelberg, 2010. URL `https://doi.org/10.1007/978-3-642-14168-3_16`.

B. J. Bayly. Three-dimensional instability of elliptical flow. *Physical Review Letters*, 57 (17):2160–2163, October 1986. URL `https://doi.org/10.1103/physrevlett.57.2160`.

G Berkooz, P Holmes, and J L Lumley. The proper orthogonal decomposition in the analysis of turbulent flows. *Annual Review of Fluid Mechanics*, 25(1):539–575, jan 1993. URL `https://doi.org/10.1146/annurev.fl.25.010193.002543`.

D. K. Bisset, J. C. R. Hunt, and M. M. Rogers. The turbulent/non-turbulent interface bounding a far wake. *Journal of Fluid Mechanics*, 451:383–410, January 2002. doi: 10.1017/s0022112001006759. URL https://doi.org/10.1017/s0022112001006759.

R. B. Blackman and J. W. Tukey. The measurement of power spectra from the point of view of communications engineering — part i. *The Bell System Technical Journal*, 37(1):185–282, January 1958. URL https://doi.org/10.1002/j.1538-7305.1958.tb03874.x.

J. Blazek. *Computational Fluid Dynamics: Principles and Applications*. Elsevier, 2005. URL https://doi.org/10.1016/b978-0-08-044506-9.x5000-0.

M. Susan Bloor. The transition to turbulence in the wake of a circular cylinder. *Journal of Fluid Mechanics*, 19(02):290, June 1964. URL https://doi.org/10.1017/s0022112064000726.

Y. Bmegaptche, A. Giraud, A. Marouf, A. Polo Domingez, G. Harran, M. Braza, and J.F. Rouchon. Design and experimental validation of A320 large scale morphing flap based on electro-mechanical actuators. In *5th Symposium on Fluid-Structure-Sound Interactions and Control*. Springer International Publishing, August 2019.

A. Bouhadji and M. Braza. Organised modes and shock–vortex interaction in unsteady viscous transonic flows around an aerofoil. *Computers & Fluids*, 32(9):1261–1281, November 2003a. URL https://doi.org/10.1016/s0045-7930(02)00101-9.

A. Bouhadji and M. Braza. Organised modes and shock–vortex interaction in unsteady viscous transonic flows around an aerofoil. *Computers & Fluids*, 32(9):1233–1260, November 2003b. URL https://doi.org/10.1016/s0045-7930(02)00100-7.

S. Bourdet, M. Braza, Y. Hoarau, R. El Akoury, A. Ashraf, G. Harran, P. Chassaing, and H. Djeridi. Prediction and physical analysis of unsteady flows around a pitching airfoil with the dynamic mesh approah. *European Journal of Computational Mechanics*, 16(3-4):451–476, jan 2007. URL https://doi.org/10.3166/remn.16.451-476.

R. Bourguet. *Analyse physique et modélisation d'écoulements turbulents instationnaires compressibles autour de surfaces portantes par approches statistiques haute-fidélité et de dimension réduite dans le contexte de l'interaction fluide-structure.* PhD thesis, 2008. URL https://oatao.univ-toulouse.fr/7756/. Thèse de doctorat dirigée par Braza, Marianna Dynamique des Fluides, université de Toulouse.

R. Bourguet, M. Braza, R. Perrin, and G. Harran. Anisotropic eddy-viscosity concept for strongly detached unsteady flows. *AIAA Journal*, 45(5):1145–1149, May 2007. URL `https://doi.org/10.2514/1.27916`.

R. Bourguet, M. Braza, G. Harran, and R. El Akoury. Anisotropic Organised Eddy Simulation for the prediction of non-equilibrium turbulent flows around bodies. *Journal of Fluids and Structures*, 24(8):1240–1251, 2008. URL `https://doi.org/10.1016/j.jfluidstructs.2008.07.004`.

R. Bourguet, M. Braza, A. Sévrain, and A. Bouhadji. Capturing transition features around a wing by reduced-order modeling based on compressible navier–stokes equations. *Physics of Fluids*, 21(9):094104, September 2009. URL `https://doi.org/10.1063/1.3234398`.

R. Bourguet, M. Braza, and A. Dervieux. Reduced-order modeling of transonic flows around an airfoil submitted to small deformations. *Journal of Computational Physics*, 230(1):159–184, January 2011. URL `https://doi.org/10.1016/j.jcp.2010.09.019`.

P. Bradshaw and P. V. Galea. Step-induced separation of a turbulent boundary layer in incompressible flow. *Journal of Fluid Mechanics*, 27(1):111–130, January 1967. URL `https://doi.org/10.1017/s0022112067000084`.

M. Braza, P. Chassaing, and H. Ha Minh. Numerical study and physical analysis of the pressure and velocity fields in the near wake of a circular cylinder. *Journal of Fluid Mechanics*, 165(-1):79, April 1986. URL `https://doi.org/10.1017/s0022112086003014`.

M. Braza, P. Chassaing, and H. Ha Minh. Prediction of large-scale transition features in the wake of a circular cylinder. *Physics of Fluids A: Fluid Dynamics*, 2(8):1461–1471, August 1990. URL `https://doi.org/10.1063/1.857594`.

M. Braza, D. Faghani, and H. Persillon. Successive stages and the role of natural vortex dislocations in three-dimensional wake transition. *Journal of Fluid Mechanics*, 439:1–41, July 2001. URL `https://doi.org/10.1017/s002211200100458x`.

M. Braza, R. Perrin, and Y. Hoarau. Turbulence Properties in the cylinder wake at high Reynolds number. *Journal of Fluids and Structures*, 22:757 – 771, 2006. URL `https://doi.org/10.1016/j.jfluidstructs.2006.04.021`.

G. L. Brown and A. Roshko. On density effects and large structure in turbulent mixing layers. *Journal of Fluid Mechanics*, 64(4):775–816, July 1974. URL `https://doi.org/10.1017/s002211207400190x`.

B. Cantwell and D. Coles. An experimental study of entrainment and transport in the turbulent near wake of a circular cylinder. *Journal of Fluid Mechanics*, 136(-1):321, November 1983. URL `https://doi.org/10.1017/s0022112083002189`.

Kuei-Yuan Chien. Predictions of channel and boundary-layer flows with a low-reynolds-number turbulence model. *AIAA Journal*, 20(1):33–38, January 1982. URL `https://doi.org/10.2514/3.51043`.

M. Chinaud, A. Boussaid, J. F. Rouchon, E. Duhayon, E. Deri, D. Harribey, and M. Braza. Thermo-mechanical coupling in nitinol. application to an electro-morphing plate. In *2012 XXth International Conference on Electrical Machines*. IEEE, September 2012. URL `https://doi.org/10.1109/icelmach.2012.6350249`.

M. Chinaud, J.F. Rouchon, E. Duhayon, J. Scheller, S. Cazin, M. Marchal, and M. Braza. Trailing-edge dynamics and morphing of a deformable flat plate at high reynolds number by time-resolved PIV. *Journal of Fluids and Structures*, 47:41–54, may 2014. URL `https://doi.org/10.1016/j.jfluidstructs.2014.02.007`.

A. J. Chorin. A numerical method for solving incompressible viscous flow problems. *Journal of Computational Physics*, 2(1):12–26, August 1967. URL `https://doi.org/10.1016/0021-9991(67)90037-x`.

A. Concilio, I. Dimino, L. Lecce, and R. Pecora. *Morphing Wing Technologies Large Commercial Aircraft and Civil Helicopters*. Elsevier, 2018. ISBN 978-0-08-100964-2. URL `https://doi.org/10.1016/c2015-0-01317-x`.

S. Corrsin and A. L. Kistler. Free-stream boundaries of turbulent flows. Technical report, 1955. URL `https://ntrs.nasa.gov/search.jsp?R=19930092246`.

J. Cruz and E. J. Miller. Evaluation of load analysis methods for NASA's GIII adaptive compliant trailing edge project. In *54th AIAA Aerospace Sciences Meeting*. American Institute of Aeronautics and Astronautics, January 2016. URL `https://doi.org/10.2514/6.2016-0804`.

T. Deloze. *Couplage fluide-solide appliqué à l'étude de mouvement d'une sphère libre dans un tube vertical*. PhD thesis, 2011. URL `http://www.theses.fr/2011STRA6033`. Thèse de doctorat dirigée par Dusek, Jan Mécanique des fluides Strasbourg 2011.

H. Djeridi, M. Braza, R. Perrin, G. Harran, E. Cid, and S. Cazin. Near-wake turbulence properties around a circular cylinder at high reynolds number. *Flow, Turbulence and Combustion (formerly Applied Scientific Research)*, 71(1-4):19–34, 2003. URL `https://doi.org/10.1023/b:appl.0000014930.49408.53`.

P. Doerffer, P. Flaszynski, J-P. Dussauge, H. Babinsky, P. Grothe, A. Petersen, and F. Billard, editors. *Transition Location Effect on Shock Wave Boundary Layer Interaction*. Springer International Publishing, 2020. URL `https://doi.org/10.1007/978-3-030-47461-4`.

J. Donea, S. Giuliani, and J.P. Halleux. An arbitrary lagrangian-eulerian finite element method for transient dynamic fluid-structure interactions. *Computer Methods in Applied Mechanics and Engineering*, 33(1-3):689–723, sep 1982. URL `https://doi.org/10.1016/0045-7825(82)90128-1`.

R. El-Akoury. *Physical analysis of the wall rotation effects in transitional flows and modelling of turbulent flows around lifting bodies.* PhD thesis, Toulouse, France, 2007. URL `http://ethesis.inp-toulouse.fr/archive/00000567/`. Thèse de doctorat dirigée par Braza, Marianna Dynamique des fluides.

R. El-Akoury, M. Braza, R. Perrin, G. Harran, and Y. Hoarau. The three-dimensional transition in the flow around a rotating cylinder. *Journal of Fluid Mechanics*, 607: 1–11, June 2008. URL `https://doi.org/10.1017/s0022112008001390`.

A. Giraud, C. Raibaudo, M. Cronel, P. Mouyon, I. Ramos, and C. Doll. Camber Setting of a morphing wing with macro-actuator feedback control. In *5th Symposium on Fluid-Structure-Sound Interactions and Control*. Springer International Publishing, August 2019.

F. Grossi. *Physique et modélisation d'interactions instationnaires onde de choc/couche limite autour de profils d'aile transsoniques par simulation numérique*. PhD thesis, 2014. URL `http://www.theses.fr/2015INPT0105`. These de Doctorat, Institut National Polytechnique de Toulouse.

F. Grossi, M. Braza, and Y. Hoarau. Prediction of transonic buffet by delayed detached-eddy simulation. *AIAA Journal*, 52(10):2300–2312, oct 2014. URL `https://doi.org/10.2514/1.j052873`.

M. Guillaume, A. Gehri, P. Stephani, J. Vos, and G. Mandanis. F/a-18 vertical buffeting calculations using unsteady fluid structure interaction. *The Aeronautical Journal*, 115:285–294, 2011. URL `https://doi.org/10.1017/S0001924000005777`.

W. Haase, M. Braza, and A. Revell. *DESider – A European Effort on Hybrid RANS-LES Modelling*. Springer Berlin Heidelberg, 2009. doi: 10.1007/978-3-540-92773-0. URL `https://doi.org/10.1007/978-3-540-92773-0`.

A. Harten. High resolution schemes for hyperbolic conservation laws. *Journal of Computational Physics*, 135(2):260–278, August 1997. URL `https://doi.org/10.1006/jcph.1997.5713`.

A. Harten, B. Engquist, S. Osher, and S. R. Chakravarthy. Uniformly high order accurate essentially non-oscillatory schemes, III. *Journal of Computational Physics*, 71(2): 231–303, August 1987. URL `https://doi.org/10.1016/0021-9991(87)90031-3`.

J.O. Hinze. *Turbulence*. McGraw-Hill, 1987. URL `https://books.google.fr/books?id=Pm-0nQAACAAJ`.

Y. Hoarau. *Analyse physique par simulation numérique et modélisation des écoulements décollés instationnaires autour de surfaces portantes*. PhD thesis, Toulouse, France, 2002. URL `http://theses.fr/2002INPT013H`. Thèse de doctorat dirigée par Braza, Marianna Dynamique des fluides.

Y. Hoarau, M. Braza, Y. Ventikos, D. Faghani, and G. Tzabiras. Organized modes and the three-dimensional transition to turbulence in the incompressible flow around a NACA0012 wing. *Journal of Fluid Mechanics*, 496:63–72, December 2003. URL `https://doi.org/10.1017/s0022112003006530`.

Y. Hoarau, M. Braza, Y. Ventikos, and D. Faghani. First stages of the transition to turbulence and control in the incompressible detached flow around a NACA0012 wing. *International Journal of Heat and Fluid Flow*, 27(5):878–886, oct 2006. URL `https://doi.org/10.1016/j.ijheatfluidflow.2006.03.026`.

Y. Hoarau, D. Pena, J. B. Vos, D. Charbonnier, A. Gehri, M. Braza, T. Deloze, and E. Laurendeau. Recent Developments of the Navier Stokes Multi Block (NSMB) CFD solver. In *54th AIAA Aerospace Sciences Meeting*, 2016. URL `10.2514/6.2016-2056`.

J. C. R. Hunt, T. Ishihara, D. Szubert, I. Asproulias, Y. Hoarau, and M. Braza. Turbulence near interfaces—modelling and simulations. In *Notes on Numerical Fluid Mechanics and Multidisciplinary Design*, pages 283–292. Springer International Publishing, 2016. URL `https://doi.org/10.1007/978-3-319-27386-0_17`.

J. C.R Hunt and P.A. Durbin. Perturbed vortical layers and shear sheltering. *Fluid Dynamics Research*, 24(6):375–404, jun 1999. URL `https://doi.org/10.1016/s0169-5983(99)00009-x`.

J.C.R. Hunt, I. Eames, and J. Westerweel. Vortical interactions with interfacial shear layers. In *In Kaneda, Y.(Ed.), IUTAM Symposium on Computational Physics and New Perspectives in Turbulence, IUTAM Bookseries, vol.4, Springer, Nagoya, Japan, pp.331–338*, 2008. URL `https://doi.org/10.1007/978-1-4020-6472-2_50`.

A. K. M. F. Hussain and W. C. Reynolds. The mechanics of an organized wave in turbulent shear flow. *Journal of Fluid Mechanics*, 41(2):241–258, April 1970. URL `https://doi.org/10.1017/s0022112070000605`.

T. Ishihara, H. Ogasawara, and J. C.R. Hunt. Analysis of conditional statistics obtained near the turbulent/non-turbulent interface of turbulent boundary layers. *Journal of Fluids and Structures*, 53:50–57, feb 2015. URL `https://doi.org/10.1016/j.jfluidstructs.2014.10.008`.

L. Jacquin, P. Molton, S. Deck, B. Maury, and D. Soulevant. Experimental study of shock oscillation over a transonic supercritical profile. *AIAA Journal*, 47(9):1985–1994, September 2009. URL `https://doi.org/10.2514/1.30190`.

L. Jenkins, M. Khorrami, M. Choudhari, and C. McGinley. Characterization of unsteady flow structures around tandem cylinders for component interaction studies in airframe noise. In *11th AIAA/CEAS Aeroacoustics Conference*. American Institute of Aeronautics and Astronautics, May 2005. doi: 10.2514/6.2005-2812. URL `https://doi.org/10.2514/6.2005-2812`.

G. Jin and M. Braza. Two-equation turbulence model for unsteady separated flows around airfoils. *AIAA Journal*, 32(11):2316–2320, nov 1994. URL `https://doi.org/10.2514/3.12292`.

G. Jodin, V. Motta, J. Scheller, E. Duhayon, C. Döll, J.F. Rouchon, and M. Braza. Dynamics of a hybrid morphing wing with active open loop vibrating trailing edge by time-resolved PIV and force measures. *Journal of Fluids and Structures*, 74:263–290, October 2017. URL `https://doi.org/10.1016/j.jfluidstructs.2017.06.015`.

G Jodin, Y Bmegaptche Tekap, J M Saucray, J F Rouchon, M Triantafyllou, and M Braza. Optimized design of real-scale a320 morphing high-lift flap with shape memory alloys and innovative skin. *Smart Materials and Structures*, 27(11):115005, October 2018. URL `https://doi.org/10.1088/1361-665x/aae2ef`.

M. J. Landman and P. G. Saffman. The three-dimensional instability of strained vortices in a viscous fluid. *Physics of Fluids*, 30(8):2339, 1987. URL `https://doi.org/10.1063/1.866124`.

J. Lawley, H. Ben-Gida, K. Krishnamoorthy, E. E Hackett, G. A Kopp, G. Morgan, C. G. Guglielmo, and R. Gurka. Flow features of the near wake of the australian boobook owl (ninox boobook) during flapping flight suggest an aerodynamic mechanism of sound suppression for stealthy flight. *Integrative Organismal Biology*, 1(1), January 2019. URL `https://doi.org/10.1093/iob/obz001`.

Meng-Sing Liou and Christopher J. Steffen. A new flux splitting scheme. *Journal of Computational Physics*, 107(1):23–39, July 1993. URL `https://doi.org/10.1006/jcph.1993.1122`.

Xu-Dong Liu, Stanley Osher, and Tony Chan. Weighted essentially non-oscillatory schemes. *Journal of Computational Physics*, 115(1):200–212, November 1994. URL `https://doi.org/10.1006/jcph.1994.1187`.

Weishuang LU, Yun TIAN, and Peiqing LIU. Aerodynamic optimization and mechanism design of flexible variable camber trailing-edge flap. *Chinese Journal of Aeronautics*, 30(3):988–1003, June 2017. URL `https://doi.org/10.1016/j.cja.2017.03.003`.

G. Martinat, M. Braza, Y. Hoarau, and G. Harran. Turbulence modelling of the flow past a pitching NACA0012 airfoil at and reynolds numbers. *Journal of Fluids and Structures*, 24(8):1294–1303, nov 2008. URL `https://doi.org/10.1016/j.jfluidstructs.2008.08.002`.

J. B. McDevitt, L. L. Levy, and G. S. Deiwert. Transonic flow about a thick circular-arc airfoil. *AIAA Journal*, 14(5):606–613, may 1976. URL `https://doi.org/10.2514/3.61402`.

F. R. Menter. Two-equation eddy-viscosity turbulence models for engineering applications. *AIAA Journal*, 32(8):1598–1605, August 1994. URL `https://doi.org/10.2514/3.12149`.

F. R. Menter and M. Kuntz. Adaptation of eddy-viscosity turbulence models to unsteady separated flow behind vehicles. In *The Aerodynamics of Heavy Vehicles: Trucks, Buses, and Trains*, pages 339–352. Springer Berlin Heidelberg, 2004. URL `https://doi.org/10.1007/978-3-540-44419-0_30`.

C. Moussaed, S. Wornom, B. Koobus, A. Dervieux, T. Deloze, R. El Akoury, D. Szubert, Y. Hoarau, and M. Braza. VMS and OES-based hybrid simulations of bluff body flows. In *Notes on Numerical Fluid Mechanics and Multidisciplinary Design*, pages 293–308. Springer International Publishing, 2016. URL `https://doi.org/10.1007/978-3-319-27386-0_18`.

V. C. Patel, W. Rodi, and G. Scheuerer. Turbulence models for near-wall and low reynolds number flows - a review. *AIAA Journal*, 23(9):1308–1319, September 1985. URL `https://doi.org/10.2514/3.9086`.

R Perrin. *Analyse physique et modelisation d'ecoulements incompressibles instationnaires turbulents autour d'un cylindre circulaire a grand nombre de Reynolds*. PhD thesis, 2005. URL `http://www.theses.fr/2015INPT0105`. Thèse de doctorat dirigée par Marianna Braza Dynamique des Fluides, Toulouse INP.

R. Perrin, M. Braza, E. Cid, S. Cazin, P. Chassaing, C. Mockett, T. Reimann, and F. Thiele. Coherent and turbulent process analysis in the flow past a circular cylinder at high reynolds number. *Journal of Fluids and Structures*, 24(8):1313–1325, November 2008. doi: 10.1016/j.jfluidstructs.2008.08.005. URL `https://doi.org/10.1016/j.jfluidstructs.2008.08.005`.

H. Persillon and M. Braza. Physical analysis of the transition to turbulence in the wake of a circular cylinder by three-dimensional navier–stokes simulation. *Journal of Fluid Mechanics*, 365:23–88, June 1998. URL `https://doi.org/10.1017/s0022112098001116`.

P. Rodes. *Contribution à l'étude d'écoulements instationnaires transtionnels et turbulents autour d'une aile par simulation numérique et modélisation*. PhD thesis, 1999. URL `http://www.theses.fr/1998AIX22059`. Thèse de doctorat dirigée par Favier, Daniel et Braza, Marianna, Physique Aix-Marseille 2 1999.

J. Scheller. *Electroactive morphing for the aerodynamic performance improvement of next generation airvehicles*. PhD thesis, 2015. URL `http://www.theses.fr/2015INPT0105`. Thèse de doctorat dirigée par Rouchon, Jean-François et Braza, Marianna Génie électrique, Toulouse INP.

J. Scheller, M. Chinaud, JF. Rouchon, E. Duhayon, S. Cazin, M. Marchal, and M. Braza. Trailing-edge dynamics of a morphing NACA0012 aileron at high Reynolds number by high-speed PIV. *Journal of Fluids and Structures*, 55:42–51, May 2015. URL `https://doi.org/10.1016/j.jfluidstructs.2014.12.012`.

H. Schlichting and K. Gersten. *Boundary-Layer Theory*. Springer Berlin Heidelberg, 2000. URL `https://doi.org/10.1007/978-3-642-85829-1`.

H. L. Seegmiller, J. G. Marvin, and L. L. Levy. Steady and unsteady transonic flow. *AIAA Journal*, 16(12):1262–1270, dec 1978. URL `https://doi.org/10.2514/3.61042`.

V. Shinde, T. Marcel, Y. Hoarau, T. Deloze, G. Harran, F. Baj, J. Cardolaccia, J.P. Magnaud, E. Longatte, and M. Braza. Numerical simulation of the fluid-structure interaction in a tube array under cross flow at moderate and high reynolds number. *Journal of Fluids and Structures*, 47:99–113, May 2014. URL `https://doi.org/10.1016/j.jfluidstructs.2014.02.013`.

N. Simiriotis. *Numerical study and physical analysis of electroactive morphing wings and hydrodynamic profiles at high Reynolds number turbulent flows*. PhD thesis, 2020. URL `http://theses.fr/s167856/`. Thèse de doctorat dirigée par Braza, Marianna , Institut National Polytechnique de Toulouse.

N. Simiriotis, G. Jodin, A. Marouf, P. Elyakime, Y. Hoarau, J.C.R. Hunt, J.F. Rouchon, and M. Braza. Morphing of a supercritical wing by means of trailing edge deformation and vibration at high Reynolds numbers: Experimental and numerical investigation. *Journal of Fluids and Structures*, 91:102676, November 2019. URL `https://doi.org/10.1016/j.jfluidstructs.2019.06.016`.

L. Sirovich. Turbulence and the dynamics of coherent structures. i. coherent structures. *Quarterly of applied mathematics*, 45(3):561–571, 1987. URL `refhub.elsevier.com/S0889-9746(15)00060-2/sbref57`.

M. Gual Skopek, M. Braza, Y. Hoarau, and F. Thiele. Hybrid RANS-LES modeling of a strongly detached turbulent flow around a tandem cylinders configuration. In *Progress in Hybrid RANS-LES Modelling*, pages 219–229. Springer Berlin Heidelberg, 2012. doi: 10.1007/978-3-642-31818-4_19. URL `https://doi.org/10.1007/978-3-642-31818-4_19`.

L. Smaguina Laval. *Analyse physique et modélisation d'écoulements instationnaires turbulents autour de structures portantes en aérodynamique externe*. PhD thesis, 1998. URL `http://www.theses.fr/1998AIX22059`. Thèse de doctorat dirigée par Favier, Daniel Physique Aix-Marseille 2 1998.

L. Soulat, A. Fosso Pouangué, and S. Moreau. A high-order sensitivity method for multi-element high-lift device optimization. *Computers & Fluids*, 124:105–116, January 2016. URL `https://doi.org/10.1016/j.compfluid.2015.10.013`.

P. Spalart and S. Allmaras. A one-equation turbulence model for aerodynamic flows. In *30th Aerospace Sciences Meeting and Exhibit*. American Institute of Aeronautics and Astronautics, January 1992. URL `https://doi.org/10.2514/6.1992-439`.

P. R. Spalart. Detached-eddy simulation. *Annual Review of Fluid Mechanics*, 41(1):181–202, jan 2009. URL `https://doi.org/10.1146/annurev.fluid.010908.165130`.

P. R. Spalart and C. L. Rumsey. Effective inflow conditions for turbulence models in aerodynamic calculations. *AIAA Journal*, 45(10):2544–2553, oct 2007. URL `https://doi.org/10.2514/1.29373`.

P. R. Spalart, S. Deck, M. L. Shur, K. D. Squires, M. Kh. Strelets, and A. Travin. A new version of detached-eddy simulation, resistant to ambiguous grid densities. *Theoretical and Computational Fluid Dynamics*, 20(3):181–195, may 2006. URL `https://doi.org/10.1007/s00162-006-0015-0`.

C. G. Speziale. Turbulence modeling for time-dependent RANS and VLES: A review. *AIAA Journal*, 36(2):173–184, February 1998. URL `https://doi.org/10.2514/2.7499`.

P. Stoica and R.L. Moses. *Spectral Analysis of Signals*. Pearson Prentice Hall, 2005. ISBN 9780131139565. URL `https://books.google.fr/books?id=h78ZAQAAIAAJ`.

W. Sutherland. LII. the viscosity of gases and molecular force. *The London, Edinburgh, and Dublin Philosophical Magazine and Journal of Science*, 36(223):507–531, dec 1893. URL `https://doi.org/10.1080/14786449308620508`.

D. Szubert. *Physics and modelling of unsteady turbulent flows around aerodynamic and hydrodynamic structures at high Reynold number by numerical simulation*. PhD thesis, 2015. URL `http://www.theses.fr/2015INPT0105`. Thèse de doctorat dirigée par Braza, Marianna , Institut National Polytechnique de Toulouse.

D. Szubert, F. Grossi, A. J. Garcia, Y. Hoarau, J. C. R. Hunt, and M. Braza. Shock-vortex shear-layer interaction in the transonic flow around a supercritical airfoil at high Reynolds number in buffet conditions. *Journal of Fluids and Structures*, 55:276–302, 2015. URL `https://doi.org/10.1016/j.jfluidstructs.2015.03.005`.

J.-B. Tô, N. Simiriotis, A. Marouf, D. Szubert, I. Asproulias, D.M. Zilli, Y. Hoarau, J.C.R. Hunt, and M. Braza. Effects of vibrating and deformed trailing edge of a morphing supercritical airfoil in transonic regime by numerical simulation at high Reynolds number. *Journal of Fluids and Structures*, 91:102595, November 2019. URL `https://doi.org/10.1016/j.jfluidstructs.2019.02.011`.

Bram van Leer. Towards the ultimate conservative difference scheme. v. a second-order sequel to godunov s method. *Journal of Computational Physics*, 32(1):101–136, July 1979. URL `https://doi.org/10.1016/0021-9991(79)90145-1`.

S. Venkateswaran and C. Merkle. Dual time-stepping and preconditioning for unsteady computations. In *33rd Aerospace Sciences Meeting and Exhibit*. American Institute of Aeronautics and Astronautics, January 1995. URL `https://doi.org/10.2514/6.1995-78`.

J. Vos, A. Rizzi, A. Corjon, E. Chaput, and E. Soinne. Recent advances in aerodynamics inside the NSMB (Navier Stokes Multi Block) consortium. In *36th AIAA Aerospace Sciences Meeting and Exhibit*, 1998. URL `https://doi.org/10.2514/6.1998-225`.

F. Waleffe. On the three-dimensional instability of strained vortices. *Physics of Fluids A: Fluid Dynamics*, 2(1):76–80, January 1990. URL `https://doi.org/10.1063/1.857682`.

J. M. Weiss and W. A. Smith. Preconditioning applied to variable and constant density flows. *AIAA Journal*, 33(11):2050–2057, nov 1995. URL `https://doi.org/10.2514/3.12946`.

P. Welch. The use of fast fourier transform for the estimation of power spectra: A method based on time averaging over short, modified periodograms. *IEEE Transactions on Audio and Electroacoustics*, 15(2):70–73, jun 1967. URL `https://doi.org/10.1109/tau.1967.1161901`.

C. H. K. Williamson. The existence of two stages in the transition to three-dimensionality of a cylinder wake. *Physics of Fluids*, 31(11):3165, 1988. URL `https://doi.org/10.1063/1.866925`.

C. H. K. Williamson. The natural and forced formation of spot-like 'vortex dislocations' in the transition of a wake. *Journal of Fluid Mechanics*, 243(-1):393, oct 1992. URL `https://doi.org/10.1017/s0022112092002763`.

C. H. K. Williamson. Vortex dynamics in the cylinder wake. *Annual Review of Fluid Mechanics*, 28(1):477–539, January 1996. URL `https://doi.org/10.1146/annurev.fl.28.010196.002401`.

Appendix B

Résumé étendu en Français

Résumé étendu en Français

Cette thèse vise à étudier la modélisation et l'analyse physique des ailes en morphing à différentes échelles et phases du vol en régime subsonique à l'aide de la simulations numérique haute-fidélité. Une attention particulière est portée à la compréhension physique fondamentale de l'écoulement autour des ailes d'Airbus et de son comportement lorsque le morphing est activé. Les concepts de morphing électroactifs sont mis en œuvre dans le solveur NSMB et examinés par une analyse d'amplitude et de fréquence suivant un comportement similaire à celui des patches piézo-électriques intégrés dans le bord de fuite de l'aile permettant d'avoir des déformations de basse amplitude couplées à des hautes fréquences et une série d'actionneurs électromécaniques (EMA) utilisés pour la cambrure des volets afin d'obtenir des grandes déformations avec bas fréquences. Des simulations bidimensionnelles et tridimensionnelles ont été effectuées en utilisant des approches de modélisation de la turbulence comme le modèles OES 'Organised Eddy Simulation' et les méthodes hybrides (RANS-LES) pour révéler les instabilités prédominantes du sillage sous forme de couches de cisaillement, Kelvin Helmholtz et les tourbillons de type von Kármán par l'analyse spectrale. Ces modèles sont capables de capturer les effets de morphing dans le sillage grâce aux actionnements. Un effort important est ensuite consacré afin de fournir des approches haute-fidélité Hi-Fi efficaces et d'effectuer une analyse modale avec la Décomposition Orthogonale aux valeurs Propres (POD) pour développer une Modélisation par Ordre Réduit (ROM) à travers les modes spatiaux et temporels de l'écoulement. Enfin, les forces aérodynamiques sont évaluées d'une échelle réduite des ailes vers une échelle réelle d'un avion réel. Ces études ont été menées dans le cadre de programme Européen de recherche du projet H2020 de Smart Morphing and Sensing (SMS).

INTRODUCTION

Chaque année 3 milliards des personnes dans la planète (soit 39 %) prennent un vol pour différentes raisons, soit pour le travail ou des voyages touristiques, mais aussi 50 milliards d'Euro de biens transportés autour du monde. L'augmentation des passagers est prévue d'atteindre 6 milliards vers 2030 selon les statistiques actuelles. La pollution atmosphérique à cause des gaz à effet de serre (due à l'échappement) produite par les avions et le bruit généré dans les phases de décollage et atterrissage sont aussi en augmentation. Les constructeurs d'avions comme Airbus et les institutions de recherches Européennes sont continuellement en recherche des solutions innovantes afin de construire des avions plus légers avec des géométries optimisées pour accroitre les performances aérodynamiques et réduire la consommation de carburant en même temps.

Notre équipe MécaFlu participe avec une grande collaboration de l'institut IMFT au sein d'un projet Européen 'Smart Morphing & Sensing' H2020 qui regroupe 10 partenaires depuis 5 différents pays avec un but de construire différentes échelles de prototype d'ailes en morphing d'Airbus A320 pour différentes phases de vol. Un concept innovant des ailes de futur ayant le but de réduire les émissions des gaz, réduire la consommation de carburant et le bruit aérodynamique avec une augmentation simultanée des performances aérodynamiques. Cela est réalisé par les matériaux électroactifs capables d'optimiser la forme aérodynamique des ailes dans toutes les phases des vols (décollage, montée, en palier, l'approche et l'atterrissage).

La technologie du morphing peut contribuer à diminuer le poids lié aux systèmes hydromécaniques montés sur l'aile pour piloter les volets et les becs pour différentes phases de vol. Il a été noté que si une réduction de 1 % de la trainée pouvait être obtenue grâce à ce concept, 140 millions de dollars par an pourraient être économisés sur la consommation de carburant nécessaire au fonctionnement de la flotte américaine.

La bio-inspiration de la nature était l'objet des observations de Clement Ader, Otto Lilienthal et les Wright Brothers qui ont parfaitement imités les oiseaux et appris comment voler. En fait, grâce à des expériences et à des comparaisons les chercheurs ont découvert que les avions peuvent atteindre une meilleure efficacité s'ils peuvent se comporter davantage comme les oiseaux en vol et la technologie du morphing le rend possible.

Les écoulements à grand nombre de Reynolds (vitesse) autour d'une configuration d'aile sont très complexes et donc leur compréhension est nécessaire afin d'obtenir des meilleures performances avec les ailes en morphing. les instabilités créées à cause de la présence d'un objet conduisent à une amplification drastique des paramètres locaux (pression pariétale, rotationnel dans la région proche), globaux (traînée et portance) et/ou à des cycles limites d'oscillation, pouvant provoquer la fatigue, voir la rupture de matériaux. La physique tridimensionnelle de ces phénomènes est gouvernée par l'interaction non-linéaire entre les vibrations de la structure, même de très faible amplitude et les modes d'instabilité naturelle développés dans la région proche du sillage. Cet échange énergétique entre le fluide turbulent et la structure apparaît dans des intervalles bien spécifiques du nombre de Reynolds et du nombre. Les vibrations induites ont des conséquences importantes en termes de rayonnement acoustique et de tenue en fatigue des structures soumises à ces instabilités ; ces effets sont donc à prendre en compte dans le dimensionnement des structures afin de répondre en particulier aux exigences de discrétion acoustique et de durée de vie des éléments profilés (gouvernes, propulseurs). Les méthodes utilisées actuellement nécessitent des améliorations quant au dimensionnement de ces différentes structures. Le développement de méthodes numériques de simulation d'Haute-Fidélité (Hi-Fi) d'écoulements turbulents permet d'envisager actuellement l'utilisation de techniques avancées pour répondre à des exigences de dimensionnement de structures en vibrations sous écoulement.

Le développement de ces méthodes de simulations est le fruit d'un travail académique de longue haleine au sein des programmes européens fédératifs impliquant ICUBE, qui trouve actuellement un intérêt dans des applications industrielles en vibrations sous écoulement. Le problème de prédiction de ces phénomènes dans les situations à grand nombre de Reynolds et l'élaboration de méthodes rapides et efficaces pour le 'design' par réduction de modèles, constituent ainsi une des priorités tant sur le plan de recherche fondamentale que dans le domaine des applications en interaction fluide-structure, pour le contrôle des instabilités par optimisation de forme et du comportement vibratoire.

Le projet Européen Smart Morphing and Sensing, est un projet Européen d'une durée

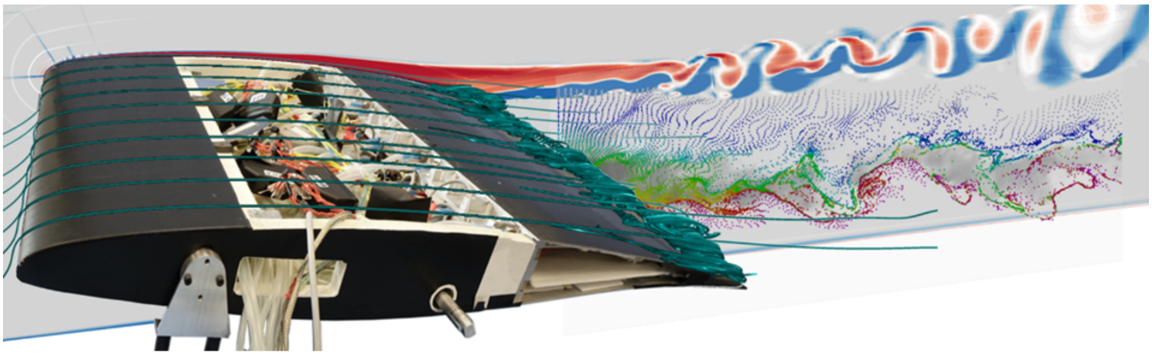

FIGURE 1: Le prototype à échelle réduite (Reduced-Scale) du projet Européen SMS (IMFT-LAPLACE) : experimentation TR-PIV de la soufflerie S4 de l'IMFT et résultats numérique CFDSM

de 3 ans. Il regroupe 10 partenaires Européen et a pour but d'augmenter la portance, diminuer la traînée et le bruit aérodynamique tout en utilisant les matériaux électroactifs (voir figure. 1) pour adapter la forme de l'aile selon différentes phases de vol. Ce projet a pour but de construire différents prototypes d'ailes d'avion d'Airbus A320 dédiés pour différentes phases de vol. Le prototype Transonic Reduced-Scale (TRS) de chorde 15cm est conçus par IMFT/LAPLACE et testé expérimentalement par l'IMP-PAN, Pologne partenaire du projet dans la soufflerie transsonique. Les prototypes Reduced-Scale (RS) et Large-Scale (LS) de chordes 0.7m et 2.40m respectivement sont construits et testé pour le régime subsonique correspondant aux phases du vol décollage et atterrissage.

METHODES NUMERIQUES ET MODELISATION DE TURBULENCE

Le morphing est implémenté dans le code NSMB en utilisant des lois de déformations similaires au morphing expérimental. Une déformation de l'aile est imposée avec un déplacement quadratique ou polynomial avec une dépendance de temps périodique (sinusoidal). La méthode Newtonienne est utilisée pour incrémenter ce déplacement au cours de la simulation. Ensuite, Les méthodes Trans-Finite Interpolation et Volume Spline Interpolation TFI et VSI sont utilisées pour la déformation du maillage et son adaptation à la nouvelle géométrie. Enfin, La méthode Arbitrary Lagrangian Eulerian ALE prend en charge cette déformation dans la résolution des équations de Navier-Stokes.

Les paramètres numériques sont choisis à la base d'une étude bien détaillée. La discrétisation numérique temporelle utilise un schéma implicite (dual time stepping). Pour la discrétisation spatial deux différents schémas sont sélectionnés. Les termes d'advection sont traités par un schéma central de 4ème ordre (4th order Skew Symmetric) et ceux de la diffusion avec un schéma 2ème ordre central. Dans le cadre dans ce travail nous avons utilisé pour les différentes simulations le code Navier-Stokes Multi-Block (NSMB) qui résout les équations de Navier-Stokes sous forme compressible. La méthode de la compressibilité artificielle est activée afin de simuler le régime bas subsonique selon l'hypothèse incompressible.

Dans les applications industrielles, la modélisation efficace de la turbulence pour la partie CFD présente des verrous importants : l'approche LES (Large Eddy Simulation) pure est encore peu applicable dans le contexte industriel, à cause de la naissance de la turbulence à partir de la paroi solide et de l'ordre de grandeur du nombre de Reynolds (O(10E6-10E8). Cependant la méthode DES (Detached Eddy Simulation) qui est hybride et comporte un modèle de turbulence RANS à l'intérieur de la couche limite et LES à l'extérieur. Cette méthode est très efficace pour capturer les instabilités instationnaires formées dans le sillage derrière l'aile.

Des méthodes de turbulence très avancées comme l'OES (Organised Eddy Simulation) et la DDES-OES (Delayed Detached Eddy Simulation) sont utilisées dans notre étude. L'OES est basée sur le moyennage de phase des champs de vitesse comme dans le principe de la LES. Ce principe permet des décomposer le spectre d'énergie en deux composantes, cohérentes qui seront résolues et chaotique qui seront modélisées. Cette méthode traite la non-égalité entre les termes de production et la dissipation dans les équations de transports. Cela afin de mieux capturer le comportement réel et physique de la couche limite surtout à grand angles d'incidence où se produit une séparation de la couche limite à cause d'un gradient de pression adverse. Cette dernière induit un grand cisaillement dans la zone de mélange qui peut provoquer la naissance des instabilités non-linéaires. La DDES-OES avec sa fonction de « delay » fd retarde le changement de l'OES vers la LES pour que la partie de forte gradient de vitesse dans la couche limite soit traiter par l'OES pour éviter le Modeled Stress Depletion (MSD). Ces modèles nous permettrons de valider et comparer les résultats numériques avec ceux de l'expérimental conduits par l'IMFT et POLIMI (Politecnico Di Milano).

Les modèles numériques que nous avons implémentés dans NSMB nous permettent d'obtenir un morphing hybride. Le premier axe concerne des vibrations à l'aide des patches piézo-électriques implémentés à la fin de l'aile (dans son bord de fuite) et permettent d'avoir des vibrations uniformes à grandes fréquences d'oscillation allant de 10Hz à 400 Hz avec des petites amplitudes de déformations 0.5mm – 1mm. Ce type de morphing est appliqué à 2 configurations différentes un prototype d'aile appelé Reduced-Scale d'une corde de 0.7m et un prototype Large-Scale d'une corde de 2.72m contenant deux éléments aile et volet proche de l'échelle réelle sous un régime subsonique (bas nombre de Mach).

MORPHING ELECTROACTIF DU REDUCED-SCALE AVEC LES VIBRATIONS DU BORD DE FUITE

Une compréhension physique des effets du morphing est proposée en synergie avec résultats expérimentaux avec Time-Resolved PIV. Les vibrations du bord de fuite à grande fréquence de 300 Hz associées à des petites déformations de 0.7 mm induisent beaucoup de modification dans le sillage qui a un effet de feedback sur les forces aérodynamiques. Une atténuation de la croissance maximale de l'instabilité secondaire est analysée avec la méthode d'instabilité elliptique. Cela conduit à la suppression du caractère tridimensionnel du sillage proche et la disparition des dislocations tourbillonnaires. La vitesse dans la direction d'envergure est drastiquement diminuée sous l'effet du morphing. Cette dernière est la principale cause de l'apparition de la tridimensionnalité sous forme de vorticité longitudinale et amplification de la longueur d'onde de l'instabilité secondaire. Les champs moyens de la vitesse longitudinale ont montré que le sillage s'est rétrécie et orienté vers le bas ce qui conduit à une augmentation de la portance. L'analyse spectrale (PSD) des signaux temporaux a révélé que l'instabilité dominante dans le sillage correspondante à l'amplitude de fréquence de la couche de cisaillement est réduite de -20 à -30 dB de son énergie sous l'actionnement du bord de fuite. Ces vibrations produisent des tourbillons de petites échelles qui

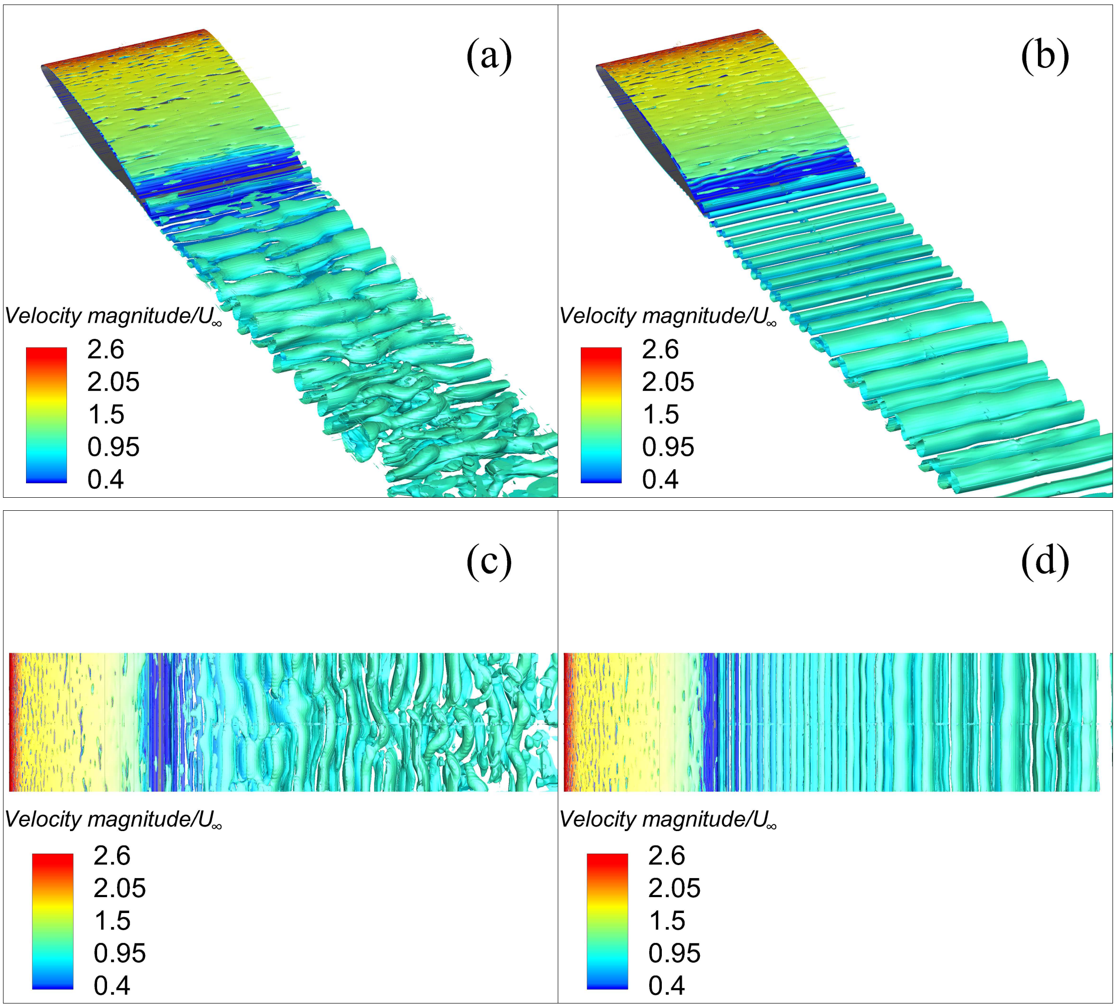

FIGURE 2: iso-surfaces du Q-criterion (Q=1500) coloré avec le champs de la vitesse non-dimensionnelle. (a) and (c) cas statique (pas de vibration), (b) and (d) cas morphing (avec vibration).

interagissent directement avec la zone de mélange. Un 'vortex breakdown' qui se produit lors de l'injection de ces tourbillons dans le sillage qui empêchent l'extension des instabilités de type von Kármán dans la direction verticale. Un rétrécissement de l'épaisseur de sillage est évalué avec la construction des modes la Décomposition Orthogonale Propre (Proper Orthogonal Decomposition) des modes spatiaux les moins énergétiques. Le morphing augmente l'énergie des structures chaotiques et fluctuantes. Ces structures interagissent avec les structures cohérentes et produisent une augmentation du transfert d'énergie turbulente ce qui cause ce rétrécissement du sillage. Ceci est similaire au forçage stochastique par l'ajout des termes sources aux équations de transport de l'énergie cinétique turbulence et celle de la dissipation examinée dans d'autres études précédentes. Cela augmente la production d'énergie turbulente et entraîne des effets similaires à ceux produits par le morphing. Un maillage raffiné de 60 millions de cellules (6 x fois le maillage utilisé par l'OES) est crée. Celui-ci est adapté à la modélisation hybride DDES-OES pour mieux capturer les structures de petites échelles avec la LES dans la partie de sillage. Les simulations hybrides ont montré les mêmes effets obtenus par le modèle OES. Des rouleaux tri-dimensionnels bien organisés injectés dans le sillage par les vibrations du bord de fuite. Ces derniers sont entourés par des petits tourbillons fins « vortex-filament » qui sont filtrés par le modèle OES. Les forces aérodynamiques sont aussi analysées, le morphing induit une augmentation considérable de la portance jusqu'à +4.28 % et refrène l'augmentation de la traînée à cause du rétrécissement du sillage qui augmentera finalement la finesse aérodynamique portance-sur-drag de +1.61 %.

MORPHING ELECTROACTIF DU LARGE-SCALE HYPERSUSTENTATEUR AVEC LES VIBRATIONS DU BORD DE FUITE

Le prototype LS contient deux éléments aile-volet fixés à la position de décollage ou le volet est translaté et orienté de 10 degrés à partir de sa position originale. L'angle d'incidence est fixé à 8.2 degrés et le Reynolds à 2.25 millions. Une comparaison des mesures de pression instationnaires est faite avec l'expérimentation conduite à la soufflerie de l'IMFT. La PSD de ces signaux est calculée et a montré différentes fréquences prédominantes liées à des instabilités situées dans le sillage. Les fréquences numériques correspondent à celles capturées en expérimentale. Le von Kármán mode a une fréquence de 10 à 30 Hz et les zone de cisaillement créée par l'aile et le volet ont des fréquences plus hautes. Le morphing est ensuite analysé par les vibrations du bord de fuite du volet. Une étude paramétrique de la fréquence et l'amplitude est effectuée et a montré une augmentation de la fréquence d'actuation entraîne une diminution du mode de von Kármán et un rétrécissement de sillage (voir figure 3). La PSD est ensuite calculée pour différents endroits situés dans le sillage proche et lointain et a révélé une diminution de ces sources de bruit jusqu'à – 15 dB. La POD a dévoilé que ces vibrations a haute fréquence associées à des petites déformations induisent une atténuation de ces modes d'instabilités observé de la PSD des coefficients temporaux des modes de la POD. Les simulations avec la DDES-OES sont aussi analysées pour un maillage de 30 millions avec une envergure minimale. Une suppression des dislocations des tourbillons (source d'augmentation des RMS des signaux de la traînée) est obtenue dans le sillage proche. Le morphing augmente la force de portance aérodynamique jusqu'à +0.57 %.

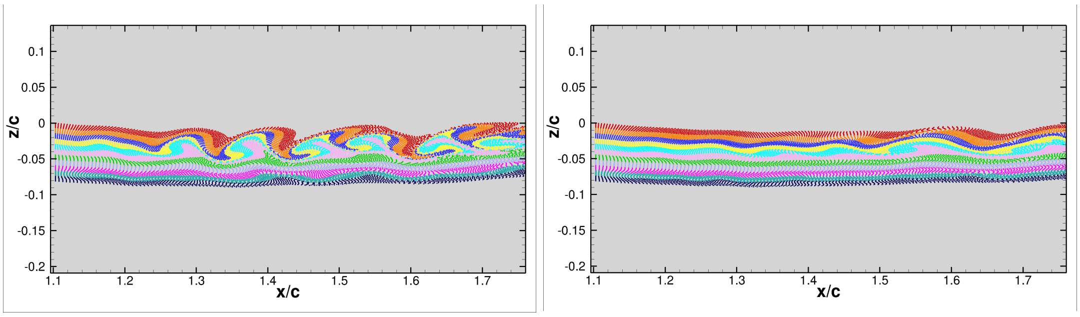

(A) Static case

(B) f_a=300 Hz

FIGURE 3: Visualisation en Streaklines pour le système hypersustentateur

MORPHING ELECTROACTIF DU SYSTEME HYPERSUSTENTATEUR AVEC CAMBRURE DU VOLET

Le second axe concerne un autre modèle aérodynamique basé sur la configuration d'une soufflerie de l'IMFT qui a la capacité de contenir le modèle Large-Scale, celle-ci est équipée d'une vaine ouverte facilitant la génération de maillage et de réaliser des simulations aux conditions proches de la réalité. Nous avons ainsi développé un modèle similaire visant à déformer le volet aérodynamique de 2 mètres d'envergure avec des Actionneurs Electro-Mécanique « Electro-Mechanical Actuators ». Ces actionneurs implémentés à l'intérieur du volet hypersustentateur peuvent résister à des grandes forces de pression imposées par l'écoulement de l'air. Des grandes déformations de l'ordre 10 cm portant sur 85 % de la corde du volet depuis son bord de fuite sont associées à des fréquences lentes sont obtenues numériquement dans le code NSMB avec les mêmes lois de comportement expérimental ayant un but de produire une forte augmentation des performances aérodynamiques. Une étude approfondie de l'effet de la descente dynamique et l'hypothèse quasi-statique est faite par rapport à l'évolution de la trainée et la portance. De plus, différentes positions de cambrure du volet hypersustentateur ont été sélectionnées afin d'optimiser la finesse aérodynamique. Des résultats obtenus par une validation numérique et expérimentale ont montré une augmentation de la dépression (accélération d'écoulement) dans l'extrados du volet (partie supérieure) et celui de l'aile à cause de la grande cambrure apportant des taux élevés de performances aérodynamiques (plus de portance). Mais à grands angles d'incidence, une perte de finesse aérodynamique est constatée, celle-ci créée à cause l'effet corps dominant de l'ensemble de l'aile et le volet et aussi la séparation de la couche limite proche du bord de fuite cela augmentera l'épaisseur du sillage et induira beaucoup de trainée. L'effet de la vitesse est aussi examiné qui montre que en augmentant le Reynolds la couche limite autour de la paroi de l'aile et le volet devient plus turbulente et énergétique, ce qui cause un retard dans la séparation et une diminution du taux d'augmentation de la trainée. Ceci est finalement bénéfique pour des cas des vols réels à très grand nombre de Reynolds. En utilisant une cambrure avec un angle d'incidence intermédiaire, nous pouvons augmenter la finesse aérodynamique jusqu'à +3.26 % et +8 % comparé à une configuration de référence en décollage normal.

D'après ces résultats prometteurs, un modèle de cambrure est ensuite implémenté dans le code afin de modéliser la cambrure des volets hypersustentateurs de l'avion complet Airbus A320 (fuselage, une aile en flèche, deux volets, deux becs, des gouvernes horizontales, verticale et une structure d'un turbo-fan avec son attache) à une échelle réelle. Une cambrure intermédiaire est examinée et comparée à une configuration de référence (sans cambrure). Les champs de dépression sur les volets, l'aile et la jonction aile-fuselage sont augmentés (voir figure 4) cela produit une augmentation dans les forces aérodynamiques qui est de +2.24 % sur la finesse aérodynamique comparée à la référence.

Plus récemment Airbus a lancé un projet en interne appelé Morphing In Thor 'MinoThor' qui consiste à implémenter un volet hypersustentateur en morphing électroactif dans UAV Drone et le tester dans un vol réel. Dans ce contexte, des simulations numériques de cambrure ont été faites. La cambrure en descente a montré les mêmes effets que le chapitre précédent. De plus, la cambrure vers le haut testée à des grands angles d'incidences dans des conditions extrêmes ou le détachement de la couche limite est très importants qui peut induire un décrochage et une grande perte de performances. A l'aide de cette cambrure en haut, un re-attachement la couche limite sur l'extrados de l'aile et une suppression de cette recirculation. Cette dernière s'approche du bord d'attaque lorsque l'angle d'incidence augmente. Cela induit une forte diminution

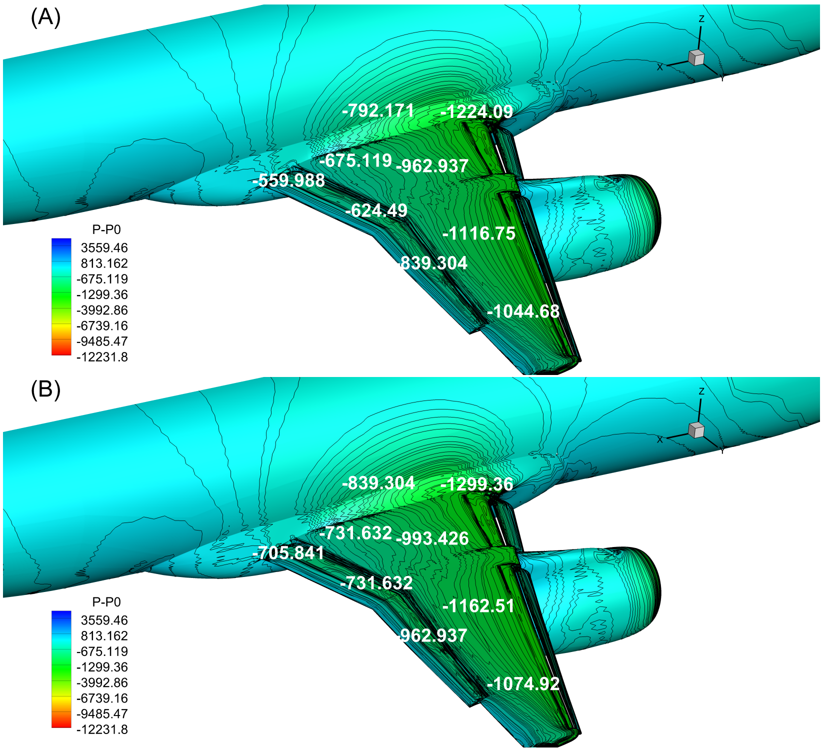

FIGURE 4: Iso-surfaces de la difference de pression pour l'avion Airbus A320, angle d'incidence 4°. (A) : reference, (B) : cambrure position P1

des instabilités créées à cause du cisaillement fort. En résultats, la trainée est fortement réduite et une augmentation de la finesse aérodynamique tout en retardant le décrochage aérodynamique. Cela induit une forte baisse de consommation de carburant (Kérosène) et produire moins de gaz à effet de serre point de vue environnementale.

MORPHING ELECTROACTIF HYBRIDE DE L'AVION AIRBUS A320 EN POSITION DECOLLAGE

Les oiseaux changent la forme de leur aile selon chaque phase de vol en utilisant des plumes et des muscles. Le morphing hybride constitut à associer les deux types d'actionnement pour obtenir des déformations et des vibrations partiellement bio-inspirées. Un modèle de morphing hybride est implémenté avec succès dans le solveur, ceci permet en utilisant différentes conditions aux limites de déformer le volet avec la cambrure et en associant les vibrations de bord de fuite. Une cambrure quasi-statique intermédiaire P1 = 3cm et une vibration de bord de fuite à haute fréquence de 300 Hz sont couplés ensemble. Les forces aérodynamiques pour toutes les composantes de l'avion sont ensuite calculées pour le morphing hybride, la cambrure seule et la référence. Une diminution de la traînée totale de l'avion est atteinte en utilisant le morphing hybride jusqu'à -0.78 % comparé à la cambrure seule. Ceci est obtenu seulement en ajoutant les vibrations du bord de fuite qui rétrécissent l'épaisseur du sillage ce qui augmente la finesse aérodynamique jusqu'à +0.50 %. Le morphing hybride améliore le gain en performance aérodynamique comparé à la cambrure seule et peut atteindre jusqu'à +2.74 % en gain de finesse comparé à une configuration de décollage standard (voir figure 5).

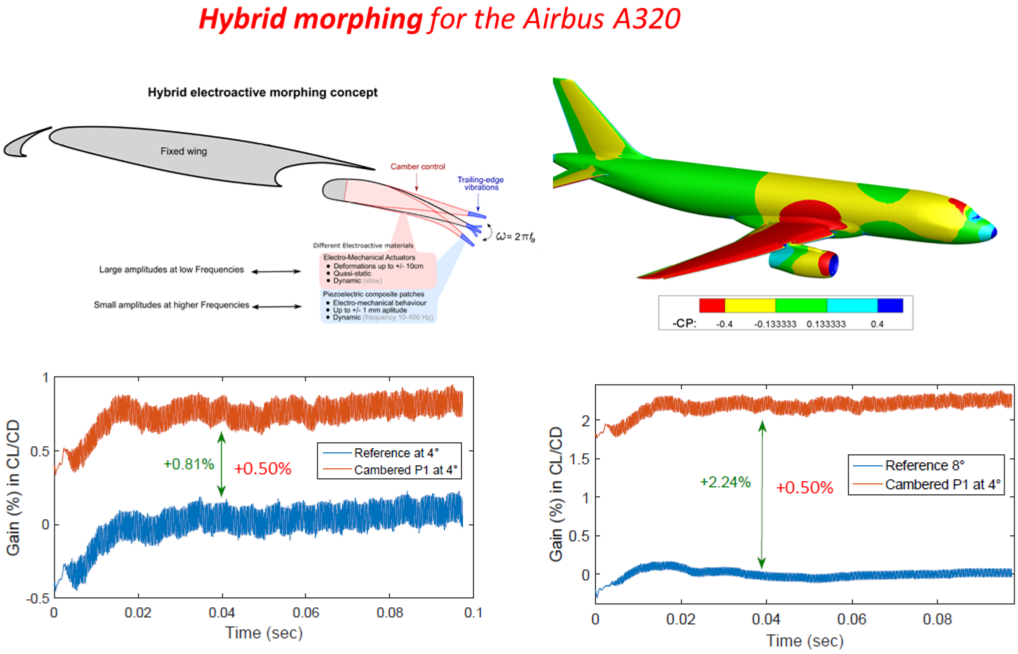

FIGURE 5: morphing hybride, concept et gain en efficacité aérodynamique

CONCLUSION

La présente thèse a étudié les concepts de morphing pour une aile A320 à échelle réduite (Reduced-Scale) et à échelle proche au réelle (Large-Scale) à l'aide des simulations numériques Haute-Fidélité impliquant une modélisation de la turbulence adaptée en nombre de Reynolds élevé.

Les concepts de morphing étudiés sont basés sur des dispositifs électroactifs embarqués dans les prototypes du projet Européen SMS "Smart Morphing and Sensing for Aeronautical configurations (`http://smartwing.org/SMS/EU/`)" H2020 N°723402 et coordonné par l'INPT (Toulouse Institut National Polytechnique).

Deux ailes de morphing électroactif différentes ont été étudiées, d'une échelle réduite de corde de 70 cm à une application à échelle réelle pour l'avion Airbus A320.
L'originalité du morphing électroactif proposé est de relier la compréhension fondamentale à travers la manipulation des tourbillons de turbulence proche de la région du bord de fuite et dans le sillage, à des différentes échelles de temps et de longueur de celles qui régissant le spectre de turbulence. Ces concepts sont bio-inspirés de la façon dont les oiseaux de chasse de grande envergure cambrent les ailes principales, leurs ailerons et leurs plumes, réalisant simultanément l'augmentation de la portance, la réduction de la traînée et la réduction du bruit aérodynamique. Une partie de cette thèse est consacrée à l'association de la basse fréquence/haute déformation avec des actionnements à haute fréquence/faible déformation, dans ce qu'on appelle par l'équipe multidisciplinaire IMFT-LAPLACE *le morphing électroactif hybride* ©.
Il est à noter que la présente thèse a été menée en synergie avec les expériences du projet SMS pour lequel les études numériques ont permis de définir les plages optimales des paramètres d'actionnement et les formes optimales à atteindre, ce qui a permis aux expériences de confirmer l' augmentation aérodynamique des performances indiquée par les présentes simulations. La présente thèse a offert une compréhension des effets de morphing qui ont aidé à découvrir les concepts optimaux et les gammes paramétriques, offrant ainsi les meilleurs avantages.
Le présent travail met en évidence les avantages considérables des concepts de morphing, en partie bio-inspirés par l'injection de structures turbulentes bénéfiques capables de manipuler la turbulence cahotique et les structures cohérentes du sillage. Les actionnements étudiés numériquement dans la présente thèse sont indépendants du type d'actionneurs de morphing. La cambrure peut être réalisée par des Alliages à Mémoire de Forme (AMF), comme dans d'autres parties du projet SMS et différents types d'actionneurs piézo (autres que les MFC) peuvent être utilisés pour réaliser les vibrations à plus haute fréquence, comme par exemple les systèmes d'actionneurs push-push concernant d'autres prototypes des équipes associées au-delà du projet SMS. Par conséquent, les bénéfices évalués par cette thèse ont un caractère plus général.
Les principaux résultats des actionnements du bord de fuite sont mis en évidence comme suit:

- Suppression des dislocations tridimensionnelles dans le sillage et atténuation de la croissance d'instabilité secondaire. Réduction de la zone de recirculation à proximité du bord de fuite et rétrécissement considérable du sillage dû à l'injection de tourbillons à plus petite échelle à une fréquence proche de la fréquence propre de l'instabilité de la couche de cisaillement, renforçant un effet de blocage et un rétrécissement de la couche de cisaillement, ainsi que déplacer le von Kármán mode plus en aval.

- Le transfert d'énergie vers le haut dans les modes POD conduit à un effet de blocage des tourbillons et contribue au rétrécissement observé du sillage.
- L'analyse spectrale du prototype RS a révélé une atténuation des sources de bruit aérodynamique de -20 dB et dans le cas du LS, -15 dB en raison du blocage, du rétrécissement des tourbillons de la couche de cisaillement et l'atténuation de la fréquence naturelle du von Kárm'an dans le sillage.
- Amélioration de la portance moyenne de $+4,28$ % et la finesse aérodynamique de $+1,61$ % dans l'échelle réduite 3D, tandis qu'une amélioration de la portance de $+0,55$ % et on observe $+2$% en portance-traînée pour le prototype LS.

Les principaux résultats du prototype LS (impliquant un volet cambré à grande échelle) sont soulignés comme suit:

- Les résultats numériques sont en bon accord avec les expériences concernant les spectres de la pression fluctuante, qui révèlent les principaux modes de fréquence et leurs interactions régissant l'aile / volet. Les résultats PIV supplémentaires obtenus de POLIMI sont en bon accord avec les résultats numériques.
- Associer une cambrure vers le bas dans le volet (cambrure 1) conduit jusqu'à + 3.26 % de gain sur les performances aérodynamiques du prototype Large-Scale.
- Augmentation de la finesse aérodynamique jusqu'à $+2,24$ en utilisant le volet cambré dans l'avion Airbus A320 en condition de décollage plus que la configuration conventionnelle de référence.
- La cambrure vers le haut à des angles d'attaque élevés a permis de re-attacher l'écoulement, de supprimer la recirculation et de réduire l'épaisseur du sillage. Par conséquent, la traînée est considérablement réduite et la finesse est amélioré jusqu'à $+108$ % bien sûr ces bénéfices sont indicatifs et suggéreraient de bonnes tendances en cas de besoins de manoeuvre (rafales modifiant brusquement l'incidence), où des angles d'attaque aussi élevés se produiraient pour de courtes phases de vol.

Enfin, les avantages du morphing hybride sont résumés comme suit:

- Implémentation et simulation du morphing hybride pour un véritable avion Airbus A320 dans le code NSMB couplant simultanément la meilleure cambrure et la meilleure vibration de bord de fuite des étapes précédentes.

- Les performances aérodynamiques sont plus améliorées en utilisant le morphing hybride sur l'avion Airbus A320 mieux que le contrôle seul de cambrure ou uniquement les vibrations de bord de fuite. Une diminution de la traînée de -0,78 % et une augmentation de la finesse de +0,50 % sont obtenues par rapport à la seule utilisation du cambrure.

Une caractéristique principale associée à tous les concepts de morphing analysés dans la présente thèse est l'énorme bénéfice provenant des effets du morphing manipulant la turbulence dans la partie arrière et redistribuant de manière optimale la pression sur toute la surface de l'aile, grâce à l'interaction avec le les couches de cisaillement et le sillage. Par conséquent, nous avons utilisé l'instabilité pour couper les tourbillons nuisibles et pour améliorer les tourbillons bénéfiques, en partie comme le font les oiseaux de chasse de grande envergure. Cette idée principale de *"Smart wing design through Turbulence Control - Science imitating Nature"*, issue des dix dernières années d'études de l'équipe pluridisciplinaire IMFT-LAPLACE (voir le film dédié du CNRS Journal, `https://lejournal.cnrs.fr/videos/the-wings-of-the-future` a été vérifié, confirmé et développé par la présente thèse dans le cadre du projet SMS EU, `www.smartwing.org/SMS/UE`.